Development of Bioorthogonal Reactions Using 3-Oxidopyridiniums and Expanding the Biological Applications of Cyclic Nitrones

Mariam Serhan

A Thesis Submitted In Partial Fulfillment of the Requirements for the Master's Degree in Chemistry and Biomolecular Sciences

Department of Chemistry and Biomolecular Sciences
Faculty of Science
University of Ottawa

Abstract

Bioorthogonal chemistry is a rapidly growing field that enables spatiotemporal monitoring of biomolecules using targeted probes. The development of bioorthogonal reactions therefore requires several criteria to be met. Reactions need to be selective, and fast enough so lower concentrations of reagents are used to mitigate toxicity, and they need to be stable in biological environments. 3-oxidopyridiniums are a class of water stable six-membered heteroaromatic latent dipoles, and have been previously reported to undergo [3+2] cycloadditions with electron deficient dipolarophiles, but have yet to be investigated for bioorthogonal use. To test their applicability as a bioorthogonal reagent, a series of N-methyl-3-oxidopyridiniums were synthesized with varying substituents on the 5 position and were reacted with DIBO (dibenzocyclooctyne). Electron donating 5-substituents have been shown to significantly increase the rate of the reaction, with bimolecular rate constants ranging from 3.31×10^{-4} with 5-trifluoromethyl-N-methyl-3-oxidopyridinium to 1.07 M^{-1} s^{-1} with 5-amino-N-methyl-3-oxidopyridinium, putting the faster reactions on par with commonly used bioorthogonal reactions for cell labelling.

Strain-promoted alkyne-nitrone cycloadditions (SPANC) are a class of [3+2] cycloadditions that are commonly used for bioorthogonal reactions. In comparison to their predecessor SPAAC (strain promoted azide alkyne cycloadditions), SPANC offers much better reaction tunability. icSHAPE (*in vivo* click selective hydroxyl acylation analyzed by primer extension) is a labelling technique used to determine RNA structure. This is done by selectively targeting the 2' hydroxyl on the ribose sugar of RNA that is structurally available in regions of RNA that are single stranded, and the use of SPAAC allows for an improved signal to noise ratio. Herein, DMImO (1-[(p-methoxycarbonylphenyl)methyl]-2,2-dimethyl-5-oxo-3-imidazolin-3-ium-3-olate), a previously used nitrone in SPANC reactions, has been modified to include an electron deficient carbonyl

imidazole to allow for a nucleophilic attack from the 2' hydroxyl of the RNA. Hydrolysis of the nitrone probe is on par with previous SHAPE reagents that are used for *in vivo* labelling and is able to label 5S rRNA for structure determination as effectively as previously used SHAPE reagents.

Statement of Work

The entirety of the work presented herein is my own and I take full responsibility for its content. Except for generating the computational data in Section 2.3.6 and the *in vitro* and *in vivo* 5S rRNA labelling in Section 3.3.4, all experiments were conducted by me. All analysis (regardless of source) was conducted by me as well.

Acknowledgements

My time as a graduate student at the Pezacki Lab has been an incredibly rewarding experience. I am especially grateful for having a supportive network encouraging me through my studies. To my supervisor, Dr. John Pezacki, thank you for promoting an enriching work environment that fosters both collaboration and self-reliance. As someone who enjoys being a jack-of-all-trades, I enjoyed the opportunity to hone my chemistry skills, while also being able to try my hand at some biochemistry techniques. Thank you, John, for your support, encouragement, and understanding over these last few years, and for ensuring that I reach my potential. A special thank you to the members of my advisory committee, Dr. Adam Shuhendler, and Dr. Christopher Boddy for your advice and for taking the time to read my thesis. I look forward to hearing your comments.

Another big thank you goes to my colleagues at the Pezacki Lab, especially to Dr. Shadi Sedghi Masoud. Working alongside you and learning from you has been a highlight of my time here and I am very grateful for your mentorship. To Didier Bilodeau and Kaitlyn Margison, thank you for training me when I first joined the lab and for your support. To the rest of the chemists, thank you for the camaraderie. My thanks also go out to the senior biochemists in the lab for always willing to answer my questions and especially to Nadine and Noreen Ahmed for helping me plan my biochemistry experiments. Outside the lab I'd like to also thank Amrah Nasim and Salma Alasmar-Abdou of the Newman and Ben lab respectively for their constant friendship and support. Another big thank you goes to Dr. Peter Pallister and Dr. Sharon Curtis for their help with NMR and MS experiments respectively.

Outside of the lab, I have been blessed to be surrounded by amazing people. To my parents, you have supported me in ways that I don't know how to repay, and I am forever grateful to know that I can

always rely on you. You have both survived the impossible only to start over in a new country so my brothers and I have the luxury of chasing our dreams. I'm proud to be your daughter. To my brothers, the OG besties, the OG partners in crime, thank you for always having my back, cheering me up, and always willing to be my culinary experiment testers. To my friends, words aren't enough to explain how much your love and support over these last years mean to me. You have all been my rock, thank you.

Dedication

To my grandmothers, Aziza and Mariam. Your bravery, intelligence, grace, and compassion has given me the courage to face the world with open arms. Your *dua'a* are still protecting me to this day, and I miss you both very much.

List of Figures

List of Tables

List of Schemes

List of Abbreviations

1M7	-	1-methyl-7-nitroisatoic anhydride
3-OXP	-	3-oxidopyridinium
ABPP	-	activity based protein profiling
AcN	-	acetonitrile
ATP	-	adenosine triphosphate
BARAC	-	biarylazacyclooctynone
BCN	-	bicyclo[6.1.0]non-4-yne
CDI	-	carbonyl diimidazole
CMPO	-	2H-Pyrrole-2-carboxylic acid, 3,4-dihydro-2-methyl-,1-oxide
COSY	-	correlation spectroscopy
CuAAC	-	copper(I)-Catalyzed Azide-Alkyne Cycloaddition
CuANCR	-	copper-catalyzed alkyne-nitrone cycloaddition followed by rearrangement
CuSAC	-	copper-promoted sydnone–alkyne cycloaddition
D/I	-	distortion/interaction
d-ATP	-	deoxyadenosine triphosphate
DBCO	-	dibenzoazacyclooctyne
DCM	-	dichloromethane
DIBAC	-	dibenzoazacyclooctyne
DIBO	-	dibenzocyclooctynol
DIFO	-	difluorinated cyclooctyne
DMAD	-	dimethyl acetylene dicarboxylate
DMImO	-	1-[(p-Methoxycarbonylphenyl)methyl]-2,2-dimethyl-5-oxo-3-imidazolin-3-ium-3-olate
DMPO	-	5,5-dimethyl-1-Pyrroline-N-Oxide
DMS	-	dimethyl sulfate
DMSO	-	dimethyl sulfixide
DNA	-	deoxyribonucleic acid
EDG	-	electron donating group
EGF	-	epidermal growth factor
EtOAc	-	ethyl acetate
EWG	-	electron withdrawing group
FAI	-	2-methyl-3-furoic acid imidazolide
FMO	-	fronteir molecular orbital
FP	-	fluorescent protein
FTIC	-	Fluorescein isothiocyanate
HEPES	-	N-2-hydroxyethylpiperazine-N'-2-ethanesulfonic acid
HER2	-	human epidermal growth factor receptor 2
HOMO	-	highest occupied molecular orbital
HRMS	-	high resolution mass spectrometry
HSQC	-	heteronuclear single quantum correlation
icSHAPE	-	in vivo click selective hydroxyl acylation analyzed by primer extension
IEDDA	-	inverse electron demand Diels-Alder

lncRNA	-	long non-coding RNA
LUMO	-	lowest unoccupied molecular orbital
MeOH	-	methanol
mESC	-	mouse embryonic stem cell
miRNA	-	micro RNA
MOFO	-	monofluorinated cyclooctyne
mRNA	-	messenger RNA
MS	-	mass spectrometry
NAI	-	2-methylnicotinic acid imidazolide
NAI-N3	-	2-methylnicotinic acid imidazolide - azide
ncRNA	-	non-coding RNA
NMIA	-	N-methylisatoic anhydride
NMR	-	nuclear magentic resonance
nOe	-	nuclear Overhauser effect
NOSY	-	nuclear Overhauser effect spectroscopy
nt	-	nucleotide
OCT	-	cyclooctyne
PET	-	positron emission tomography
piRNA	-	piwi-interacting RNA
POI	-	protein of interest
RNA	-	ribonucleic acid
ROS	-	reactive oxygen species
rRNA	-	ribosomal RNA
scFv	-	single chain variable fragment
SHAPE	-	selective hydroxyl acylation analyzed by primer extension
siRNA	-	small interfering RNA
sncRNA	-	small non-coding RNA
snoRNA	-	small nucleolar RNA
snRNA	-	small nuclear RNA
SPAAC	-	Strain-Promoted Azide-Alkyne Cycloaddition
SPANC	-	Strain-Promoted Alkyne-Nitrone Cycloaddition
SPSAC	-	strain promoted sydnone-alkyne cycloaddition
sTCO	-	strained trans-cyclooctene
TLC	-	thin layer chromatography
TMS	-	trimethyl sliane
TMTH	-	3,3,6,6-tetramethylthiacycloheptyne
tRNA	-	transfer RNA
TS	-	transition state
UAA	-	unnatural amino acid
UV-Vis	-	ultra violet-visible

Table of Contents

Chapter 1

Introduction

1.1 Bioorthogonal Chemistry: Click Chemistry Adapted for Biological Environments

1.1.1 Bioorthogonal Chemistry as a Tool for Labeling Biomolecules

For a comprehensive understanding of the cellular and molecular processes of life, biomolecules such as lipids, nucleic acids, proteins, glycans, or metabolites, must be spatiotemporally monitored and tracked in their native environment.[1] Gene sequencing can shed light on gene and protein expression; biomolecules can be purified and isolated for elucidation, but none of these techniques allow for spatiotemporal monitoring. While attempts at genetically incorporating a tag such fluorescent proteins (FP) onto a protein of interest (POI) for cellular imaging have been highly successful for spatiotemporal monitoring and tracking, they are not without their pitfalls. FPs are relatively larger proteins and can potentially disrupt the POI's structure, localization, and function. Tracking POIs with genetically incorporated FPs are also limited to optical methods. Most importantly, FP tagging can only be used on proteins, excluding a wide range of biomolecules.[2] Antibody conjugates can be designed for specificity for any epitope which can include a wide range of biomolecules. However, similarly to FP tagging, the sheer size of antibodies limit which antigens can be tracked inside and outside the cell.[3]

The gap between the biochemistry techniques of the late 1990's and the need for a thorough understanding of biological processes lead to the development of bioorthogonal chemistry. Over the last two decades, bioorthogonal reactions have emerged as versatile and precise forms of tracking, labelling, quantifying, and manipulating various biomolecules in their respective biological environment. Bioorthogonal reactions, as coined by Carolyn Bertozzi and colleagues in 2003[4], refers to reactions that are orthogonal to all native biological functional groups, highly selective for the

reaction partner, have minimal to no side products, and exhibit fast kinetics. Bioorthogonal reagents and their products must be non-toxic, stable at physiological conditions (biological temperature, pH, and aqueous compatible), and have minimal structural and functional perturbation of the targeted biomolecule.[5,6]

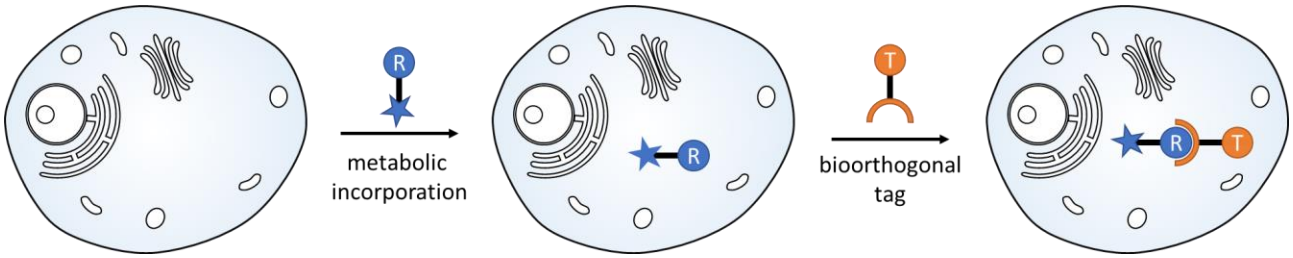

Figure 1.1: Typical use of bioorthogonal reactions in biological environments. Star = metabolic substrate R = chemical reporter, T = bioorthogonal tag. Adapted from E. M. Sletten et al[1].

Typically, the use of bioorthogonal chemistry to label biomolecules occurs in two steps (Figure 1.1). The first step involves the incorporation of a chemical reporter into a biological system. Chemical reporters are metabolic substrates, ligands, or enzyme inhibitors that have a minimally invasive bioorthogonal functional group (Figure 1.1 R) and as such are easily incorporated into the biomolecule using the cell's biosynthetic machinery or through genetic encoding. Once the reporter is incorporated into its target, the second step is a bioorthogonal reaction using an exogenously delivered bioorthogonal tag. These tags contain the complementary functional group and a probe (ie: affinity handle or fluorophore) to either label, track, isolate or visualize the targeted biomolecule.

1.1.2 Click Chemistry

In bioorthogonal reactions, faster reaction rates with high specificity are sought after as it can minimize the amounts of reagent used in a labeling experiment, thereby mitigating potential cytotoxicity. Faster kinetic rates, in general, can be achieved by increasing the temperature of the reaction, the introduction of a catalyst, or increasing the concentration or surface area of a reagent. However, for the most part, these methods cannot be applied to bioorthogonal reactions and so from

an organic chemistry perspective, the requirements for bioorthogonal reactions are highly limiting in terms of what reagents or reactions can be adapted into bioorthogonal reactions.

Click chemistry, as initially described by Kolb, Finn, and Sharpless in 2001[7], refers to a specific subset of reactions that takes inspiration from nature's preference to form carbon-heteroatom bonds over carbon-carbon bonds in the synthesis of the primary metabolites used to form much larger and intricate secondary metabolites. Click chemistry is therefore used to synthesize larger, more complex structures reliably and easily by conjugating smaller, highly reactive, and very stable substrates with heteroatom links. For a click reaction to be effective, it must follow a specific set of rules. The reaction must be modular and tunable with a wide scope, involve simple reaction conditions, insensitive to both oxygen and water, use easily accessible reagents, and use easily removable solvents or no solvent. Ideally a single stereospecific product is formed in high yields, can be easily isolated and purified, any side products are innocuous, and all products are stable at physiological conditions. This combination of conditions can only be achieved with "spring-loaded' reactions which have a thermodynamic driving force of greater than 20 kcal mol^{-1} and are highly chemoselective for a single product[7].

1.2 Common Bioorthogonal Reactions

1.2.1 Carbonyl Condensation with Amine Nucleophiles

In acidic conditions, weakly nucleophilic amines attack carbonyl electrophiles to form a Schiff base that is not favoured by equilibrium. In an analogous reaction that uses amines enhanced by the α effect such as hydrazides and alkoxyamines, the formation of an imine is favoured instead, forming stable hydrazone and oxime adducts. While carbonyls are susceptible to attack by biological nucleophiles (ie: alcohols, thiols, amines), at physiological conditions, the carbonyl is favoured, making them useful bioorthogonal chemical reporters. Their smaller size also enables for easy incorporation onto biomolecules with a lower chance of perturbing native functionality.[8]

However, in complex biological settings, carbonyl chemical reporters are "biorestricted"[2]. Within cells and in biological fluids are plenty of keto and aldehydic metabolites such as free sugars, pyruvate, oxaloacetate, and co-factors like pyridoxal phosphate, limiting effective bioorthogonal reactions to the cell surface or extracellular environment.[2] The optimal pH of this reaction is within 5-6, which is unfeasible in typical intercellular environments, and even at optimal pH levels, the reaction still requires significantly higher concentrations of reagent to compensate for slower kinetics (Scheme 1.1a). These limitations were addressed by Zeng et. al in a 2009 paper that demonstrated effective labeling of cell-surface sialic acid containing glycans on live cells.[9] Aldehydes were introduced either *in-situ* with $NaIO_4$ or by metabolically incorporating sialic acid analogs that were taken up by the cell and presented on the surface. Aniline catalysis was able to drastically improve the reaction rate, even at neutral pH, to allow for efficient labelling of cells using aminooxy-biotin at lower concentrations (Scheme 1.1b).

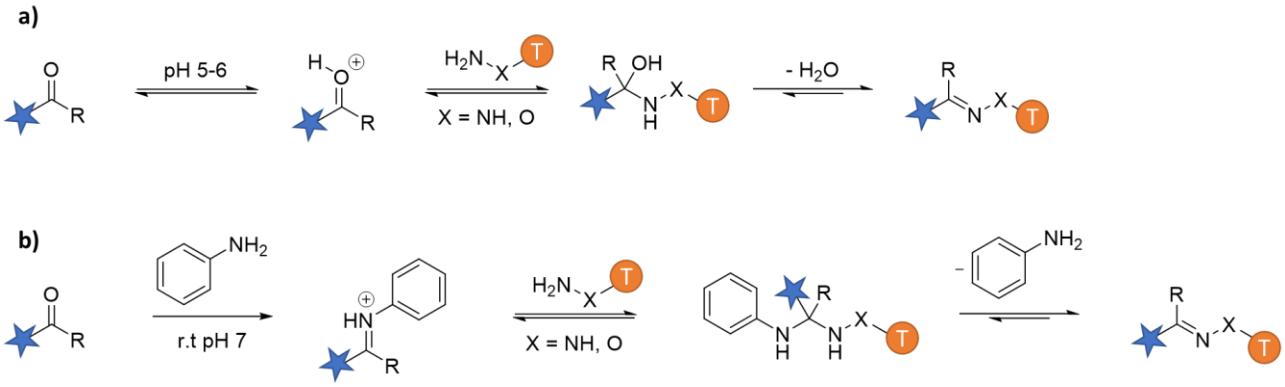

Scheme 1.1: Condensation of aldehyde/ketones with reactive amines for bioorthogonal labelling. a) acid-catalyzed b) aniline-catalyzed. Star = biomolecule, T = biotin tag.

1.2.2 Staudinger Ligation

With the exception of one naturally occurring metabolite, azides are not found in biological systems[10], removing many of the spatial limitations found in bioorthogonal reactions involving carbonyl condensations with nucleophilic amines. In terms of stability, azides are resistant to oxidation and don't react appreciably with water further lending its applicability to bioorthogonal

reactions. While slightly electrophilic, azides do not react with "hard" nucleophiles in biological systems like aldehydes or ketones would, but with "soft" nucleophiles instead, making them susceptible to reduction by free thiols. However, this reduction typically occurs at elevated temperatures, as does azide decomposition, making azides stable at physiological conditions[2].

The first iteration of the Staudinger ligation is the Staudinger reaction, reported by Staudinger in 1919, which involves the formation of primary amines at room temperature from azides when treated with triphenylphosphines, forming a phosphazide intermdiate[11]. The phosphazide loses nitrogen gas to form the aza-ylide intermediate which is hydrolyzed to form the amine and respective phosphine oxide. The Staudinger ligation is a modified version of the classic Staudinger reaction where one of the aryl substituents on the phosphine is replaced with an ester group as an electrophilic trap, capturing the nucleophilic aza-ylide, ultimately forming an amide bond[12]. This reaction was first used in a bioorthogonal setting to label cell surfaces of both HeLa and Jurkat cells using an azide modified mannose, N-azidoacetylmannosamine, that is incorporated into the sialic acid biosynthesis pathway. A biotinylated phosphine was used to detect the ligation of the azido-sugar with the phosphine moiety using an FTIC (Fluorescein isothiocyanate) -avidin stain.[13]

Shortly after the development of the Staudinger ligation, various phosphine reacting partners were developed, including phosphines with cleavable electrophilic traps. When reacted with an azide, an amide bond is formed through an acyl group transfer and phosphine expulsion, effectively leaving no "trace" of the phosphine in the traceless Staudinger ligation product[14,15]. This reaction has been proven to be versatile and chemoselective and as a result of the native amide bond formation, the traceless Staudinger ligation has been consistently used in natural and unnatural oligopeptide synthesis and modification, along with whole protein synthesis[16].

The biggest drawback to the Staudinger Ligation has been its slower reaction rates in comparison to other bioorthogonal reactions with k_2 values on the order of 10^{-3} M^{-1} s^{-1}.[1] Despite this, the Staudinger ligation is still popular for *in vivo* applications because of its compatibility and

selectivity[17]. Over the last decade, significant strides have been taken to improve kinetic rates, with the use of electron-poor aryl azides to react with phosphine probes, that prevents the hydrolysis of the iminophosphorane intermediate seen in Staudinger ligations[18,19]. The nonhydrolysis Staudinger ligation has reported rates with a range of k_2 = 0.63–139 $M^{-1} s^{-1}$, putting them on par with many other effective bioorthogonal reactions[12]. Azides, phosphorus nucleotides, products, and the rates of each iteration of the Staudinger ligation is summarized below (Table 1.1).

Table 1.1: Staudinger Ligations used in Bioorthogonal Chemistry. Star = biomolecule, T = bioorthogonal tag. Table adapted from T. K. Heiss et. al[12].

Reaction	***Azide***	***Phosphorus Nucleophile***	***Product(s)***	***Rates ($M^{-1} s^{-1}$)***
Staudinger Ligation		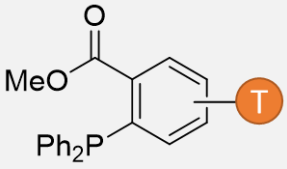	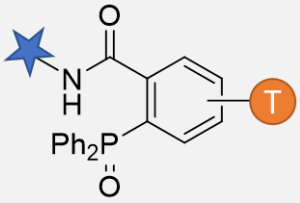	~10^{-3}
Traceless Staudinger Ligation		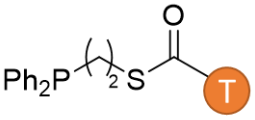	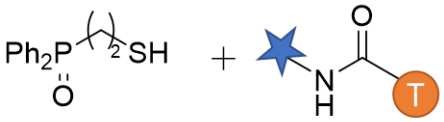	~10^{-3}
Nonhydrolysis Staudinger Ligation	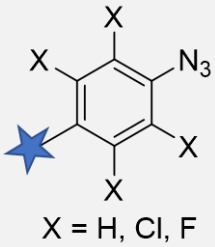	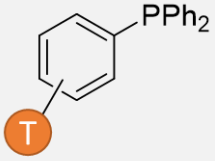	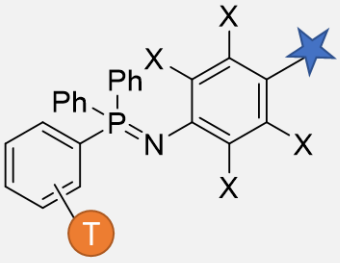	0.63 – 139

1.2.3 1,3-Dipolar Cycloadditions

Of the click reactions outlined by Sharpless and colleagues, many have been further developed into bioorthogonal reactions because of their chemoselectivity and fast kinetics. One of the most commonly known click reactions, the concerted 1,3-dipole cycloaddition reaction (also known as the [3+2] cycloaddition), is between a polarized 1,3-dipole of three atoms and a two atom dipolarophile forming a 5-membered ring system in a [$\pi 4_s + \pi 2_s$] fashion[20] (Scheme 1.2). Since its introduction by Huisgen in the 1960s[21], the [3+2] cycloaddition has been used in various

bioorthogonal reactions with a variety of different dipoles and dipolarophiles, but the fundamental theoretical basics of the 1,3-dipole cycloaddition are conserved between each reaction.

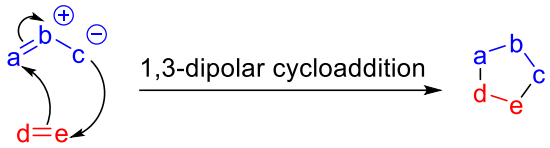

Scheme 1.2: General mechanism of concerted 1,3-dipolar cycloaddition reactions with dipoles and dipolarophiles.

Concerted cycloaddition reactions are controlled by frontier molecular orbital (FMO) theory and orbital symmetry conservation. FMO theory takes into consideration only the interactions (or overlaps) between the highest occupied molecular orbital (HOMO) and the lowest unoccupied molecular orbital (LUMO) and is used to offer a simpler and more efficient understanding of the reaction mechanisms of concerted reactions. According to the Woodward-Hoffmann rules, concerted cycloadditions occur so long as the reaction maintains bonding along the proposed concerted mechanism (ie: bonding orbital of one reactant overlaps with a bonding orbital of the other), whereas forbidden reactions would have antisymmetric overlap (ie: bonding orbital of one reactant overlaps with an anti-bonding orbital of the other)[22]. Figure 1.2 shows the which [3+2] concerted cycloadditions are allowed or forbidden based on its orbital symmetry and FMOs.

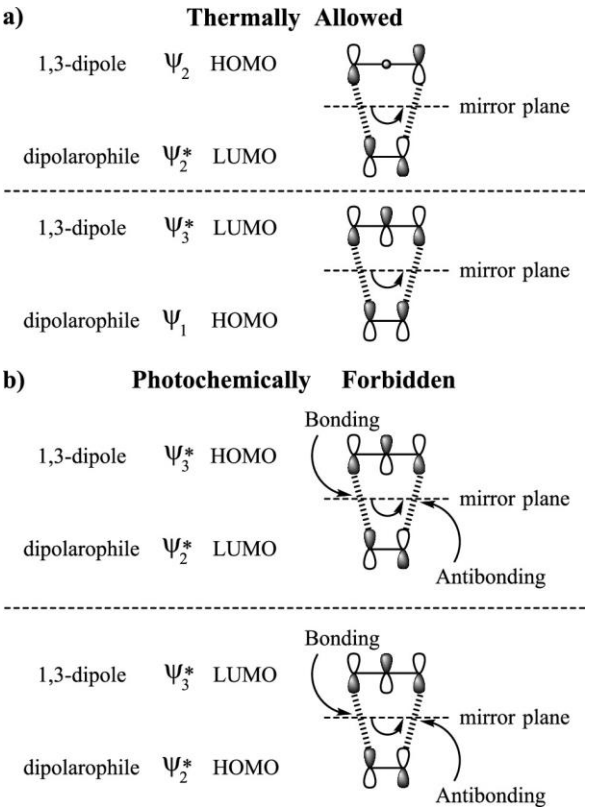

Figure 1.2: Frontier molecular orbital interactions of dipoles and dipolarophiles in [3+2] cycloadditions. Thermally allowed reactions (a) are allowed as the FMO are in a bonding orientation (b) photochemically forbidden since the FMO are not symmetrical and lead to anti-bonding orbitals. Reprinted with permission from Chem. Rev. ***2021****, 121 (12), 6850–6914. Copyright 2021 American Chemical Society*[20]*.*

Roughly a decade after the Woodward-Hoffmann rules were introduced, 1,3-dipolar cycloadditions were classified into three types by Sustmann based on the relative HOMO and LUMO energies of either the 1,3-dipole or the dipolarophile [23–25]. (Figure 1.3) In type I cycloadditions, the dominant interaction at the transition state is between the HOMO of the dipole and the LUMO of the dipolarophile. In other words, the HOMO-controlled dipole (also referred to as nucleophilic dipole), reacts with electrophilic dipolarophiles. The addition of electron withdrawing groups (EWG) to the dipolarophile would increase the rate of a type I reaction as it lowers the relative energy of the LUMO of the dipolarophile, while the addition of EDGs to a dipolarophile would increase the relative energy of the HOMO resulting in a slower reaction. For type III cycloadditions, the transition state is dominated by the interactions between the LUMO of the dipole and the HOMO of the dipolarophile.

The LUMO-controlled or electrophilic dipole reacts with a nucleophilic dipole. The addition of an EDG to a dipolarophile elevates the HOMO on the dipolarophile resulting in a faster type III reaction and EWG on dipolarophiles would decelerate a reaction as it lowers the LUMO. This type is also referred to as inverse electron demand and is featured in the tetrazine ligation (Section 1.2.4). In type II dipolar cycloadditions, the energy gap between each HOMO/LUMO pair is similar meaning that the transition state is dominated by the interaction between either the HOMO or LUMO of the dipole and the respective LUMO or HOMO of the dipolarophile (HOMO,LUMO-controlled).[26]

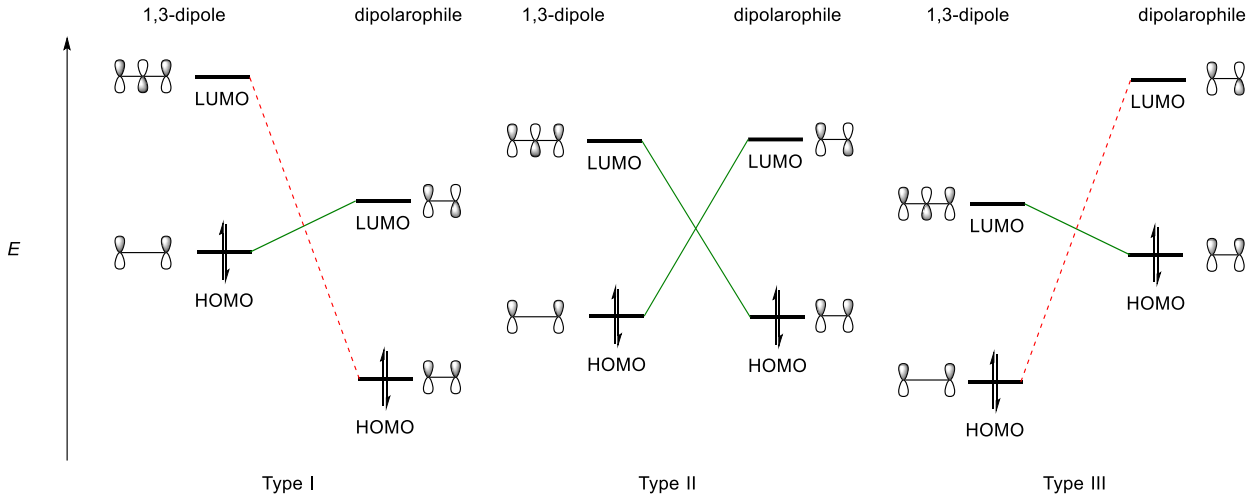

Figure 1.3: The three classifications of [3+2] cycloadditions based on the dominating orbital interaction. Type I reactions are HOMO controlled, type II is both HOMO and LUMO controlled, type III are LUMO controlled. Adapted from M. Breugst[26].

Dipoles in [3+2] cycloadditions are 3 atom systems, typically depicted as having an a-b-c structure with four π electrons delocalized across the three atoms. They are categorized into two general categories: allyl anion or propargyl/allenyl anion systems that describe their resonance systems (Figure 1.4). Allyl anion dipoles, such as nitrones, nitro compounds, and carbonyl ylides to name a few, have four resonance structures with either the central atom having an electron octet or as atom a or c having an electron sextet. The 4π electrons in allyl systems are in three parallel p_z orbitals that are perpendicular to the dipole plane, giving it a bent structure. For propargyl/allenyl

type anion dipoles such as nitrile oxides or azides, two resonance structures are drawn with the octet on the central atom[22].

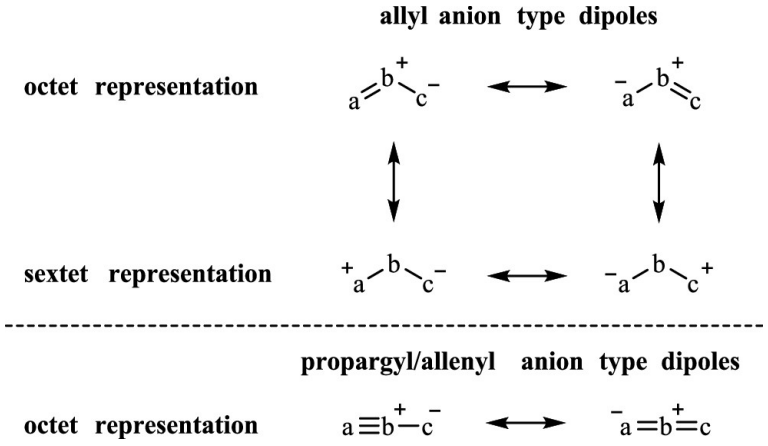

Figure 1.4: Two general categories of dipoles in [3+2] cycloadditions. Reprinted with permission from Chem. Rev. ***2021****, 121 (12), 6850–6914. Copyright 2021 American Chemical Society*[20]*.*

1.2.3.1 Copper(I)-Catalyzed Azide-Alkyne Cycloaddition (CuAAC)

As mentioned in Section 1.2.2, the azide functional group lends itself well for bioorthogonal reactions due to its relative inertness and small size. Alkynes, especially terminal alkynes, are unreactive with biological functional groups, stable in biological environment, and do not appear in higher eukaryotes, making them suitable for bioorthogonal reactions[27]. The Huisgen 1,3-dipolar cycloaddition between azides and terminal alkynes form 1,2,3-triazoles. However, the reaction is far too slow for use in biological environments, and would require high pressures and temperatures to go to completion[21]. Copper (I)catalyzed azide-alkyne cycloadditions were introduced in 2002[28,29], significantly increasing the rate of the Huisgen 1,3-dipoloar cycloaddition by a factor of ~10^7, and improving the regioselectivity for only the 1,4-disubstituted triazole[30]. These improvements, in combination with its versatility, tolerance for biological environments, and product resistance to chemical cleavage, resulted in the ubiquity of reaction in bioorthogonal settings[17]. The mechanism of the reaction was fully elucidated in 2013[31], describing that in the catalytic cycle, two equivalents of copper are used to activate the terminal alkyne towards the azide and the acetylide intermediate

contains two copper centers that coordinate both reagents (Scheme 1.3). Outside of biological contexts, CuAAC has been used in organic synthesis, polymer and materials chemistry[32]. The first biological application of the CuAAC reaction was the bioconjugation of dyes to the exterior surface of the capsid for cowpea mosaic virus[33]. Since then, CuAAC has been the bioorthogonal reaction of choice for visualizing biomolecules in fixed cells, isolating proteins in proteomics studies, activity based protein profiling (ABPP), and for monitoring small molecules such as enzyme inhibitors and therapeutic drugs[30].

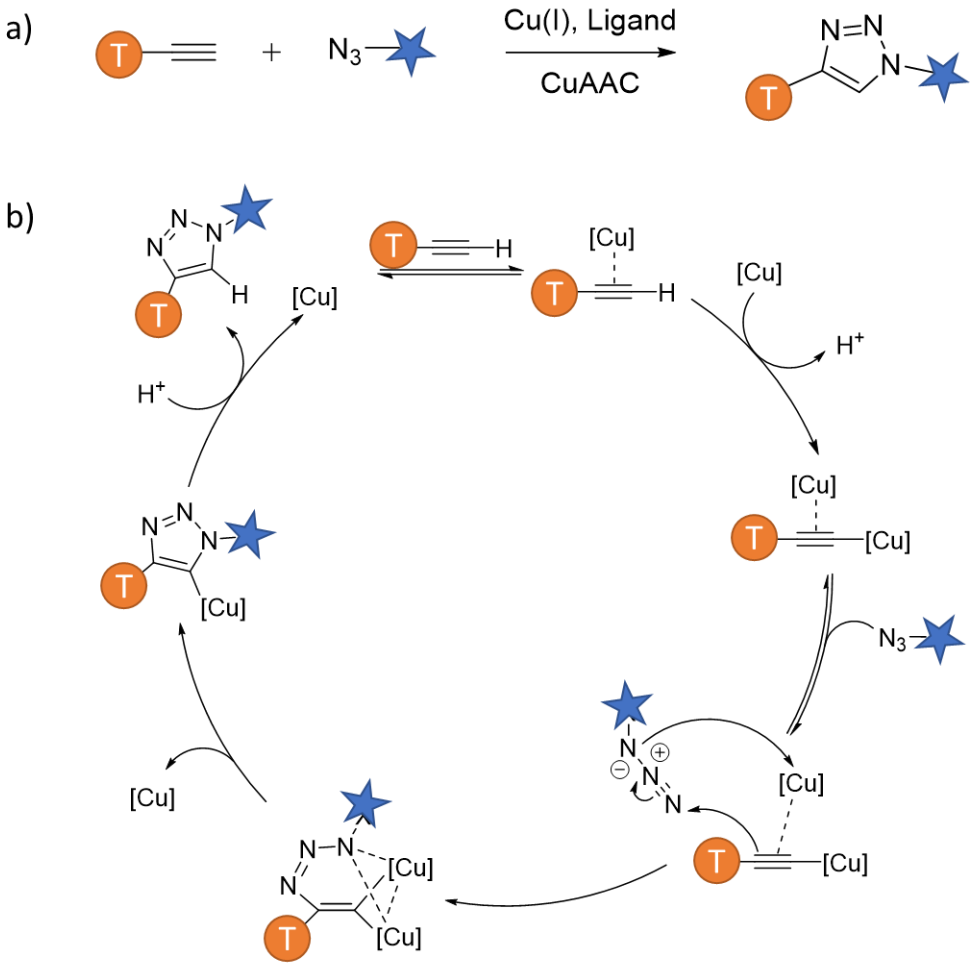

Scheme 1.3: a) General Reaction scheme and b) full catalytic cycle of CuAAC. Catalytic cycle adapted from C. S. McKay et. al[17].

Despite its success *in vitro*, CuAAC is not used as much *in vivo* studies due to its reliance on a copper catalyst. The use of copper catalyst in CuAAC reactions is associated with cytotoxicity arising

from the Cu(I)-promoted formation of reactive oxygen species (ROS) from O_2.[34,35] Cu(I) gets oxidized quickly in biological environments, requiring a reducing agent such as sodium ascorbate to regenerate Cu(I). This redox cycle generates reactive oxygen species, making the addition of copper in excess amounts infeasible due to toxicity concerns.[36]

Oftentimes a ligand is used to coordinate the copper to stabilize the Cu(I) oxidation state, prevent side products and increase the rate of the reaction. These ligands can also be used to mitigate cytotoxicity and scavenge copper. Typically, these ligands contain triazoles, and while they do diminish ROS, oxidation still occurs to free histidine and cysteine residues in proteins[37]. The addition of excess ligand in these conditions would scavenge ROS, but the increased ratio of ligand to catalyst would diminish the catalytic activity of Cu(I)[36]. The use of L-histidine as a catalytic ligand in CuAAC to form a Cu(I)-L-histidine complex is not only on par with the rates seen with other ligands, but is tolerated by human hepatoma cells at the millimolar concentration for up to 72 hours, where use with other ligands will result in cell death[35]. Another application for *in vivo* use was the successful labelling of zebrafish embryos using implanted copper nanoparticles. The embryos were able to develop to their larval stage, avoiding the reliance on the ligand[38].

1.2.3.2 Strain-Promoted Azide-Alkyne Cycloaddition (SPAAC)

The easiest way to mitigate the copper cytotoxicity prevalent in CuAAC is to completely eliminate the use of copper (I) catalyst in bioorthogonal reactions. In order to do that without the use of metals however, the ground state of either the azide or alkyne would have to be destabilized achieve fast enough rates. Strain-promoted azide-alkyne cycloadditions (SPAAC, Scheme 1.4), introduced by Agard N.J. et al[39], demonstrates that a reaction between an azide and an alkyne can occur at room temperature without a catalyst by introducing ring strain to the alkyne by way of a cyclooctyne (OCT). Adding structural stress to an endocyclic alkyne by changing its conformation or deviating from standard bond angles and lengths, results in increasing its internal energy. During

cycloaddition reactions, there is a release of ring strain due to a decrease in bond order, which results in an improvement in reaction rate[20].

Scheme 1.4: Strain promoted azide alkyne cycloaddition for bioorthogonal use. Star = biomolecule, T = bioorthogonal tag

Strain alone can only offer a surface level explanation of the fast kinetics seen with strained cyclooctynes. The distortion/interaction model (D/I model, also referred to as activation-strain model) postulates that the activation energy of a reaction is composed of the distortion energy ($\Delta E^{\ddagger}_{dist}$) and interaction energy ($\Delta E^{\ddagger}_{int}$) [40,41]. (Figure 1.5) Distortion energy is the energy needed to for the reactants to be distorted into their transition state configurations, it involves both the geometric and electronic changes from the ground state[40]. A transition state that's earlier along the reaction coordinate indicates that the reagents in their ground state are "pre-distorted" into their transition state geometry, resulting in a lowered $\Delta E^{\ddagger}_{dist,}$ which also correlates to a lower activation energy, suggesting that the reactivity of a reaction is indicated by $\Delta E^{\ddagger}_{dist}$. Interaction energy consists of attractive electrostatic and orbital interactions, and repulsive Pauli interactions. In the event of similar transition states amongst a series of dipolarophiles, interaction energies are the controlling factor[20,40].

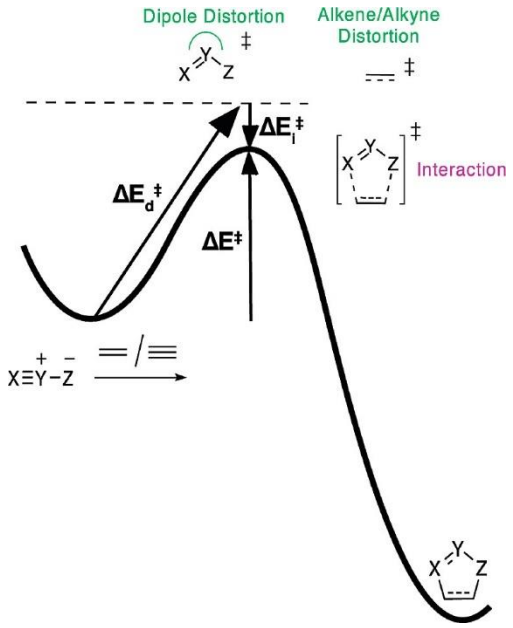

Figure 1.5: The relative relationships between distortion, interaction, and activation energies of a [3+2] cycloaddition. Reprinted with permission from J. Am. Chem. Soc. ***2008****, 130 (31), 10187–10198. Copyright 2021 American Chemical Society.*[40]

As a result of the development of strained alkynes, copper is no longer required for catalyzing the cycloaddition between an azide and alkyne, effectively improving the biocompatibility of the cycloaddition. While the first SPAAC cycloaddition with OCT and azide were used to fluorescently label cell surfaces, the rate of the reaction with benzyl azide was slow at a rate of 0.0012 M^{-1} s^{-1}.[39] Since then, various strained alkynes have been developed to increase strain and in turn increase the rate of the SPAAC reaction (Figure 1.6). Modifications to the initial cyclooctyne scaffold include the addition of electron withdrawing groups (fluorine) on the propargyl carbon (ie: MOFO and DIFO[42]), benzannulated cyclooctynes (ie: DIBO[43], DIBAC[44], and BARAC[45]), the addition of a cyclopropyl group opposite of the alkyne (ie: BCN[46]), and forming seven membered cyclic alkynes with a sulfur in place of the methylene group opposite to the alkyne (ie: TMTH[47])[48].

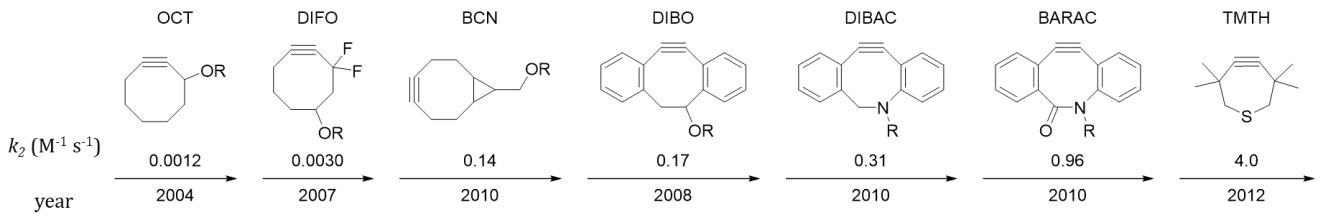

Figure 1.6: Kinetic rates of cycloadditions of benzyl azide and the respective strained alkyne along with the year in which the rates were reported. Adapted from C. P. Ramil et. al[48].

SPAAC has been used in a wide variety of biological applications from cell surface labelling as seen in the first published paper on SPAAC[39], into living organisms. Despite their faster kinetics, alkynes still pose some limitations in their biocompatibility. For example, BARAC is prone to hydrolysis in phosphate buffered saline and can intramolecularly rearrange in acidic conditions[49]. Cyclooctynes in general are also susceptible to nucleophilic attack by biological nucleophiles like glutathione and react with cysteine sulfenic acids[17]. Due to the hydrophobicity of these cyclooctynes, they can interact with off-target biomolecules, and/or get "stuck" into cell membranes[50].

1.2.3.3 Strain-Promoted Alkyne-Nitrone Cycloaddition (SPANC)

While SPAAC reactions are able to achieve fast rates and are applicable *in vivo*, azides have only one site for modifications, setting a limit to how much azides can be tuned for reaction optimization. Nitrones are a class of allyl type 1,3-dipoles that have 3 sites for modification, resulting in a highly versatile dipole that can be stereoelectronically tuned to optimize reactivity for a specific alkyne[51]. Nitrones are easily synthesized from the condensation of N-monosubstituted hydroxylamines with aldehydes, the oxidation of imines, trisubstituted N,N-disubstituted hydroxylamines, and isoxazolidines, and reactions between oximes and electrophiles[52]. Strain-promoted alkyne-nitrone cycloadditions (SPANC) was first developed in the Pezacki Lab by McKay et al[53], and involves a [3+2] cycloaddition between the reacting partners, and demonstrates rates up to 59 times faster than the analogous reaction between DIBO and benzyl azide[54]. The nitrone in question is a cyclic nitrone and not only offers higher rates since there is strain applied to the nitrone

but also offers prolonged stability in comparison to their acyclic version in water as they are prone to hydrolysis. Later on, the Pezacki group developed the cycloadditions of nitrones with strained cyclooctenes and applied the Kinugasa reaction in bioorthogonal settings using CuANCR (copper-catalyzed alkyne-nitrone cycloaddition followed by rearrangement) (Figure 1.7).

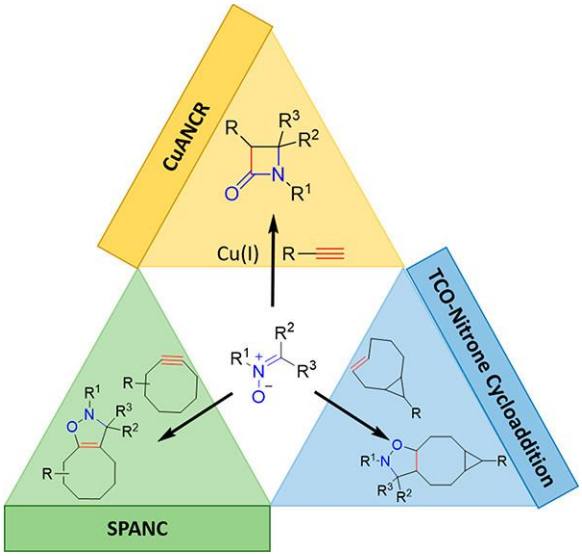

Figure 1.7: Bioorthogonal reactions using nitrones. Reprinted with permission from Chem. Rev. 2021, 121, 12, 6699–6717. Copyright 2021. American Chemical Society.

One of the main advantages of nitrones over azides is the ability to stereoelectronically tune the reaction to various dipolarophiles. In the first reported SPANC reaction with DIBO, a faster reaction was observed when an EWG was placed on the C-aryl para position of an acyclic nitrone rather than an EDG. The rates for SPANC reactions with BARAC and acyclic nitrones ranged from 2.8 to 58.8 M^{-1} s^{-1} and had a Hammett ρ value of 0.25 indicating that the reaction isn't sensitive to substituent effects and that the reaction goes through a synchronous transition state[55]. This isn't the case however, when acyclic nitrones react with a more electron rich alkyne such as BCN, the observed Hammett ρ value is 1.25 over a rate constant range from 0.0011 and 0.029 M^{-1} s^{-1} with higher rates associated with nitrones tuned with EWGs. The ρ value suggests that the transition state of the reaction is asynchronous and that there is a build up of electron density[56,57]. In short, electron poor

nitrones, regardless of whether they are cyclic or acyclic preferentially react with electron rich alkynes and vice versa. This was demonstrated in a 2014 paper, where the Pezacki lab compared the reactivity of two cyclic nitrones, DMPO that is electron rich and a DMImO derivative that is electron poor with BCN and DIBO. The electron rich nitrone reacted preferentially with DIBO (electron poor) over BCN (electron rich) in a 2:1 ratio, while the DMImO derivative favoured BCN over DIBO in a 5:1 ratio[58] (Figure 1.8). As this experiment was done in one-pot, it suggests that two bioorthogonal reactions can happen simultaneously while also being orthogonal to each other.

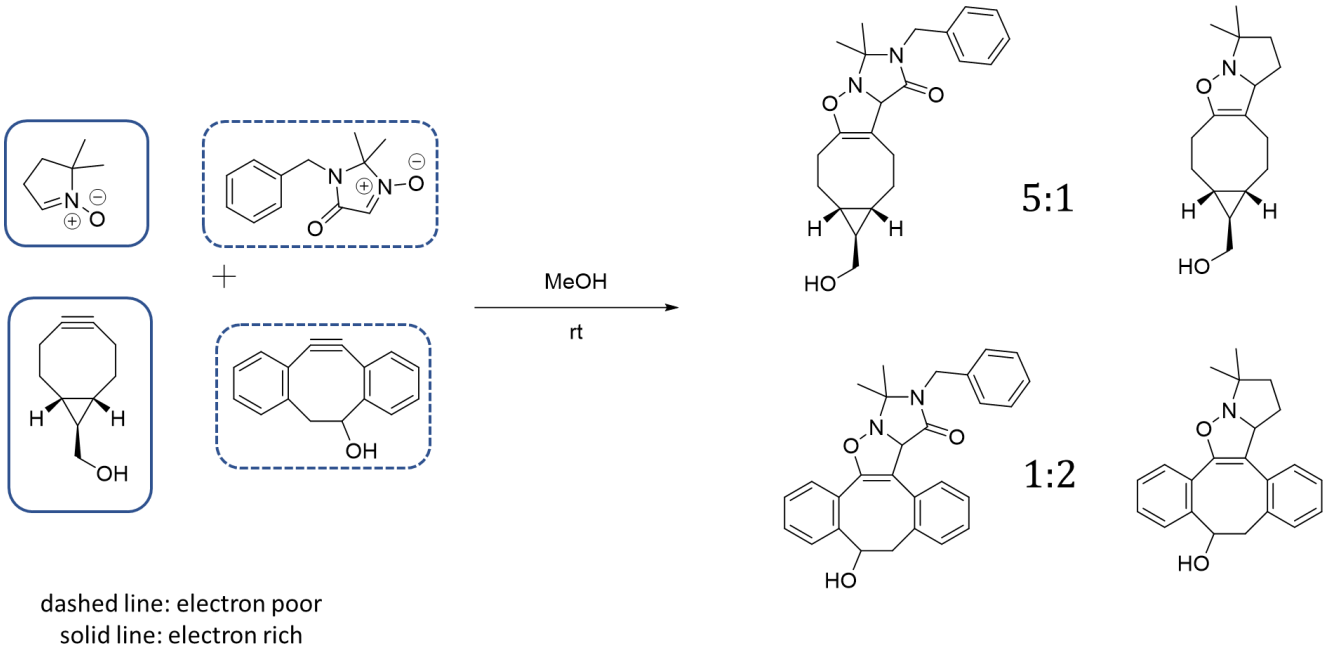

Figure 1.8: Product ratios from a one pot experiment with electron poor (dashed box) or electron rich (solid box). The electron rich nitrone reacted with electron poor DIBO and vice versa for BCN. Figure adapted from D. A. MacKensie[57].

Similarly to the CuAAC reaction with azides, nitrones have been able to react with terminal alkynes to form β-lactams. The Kinugasa reaction, also referred to as copper-catalyzed alkyne-nitrone cycloaddition followed by rearrangement (CuANCR), was first reported in 1972, outlining that the reaction between nitrones and copper(I) phenylacetylide in dry pyridine in the presence of N_2 gas yields β-lactams in moderate yields[59]. Since then, the scope of the reaction has been expanded[60], with research groups more recently adapting the reaction to aqueous solvents[61,62].

Nitrones have had a wide range of applicability in both materials chemistry and biology due to its versatility and ease of synthesis. They are also non-native to biological environments, and as a result has featured in both *in vitro* and *in vivo* applications[51]. Tuning the stereoelectronics of nitrones can result in duplex and multiplex labeling of biomolecules. An in-depth discussion on the biological applications of nitrones is found in Section 1.3.

1.2.3.4 Sydnones in Bioorthogonal Reactions

Recent trends in bioorthogonal reaction development have been the use of mesoionics in bioorthogonal reactions. The term mesoionic is a portmanteau of the "mesomeric" and "ionic" and describes an unconventional five membered heterocycle that contains two opposing charges[63]. Mesoionics are also a class of 5 membered heterocycles that can't be fully represented by one Lewis structure, but rather a set of resonance structures. The structure of these dipoles has been of much debate, with reports for the longest time indicating that mesoionics are aromatic despite their structural differences from benzenoid compounds, as the 6π are in a conjugated ring system, following Hückel's rule[64]. Initially mesoionics were thought to have the negative charge on the exocyclic oxygen atom creating an enolate type structure, and the positive charge is delocalized around the ring[63]. However, more recent studies indicate that the exocyclic carbon oxygen bond has a stretching frequency of 1730 cm^{-1}, suggesting a carbonyl. This is also supported by X-ray crystallography and density functional theory calculation[65,66].

Mesoionics in general undergo similar cycloadditions with alkynes. The reaction initially goes through the typical [3+2] cycloaddition, followed by a retro-Diels-Alder reaction. Of the mesoionics, sydnones have been most commonly used in bioorthogonal reactions for their stability and easier synthesis[67]. The first bioorthogonal reaction with sydnones and alkynes was published in 2013 and was discovered by high-throughput immunoassay screening and relied on copper catalysis. The copper-promoted sydnone–alkyne cycloaddition (CuSAC) was used to label BSA (bovine serum albumin) in buffer by coupling the sydnone in situ with the terminal amine of BSA and then adding a

dansyl functionalized terminal alkyne for imaging[68]. Shortly after, the first strain promoted sydnone-alkyne cycloaddition (SPSAC) was published by reacting N-phenylsydnone with BCN with a k_2 rate of 0.054 M^{-1} s^{-1} and its biocompatibility was demonstrated by the incorporation of a BCN functionalized unnatural amino acid (UAA) into GFP that was labeled by a BODIPY functionalized sydnone[69]. Successful attempts at improving SPSAC reaction rates by modifying the sydnone include the addition of EWG on the 4-position of the phenyl of N-phenylsydnone, the addition of 4-halogen substituents[70], and by replacing the exocyclic oxygen with a nitrogen forming iminosydnones. The use of BARAC as an alternative alkyne also increased reaction rates allowing for *in vivo* use[71].

1.2.4 Inverse Electron Demand Diels-Alder (IEDDA) Cycloadditions

Diels-Alder cycloadditions involve a reaction between a conjugated 4π 1,3-diene to a 2π system (also known as dienophile) to form a six-membered ring in a concerted [π4s + π2s] cycloaddition and are some of the most commonly used reactions in organic chemistry[20]. In a normal electron-demand Diels-Alder cycloaddition, the highest occupied molecular orbital (HOMO) of an electron rich diene interacts with the lowest unoccupied molecular orbital (LUMO) of the electron poor dienophile. However, in an inverse electron-demand Diels-Alder (IEDDA) cycloaddition, the HOMO of an electron rich dienophile overlaps with the LUMO an electron poor diene[72]. By the addition of electron withdrawing groups on the diene and electron donating groups on the dienophile, the LUMO of the diene is lowered and the HOMO of the dienophile is elevated, resulting in an accelerated IEDDA reaction[20].

These cycloadditions in bioorthogonal chemistry are favoured over other bioorthogonal reactions because of their efficiency and very fast kinetic rates[73], and were first independently identified by both Blackman M.L. et al[74] and Devaraj N.K. et al[75] in 2008. In both cases, the authors used 1,2,4,5-tetrazines as the diene with a strained alkene as the dienophile. In an IEDDA cycloaddition with tetrazines, the -C=N-N=C- diene system reacts with the alkene in an 1,4-addition resulting in a very strained bicyclic intermediate. With the expulsion of one equivalent of N_2 gas, a

retro-Diels-Alder reaction occurs, forming a 4,5-dihydropyridazine which isomerizes to 1,4-dihydropyridazine and is oxidized to the pyridazine final product. When tetrazines react with alkynes, the pyridazine is directly formed.[72]

The 2008 paper by Blackman and coworkers from the Fox lab uses trans-cyclooctenes as their dienophile, achieving an impressive k_2 rate of 2000 M^{-1} s^{-1}.[74] Since then, the Fox group has spearheaded the development of tetrazine ligations (IEDDA cycloadditions involving tetrazines), and have measured the fastest bioorthogonal reaction to date with rate constants as fast as 3.3 x 10^6 M^{-1} s^{-1} using conformationally strained trans-cyclooctene (sTCO), (1R,8S,E)-bicyclo[6.1.0]non-4-en-9-ylmethanol[76]. Rate constants for tetrazine ligations are similar to the rates for biomolecule association[77], lending tetrazine ligations for use at similar concentrations and timescales of biological processes. As a result, tetrazine ligations are the bioorthogonal reaction of choice for biological use, expanding beyond the typical protein[78], cell surface[79], and nucleic acid[80] labelling, that is ubiquitous among bioorthogonal reactions, into much more complex applications. These include pre-targeted radioimmunoimaging for tumors and radiotherapy[73,81–83], F-18 probes for PET imaging[84,85], and prodrug delivery and activation of anti-cancer drugs[77]. Most notable and recent of these applications is the delivery of a trans-cyclooctene modified doxorubicin to a soft tissue sarcoma or solid tumors in humans that have been pretreated by a tetrazine modified sodium hyaluronate polymer[86]. At the time of writing, this anti-cancer treatment is still undergoing Phase I clinical trials[87].

1.3 Applications of Nitrones in Biological Environments

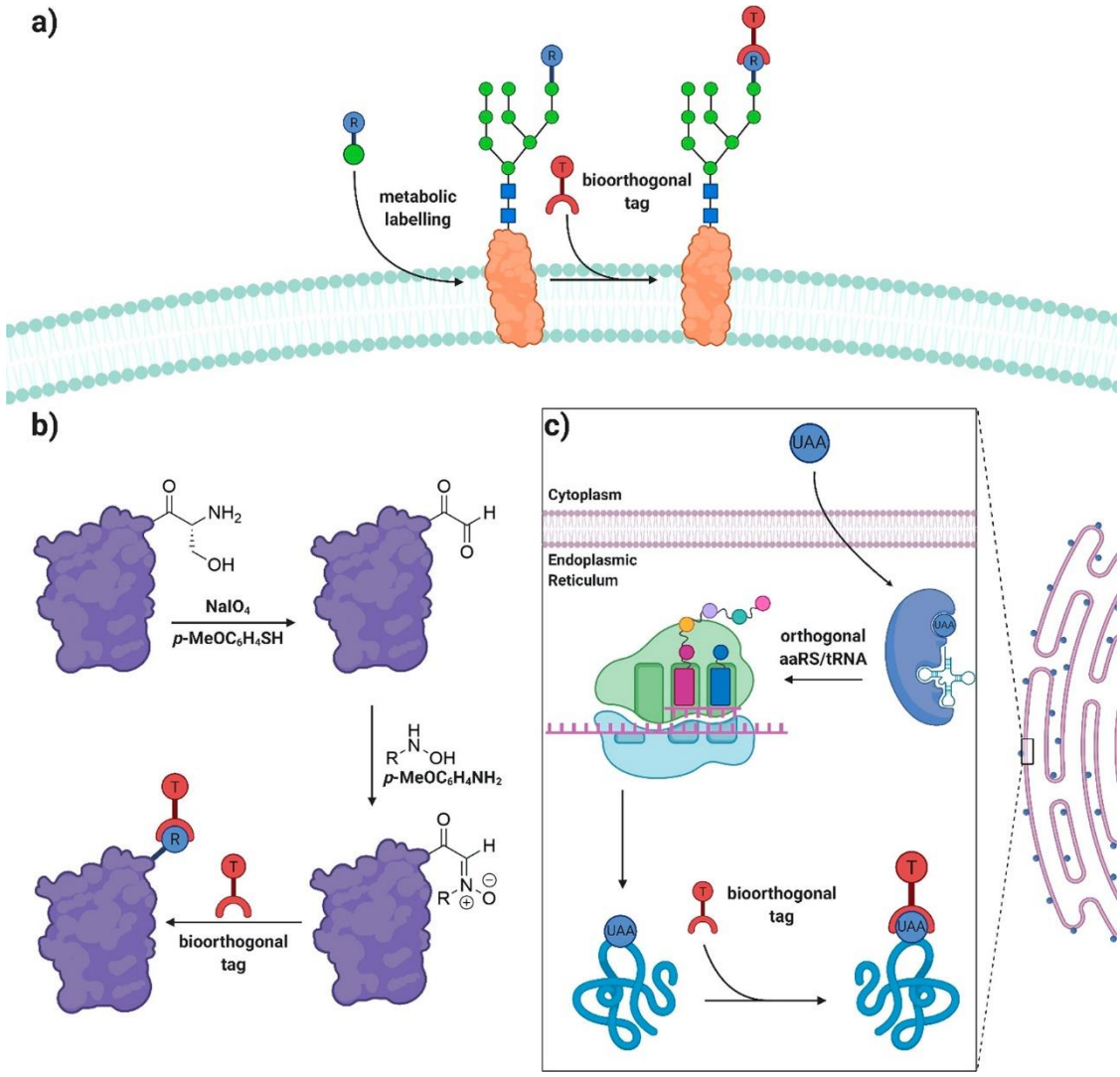

Figure 1.9: Strategies used to incorporate nitrone functionalities into nitrones. a) metabolic labelling, b) in situ nitrone functionalization of proteins by N-terminal serine oxidation to an aldehyde, and c) genetic code expansion of for site-specific protein labelling. Reprinted with permission from Chem. Rev. 2021, 121, 12, 6699–6717. Copyright 2021. American Chemical Society.

1.3.1 Cellular and Bacterial Labeling

Initial reports for the incorporation of nitrones for cell surface labelling using D-mannosamine derivatives did not show any labeling and was speculated by the authors that this could be due to acyclic nitrones hydrolyzing[88]. As a result, Ning X et al, took advantage of the ease of nitrone synthesis and installed an acyclic nitrone onto the N-terminal serine of chemokine

interleukin-8 (IL-8) for *in-situ* labelling. This three-step one-pot reaction starts off with the N-terminal serine oxidized with sodium periodate to an aldehyde. For the second step, *p*-methoxybenzenethiol was added along with *N*-methylhydroxylamine and *p*-anisidine. Finally, DIBO was added to get the final isoxazoline product[88]. *In-situ* nitrone formation for labeling was also applied to an N-terminal serine mutant of recombinant single chain variable fragment (scFv) antibodies that are against human epidermal growth factor receptor 2 (HER2). The nitrone modified antibody was then conjugated to a DIBO modified polymer-coated magnetofluorescent nanoparticle by SPANC. The nanoparticle conjugated antibody was then used to effectively target and label HER2 containing breast cancer cells[89].

The first example of cell surface labelling using SPANC came from McKay et al in 2011 by incorporating a cyclic nitrone into epidermal growth factor (EGF) that targeted EGF receptors that are overexpressed on the surfaces of human breast cancer. Nitrone modified EGFs and DIBO-biotin would react in a SPANC reaction, followed by secondary labelling with streptavidin-FITC for imaging[54].

The development of nitrone containing unnatural amino acids (UAA) opened the door for SPANC use in living bacteria. UAAs with endocyclic nitrones CMPO (electron rich) and DMImO (electron poor) were used to metabolically label the peptidoglycan layer of gram-positive *Listeria innocua* and *Lactococcus lactis.* Upon addition of the fluorophore, DIBO-Alexa 488, UAAs that were successfully incorporated into the peptidoglycan layer are detected via SPANC. Nitrone modified UAAs were able to show faster and brighter labeling when compared to an azide modified D-alanine. Gram-negative bacteria, *E coli,* proved to be trickier to label using nitrone UAAs as it would need to pass through the outer cell membrane to get to the peptidoglycan layer, with less prominent labelling observed[90]. Similar effective peptidoglycan labelling was observed in gram-positive bacteria with nitrone modified UAAs in a click reaction with sTCO, a strained cyclooctene[91].

Labeling of gram-negative bacteria, such as *E coli*, has been efficiently achieved by the incorporation of cyclic nitrone functionalized ketodeoxyoctonic acid into the peptidoglycan layer. Once incorporated, CuANCR was used with a terminal alkyne functionalized Alexa-488 for imaging of the live bacterium using fluorescence microscopy[92]. CuANCR was also used to label Huh-7 human hepatoma cells, this time by the incorporation of a terminal alkyne functionalized mannosamine derivative. CuANCR bioconjugation with a CMPO modified biotin tag was detected after staining with FTIC-streptavidin[92].

1.3.2 Double Click and Simultaneous Bioorthogonal Reactions

One of the biggest advantages of nitrones over other dipoles in the ability to tune the electronics of the nitrone to bias it to react with one alkyne over the other. This was demonstrated by the dual SPANC labeling of both *L. innocua* and *L. lactis* with D-ala-DMImO (electron poor) and D-ala-CMPO (electron rich), respectively[93]. Both bacteria were separately incubated with their respective UAA, and when combined, were treated with DBCO-TAMRA and BCN-CF488. Since DMImO has been proven to react preferentially to BCN, *L. innocua* was labelled with BCN-CF488, while both bacterium were labelled with DBCO-TAMRA. Mutual orthogonality with SPAAC was also demonstrated by incubating a coculture of *L. innocua* and *E. coli* the DMImO UAA and an azide UAA (D-ala-Azide). Since *L. innocua* favours DMImO and *E. coli* prefers the azide UAA over other UAAs, dual labelling was used to discriminate between the two strains. After treatment with BCN-CF488 and DBCO-TAMRA, *L. innocua* showed labelling with both BCN-CF488 and DBCO-TAMRA while E. coli was labelled with only DBCO-TAMRA (Figure 1.10) [93].

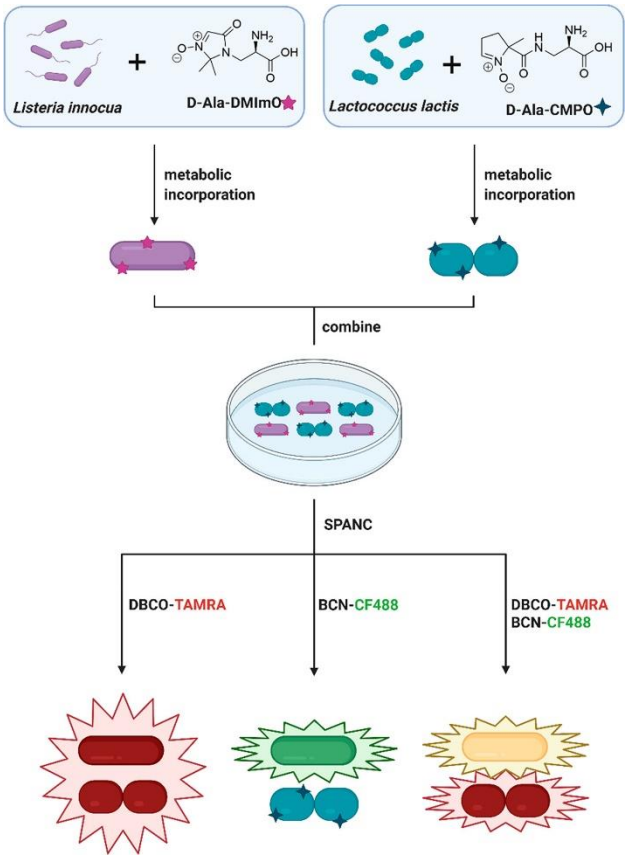

Figure 1.10: Dual SPANC labelling of L. innocua and L. lactis with cyclic nitrone functionalised unnatural amino acids, d-ala-DMImO and d-ala-CMPO, respectively. Reprinted with permission from Chem. Rev. 2021, 121, 12, 6699–6717. Copyright 2021. American Chemical Society.

SPANC can also be orthogonal to CuAAC as demonstrated by Temming et al, by introducing a dual functionalized nitrone on the N-terminus of enhanced GFP[94]. Similar to the aforementioned *in-situ* formation of nitrones using N-terminal serines[88], N-propargyl hydroxylamine was used to install both a terminal alkyne and nitrone. Upon a SPANC reaction with BCN-biotin, the expected isoxazoline product was formed and then CuAAC was used on the alkyne with an azide containing fluorescein derivative, combining both labelling techniques for protein labelling[94] (Figure 1.9b).

1.4 Bioorthogonal Reaction Development

The development of bioorthogonal reactions is a very iterative process as it needs to satisfy the criteria for both bioorthogonality and click chemistry[27]. That being said, there is a general consensus to the steps that need to be taken to develop effective bioorthogonal reactions. It starts off by identifying a prototype reaction, usually these are also click reactions that have fast kinetic rates. Prototype reactions should ideally also include functional groups and reactivities not found in biology to mitigate off-target labelling, and the reagents and products should also be small in size, chemically stable in biological environments, and are soluble in aqueous environments[95]. Many of the reactions that end up becoming bioorthogonal reactions are either polar reactions or cycloadditions[50]. Once selected, the mechanism of the reaction is identified and analyzed to mitigate incompatibility in biological environments and to improve reactivity, which includes stereoelectronic tuning and ring strain activation.

Once fast enough rates have been achieved, the next step is to apply the reaction in biological environments to assess bioorthogonality. This starts off by conducting the reaction in aqueous buffer with biological nucleophiles and electrophiles (ie: amino acids, sugars) to determine if similar reactivity and the same product formation is achieved[1]. Then the bioorthogonal reaction candidate is tested on biomolecules and in live cells. This is as far as the majority of bioorthogonal reactions can go in terms of bioorthogonality. Not many bioorthogonal reactions can end up being used in animals and only tetrazine ligations have been used in humans[87].

Oftentimes during the development of bioorthogonal reactions, there is a trade off between biocompatibility and fast kinetic rates, and so subsequent iterations of the reaction attempt to remedy the pitfalls. For example, azides and terminal alkynes are both easily incorporated into biomolecules, not found in higher level eukaryotes, and are nonperturbing to the biological environment, making the reaction between highly biocompatible. However, because ROS generating copper is used to catalyze the CuAAC reaction for faster kinetics, it loses its bioorthogonality.

Subsequent publications on CuAAC included ligands that can be used to eliminate copper toxicity[35], and eliminating the reliance on copper completely with SPAAC. This was similarly seen with the first publications of the tetrazine ligation – the rates achieved are by far the fastest amongst the other bioorthogonal reactions. However, the most reactive tetrazines have poor probe stability and also react with thiols causing off-target labeling which results in a loss of bioorthogonality. This phenomenon underscores the importance of developing novel bioorthogonal reactions[6].

1.5 Thesis Objective

While the aforementioned bioorthogonal reactions have been widely successful in their own right, it can be argued that the "perfect" bioorthogonal reaction has yet to be designed. 3-Oxidopyridinums are a six-membered heteroaromatic rings that were very popular in the 70s up until the 90s for their ability to react as a 1,3-latent dipole in a [3+2] cycloaddition with a wide range of electron poor alkenes, but they have yet to be used in a bioorthogonal setting. Given their ease of synthesis and excellent solubility in water, I sought out to investigate the use of 3-oxidopyridiniums as a novel dipole for bioorthogonal reaction development. In the following chapter, I expand on the applications of the SPANC reaction by labeling RNA for structure elucidation.

1.6 References

(1) Sletten, E. M.; Bertozzi, C. R. From Mechanism to Mouse: A Tale of Two Bioorthogonal Reactions. *Acc. Chem. Res.* **2011**, *44* (9), 666–676. https://doi.org/10.1021/ar200148z.

(2) Prescher, J. A.; Bertozzi, C. R. Chemistry in Living Systems. *Nat. Chem. Biol.* **2005**, *1* (1), 13–21. https://doi.org/10.1038/nchembio0605-13.

(3) Hudson, P. J.; Souriau, C. Engineered Antibodies. *Nat. Med. 2003 91* **2003**, *9* (1), 129–134. https://doi.org/10.1038/nm0103-129.

(4) Hang, H. C.; Yu, C.; Kato, D. L.; Bertozzi, C. R. A Metabolic Labeling Approach toward Proteomic Analysis of Mucin-Type O-Linked Glycosylation. *Proc. Natl. Acad. Sci.* **2003**, *100* (25), 14846–14851. https://doi.org/10.1073/PNAS.2335201100.

(5) Albada, B.; Keijzer, J. F.; Zuilhof, H.; van Delft, F. Oxidation-Induced "One-Pot" Click Chemistry. *Chem. Rev.* **2021**, *121* (12), 7032–7058. https://doi.org/10.1021/acs.chemrev.0c01180.

(6) Devaraj, N. K. The Future of Bioorthogonal Chemistry. *ACS Cent. Sci.* **2018**, *4* (8), 952–959. https://doi.org/10.1021/acscentsci.8b00251.

(7) Kolb, H. C.; Finn, M. G.; Sharpless, K. B. Click Chemistry : Diverse Chemical Function from a Few Good Reactions. *Angew. Chemie - Int. Ed.* **2001**, *40* (11), 2004–2021.

(8) Lim, R. K. V.; Lin, Q. Bioorthogonal Chemistry: Recent Progress and Future Directions. *Chem. Commun.* **2010**, *46* (10), 1589. https://doi.org/10.1039/b925931g.

(9) Zeng, Y.; Ramya, T. N. C.; Dirksen, A.; Dawson, P. E.; Paulson, J. C. High-Efficiency Labeling of Sialylated Glycoproteins on Living Cells. *Nat. Methods 2009 63* **2009**, *6* (3), 207–209. https://doi.org/10.1038/nmeth.1305.

(10) Griffin, R. J. The Medicinal Chemistry of the Azido Group. *Prog. Med. Chem.* **1994**, *31* (C), 121–232. https://doi.org/10.1016/S0079-6468(08)70020-1.

(11) Staudinger, H.; Meyer, J. Über Neue Organische Phosphorverbindungen III. Phosphinmethylenderivate Und Phosphinimine. *Helv. Chim. Acta* **1919**, *2* (1), 635–646. https://doi.org/10.1002/HLCA.19190020164.

(12) Heiss, T. K.; Dorn, R. S.; Prescher, J. A. Bioorthogonal Reactions of Triarylphosphines and Related Analogues. *Chem. Rev.* **2021**, *121* (12), 6802–6849. https://doi.org/10.1021/ACS.CHEMREV.1C00014.

(13) Saxon, E. Cell Surface Engineering by a Modified Staudinger Reaction. *Science (80-.).* **2000**, *287* (5460), 2007–2010. https://doi.org/10.1126/science.287.5460.2007.

(14) Saxon, E.; Armstrong, J. I.; Bertozzi, C. R. A "Traceless" Staudinger Ligation for the Chemoselective Synthesis of Amide Bonds. *Org. Lett.* **2000**, *2* (14), 2141–2143. https://doi.org/10.1021/OL006054V.

(15) Nilsson, B. L.; Kiessling, L. L.; Raines, R. T. Staudinger Ligation: A Peptide from a Thioester and Azide. *Org. Lett.* **2000**, *2* (13), 1939–1941. https://doi.org/10.1021/OL0060174/SUPPL_FILE/OL0060174_S1.PDF.

(16) Tam, A.; Raines, R. T. Chapter 2 Protein Engineering with the Traceless Staudinger Ligation.

Methods Enzymol. **2009**, *462*, 25–44. https://doi.org/10.1016/S0076-6879(09)62002-4.

(17) McKay, C. S.; Finn, M. G. Click Chemistry in Complex Mixtures: Bioorthogonal Bioconjugation. *Chem. Biol.* **2014**, *21* (9), 1075–1101. https://doi.org/10.1016/j.chembiol.2014.09.002.

(18) Sundhoro, M.; Jeon, S.; Park, J.; Ramström, O.; Yan, M. Perfluoroaryl Azide Staudinger Reaction: A Fast and Bioorthogonal Reaction. *Angew. Chemie* **2017**, *129* (40), 12285–12289. https://doi.org/10.1002/ANGE.201705346.

(19) Meguro, T.; Terashima, N.; Ito, H.; Koike, Y.; Kii, I.; Yoshida, S.; Hosoya, T. Staudinger Reaction Using 2,6-Dichlorophenyl Azide Derivatives for Robust Aza-Ylide Formation Applicable to Bioconjugation in Living Cells. *Chem. Commun.* **2018**, *54* (57), 7904–7907. https://doi.org/10.1039/C8CC00179K.

(20) Deb, T.; Tu, J.; Franzini, R. M. Mechanisms and Substituent Effects of Metal-Free Bioorthogonal Reactions. *Chem. Rev.* **2021**, *121* (12), 6850–6914. https://doi.org/10.1021/acs.chemrev.0c01013.

(21) Huisgen, R. 1,3-Dipolar Cycloadditions. Past and Future. *Angew. Chemie - Int. Ed.* **1963**, *2* (10), 565–598. https://doi.org/10.1002/ANIE.196305651.

(22) Huisgen, R. Kinetics and Mechanism of 1,3-Dipolr Cycloadditions. *Angew. Chemie Int. Ed. English* **1963**, *2* (11), 633–645. https://doi.org/10.1002/anie.196306331.

(23) Sustmann, R. Orbital Energy Control of Cycloaddition Reactivity. *Pure Appl. Chem.* **1974**, *40* (4), 569–593. https://doi.org/10.1351/PAC197440040569/PDF/FIRSTPAGE.

(24) Sustmann, R.; Trill, H. Substituent Effects in 1,3-Dipolar Cycloadditions of Phenyl Azide. *Angew. Chemie Int. Ed. English* **1972**, *11* (9), 838–840. https://doi.org/10.1002/ANIE.197208382.

(25) Sustmann, R. A Simple Model for Substituent Effects in Cycloaddition Reactions. I. 1,3-Dipolar Cycloadditions. *Tetrahedron Lett.* **1971**, *12* (29), 2717–2720. https://doi.org/10.1016/S0040-4039(01)96961-8.

(26) Breugst, M.; Reissig, H. U. The Huisgen Reaction: Milestones of the 1,3-Dipolar Cycloaddition. *Angew. Chemie Int. Ed.* **2020**, *59* (30), 12293–12307. https://doi.org/10.1002/ANIE.202003115.

(27) Nguyen, S. S.; Prescher, J. A. Developing Bioorthogonal Probes to Span a Spectrum of Reactivities. *Nat. Rev. Chem.* **2020**, *4* (9), 476–489. https://doi.org/10.1038/s41570-020-0205-0.

(28) Rostovtsev, V. V.; Green, L. G.; Fokin, V. V.; Sharpless, K. B. A Stepwise Huisgen Cycloaddition Process: Copper(I)-Catalyzed Regioselective "Ligation" of Azides and Terminal Alkynes. *Angew. Chemie Int. Ed.* **2002**, *41* (14), 2596–2599. https://doi.org/10.1002/1521-3773(20020715)41:14<2596::AID-ANIE2596>3.0.CO;2-4.

(29) Tornøe, C. W.; Christensen, C.; Meldal, M. Peptidotriazoles on Solid Phase: [1,2,3]-Triazoles by Regiospecific Copper(I)-Catalyzed 1,3-Dipolar Cycloadditions of Terminal Alkynes to Azides. *J. Org. Chem.* **2002**, *67* (9), 3057–3064. https://doi.org/10.1021/jo011148j.

(30) Li, L.; Zhang, Z. Development and Applications of the Copper-Catalyzed Azide-Alkyne Cycloaddition (CuAAC) as a Bioorthogonal Reaction. *Molecules* **2016**, *21* (10), 1–22. https://doi.org/10.3390/molecules21101393.

(31) Worrell, B. T.; Malik, J. A.; Fokin, V. V. Direct Evidence of a Dinuclear Copper Intermediate in Cu(I)-Catalyzed Azide-Alkyne Cycloadditions. *Science (80-.).* **2013**, *340* (6131), 457–460. https://doi.org/10.1126/SCIENCE.1229506/SUPPL_FILE/WORRELL.SM.PDF.

(32) Sletten, E. M.; Bertozzi, C. R. Bioorthogonal Chemistry: Fishing for Selectivity in a Sea of Functionality. *Angew. Chemie Int. Ed.* **2009**, *48* (38), 6974–6998. https://doi.org/10.1002/anie.200900942.

(33) Wang, Q.; Chan, T. R.; Hilgraf, R.; Fokin, V. V.; Sharpless, K. B.; Finn, M. G. Bioconjugation by Copper(I)-Catalyzed Azide-Alkyne [3 + 2] Cycloaddition. *J. Am. Chem. Soc.* **2003**, *125* (11), 3192–3193. https://doi.org/10.1021/ja021381e.

(34) Hong, V.; Steinmetz, N. F.; Manchester, M.; Finn, M. G. Labeling Live Cells by Copper-Catalyzed Alkyne–Azide Click Chemistry. *Bioconjug. Chem.* **2010**, *21* (10), 1912–1916. https://doi.org/10.1021/BC100272Z.

(35) Kennedy, D. C.; McKay, C. S.; Legault, M. C. B. B.; Danielson, D. C.; Blake, J. A.; Pegoraro, A. F.; Stolow, A.; Mester, Z.; Pezacki, J. P. Cellular Consequences of Copper Complexes Used to Catalyze Bioorthogonal Click Reactions. *J. Am. Chem. Soc.* **2011**, *133* (44), 17993–18001. https://doi.org/10.1021/ja2083027.

(36) Li, S.; Cai, H.; He, J.; Chen, H.; Lam, S.; Cai, T.; Zhu, Z.; Bark, S. J.; Cai, C. Extent of the Oxidative Side Reactions to Peptides and Proteins during the CuAAC Reaction. *Bioconjug. Chem.* **2016**, *27* (10), 2315–2322. https://doi.org/10.1021/ACS.BIOCONJCHEM.6B00267/SUPPL_FILE/BC6B00267_SI_001.PDF.

(37) Nairn, N. W.; Bariola, P. A.; Graddis, T. J.; VanBrunt, M. P.; Wang, A.; Li, G.; Grabstein, K. Cysteine as a Monothiol Reducing Agent to Prevent Copper-Mediated Oxidation of Interferon Beta during PEGylation by CuAAC. *Bioconjug. Chem.* **2015**, *26* (10), 2070–2075. https://doi.org/10.1021/ACS.BIOCONJCHEM.5B00320/SUPPL_FILE/BC5B00320_SI_001.PDF.

(38) Clavadetscher, J.; Hoffmann, S.; Lilienkampf, A.; Mackay, L.; Yusop, R. M.; Rider, S. A.; Mullins, J. J.; Bradley, M. Copper Catalysis in Living Systems and In Situ Drug Synthesis. *Angew. Chemie* **2016**, *128* (50), 15891–15895. https://doi.org/10.1002/ANGE.201609837.

(39) Agard, N. J.; Prescher, J. A.; Bertozzi, C. R. A Strain-Promoted [3 + 2] Azide-Alkyne Cycloaddition for Covalent Modification of Biomolecules in Living Systems. *J. Am. Chem. Soc.* **2004**, *126* (46), 15046–15047. https://doi.org/10.1021/JA044996F/SUPPL_FILE/JA044996FSI20041012_011904.PDF.

(40) Ess, D. H.; Houk, K. N. Theory of 1,3-Dipolar Cycloadditions: Distortion/Interaction and Frontier Molecular Orbital Models. *J. Am. Chem. Soc.* **2008**, *130* (31), 10187–10198. https://doi.org/10.1021/JA800009Z/SUPPL_FILE/JA800009Z-FILE001.PDF.

(41) Ess, D. H.; Houk, K. N. Distortion/Interaction Energy Control of 1,3-Dipolar Cycloaddition Reactivity. *J. Am. Chem. Soc.* **2007**, *129* (35), 10646–10647. https://doi.org/10.1021/JA0734086/SUPPL_FILE/JA0734086SI20070703_044332.PDF.

(42) Ess, D. H.; Jones, G. O.; Houk, K. N. Transition States of Strain-Promoted Metal-Free Click Chemistry: 1,3-Dipolar Cycloadditions of Phenyl Azide and Cyclooctynes. *Org. Lett.* **2008**, *10* (8), 1633–1636. https://doi.org/10.1021/OL8003657/SUPPL_FILE/OL8003657-FILE001.PDF.

(43) Ning, X.; Guo, J.; Wolfert, M. A.; Boons, G.-J. Visualizing Metabolically Labeled Glycoconjugates of Living Cells by Copper-Free and Fast Huisgen Cycloadditions. *Angew. Chemie Int. Ed.* **2008**, *47* (12), 2253–2255. https://doi.org/10.1002/anie.200705456.

(44) Debets, M. F.; van Berkel, S. S.; Schoffelen, S.; Rutjes, F. P. J. T.; van Hest, J. C. M.; van Delft, F. L. Aza-Dibenzocyclooctynes for Fast and Efficient Enzyme PEGylation via Copper-Free (3+2) Cycloaddition. *Chem. Commun.* **2010**, *46* (1), 97–99. https://doi.org/10.1039/B917797C.

(45) Jewett, J. C.; Sletten, E. M.; Bertozzi, C. R. Rapid Cu-Free Click Chemistry with Readily Synthesized Biarylazacyclooctynones. *J. Am. Chem. Soc.* **2010**, *132* (11), 3688–3690. https://doi.org/10.1021/ja100014q.

(46) Dommerholt, J.; Schmidt, S.; Temming, R.; Hendriks, L. J. A.; Rutjes, F. P. J. T.; van Hest, J. C. M.; Lefeber, D. J.; Friedl, P.; van Delft, F. L.; van Hest, J. C. M.; Schmidt, S.; Lefeber, D. J.; Dommerholt, J.; Hendriks, L. J. A.; Friedl, P.; Temming, R.; Rutjes, F. P. J. T.; van Delft, F. L. Readily Accessible Bicyclononynes for Bioorthogonal Labeling and Three-Dimensional Imaging of Living Cells. *Angew. Chemie Int. Ed.* **2010**, *49* (49), 9422–9425. https://doi.org/10.1002/anie.201003761.

(47) de Almeida, G.; Sletten, E. M.; Nakamura, H.; Palaniappan, K. K.; Bertozzi, C. R.; De Almeida, G.; Sletten, E. M.; Nakamura, H.; Palaniappan, K. K.; Bertozzi, C. R. Thiacycloalkynes for Copper-Free Click Chemistry. *Angew. Chemie - Int. Ed.* **2012**, *51* (10), 2443–2447. https://doi.org/10.1002/anie.201106325.

(48) Ramil, C. P.; Lin, Q. Bioorthogonal Chemistry: Strategies and Recent Developments. *Chem. Commun.* **2013**, *49* (94), 11007–11022. https://doi.org/10.1039/c3cc44272a.

(49) Chigrinova, M.; McKay, C. S.; Beaulieu, L.-P. B. P. B.; Udachin, K. A.; Beauchemin, A. M.; Pezacki, J. P. Rearrangements and Addition Reactions of Biarylazacyclooctynones and the Implications to Copper-Free Click Chemistry. *Org. Biomol. Chem.* **2013**, *11* (21), 3436–3441. https://doi.org/10.1039/c3ob40683k.

(50) Patterson, D. M.; Nazarova, L. A.; Prescher, J. A. Finding the Right (Bioorthogonal) Chemistry. *ACS Chem. Biol.* **2014**, *9* (3), 592–605. https://doi.org/10.1021/cb400828a.

(51) Bilodeau, D. A. D. A.; Margison, K. D. K. D.; Serhan, M.; Pezacki, J. P. J. P. Bioorthogonal Reactions Utilizing Nitrones as Versatile Dipoles in Cycloaddition Reactions. *Chem. Rev.* **2021**, *121* (12), 6699–6717. https://doi.org/10.1021/acs.chemrev.0c00832.

(52) Murahashi, S. I.; Imada, Y. Synthesis and Transformations of Nitrones for Organic Synthesis. *Chem. Rev.* **2019**, *119* (7), 4684–4716. https://doi.org/10.1021/ACS.CHEMREV.8B00476.

(53) McKay, C. S.; Moran, J.; Pezacki, J. P. Nitrones as Dipoles for Rapid Strain-Promoted 1,3-Dipolar Cycloadditions with Cyclooctynes. *Chem. Commun.* **2010**, *46* (6), 931–933. https://doi.org/10.1039/B921630H.

(54) McKay, C. S.; Blake, J. A.; Cheng, J.; Danielson, D. C.; Pezacki, J. P. Strain-Promoted Cycloadditions of Cyclic Nitrones with Cyclooctynes for Labeling Human Cancer Cells. *Chem. Commun.* **2011**, *47* (36), 10040–10042. https://doi.org/10.1039/c1cc13808a.

(55) McKay, C. S.; Chigrinova, M.; Blake, J. A.; Pezacki, J. P. Kinetics Studies of Rapid Strain-Promoted [3 + 2]-Cycloadditions of Nitrones with Biaryl-Aza-Cyclooctynone. *Org. Biomol. Chem.* **2012**, *10* (15), 3066–3070. https://doi.org/10.1039/c2ob07165g.

(56) MacKenzie, D. A.; Sherratt, A. R.; Chigrinova, M.; Cheung, L. L. W.; Pezacki, J. P. Strain-

Promoted Cycloadditions Involving Nitrones and Alkynes-Rapid Tunable Reactions for Bioorthogonal Labeling. *Curr. Opin. Chem. Biol.* **2014**, *21*, 81–88. https://doi.org/10.1016/j.cbpa.2014.05.023.

(57) MacKenzie, D. A.; Pezacki, J. P. Kinetics Studies of Rapid Strain-Promoted [3+2] Cycloadditions of Nitrones with Bicyclo[6.1.0]Nonyne. *Can. J. Chem.* **2014**, *92* (4), 337–340. https://doi.org/10.1139/cjc-2013-0577.

(58) Mackenzie, D. A.; Pezacki, J. P. Kinetics Studies of Rapid Strain-Promoted [3+2] Cycloadditions of Nitrones with Bicyclo[6.1.0]Nonyne. *Can. J. Chem.* **2014**, *92* (4), 337–340. https://doi.org/10.1139/cjc-2013-0577.

(59) Kinugasa, M.; Hashimoto, S. The Reactions of Copper(I) Phenylacetylide with Nitrones. *J. Chem. Soc. Chem. Commun.* **1972**, *0* (8), 466–467. https://doi.org/10.1039/C39720000466.

(60) Stecko, S.; Furman, B.; Chmielewski, M. Kinugasa Reaction: An 'Ugly Duckling' of β-Lactam Chemistry. *Tetrahedron* **2014**, *70* (43), 7817–7844. https://doi.org/10.1016/J.TET.2014.06.024.

(61) McKay, C. S.; Kennedy, D. C.; Pezacki, J. P. Studies of Multicomponent Kinugasa Reactions in Aqueous Media. *Tetrahedron Lett.* **2009**, *50* (17), 1893–1896. https://doi.org/10.1016/J.TETLET.2009.02.035.

(62) Basak, A.; Chandra, K.; Pal, R.; Ghosh, S. C. Kinugasa Reaction under Click Chemistry Conditions. *Synlett* **2007**, *2007* (10), 1585–1588. https://doi.org/10.1055/S-2007-980383/BIB.

(63) Decuypère, E.; Plougastel, L.; Audisio, D.; Taran, F. Sydnone–Alkyne Cycloaddition: Applications in Synthesis and Bioconjugation. *Chem. Commun.* **2017**, *53* (84), 11515–11527. https://doi.org/10.1039/C7CC06405E.

(64) Badami, B. V. Mesoionic Compounds. *Reson. 2006 1110* **2006**, *11* (10), 40–48. https://doi.org/10.1007/BF02835674.

(65) Champagne, P. A.; Houk, K. N. Influence of Endo- and Exocyclic Heteroatoms on Stabilities and 1,3-Dipolar Cycloaddition Reactivities of Mesoionic Azomethine Ylides and Imines. *J. Org. Chem.* **2017**, *82* (20), 10980–10988. https://doi.org/10.1021/ACS.JOC.7B01928/SUPPL_FILE/JO7B01928_SI_001.PDF.

(66) Wiechmann, S.; Freese, T.; Drafz, M. H. H.; Hübner, E. G.; Namyslo, J. C.; Nieger, M.; Schmidt, A. Sydnone Anions and Abnormal N-Heterocyclic Carbenes of O-Ethylsydnones. Characterizations, Calculations and Catalyses. *Chem. Commun.* **2014**, *50* (80), 11822–11824. https://doi.org/10.1039/C4CC05461J.

(67) Porte, K.; Riomet, M.; Figliola, C.; Audisio, D. Click and Bio-Orthogonal Reactions with Mesoionic Compounds. *Chem. Rev.* **2021**, *121* (12), 6718–6743. https://doi.org/10.1021/acs.chemrev.0c00806.

(68) Kolodych, S.; Rasolofonjatovo, E.; Chaumontet, M.; Nevers, M. C.; Créminon, C.; Taran, F. Discovery of Chemoselective and Biocompatible Reactions Using a High-Throughput Immunoassay Screening. *Angew. Chemie Int. Ed.* **2013**, *52* (46), 12056–12060. https://doi.org/10.1002/ANIE.201305645.

(69) Wallace, S.; Chin, J. W. Strain-Promoted Sydnone Bicyclo-[6.1.0]-Nonyne Cycloaddition. *Chem. Sci.* **2014**, *5* (5), 1742–1744. https://doi.org/10.1039/C3SC53332H.

(70) Tao, H.; Liu, F.; Zeng, R.; Shao, Z.; Zou, L.; Cao, Y.; Murphy, J. M.; Houk, K. N.; Liang, Y. Origins of Halogen Effects in Bioorthogonal Sydnone Cycloadditions. *Chem. Commun.* **2018**, *54* (40), 5082–5085. https://doi.org/10.1039/C8CC02128G.

(71) Narayanam, M. K.; Liang, Y.; Houk, K. N.; Murphy, J. M. Discovery of New Mutually Orthogonal Bioorthogonal Cycloaddition Pairs through Computational Screening. *Chem. Sci.* **2016**, *7* (2), 1257–1261. https://doi.org/10.1039/C5SC03259H.

(72) Oliveira, B. L.; Guo, Z.; Bernardes, G. J. L. Inverse Electron Demand Diels-Alder Reactions in Chemical Biology. *Chem. Soc. Rev.* **2017**, *46* (16), 4895–4950. https://doi.org/10.1039/c7cs00184c.

(73) Mushtaq, S.; Yun, S.-J.; Jeon, J. Recent Advances in Bioorthogonal Click Chemistry for Efficient Synthesis of Radiotracers and Radiopharmaceuticals. *Molecules* **2019**, *24* (19). https://doi.org/10.3390/molecules24193567.

(74) Blackman, M. L.; Royzen, M.; Fox, J. M. Tetrazine Ligation: Fast Bioconjugation Based on Inverse-Electron-Demand Diels-Alder Reactivity. *J. Am. Chem. Soc.* **2008**, *130* (41), 13518–13519. https://doi.org/10.1021/JA8053805/SUPPL_FILE/JA8053805_SI_002.PDF.

(75) Devaraj, N. K.; Weissleder, R.; Hilderbrand, S. A. Tetrazine-Based Cycloadditions: Application to Pretargeted Live Cell Imaging. *Bioconjug. Chem.* **2008**, *19* (12), 2297–2299. https://doi.org/10.1021/BC8004446/SUPPL_FILE/BC8004446_SI_001.PDF.

(76) Darko, A.; Wallace, S.; Dmitrenko, O.; Machovina, M. M.; Mehl, R. A.; Chin, J. W.; Fox, J. M. Conformationally Strained Trans-Cyclooctene with Improved Stability and Excellent Reactivity in Tetrazine Ligation. *Chem. Sci.* **2014**, *5* (10), 3770–3776. https://doi.org/10.1039/C4SC01348D.

(77) Scinto, S. L.; Bilodeau, D. A.; Hincapie, R.; Lee, W.; Nguyen, S. S.; Xu, M.; am Ende, C. W.; Finn, M. G.; Lang, K.; Lin, Q.; Pezacki, J. P.; Prescher, J. A.; Robillard, M. S.; Fox, J. M. Bioorthogonal Chemistry. *Nat. Rev. Methods Prim. 2021 11* **2021**, *1* (1), 1–23. https://doi.org/10.1038/s43586-021-00028-z.

(78) Blizzard, R. J.; Backus, D. R.; Brown, W.; Bazewicz, C. G.; Li, Y.; Mehl, R. A. Ideal Bioorthogonal Reactions Using a Site-Specifically Encoded Tetrazine Amino Acid. *J. Am. Chem. Soc.* **2015**, *137* (32), 10044–10047. https://doi.org/10.1021/JACS.5B03275/SUPPL_FILE/JA5B03275_SI_001.PDF.

(79) Neves, A. A.; Stöckmann, H.; Wainman, Y. A.; Kuo, J. C. H.; Fawcett, S.; Leeper, F. J.; Brindle, K. M. Imaging Cell Surface Glycosylation in Vivo Using "Double Click" Chemistry. *Bioconjug. Chem.* **2013**, *24* (6), 934–941. https://doi.org/10.1021/BC300621N/SUPPL_FILE/BC300621N_SI_001.PDF.

(80) Pyka, A. M.; Domnick, C.; Braun, F.; Kath-Schorr, S. Diels-Alder Cycloadditions on Synthetic RNA in Mammalian Cells. *Bioconjug. Chem.* **2014**, *25* (8), 1438–1443. https://doi.org/10.1021/BC500302Y/SUPPL_FILE/BC500302Y_SI_001.PDF.

(81) Rossin, R.; Van Duijnhoven, S. M. J.; Ten Hoeve, W.; Janssen, H. M.; Kleijn, L. H. J.; Hoeben, F. J. M.; Versteegen, R. M.; Robillard, M. S. Triggered Drug Release from an Antibody-Drug Conjugate Using Fast "Click-to-Release" Chemistry in Mice. *Bioconjug. Chem.* **2016**, *27* (7). https://doi.org/10.1021/acs.bioconjchem.6b00231.

(82) Handula, M.; Chen, K.-T.; Seimbille, Y.; Thomas, J.; Joseph, N.; Eremin, D. IEDDA: An Attractive

Bioorthogonal Reaction for Biomedical Applications. *Mol. 2021, Vol. 26, Page 4640* **2021**, *26* (15), 4640. https://doi.org/10.3390/MOLECULES26154640.

(83) Rossin, R.; Läppchen, T.; Van Den Bosch, S. M.; Laforest, R.; Robillard, M. S. Diels–Alder Reaction for Tumor Pretargeting: In Vivo Chemistry Can Boost Tumor Radiation Dose Compared with Directly Labeled Antibody. *J. Nucl. Med.* **2013**, *54* (11), 1989–1995. https://doi.org/10.2967/JNUMED.113.123745.

(84) Wang, M.; Svatunek, D.; Rohlfing, K.; Liu, Y.; Wang, H.; Giglio, B.; Yuan, H.; Wu, Z.; Li, Z.; Fox, J. Conformationally Strained Trans-Cyclooctene (STCO) Enables the Rapid Construction of 18F-PET Probes via Tetrazine Ligation. *Theranostics* **2016**, *6* (6), 887–895. https://doi.org/10.7150/THNO.14742.

(85) Rangger, C.; Haubner, R. Radiolabelled Peptides for Positron Emission Tomography and Endoradiotherapy in Oncology. *Pharmaceuticals* **2020**, *13* (2). https://doi.org/10.3390/ph13020022.

(86) Click chemistry sees first use in humans https://cen.acs.org/pharmaceuticals/Click-chemistry-sees-first-use/98/web/2020/10 (accessed Dec 28, 2021).

(87) Phase 1 Study of SQ3370 in Patients With Advanced Solid Tumors - Full Text View - ClinicalTrials.gov https://clinicaltrials.gov/ct2/show/NCT04106492 (accessed Dec 28, 2021).

(88) Ning, X.; Temming, R. P.; Dommerholt, J.; Guo, J.; Ania, D. B.; Debets, M. F.; Wolfert, M. A.; Boons, G.-J.; van Delft, F. L. Protein Modification by Strain-Promoted Alkyne-Nitrone Cycloaddition. *Angew. Chemie Int. Ed.* **2010**, *49* (17), 3065–3068. https://doi.org/10.1002/anie.201000408.

(89) Colombo, M.; Sommaruga, S.; Mazzucchelli, S.; Polito, L.; Verderio, P.; Galeffi, P.; Corsi, F.; Tortora, P.; Prosperi, D. Site-Specific Conjugation of ScFvs Antibodies to Nanoparticles by Bioorthogonal Strain-Promoted Alkyne–Nitrone Cycloaddition. *Angew. Chemie Int. Ed.* **2012**, *51* (2), 496–499. https://doi.org/10.1002/ANIE.201106775.

(90) MacKenzie, D. A.; Sherratt, A. R.; Chigrinova, M.; Kell, A. J.; Pezacki, J. P. Bioorthogonal Labelling of Living Bacteria Using Unnatural Amino Acids Containing Nitrones and a Nitrone Derivative of Vancomycin. *Chem. Commun.* **2015**, *51* (62), 12501–12504. https://doi.org/10.1039/c5cc04901f.

(91) Margison, K. D.; Bilodeau, D. A.; Mahmoudi, F.; Pezacki, J. P. Cycloadditions of Trans-Cyclooctenes and Nitrones as Tools for Bioorthogonal Labelling. *ChemBioChem* **2020**, *21* (7), 948–951. https://doi.org/10.1002/CBIC.201900627.

(92) Sherratt, A. R.; Chigrinova, M.; McKay, C. S.; Beaulieu, L. P. B.; Rouleau, Y.; Pezacki, J. P. Copper-Catalysed Cycloaddition Reactions of Nitrones and Alkynes for Bioorthogonal Labelling of Living Cells. *RSC Adv.* **2014**, *4* (87), 46966–46969. https://doi.org/10.1039/c4ra07851a.

(93) Sherratt, A. R.; Chigrinova, M.; Mackenzie, D. A.; Rastogi, N. K.; Ouattara, M. T. M.; Pezacki, A. T.; Pezacki, J. P. Dual Strain-Promoted Alkyne-Nitrone Cycloadditions for Simultaneous Labeling of Bacterial Peptidoglycans. *Bioconjug. Chem.* **2016**, *27* (5), 1222–1226. https://doi.org/10.1021/ACS.BIOCONJCHEM.6B00063/SUPPL_FILE/BC6B00063_SI_001.PDF.

(94) Temming, R. P.; Eggermont, L.; Van Eldijk, M. B.; Van Hest, J. C. M.; Van Delft, F. L. N-Terminal Dual Protein Functionalization by Strain-Promoted Alkyne–Nitrone Cycloaddition. *Org. Biomol. Chem.* **2013**, *11* (17), 2772–2779. https://doi.org/10.1039/C3OB00043E.

(95) Tian, Y.; Lin, Q. Fitness Factors for Bioorthogonal Chemical Probes. *ACS Chem. Biol.* **2019**, *14* (12), 2489–2496. https://doi.org/10.1021/ACSCHEMBIO.9B00755.

Chapter 2

Investigating the use of 3-oxidopyridinium betaines in bioorthogonal reactions for labeling biomolecules

Note: all computational calculations have been conducted by Professor Masaya Nakajima of Chiba University and my colleague Jason Josephson. Analysis conducted by me.

2.1 Introduction

Bioorthogonal reactions require a strict set of criteria given their applications in biological systems. Highly selective and rapid reactions are sought after as they allow for the intended bioconjugation to occur along a shorter period of time with significantly less concentrated reagents to mitigate toxicity[1]. As a result, reaction development must also take into consideration the orthogonality of the bioorthogonal reacting partners ensuring that they are stable, non-toxic, non-reactive with biomolecules found in their native environment. Oftentimes, there is a trade-off between reaction rate and bioorthogonality. For example, fast reacting tetrazines in IEDDA (inverse electron demand Deils-Alder) cycloadditions are highly susceptible to both off-target reactions and degradation in water, resulting in a loss of bioorthogonality[2].

With the advent of SPAAC reactions, research efforts in bioorthogonal chemistry have been focused on improving the kinetic rates of 1,3-dipolar cycloadditions. This was done by introducing ring strain to the OCT by benzannulation, fusing a cyclopropyl ring opposite to the alkyne, and replacing a methylene group with a sulfur atom. The addition of electron withdrawing groups on the propargyl carbon also resulted in faster rates. However, there seems to be a limit – the benzannulation of DIFO to DIFBO resulted in DIFBO spontaneously trimerizing in solution and the fusion of a benzene ring to TMTH resulted in unstable alkynes, demonstrating that increased reactivity comes with the risk of instability[3].

Through the use of dipoles other than azides, the reactivities of bioorthogonal probes can be tuned to preferentially react with one dipolarophile over the other, expanding the toolbox of bioorthogonal reactions. Nitrone and sydnone dipoles were developed to label biomolecules, and highly reactive nitrile oxides, imines and ylides, can be generated *in situ* via photolysis or chemical uncaging and have been used as bioorthogonal reacting partners with alkynes[4]. The diversity of dipoles and dipolarophiles resulted in a range of reactivities that can be selected for specific applications and has led to the development of bioorthogonal reactions that are orthogonal to each other. Mutually orthogonal reactions have been of much interest recently because they allow for multicomponent labelling and can be used to track or label more complex biological processes simultaneously. Typically, this is done by combining bioorthogonal reactions that are mechanistically different from each other, using steric repulsions to favour the less bulky reacting partner, manipulating the electronics of a dipole so that it kinetically favours one dipolarophile, and by *in situ* activation[5]. While there have been many examples of simultaneous one-pot dual labeling with two bioorthogonal reactions, there haven't been many one-pot, triple bioorthogonal reactions[6], due to the cross reactivity of many bioorthogonal reagents. To overcome this limitation, bioorthogonal reaction development is currently focused on exploring unique modes of reactivity, to enable multicomponent labeling and a diverse range of biological applications[1,4,7,8].

Heterocycles that contain an endocyclic nitrogen and hydroxyl group, like 3-pyridinol (1), are in tautomeric equilibrium with 3-oxidopyridinium (2) (3-OXP), where the proton on the hydroxy group is transferred to the nitrogen, resulting in a zwitterionic tautomer. The aromaticity of 3-oxidopyridiniums arises from the replacement of the hydrogen on the nitrogen in the tautomeric species with a substituent (3), stabilizing the positive charge on the nitrogen and preventing the protonation of the negatively charged oxygen[9] (Scheme 2.1).

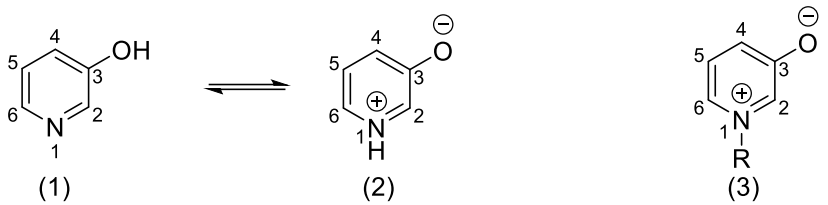

Scheme 2.1: Stabilization of the tautomeric species by replacing the hydrogen with an N-substituent

3-oxidopridinium ions (3) are water stable and soluble heteroaromatic betaines that behave as latent dipoles that undergo a wide variety of cycloadditions as a result of their different resonance structures. [10,11] Typically, 3-oxidopyridiniums react with ketenes across the oxygen and either carbon 2 or carbon 4 in a [7+2] cycloaddition, across the 2 and 4 carbons in a [5+4] cycloaddition with dienes, and most relevant to the cycloadditions in bioorthogonal chemistry, across the 2 and 6 position with alkynes and olefins in a [3+2] cycloaddition. (Scheme 2.2) Research into the cycloaddition reactions of 3-oxidopyridiniums was spearheaded by Alan R. Katritzky and collaborators from the early 70s until the late 80s[12] but have yet to be seen in a bioorthogonal application.

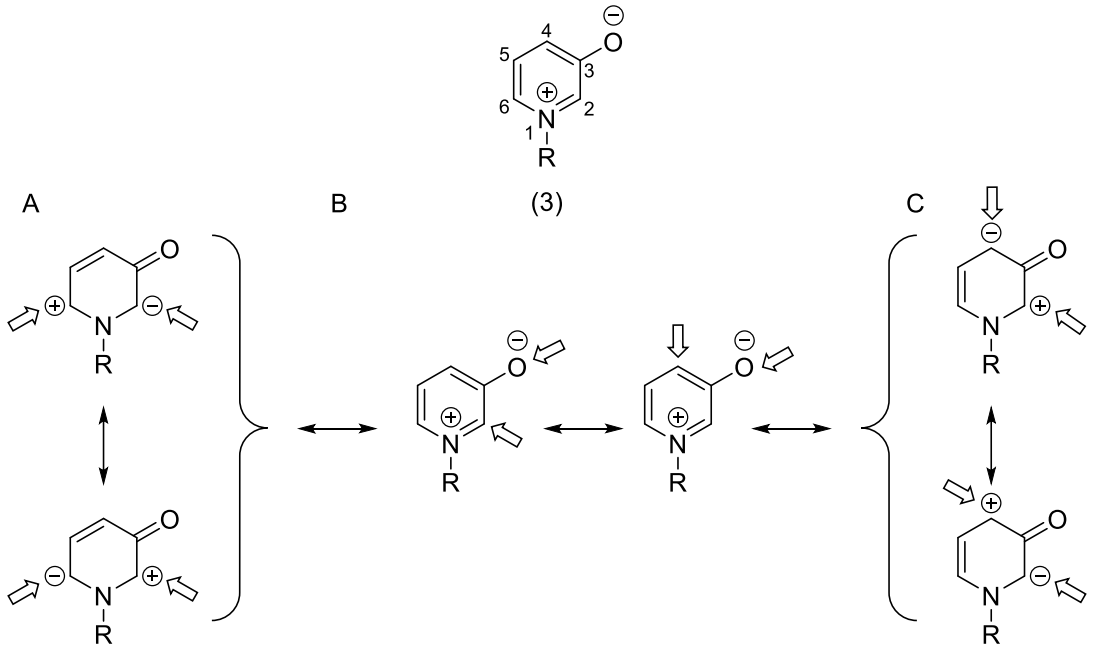

Scheme 2.2: Resonance structures and selectivity of the various cycloadditions of 3-oxidopyridiniums. A) 3-atom, 4-electron dipole with 2,6 periselectivity. B) 7-atom, 8-electron dipole with 2,O and 4,O periselectivity. C) 5-atom, 6-electron dipole with 2,4 periselectivity. Adapted from H. Ren et al[11].

The majority of the work on 3-oxidopyridiniums was focused on the effects of the N-substituent on the mode of cycloaddition with various dipolarophiles with respect to their regiochemistry, selectivity, and stereochemistry[12]. 1-methyl-3-oxidopyridinium (4) was the first 3-oxidopyridinium studied[13], and was found to react across the 2 and 6 positions as a 1,3-dipole with electron deficient unsymmetrical olefins with the oxygen anti to the substituent on the dipolarophile to form N-methyl-8-azabicyclo[3.2.1]-3-en-2-ones (Scheme 2.3). When reacted with acrylonitrile, only the *exo* isomer was observed while both isomers were observed when reacted with either methyl acrylate or methyl methacrylate. These reactions however, required refluxing for up to three days[13], with researchers postulating that faster reactions with a wider scope of olefins can be achieved by placing an electron withdrawing group on the nitrogen, making a better electron sink, or by the addition of electron donating groups to the ring to activate carbon 2.

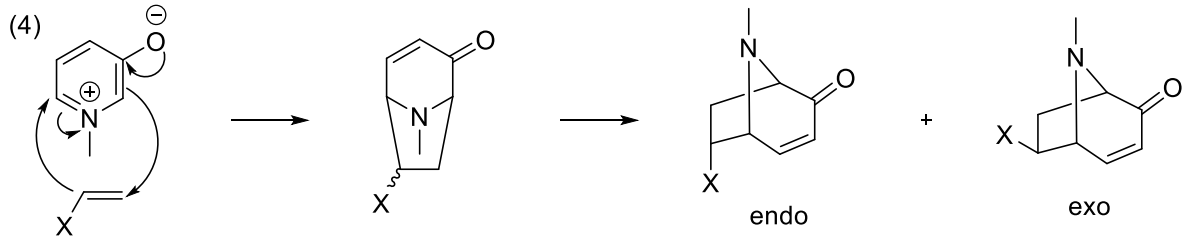

Scheme 2.3: Cycloaddition of 1-methyl-3-oxidopyridinium with asymmetric dipolarophiles. X = CN, CO2Me, (Me)CO2Me. Adapted from N. Dennis et al[9].

The addition of electron withdrawing N-substituents to 3-oxidopyridinium did indeed increase their reactivity with electron deficient dipolarophiles[14]. The most reactive 3-oxidopyridinium, 1-(5-nitro-2-pyridyl)-3-oxidpyridinium, reversibly dimerizes along its 2,2'-4,6' positions[15]. The monomers are too unstable for isolation and at higher temperatures, the thermal dimer dissociates. Upon the addition of typically unreactive styrene at higher temperatures, the 2,6 adduct is observed[16]. (Scheme 2.4)

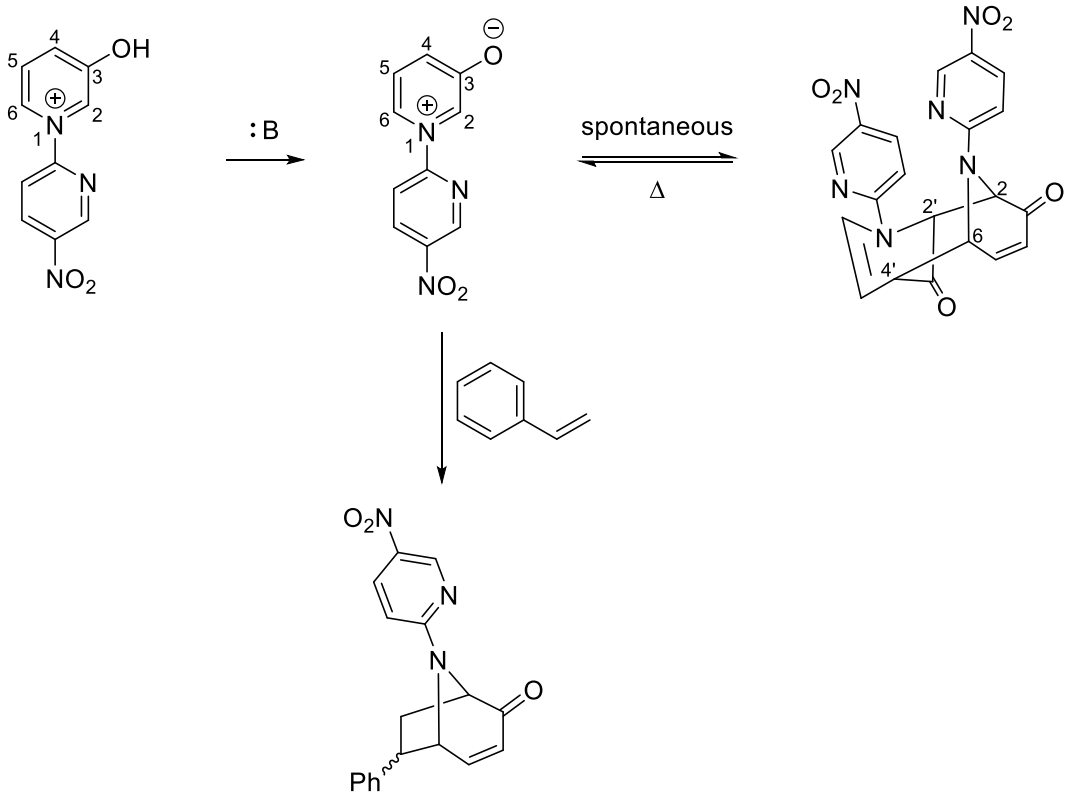

Scheme 2.4: Upon the deprotonation of the 3-hydroxy to the oxyanion, dimerization of 1-(5-nitro-2-pyridyl)-3-oxidopyridinium occurred. At higher temperatures the monomer reacts with styrene.

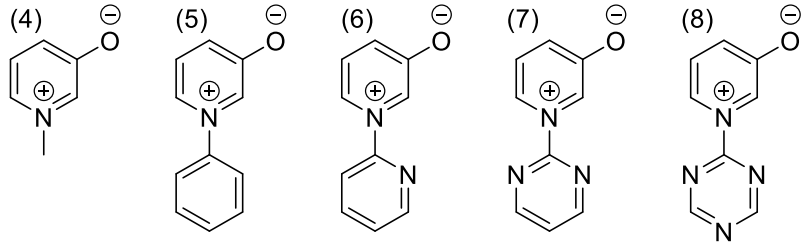

Scheme 2.5: 3-oxidopyridiniums tested by Katritzky A.R. et al[17].

In a 1979 paper, Katritzky A.R. et al correlated the regioselectivity and relative reaction rates to FMO theory. They first calculated and compared the transition state energies for the cycloaddition of methyl acrylate to a series of increasingly electron withdrawing N-substituents on 3-oxidopyridiniums: methyl (4), phenyl (5), 2-pyridyl (6), pyrimidin-2-yl (7), and triazin-2-yl (8)[17] (Scheme 2.5). HOMO and LUMO energies for the betaines and methyl acrylate were calculated using

the CNDO/2 method as were the coefficients for the possible positions of reaction. This was used to calculate the total interaction energy (ΔE_{int}) to measure transition state stabilization during bond formation. Reactivity was found to increase with N-substituents that are increasingly electron withdrawing. The calculated individual HOMO (pyridinium)-LUMO (dipolarophile) (H_PL_D) and LUMO (pyridinium)-HOMO (dipolarophile) (L_PH_D) contributions indicated that the increase in reactivity seen between N-methyl and N-phenyl 3-oxidopyridiniums is due to an increase in the H_PL_D contribution of the reaction, whereas the increase in reactivity for other electron withdrawing N-aryl substituents is due to an increase in the L_PH_D contribution. It was also found that across all pyridiniums tested, the cycloaddition with methyl acrylate was predicted to occur via a [3+2] cycloaddition across the 2,6 positions of the betaines with the 3-oxyanion anti to the methyl ester. Regioselectivity has also been explained by the high electron density calculated at the 2-position due to the oxyanion on position 3[16]. However, this rationalization only applies to electron poor dipolarophiles, while this regioselectivity is also conserved over a range of olefins. Calculated TS energies of the addition of 1-(pyrimidin-2-yl)-3-oxidopyridinium to a series of olefins indicated that for electron poor olefins H_PL_D interaction dominates, whereas the L_PH_D interaction dominates with electron rich olefins. The observed stereoselectivity of cycloadducts across the range of dipolarophiles correlated with the calculated steric interactions that took into account secondary orbital interactions and electronic repulsion[17].

While the effects of substituents on the ring weren't studied as closely as the N-substituents, they were still found to have an effect on the rate of the reaction. All of the reported ring substituted 3-oxidopyridiniums were methylated on the nitrogen[12]. (Scheme 2.6) Electron donating substituents on the 5 position (Scheme 2.6b) were not shown to affect the regio- or stereo-selectivity of the pyridinium in comparison to the unsubstituted but demonstrated increased reactivity and achieved higher yields[18]. The addition of 5-OMe allowed for the cycloaddition with styrene which wasn't previously observed with (4), and phenyl acetylene[19]. Electron withdrawing substituents on the 2

position were as expected: less reactive and low yielding in comparison to (4) with electron poor olefins, with 2-CN being the lest reactive, followed by 2-Br and 2-Cl[20]. For both sets of pyridiniums, the substituents were specifically added to access a novel route for troponoid synthesis.

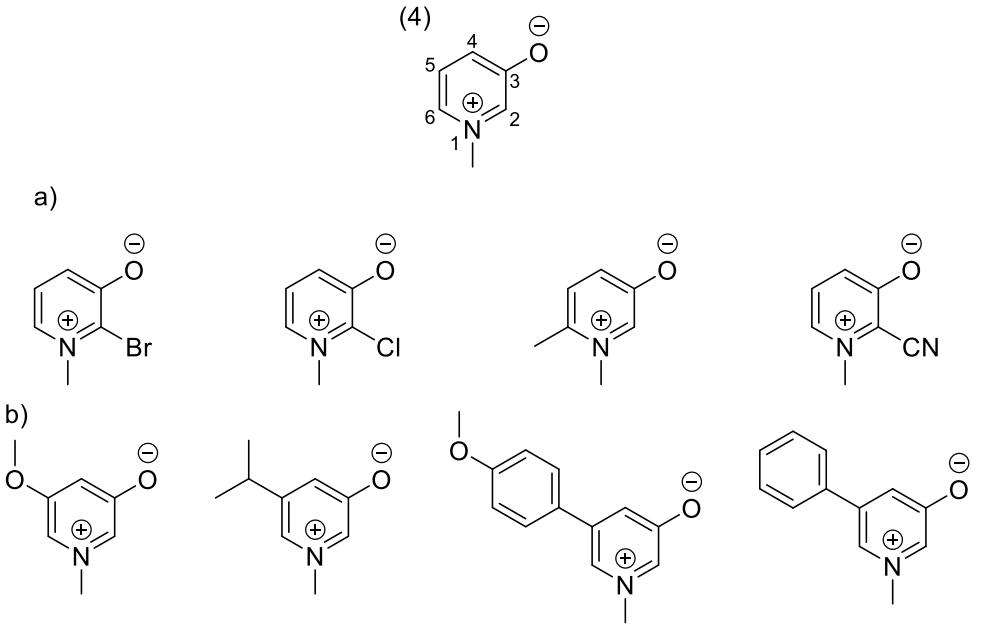

Scheme 2.6: Ring substituents of N-methyl-3-oxidopyridinium. a) substituents on the 2 position or 6 position. b) substituents on the 5 position.

Reactivity with acetylenes is also observed with 3-oxidopyridiniums. Cycloadditions with dimethyl acetylene dicarboxylate (DMAD), react with a wide range of N-substituents, resulting in an unexpected furan product (Scheme 2.7)[10]. The cycloaddition with DMAD occurred across the C2 and oxygen of the 3-oxidopyridinium that acts as an 8-electron dipole followed by a 6π rearrangement. FMO calculations indicated that the cycloaddition regioselectivity is due to the much lower LUMO energy of DMAD in comparison to other electron deficient olefins, resulting in the HOMO pyridinium – LUMO DMAD interaction dominating. The atomic orbital coefficients for most pyridinium HOMO are the highest for the oxygen and C2[17], explaining both the regioselectivity and why reactions with DMAD occurred across a range of pyridiniums. Reactivity with phenylacetylene was also reported, forming the expected cycloaddition across the 6,2 positions, but required more activated 3-oxidopyridiniums, either by the addition of EWG on the N position or EDG on the 5 position[19].

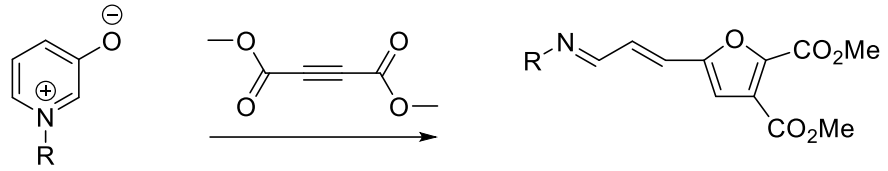

Scheme 2.7: Furan cycloadduct formation via the cycloaddition of DMAD across carbon 2 and the oxyanion, followed by a 6π rearrangement.

Benzyne was also proven to be a reactive dipolarophile, even reacting with 3-hydroxypyridine[21]. When reacted in a 2:1 molar ratio, the expected 6,2 cycloadduct is formed along with N-phenylation (Scheme 2.8a). The analogous reaction with N-methyl-3-oxidopyridinium resulted in two subsequent cycloadditions (Scheme 2.8b), whereas the reaction with N-phenyl-3-oxidopyridinium resulted in the expected addition across the 6,2 positions. The double addition isn't fully explained, but it is presumed that the double addition to either 3-hydroxypyridine or N-methyl-3-oxidopyridinium could be due to a nucleophilic attack from the bridged nitrogen after the expected 6,2 cycloaddition[9].

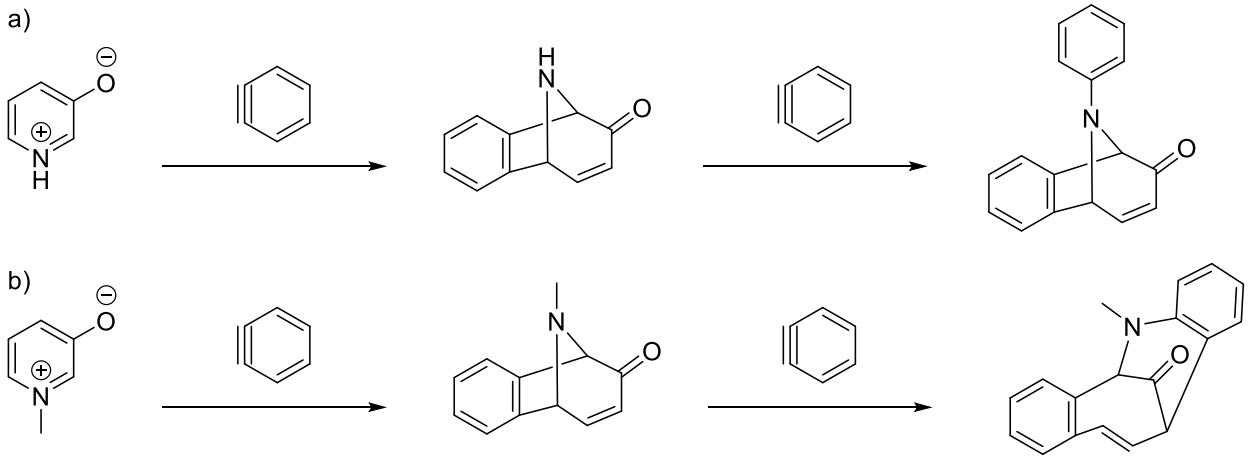

Scheme 2.8: Double addition of benzyne to (a) 3-hydroxy pyridinium and (b) N-methyl-3-oxidopyridinium

2.2 Objective

Despite the success of a lot of the pre-existing bioorthogonal reactions, expanding the bioorthogonal toolbox is required to widen the scope of bioorthogonal applications. Cycloadditions

with unique reactivities are especially sought after, especially for applications involving simultaneous duplex or triplex labelling. 3-oxidopyridiniums have been commonly used in the total synthesis of natural products due to their ability to form nitrogen containing tricyclic adducts, tropones, and tropolones[9,22]. The reactivity of 3-oxidopyridiniums have been well researched in the 70's and 80's but haven't been used in a bioorthogonal setting. In this chapter, the reactivity of 3-oxidopyridinium with commonly used dipolarophiles in bioorthogonal chemistry will be explored, along with a detailed mechanistic investigation.

2.3 Results and Discussion

2.3.1 Selection and synthesis of 3-oxidopyridiniums and dipolarophiles

As previously mentioned, the majority of 3-oxidopyridiniums tested differed by the N-substituent, and only a handful of pyridiniums were altered along its ring. When designing a bioorthogonal reaction, at least one of the reacting partners should be designed so it can in incorporate some sort of functionality, whether that be a probe to detect the targeted biomolecule or a reporter so that it can be incorporated into the targeted biomolecule. With that in mind, the most convenient location on the pyridinium to incorporate functionality was off the nitrogen. 3-oxidopyridniums can be synthesized in multiple ways, the two most common involve either an S_N2 type reaction (Scheme 2.9a) with a halogenated substituent, or via the reductive amination of furfural with a primary or secondary amine (Scheme 2.9b)[23].

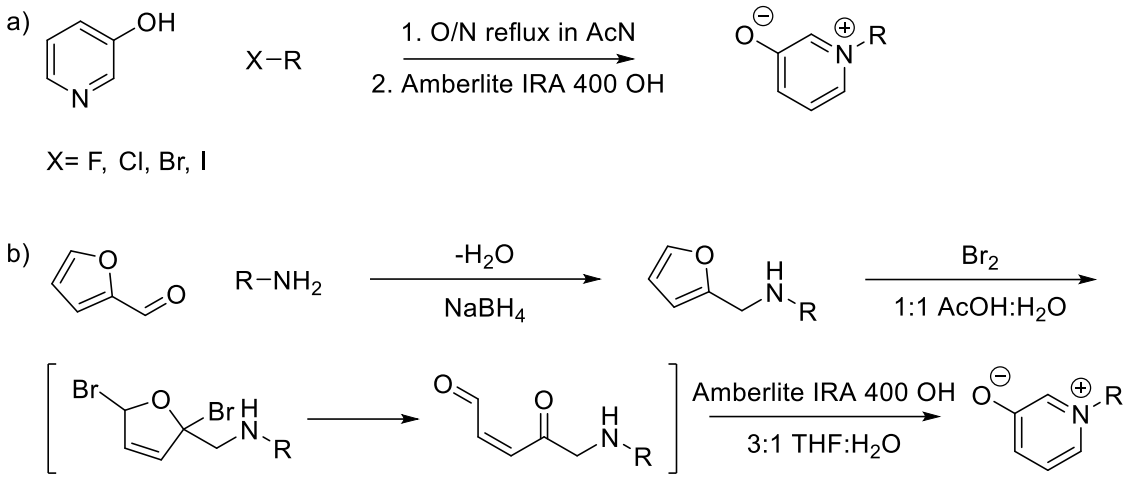

Scheme 2.9: Most common synthetic route for introducing N-substituents on 3-oxidopyridiniums

Using synthetic route (b), the primary amine of the lysine side chain can react with furfural to form an unnatural amino acid (UAA). While N-methylated 3-oxidopyridiniums are the least reactive of the N-substituted pyridiniums, it will best mimic the expected reactivity of the 3-oxidopyridinium when it is used as an UAA, as longer alkyl chains off the nitrogen haven't been shown to alter the reactivity of 3-oxidopyridiniums[14]. Using a range of different N-substituents, from a logistics standpoint, would mean that the N-substituent that offers the fastest kinetic rate would have to be altered in some way to add bioorthogonal functionality. Based on previous reports on cycloadditions of 3-oxidopyridiniums, even a slight change on the N-substituent has been shown to alter reactivity[17]. Instead, I had opted to explore the reactivity of N-methyl-3-oxidopyridiniums, by altering the substituent on the 5 position, which has been proven to not alter the regio- or stereoselectivity of the reaction, but only affect the rate of the cycloaddition[14,17]. The N-methyl-3-oxidopyridiniums below were synthesized from its 3-hydroxypyridine form via MeI as the methylating agent (Scheme 2.10). The deprotonation step via a basic resin or NEt_3 is required to delocalize the negative charge of the oxygen so it can react as a dipole[13]. By NMR, the ring and methyl protons of the deprotonated 3-OXP were much more shielded than the protonated form, indicating that the oxyanion negative charge is delocalized along the ring. The pyridiniums were observed to

readily solubilize in water and were observed to be relatively stable in water as well. Future work aims at more accurately determining the extent of their stability in water.

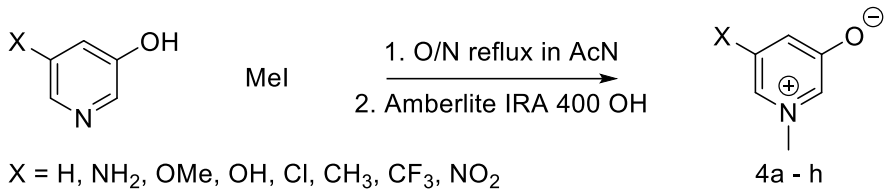

Scheme 2.10: 5-substituted N-methyl-3-oxidopyridiniums synthesized and tested.

The dipolarophiles initially chosen are commonly used in bioorthogonal reactions: bicyclo[6.1.0]nonyne (BCN) and 4-dibenzocyclooctynol (DIBO). These two alkynes were chosen for their relative ease of synthesis in comparison to other strained alkynes, and because electron rich BCN and electron poor DIBO have been shown to preferentially react with electron poor nitrones, and electron rich nitrones respectively[24]. The intent is to determine the effect of the 5-substituents on the cycloaddition between 3-oxidopyridiniums and strained cycloalkynes with opposing electron density.

2.3.2 Preliminary reactivity of N-methyl-3-oxidopyridinium with various dipolarophiles

Based on the previous work on the cycloaddition of N-methyl-3-oxidopyridinium, N-phenylmaleimide was chosen as the prototype dipolarophile to confirm the published[13] reactivity. N-phenylmaleimide was also chosen to assist in developing a purification and isolation method of the cycloadduct to minimize overuse of the synthesized strained alkynes. The expected 8-azabicyclo[3.2.l]oct-3-en-2-one scaffold of the adduct was observed and the NMR spectra was as reported[13]. N-phenylmaleimide and N-methyl-3OXP reacted in a 1:1 molar ratio and was tracked by NMR over 17 hours but did not go to completion. To isolate the product, the reaction was run in a 1.2:1 molar excess of N-phenylmaleimide and after N-methyl-3-OXP was consumed, the product was isolated using silica column chromatography, using EtOAc first to remove unreacted N-phenylmaleimide and then flushing with methanol to get the product, which was filtered with a 0.2 μm nylon filter.

Previous studies showed that N-methyl-3-oxidopyridinium was unable to react with phenyl acetylene unless the N-substituent was more electron withdrawing or if the ring was activated by the addition of an EDG[19]. Phenyl acetylenes were previously used with nitrones to label biomolecules via the Kinugasa reaction[25], and the intent was that perhaps same conditions would activate the alkyne enough such that it can react with the water stable and soluble N-methly-3-OXP. The reaction that occurred was slow, and after tracking overnight via UV-vis, did not go to completion and was not pursued further.

BCN was then reacted with N-methyl-3-OXP and was also slow. After tracking for 16 hours via UV-vis, the reaction did not go to completion. This was expected to some degree as 3-OXPs are electron-rich, and BCN is also electron-rich, but not to this extent. Further evaluation proved that the addition of a nitro substituent on the 5-position, resulted in a reaction with BCN that went to completion after 16 hours, in agreement with literature explanations of 3-OXP reactivity. NMR spectra and UV-vis traces of the kinetic experiments for reactions that were slow are included in Appendix A.

The cycloaddition of N-methyl-3-oxidopyridinium with DIBO was shown to react within 12 hours by NMR tracking, forming 4 isomers as indicated by the number of methyl peaks shown (Figure 2.2). Given that it was the only dipolarophile tested that went to completion, it was selected for further kinetic and mechanistic studies.

2.3.3 Kinetic studies of the cycloaddition of 5-substituted N-methyl-3-oxidopyridinium with DIBO

The rate constants of cycloadditions of various 5-substituted N-methyl-3-oxidopyridiniums were conducted in duplicate using UV-vis spectroscopy in acetonitrile at 25 ± 0.1 °C unless otherwise stated. Reactions were done using pseudo first order kinetic conditions where the concentration of DIBO exceeded the concentration of the pyridiniums (100 μM) by at least 50-to-125-fold excess. The

reactions were monitored for the decrease of absorbance at the wavelength specified in the table below, along with the calculated rates (Table 2.1).

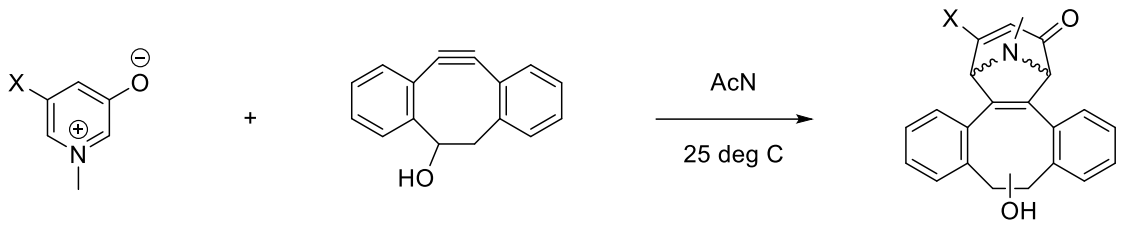

*Table 2.1: Reaction conditions, the absorbance wavelength monitored, and the rates calculated using UV-vis kinetic studies of the cycloaddition of DIBO and various 5-substituted N-methyl-3-oxidopyridiniums. *Were not fully soluble in AcN, the 4 mM stock solution of each pyridinium was made with 5% MeOH. Subsequent dilutions were done with AcN. **Reaction done in MeOH to adequately dissolve BCN.*

Alkyne	5-substituent	Wavelength λ (nm)	Rate (k_2 M^{-1} s^{-1})
DIBO	X = NH_2	345	1.07*
DIBO	X = OMe	356	0.506
DIBO	X = OH	335	0.164*
DIBO	X = Cl	361	1.33E-2
DIBO	X = CH_3	352	8.84E-3
DIBO	X = H	356	3.70E-3
DIBO	X = CF_3	365	3.31E-4
DIBO	X = NO_2	408	slow*
BCN	X = NO_2	408	1.77E-2**

Data analysis of pseudo-first order kinetics experiments tracked by UV-vis absorbance was conducted by a non-linear regression of the relative absorption values as a function of time (in seconds) to fit the first order integrated rate law $[A] = [A]_0 e^{-kt}$ by only changing the k value. Once the observed rate constant (k_{obs}) is calculated for a given excess concentration of DIBO with a pyridinium (Table 2.2), the duplicates are averaged and plotted against the varying concentrations of DIBO. The slope of the linear trend line fitted to the data points represents the second order rate constant (k_2) (Figure 2.1). Observed first order rate constants and graphical determination of k_2 values for each pyridinium tested are found in Appendix A.

Table 2.2: Observed pseudo-first order rate constants for the cycloaddition between 5-amino-N-methyl-3-oxidopyridinium and DIBO The concentration of 5-NH_2 NM3-OXP used is 100 μM.

N-methyl-3OXP structure	[DIBO] (M)	k_{obs} (s^{-1})
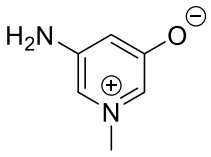	0.01	0.012079784
	0.008	0.010015418
	0.006	0.008058713
	0.004	0.005579809

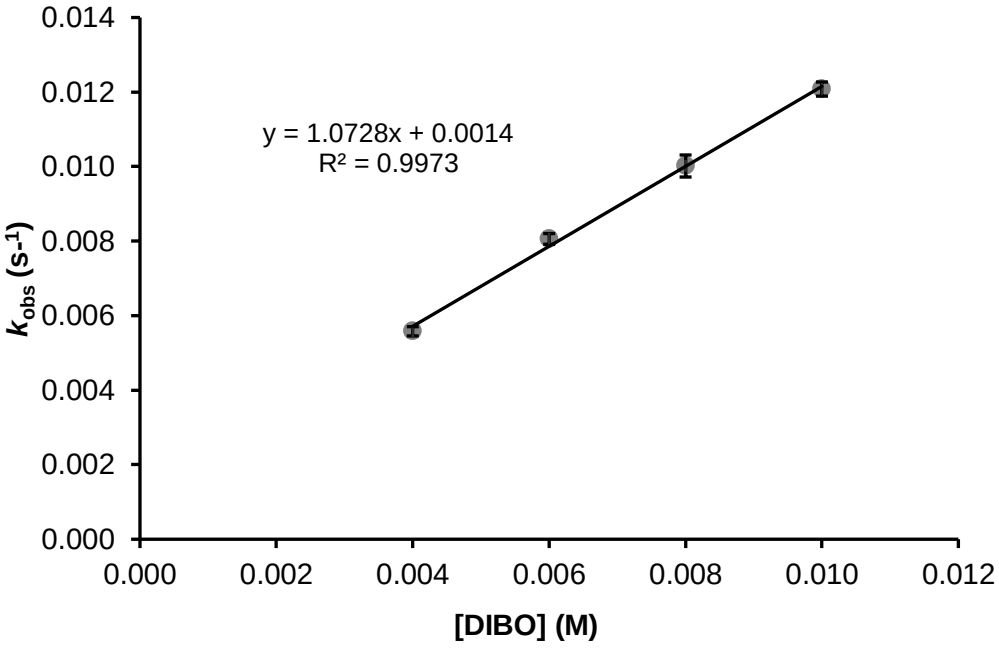

Figure 2.1: Plot of observed rate constants as a function of DIBO concentration. The slope indicates the reaction rate constant k_2 ($M^{-1}s^{-1}$).

2.3.4 Product Purification and Elucidation by NMR

The NMR spectrum of the reaction between N-methyl-3-oxidopyridinium and DIBO (Figure 2.2), showed 4 methyl peaks at around 2.7 ppm, indicating that there are 4 products (5a-d). To confirm that the four products are the stereo- and regio-isomers of the [3+2] cycloadduct, the products had to be separated. Column chromatography, preparative liquid chromatography, and preparative thin layer chromatography were all attempted to separate the products. The method that worked best was using a preparative TLC plate with an eluting solvent of 1% Et_3N in 1:1 EtOAc:hexane. After rerunning the plate 6 times, sufficient separation of the products was observed.

The scratched off silica was collected in a test tube, washed with acetone, filtered through a 0.2 µm nylon filter, and the solvent was evaporated. The NMR data is summarized below (Table 2.3), and with the assistance of two-dimensional ^{1}H-^{1}H COSY, NOSY, and ^{1}H-^{13}C HSQC NMR experiments (Appendix C), the spectra indicate that the 4 products are the regio- (DIBO hydroxy anti or syn to the enol/ketone) and stereoisomers of the 2,6 addition to DIBO (Scheme 2.11).

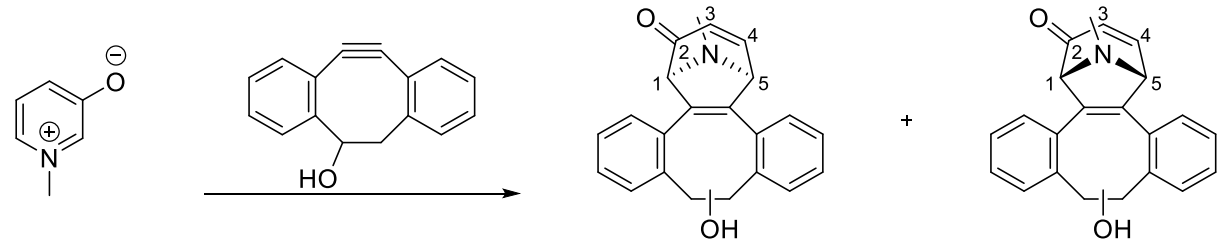

Scheme 2.11: Structures of cycloadducts 5a-d.

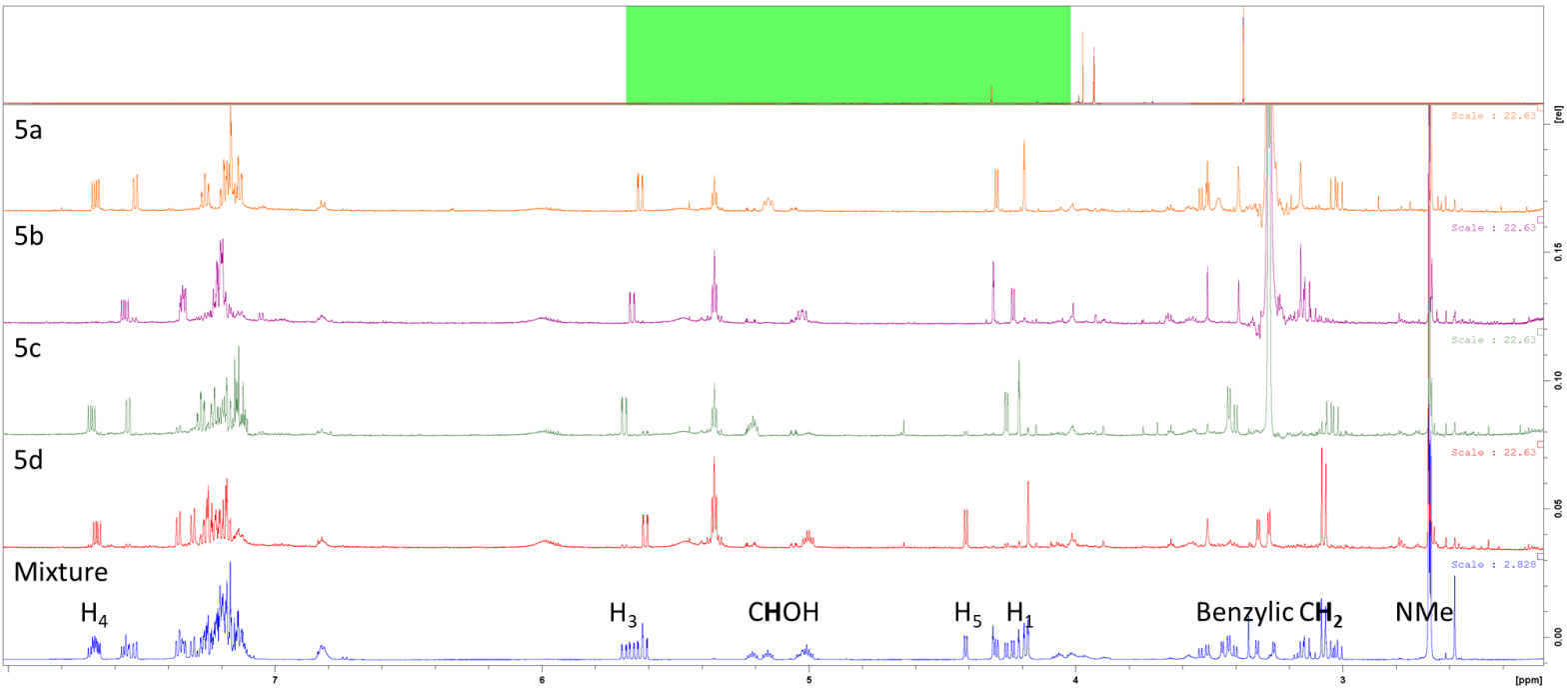

Figure 2.2: ^{1}H NMR spectra (600 MHz, d_3-AcN) of each isomer (5a-d) and the mixture of isomers prior to separation along with the general assignment of each peak. The peaks for d_3-AcN, water, AcN, and TMS were cropped to improve clarity. The full spectrum of each is included in Appendix C.

The ^{1}H NMR peaks of interest are H_1, H_3, H_4, and H_5, and have been used to determine the stereoselectivity. Across all 4 isomers similar connectivity is seen. Long range coupling is observed

between H_1 and H_3, evidenced by the relatively small J coupling value, supported by the two-dimensional ^1H-^1H COSY spectra. The chemical shift of H_4 is central to determining the relative positioning of the other protons. H_4 has a chemical shift that is consistent with what is typically seen with enone-type α-β-unsaturated carbonyls and couples with H_3 and H_5. The larger coupling constant between H_3 and H_4, is typical of *cis* substituted cyclic alkenes, while the ^3J coupling constant between H_4-H_5 is representative of constants for allylic protons.

*Table 2.3: Experimental ^1H NMR chemical shifts of the isomers of cycloadduct 5 in ppm referenced from d_3-AcN. J coupling constants in Hz. *2 overlapping dd.*

Product	***H_1***	***H_3***	***H_4***	***H_5***	***CH_2***	***CHOH***	***Aromatic***	***N-Me***
5a	4.19 (t)	5.63 (dd)	7.67 (dd)	4.30 (dd)	3.52 (dd) 3.02 (dd)	5.15 (m)	7.25-7.20 (m)	2.67 (s)
5b	4.30 (t)	5.67 (dd)	7.57 (dd)	4.23 (dd)	3.13 (dd)*	5.03 (dd)	7.26-7.15 (m)	2.68 (s)
5c	4.21 (t)	5.70 (dd)	7.68 (dd)	4.26 (dd)	3.52 (dd) 3.02 (dd)	5.21 (m)	7.33-7.09 (m)	2.67 (s)
5d	4.17 (t)	5.61 (dd)	7.64 (dd)	4.41 (d)	3.29 (dd) 3.06 (dd)	5.00 (dd)	7.34-7.06 (m)	2.68 (s)
Coupling Constants	*$H_1 - H_3$*	*$H_3 - H_4$*	*$H_4 - H_5$*					
	1.5	9.7	5.6					

These four protons were able to determine the structure of the cycloadduct but are unable to differentiate between the two stereoisomers. Molecular modeling shows that the two isomers differ by the positioning of the methyl group – either pointed toward (Figure 2.3a) or away (Figure 2.3b) from the plane of the aromatic rings of DIBO. Based on the modeled structures, the two isomers appear to be enantiomers of each other. The nOe (nuclear Overhauser effect) experiments, while conducted, could not detect any significant enhancements on the proton signals that were used to determine the structures of the products. The regioisomers could not be differentiated from experimental data.

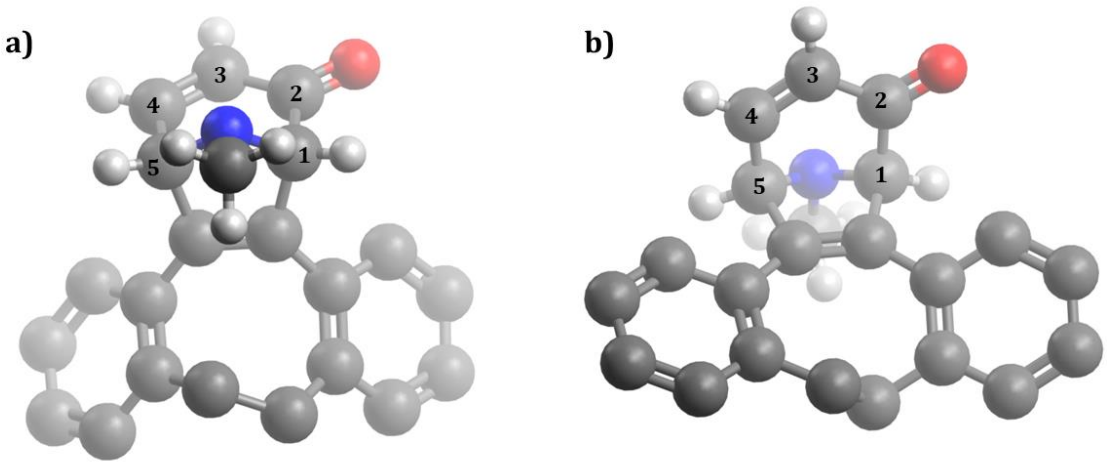

Figure 2.3: Modeled structures of the stereoisomers for cycloadduct 5. Calculations were conducted by my colleague, Jason Josephson, using the Gaussian 16 program package and geometry optimizations were caried out at the M06-2X level of theory with the 6-31+G(d,p) basis set. The DIBO hydroxy was omitted from the calculations. The DIBO protons were omitted from the model for clarity. Distances between protons were measured using Avogadro software, version 1.2.0.

The NMR spectra of the 4 isomers can also indicate the relative ratio of product yields. The H_3 peaks in the 5.6 to 5.7 ppm region of the mixture spectra can be assigned to each isomer. In each isomer, the H_3 peak is a doublet of doublet, with the overlapping of one of the doublets from 5a and 5d appearing as triplet in the mixture (Figure 2.4). The relative ratio of products was determined by integrating one doublet from each dd on the mixture spectra and then using the integral values to determine the relative amounts of each isomer. The relative ratio of each isomer is summarized in Table 2.4.

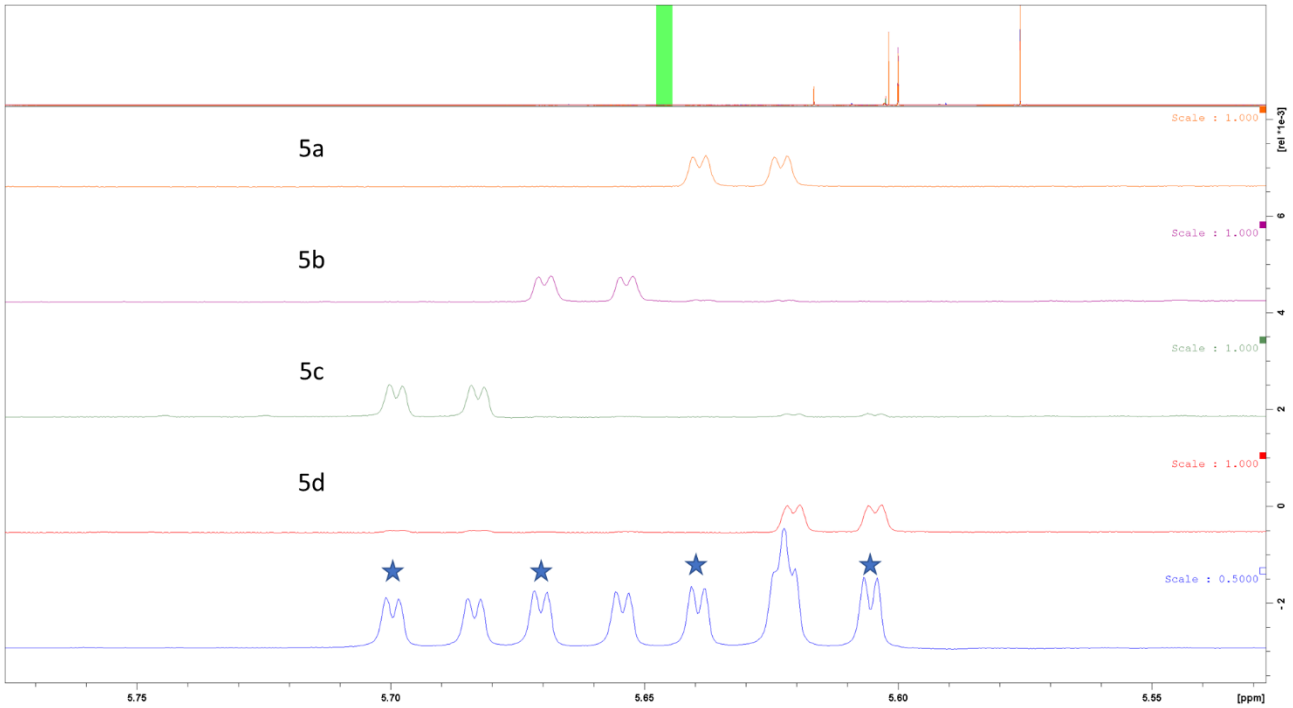

Figure 2.4: Stacked ^{1}H NMR spectra (600 MHz, d_3-AcN) of the doublets of doublets used to determine the product ratio of isomers 5a-d. The integrations were done on one of the doublets in the mixture spectra (bottom panel, starred) that do not overlap between other fractions.

Table 2.4: Product ratios of each isomer based on the integration of a doublet from each isomer. The chemical shift of each isomer is in ppm referenced from d_3-AcN.

Isomer	***Integral (abs)***	***Relative Ratio***	***Chemical Shift (ppm)***
5a	9447734	1.18	5.64
5b	9020248	1.13	5.67
5c	8004514	1	5.70
5d	10160820	1.27	5.60

H_4 was critical in determining the structure of the products between DIBO and unsubstituted N-methyl-3-OXP as it couples with both H_1 and H_5. For products of cycloadditions between 5-substituted N-methyl-3-OXPs, H_4 is replaced by the pyridinium substituent, making it harder to determine their structures. For the three fastest reactions (with 5-OH, OMe, and NH_2 N-methyl-3-OXP) the structure of their final products was determined with the assistance of the spectra of the unsubstituted products.

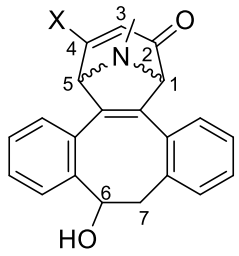

X = H (5), OH (6), OMe (7), NH_2 (8)

Figure 2.5: General structure of anticipated products. X = H (5), OH (6), OMe (7) and NH_2 (8). The positioning of the hydroxy group is arbitrary to simplify discussion and is not meant to indicate preference of one regioisomer formation over the other as the NMR data could not differentiate between the regioisomers.

The cycloadducts were obtained by reacting the 5-substituted N-methyl-3-OXPs with DIBO in a 1:1 molar ratio of 40 mM in 2 mL of methanol. Methanol was preferred over acetonitrile as the 5-OH and 5-NH_2 pyridiniums are not fully soluble in AcN. Once 95% percent conversion was achieved, the solvent was evaporated, and the product was separated by column chromatography using Et_3N-neutralized silica. Dichloromethane was used to elute out any unreacted DIBO, acetone was used to elute the product, and any remaining pyridinium was removed using methanol. Mass spectroscopy data for the 3 cycloadditions is summarized in Table 2.5. d_3-AcN was used for NMR experiments instead of d_4-MeOD for consistency but to also mitigate any interference from water or solvent peaks since the product peaks (H_1, H_3, and H_5) typically show up within a chemical shift range of 5 – 3 ppm. The number of products formed was again determined by the number of methyl peaks. The ^1H spectra of products 7 and 8 (Figure 2.6) show similar patterns to what was observed with the unsubstituted products. Determining the proton peaks from DIBO was straightforward - the C**H**OH benzylic protons of DIBO (Figure 2.5, position 6) are seen as a sightly deshielded doublet of doublets (δ approx. 5.40 – 5.00 ppm), the 2 benzylic protons (Figure 2.5, position 7) are seen as doublets of doublets within a range of 3.70 to 2.90 ppm. However, for H_1, H_3, and H_5 it is more challenging due to the nature of the products. In the general product structure (Figure 2.5), protons on the 1, 3 and 5 positions should demonstrate long range coupling and appear as triplets with H_3 being more deshielded than H_1 and H_5. For product 7 this was much more evident as the bridgehead and allylic

protons are well defined triplets, with the exception of two H_3 triplets that overlapped. For product 8 however, the triplets are much more broadened with many of them appearing as broad singlets. The NMR data for cycloadducts 7 and 8 are summarized in Table 2.6 and proton assignments in Figure 2.6 were conducted with the assistance of ^{13}C, 2D ^{1}H – ^{1}H COSY, and 2D ^{1}H – ^{13}C HSQC data (Appendix C).

Table 2.5: HRMS (ESI+) data for the 4 products elucidated.

Product	***Molecular Formula***	***Calculated Mass (m/z)***	***Mass Found (m/z)***	***Formula of Mass Found***
5	$[C_{22}H_{19}NO_2 + H]^+$	330.1516	330.1494	$[C_{22}H_{19}NO_2 + H]^+$
6	$[C_{22}H_{19}NO_3 + Na]^+$	368.1263	368.1260	$[C_{22}H_{19}NO_3 + Na]^+$
7	$[C_{23}H_{21}NO_3 + Na]^+$	382.1419	382.1423	$[C_{23}H_{21}NO_3 + Na]^+$
8	$[C_{22}H_{20}N_2O_2 + Na]^+$	367.1422	367.1392	$[C_{22}H_{20}N_2O_2 + Na]^+$

Table 2.6: Experimental ^{1}H NMR chemical shifts of the isomers of cycloadducts 7 and 8 in ppm referenced from d_3-AcN. As the products were not separated, chemical shifts are reported as ranges. Integrations and number of signals within the range are also reported. Protons are as labeled in Figure 2.5.

Product	***Number of Isomers***	***H_3***	***H_1 and H_5***	***CH_2 (H_7)***	***CHOH (H_6)***	***Aromatic***	***N-Me***	***Other***
7	4	4.90 – 4.80 (4H: 3 t, 1 q)	4.33 – 4.05 (8H: 8 t)	3.56 – 2.92 (13H, m)	5.26 – 4.96 (4H: 4 dd)	7.60 – 7.11 (32H: m)	2.68 – 2.64 (12H: 4 s)	OMe: 3.75 – 3.63 (12H: 4 s)
8	4	4.56 – 4.48 (4H: 2 br s)	4.35 – 3.84 (7H: 7 t)	3.53 – 2.91 (8H, m)	5.39 – 4.90 (4H: 4 dd)	7.64 – 7.06 (34H: m)	2.67 – 2.61 (12H: 4 s)	NH_2: 5.84 – 5.51 (4H: 2 br s)

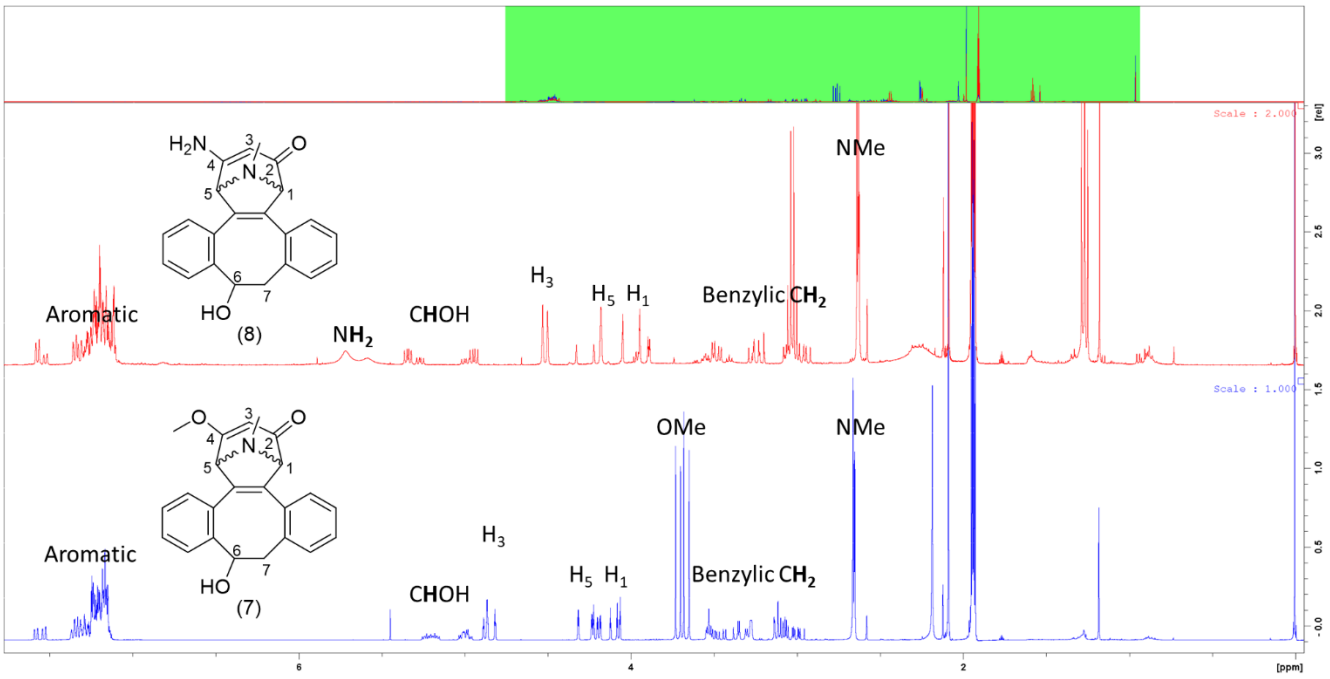

Figure 2.6: ^{1}H NMR spectra (400 MHz, d_3-AcN) of 7 (bottom) and 8 (top) along with the general assignments of each peak. Chemical shifts are in ppm referenced from d_3-AcN.

7 showed no evidence of degradation while 8 showed slight degradation. However, degradation was clearly evident in 6 (Figure 2.7). The aromatic DIBO peaks are missing, further downfield are peaks within the chemical shift range that are associated with aldehydes and carboxylic acids, further upfield are peaks in the allylic and aliphatic region that don't line up with the expected product peaks, and the characteristic methyl peak is missing. This could potentially be the product of a [7+2] cycloaddition followed by a 6π rearrangement and hydrolysis (Scheme 2.12) due to the presence of the aldehydic proton in the spectra and the absence of the methyl peak. To confirm whether the observed spectra is due to degradation during the purification step or because of a [7+2] cycloaddition, the same reaction conditions were applied for the reaction between DIBO and 5-hydroxy-N-methyl-3-OXP but was tracked by NMR in 1 mL of d_4-MeOD over 5 hours and was automated to run 13C, and 2D COSY, NOSY, and HSQC experiments directly after.

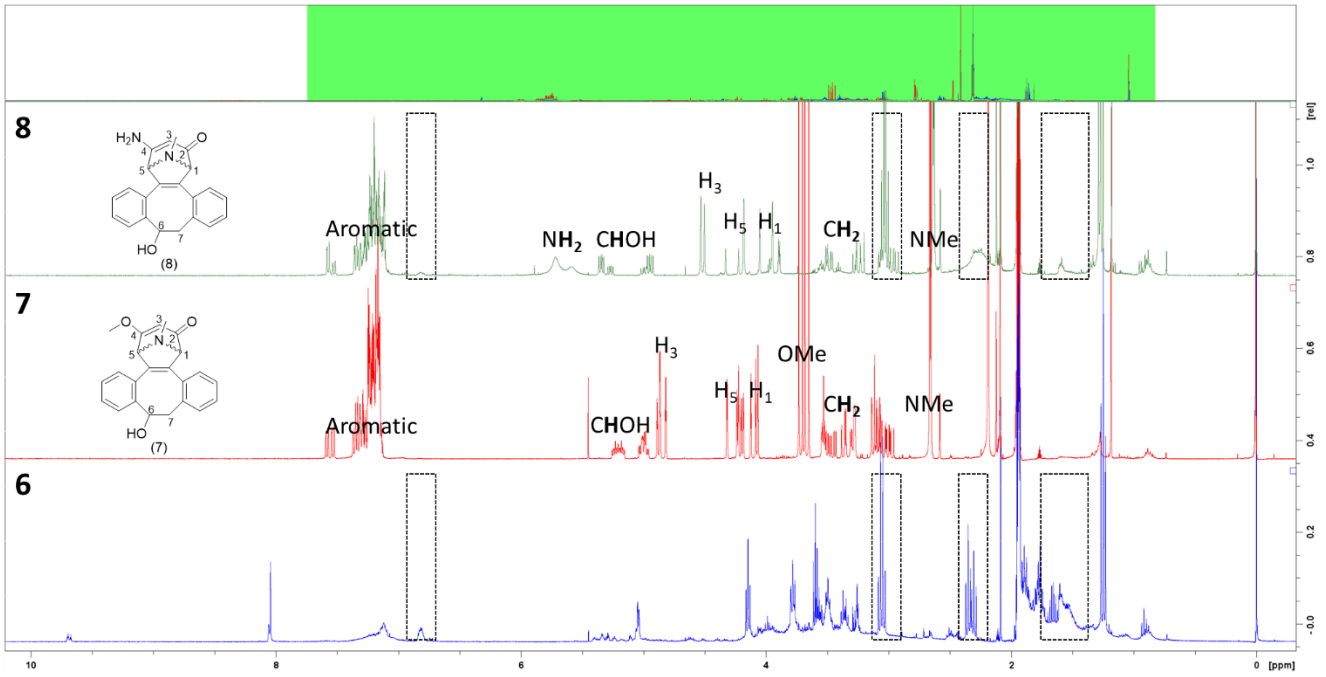

Figure 2.7: ^{1}H spectra (400 MHz, d_3-AcN) of 6 (bottom), 7 (middle), and 8 (top). Boxed peaks indicate signs of degredation. Chemical shifts in ppm from d_3-ACN

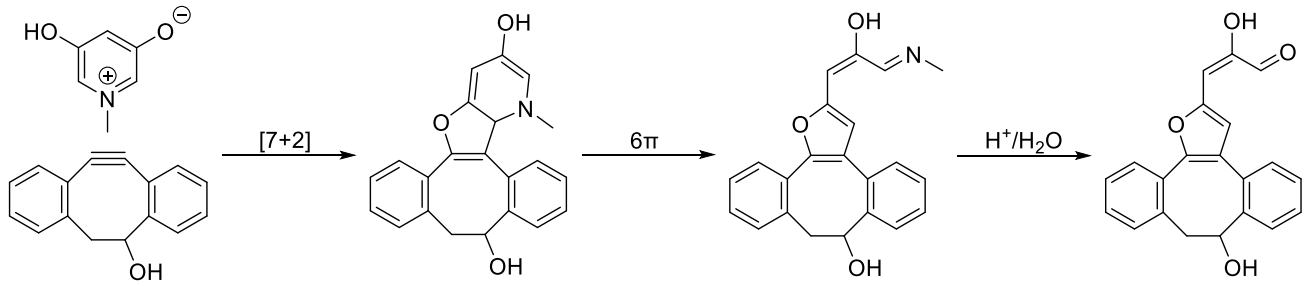

Scheme 2.12: [7+2] cycloaddition of 5-hydroxy-N-methyl-3-oxidopyridiniums with DIBO with the subsequent 6π rearrangement and acid catalyzed hydrolysis.

The NMR tracked reaction didn't show any signs of product degradation (Figure 2.8) even hours after the pyridinium had been consumed. Upon further examination of the last spectrum taken of the reaction, there are much smaller peaks along the baseline that are consistent with the product peaks of cycloadducts with other pyridiniums (Figure 2.9, boxed). However, that is not enough to definitively say that the product for 5-OH has the same spectra as other cycloadducts, especially since the water peak at 4.87 ppm in the spectrum interferes with some of the expected product peaks. The 2D NMR data does show coupling between the presumed benzylic CH_2 and C**H**OH protons of DIBO

that is consistent with what's seen with the cycloadducts (Appendix C), but the presumed allylic/bridgehead protons don't show coupling. That could be because the signals from unreacted DIBO drowned them out. Mass spectroscopy data found the calculated mass of the [3+2] cycloadduct, however, the second attempt at product purification with basic alumina and the same solvent system showed similar degradation patterns (Appendix C) confirming that the degradation of the product occurs due to purification.

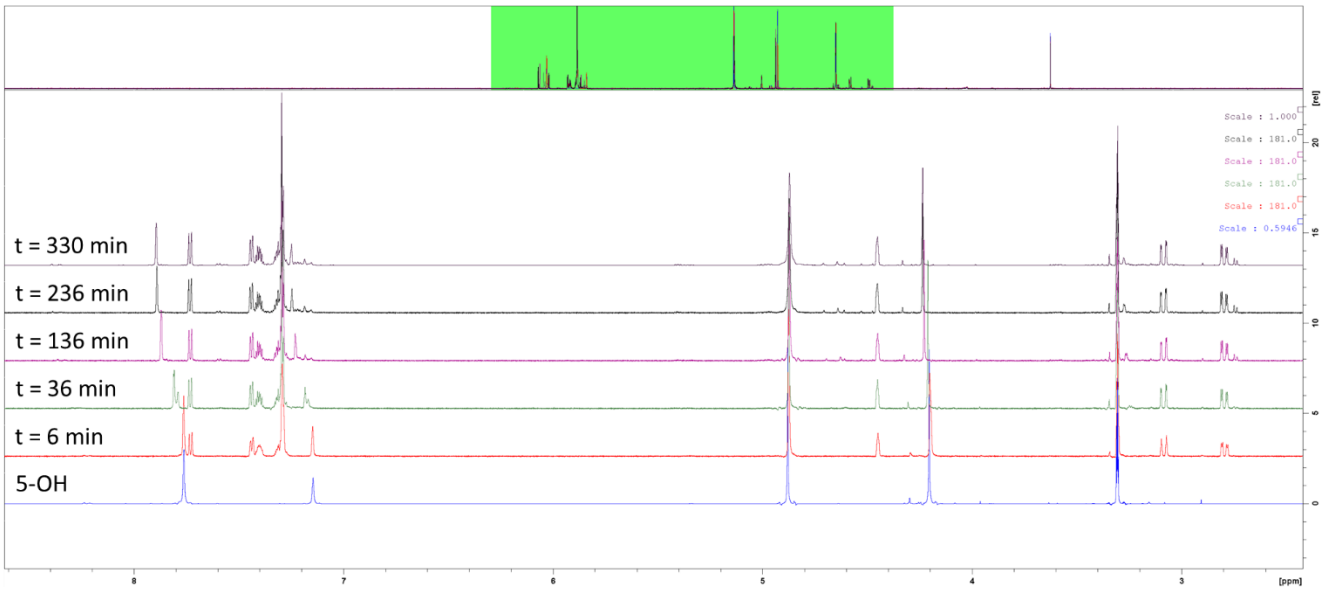

Figure 2.8: Stacked ^{1}H NMR spectra (600 MHz, d_3-MeOD) of the reaction between 5-OH-N-methyl-3-OXP and DIBO. Bottom spectrum is of the pyridinium, the second spectrum was acquired 6 minutes after the addition of DIBO to the NMR tube. Chemical shifts are in ppm referenced from d_4-MeOD. The TMS peak was cropped out for clarity.

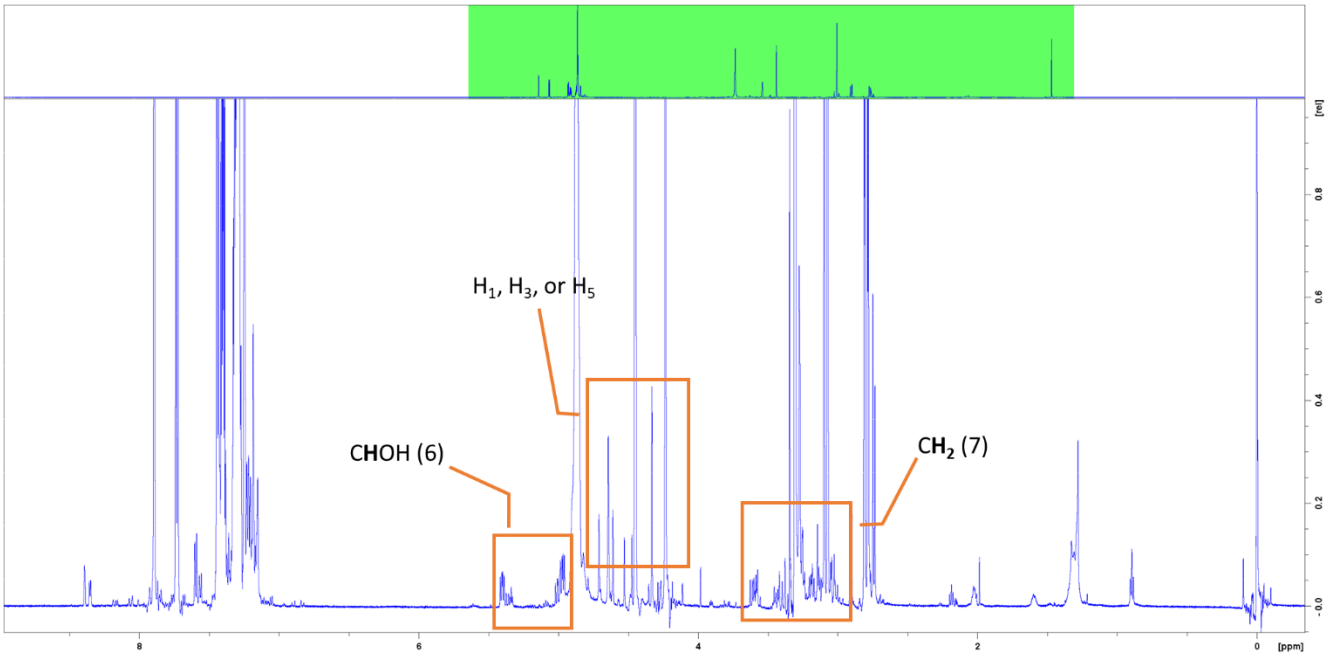

Figure 2.9: ^{1}H NMR spectra (600 MHz, d_3-MeOD) of the cycloaddition between DIBO and 5-OH substituted N-methyl-3-OXP. The boxed peaks were assigned based on what they would most likely be based on what was observed with other 2,6-cycloadducts.

Of the three fastest reactions, the pyridiniums with OH and NH_2 on the 5-position showed degradation in their cycloadducts with DIBO. Within the peaks for the CH_2 benzylic protons of 8 (Figure 2.7), a large quartet is visible that doesn't represent any of the expected peaks and doesn't line up with any residual solvents either, but lines up with peaks found in decomposed 6. What's

common between the two products is that their products can tautomerize along the enol and amine to their respective ketone and imine tautomers in products 6 and 8. (Scheme 2.13)

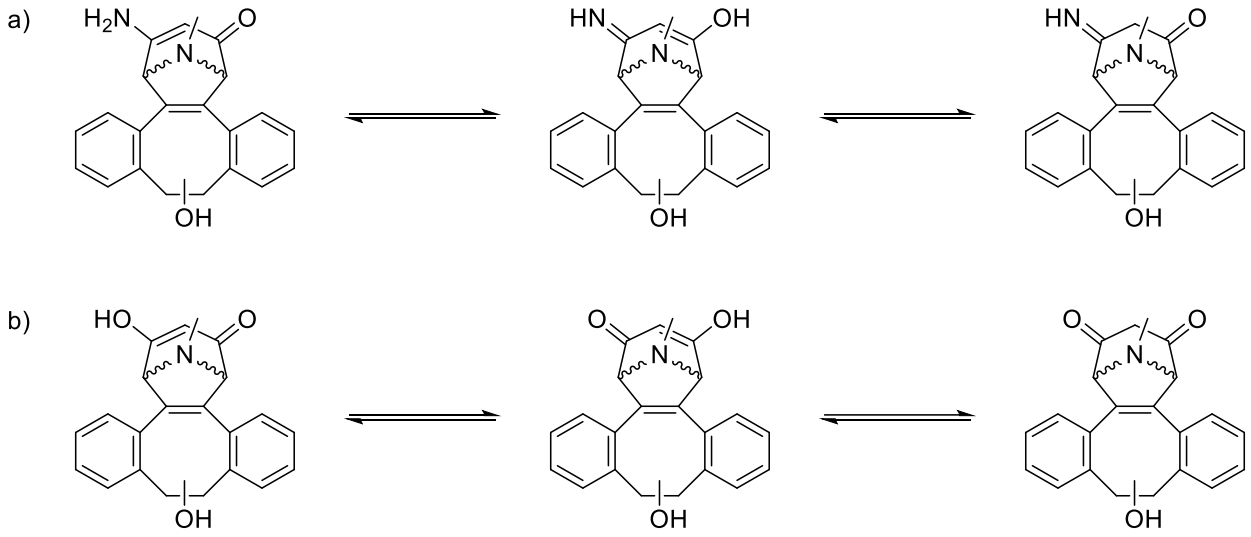

Scheme 2.13: Tautomers of products 8 (a) and 6 (b).

The tautomerization of the products would explain why the allylic and bridgehead NMR peaks for 8 appear broadened and don't exactly integrate to the expected number of protons from the amine-ketone form. Tautomerization could also explain why the two products decomposed. For 8, the enol-imine form can attack the acetone (used in column chromatography to remove product), forming an aldol, as could both enol-ketone forms of 6. The basic conditions of the purification (basic alumina and Et_3N treated silica) could also contribute to the nucleophilicity of the enol by deprotonating it to an enolate. What presumably has a bigger impact on product instability is the 1,3-diketo tautomer of 6. The slightly acidic alpha proton can be deprotonated during the purification and react with either acetone during the purification or another molecule of product along either the α,β-unsaturated enone or enol. Further studies would need to determine the full effect of the reactivity of the product.

2.3.5 Structure-Reactivity Relationships

At first glance, the kinetic data (Table 2.1) seems to indicate that the more electron donating the 5-substituent is, the faster the reaction, which is consistent with previously published data on 3-oxidopyridiniums[19]. However, to fully understand the reaction mechanism, and the effect of the 5-substituent on the reactivity of the reactions, the structure-reactivity relationship can be quantified using the Hammett equation (Eq 2.1).

$$log\frac{k}{k_0} = \rho\sigma \text{ (Eq 2.1)}$$

The Hammett equation indicates that the change of the change in Gibb's activation energy ($\Delta\Delta G^{\ddagger}$) to a studied reaction due to the addition of a substituent, is directly proportional to the change of the change in Gibb's energy ($\Delta\Delta G$) of the acid dissociation due to the effects of the same substituent. In other words, this equation correlates the effect of a substituent on the reaction rate of the studied reaction by a substituent constant σ. Substituent constants give a quantitative value to the "influences" of a substituent on a reaction: its resonance and induction effects. Because σ values are derived from the ionization of benzoic acid, they can be regularly used for determining structure reactivity relationships of meta or para substituents on phenyl rings, however they can't be used with the same ease for heterocycles like 3-oxidopyridinium.

Previous work by the Katritzky group calculated that C_2 has the highest π-electron density, which explains why many of the cycloadditions between 3-oxidopyridiniums and olefins and alkynes occurred along the 2,6 positions of the pyridinium ring[9,10,17,18]. To determine whether Hammett substituent constants can apply to 3-oxidopyridiniums, they should correlate to ^{13}C NMR shifts. The substituent constants considered are: σ_m, σ_p, σ^+, σ^-, σ_R, and σ_I are used to correlate changes in electron density caused by the substituent[26]. σ_m and σ_p are used to describe the effect of the meta or para substituent respectively on the rate of dissociation of benzoic acid. σ^+ and σ^- are substituent constants that take into consideration additional resonance interactions, with σ^+ being used for resonance interactions for a cationic center and σ^- for resonance interactions for an anionic reaction center.

Substituent constants σ_R, and σ_I, separate each substituent into its resonance and inductive effect on the reaction respectively.

NMR shifts are sensitive to electron density distribution, therefore a change in C_2 ppm that correlates well with Hammett σ values would indicate that those values can be used to construct a Hammett plot to determine the substituent effects on the cycloadditions of pyridiniums with DIBO. The experimental ^{13}C NMR chemical shifts of all 5-substituted-N-methyl-3OXPs in ppm referenced to d_3-AcN are found in Appendix A. ^{13}C chemical shifts were assigned with the complementary use of two-dimensional ^{1}H-^{13}C HSQC experiments. ^{13}C NMR chemical shifts of each carbon were then plotted as a function of published[27] σ values: σ_m, σ_p, σ^+, σ^-, σ_R, and σ_I and the findings are included in Appendix A. Looking at the relationship between the change in ppm at carbon 2 and the various σ values, the best correlation is observed with σ^+ values of the different 5-substituents (Figure 2.10) and was used to construct a Hammett plot (Figure 2.11) based on the calculated parameters (Table 2.7).

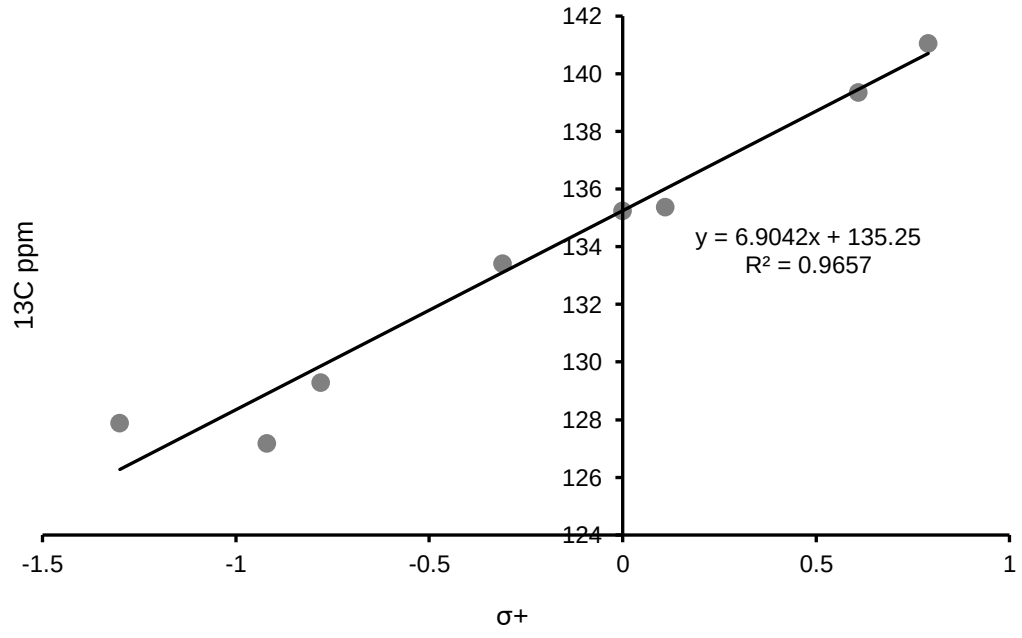

Figure 2.10: ^{13}C NMR chemical shifts of C_2 of 5-substituted N-methyl-3-OXPs as a function of substituent constants (σ^+). Spearman correlation coefficient $r_s = 0.9762$.

Table 2.7: Rate constants and Hammett σ⁺ values for 5-substituted N-methyl-3-oxidopyridiniums. σ+ values taken from reference 26

5-substituent	σ^+	k_2 (M^{-1} s^{-1})	k_x/k_H	$log(k_x/k_H)$
$X = NH_2$	-1.30	1.07	289.30	2.46134641
X = OMe	-0.78	0.506	136.81	2.13611315
X = OH	-0.92	0.163	44.07	1.64415024
X = Cl	0.11	1.33E-2	3.60	0.55581428
$X = CH_3$	-0.31	8.84E-3	2.39	0.3784149
X = H	0	3.70E-3	1.00	0
$X = CF_3$	0.61	3.31E-4	0.09	-1.04869511
$X = NO_2$	0.79	slow	-	-

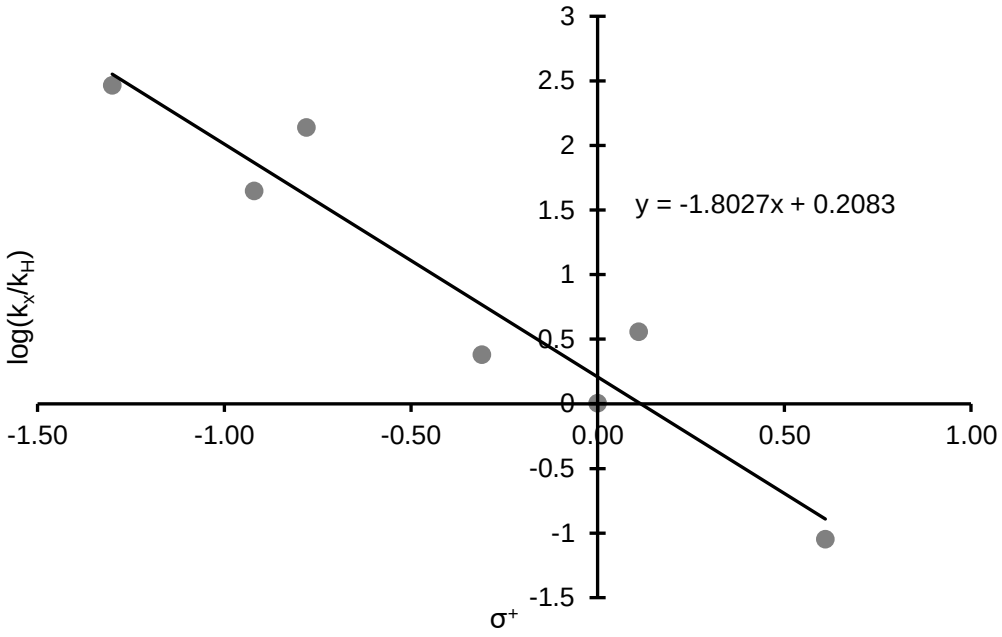

Figure 2.11: Hammett plot depicting substituent effects on the cycloadditions of 5-substituted-N-methyl-3-OXPs 4a-h with DIBO using σ⁺ constants. R^2= 0.9110, Spearman correlation coefficient r_s = -0.8571

Hammett substituent constants for para and meta substituents refer to a mixture of both resonance and inductive effects. When there is an enhanced resonance effect to a reaction, like what is seen with 3-oxidopyridiniums reacting with DIBO and previously published reactions with alkynes and olefins, where there is a resonance interaction between the EDG and a cationic reaction center

(Scheme 2.14), a different series of Hammett substituents are used, σ^+. This also explains why the highest correlation was observed between the C2 ppm and σ^+.

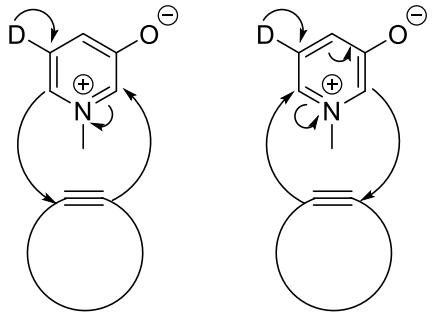

Scheme 2.14: Resonance interaction between EDGs (D) and the cationic reaction center of a generic cycloaddition reaction with strained alkynes.

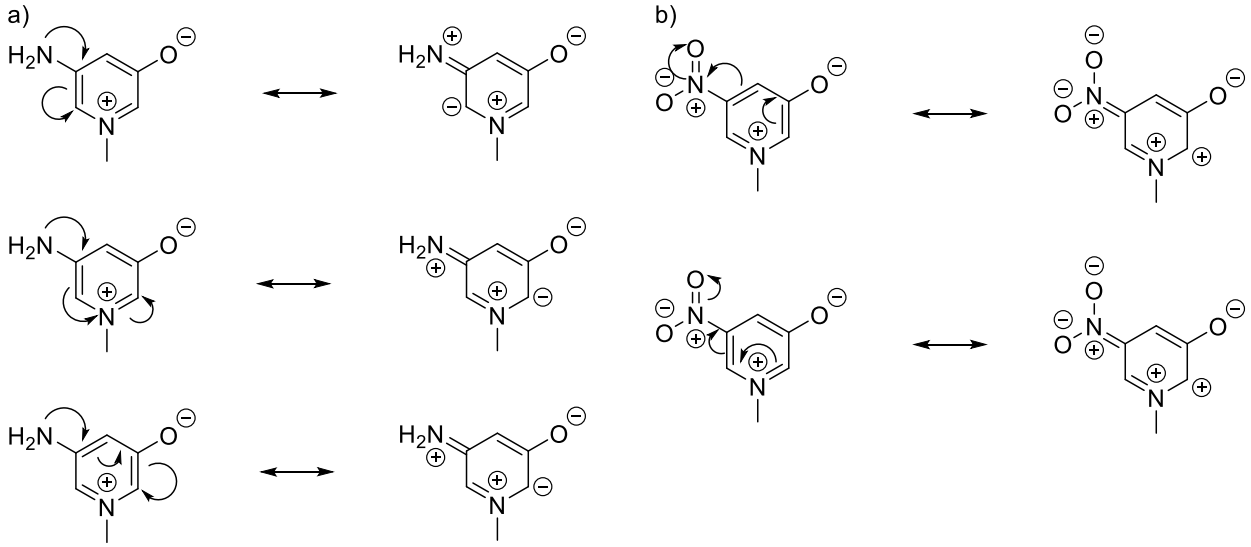

Scheme 2.15: Resonance effects of EDG (a) and EWG (b) at the C2 position of the pyridinium

The Hammett plot depicting the substituent effects of the cycloaddition between the pyridiniums 4a-h and DIBO gives a reaction constant of ρ = -1.80 with Hammett σ^+ parameters with relatively high correlation (R^2= 0.9110, r_s = -0.8571). This value suggests that the reaction is slightly sensitive to EDGs that stabilize the transition state at the C_2 position. Despite σ^+ parameters offering the best correlation with ^{13}C NMR data, the Hammett plot that has the best correlation is observed with σ_R parameters with an R^2= 0.9533, r_s = -0.9643, and a calculated ρ = -3.59 (Figure 2.12). σ_R

parameters are Hammett substituent constants that quantifies only the resonance effect of the substituent on the rate of the reaction whereas σ_I substituent constants quantifies the induction effect of the substituent. A ρ_R = -3.59 indicates that the reaction rate is very sensitive to EDGs as they stabilize the transition state and that there is a relatively larger charge redistribution at the transition state. As expected, the correlation of the Hammett plot with σ_I substituent constants was poor (R^2= 0.0035, r_s = 0), but still offered a ρ_I value of -0.40, which indicates that the reaction not appreciably sensitive to the induction effects of EDGs. (Figure 2.13)

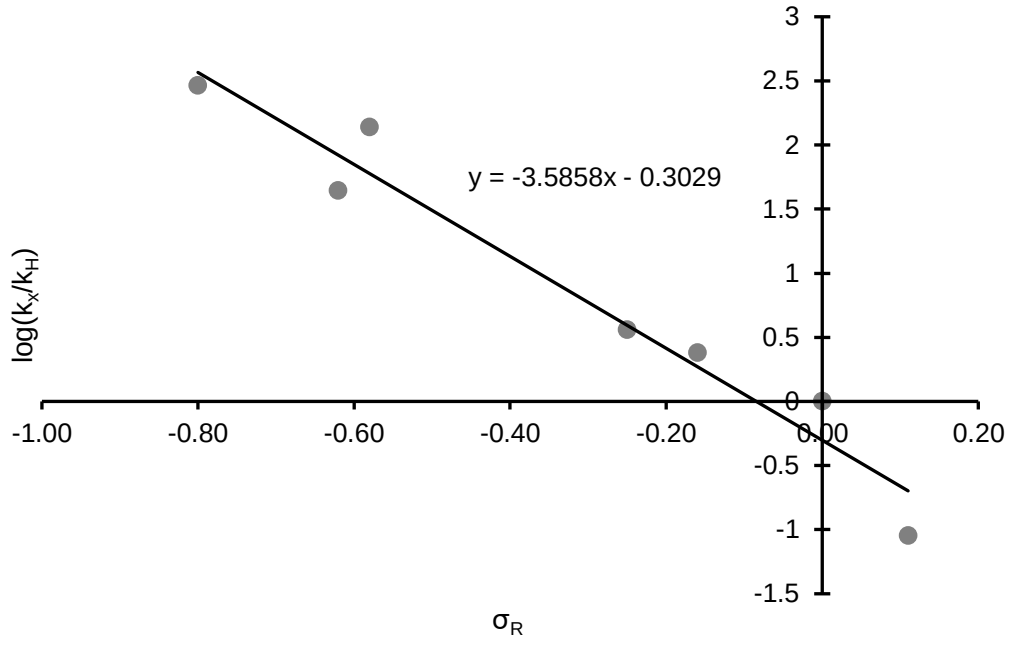

Figure 2.12: Hammett plot depicting substituent effects on the cycloadditions of 5-substituted-N-methyl-3-OXPs (4a-h) with DIBO using σ_R constants. R^2= 0.9533, Spearman correlation coefficient r_s = -0.9643

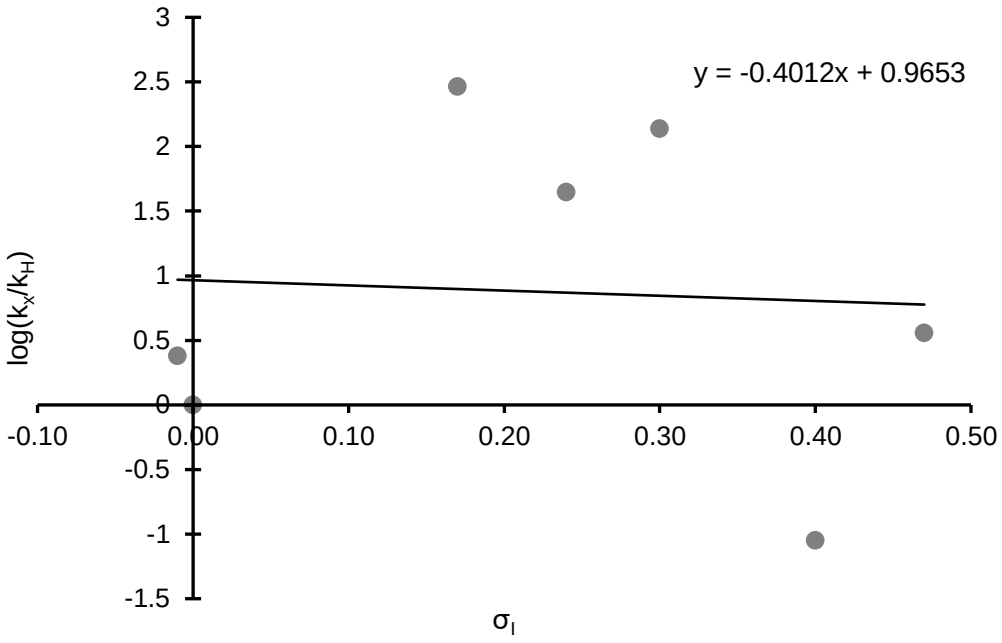

Figure 2.13: Hammett plot depicting substituent effects on the cycloadditions of 5-substituted-N-methyl-3-OXPs (4a-h) with DIBO using σ_I constants. R^2= 0.0035, Spearman correlation coefficient r_s = 0

The dual-substituent-parameter (DSP) equation (Eq 2.2) is typically used to determine the degree of sensitivity of a reaction to resonance and inductive effects separately. Theoretically, on a plot that graphs $log\,\frac{k}{k_0}$ as a function of $\sigma_I\rho_I + \sigma_R\rho_R$, the slope should equal to 1. Table 2.8 summarizes the calculated results of the DSP equation and Figure 2.14 plots the linear relationship between the reaction rates and the ρ and σ constants.

$$log\,\frac{k}{k_0} = \sigma_I\rho_I + \sigma_R\rho_R \quad \text{(Eq 2.2)}$$

Table 2.8: Calculated results of the dual-substituent-parameter equation, using rho reaction constants determined previously. Substituent constants are taken from reference 27.

5- substituent	k_2 (M^{-1} s^{-1})	$\log(k_x/k_H)$	σ_R	ρ_R	σ_I	ρ_I	$\sigma_R\rho_R + \sigma_I\rho_I$
X = NH_2	1.07	2.46134641	-0.80		0.17		2.778596
X = OMe	0.506	2.13611315	-0.58		0.30		1.94357
X = OH	0.163	1.64415024	-0.62		0.24		2.109982
X = Cl	1.33E-02	0.55581428	-0.25	-3.5585	0.47	-0.4012	0.701061
X = CH_3	8.84E-03	0.3784149	-0.16		-0.01		0.573372
X = H	3.70E-03	0	0		0		0
X = CF_3	3.31E-04	-1.0486951	0.11		0.40		-0.551915
X = NO_2	slow		0.1	-	0.67	-	

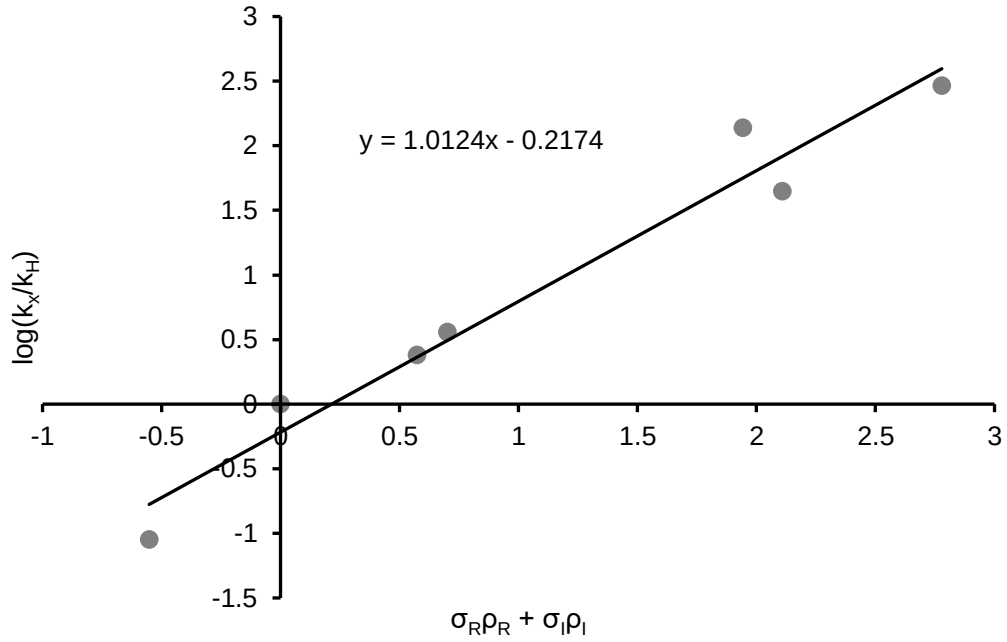

Figure 2.14: Linear relationship of the dual-substituent-parameter equation using rho reaction constants previously determined and sigma constants taken from reference 27. R^2= 0.9613, Spearman correlation coefficient r_s = 0.9643.

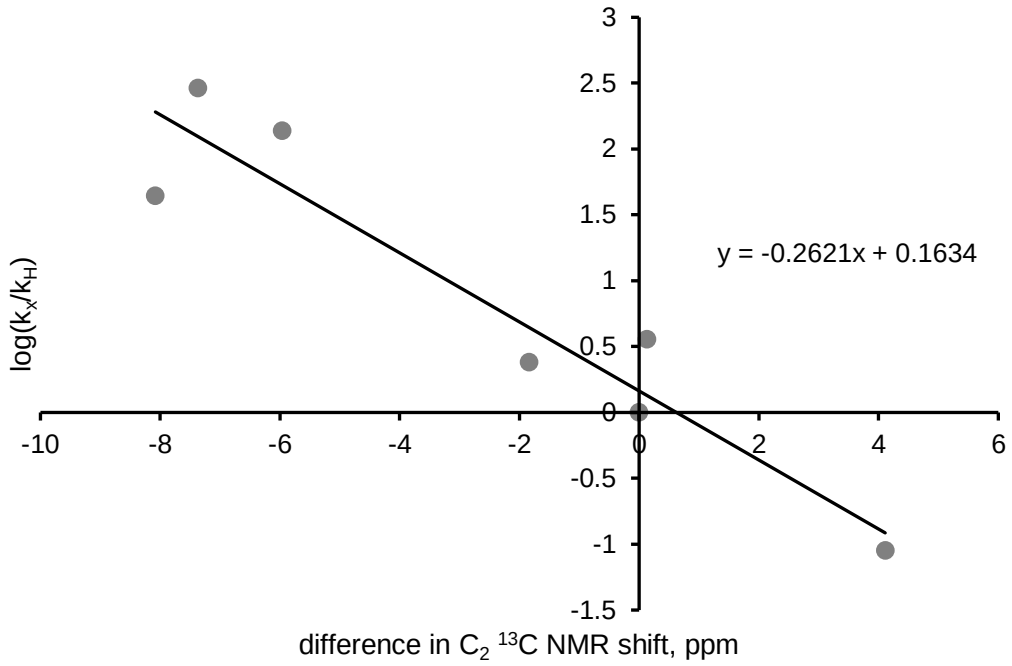

Figure 2.15: Relationship between the reported reaction rates and the difference in the ^{13}C NMR shift of C_2 of the 5-substituted 3-oxidopyridiniums in ppm referenced from d_3-AcN. R^2= 0.8942, Spearman correlation coefficient r_s = -0.7857.

Figure 2.14 shows that the resulting line of best fit has a slope of 1.01 indicating that the reaction rates correlate well to the calculated ρ reaction constants. Hammett ρ values can also offer insight into the mechanism of the reaction. Typically, smaller ρ values indicate that there isn't a significant accumulation of electron density, and are more typical among concerted mechanisms, and larger ρ values indicate a larger buildup of electron density, which typically seen in a stepwise or asynchronous mechanism[28]. With a ρ value of -3.59, this would indicate that the reaction would more likely be a stepwise mechanism, however, previous studies looking into the cycloadditions of 3-oxidopyridiniums with dipolarophiles have consistently stated that the cycloaddition reaction is concerted[12]. Based on what is known about the reactivity of 3-oxidopyridiniums, in particular the previously calculated high electron density on the C2 position of the 3-oxidopyridinium that has been referred to as "nucleophilic"[9], and that the trends observed between the mechanism and magnitude of ρ are oversimplifications, the reaction between 5-substituted-N-methyl-3-oxidopyridiniums and DIBO is most likely also a concerted and asynchronous mechanism that is very sensitive to EDG.

Analyzing the reaction rates as a function of 13C NMR shifts of C2, also offers further evidence to support that the reaction is highly dependent on the electron density at C2. (Figure 2.15).

3-oxidopyridiniums can react along the 2,6 position as 4π unit as either 5 atom fragments bridged by the nitrogen or as 3 atom fragments bridged by a three-carbon unit[9]. (Scheme 2.16) At the transition state, this means that electron density can be distributed along the 3-oxidopyridinium in two different ways. The larger ρ value from σ_R would indicate that the electron density of the transition state is distributed along the 5-carbon fragment and the smaller ρ value from σ^+ would indicate that the electron density is distributed along the 3-atom fragment.

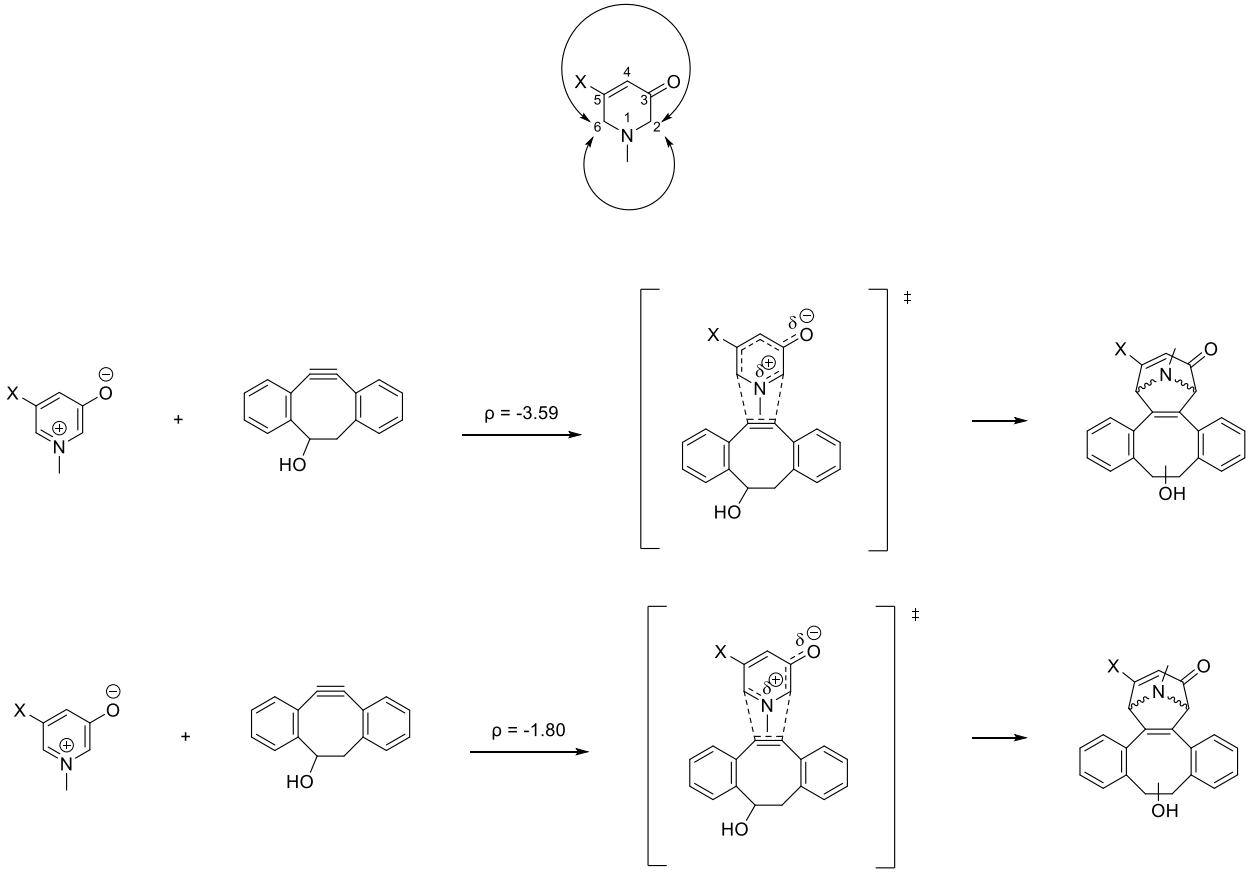

Scheme 2.16: Reaction between 5-X-N-methyl-3-OXPs and DIBO, with suggested transition state structures based off of the two ρ values.

Based on what is known in the literature about the cycloadditions of 3-oxidopyridiniums and what has been investigated herein, the reaction mechanism is clearly affected by the resonance

contributions of the substituents investigated evidenced by the high correlations of the Hammett plots that use σ_R and σ^+ constants. While both constructed Hammett plots can offer a reasonable explanation of the observed reaction, the plot that would more accurately represent the reaction mechanism uses σ_R constants. Looking at the proposed mechanisms, the rate of the reaction is determined by the resonance contributions of the substituents, so much so, that the inductive effect of each substituent is minimal as demonstrated by the DSP equation (Figure 2.14). When looking at the relationship between σ_R and σ_I substituent constants[27], the substituents can be described as electron donating by induction or resonance, and electron withdrawing by induction or resonance. The three fastest reactions involved OH, OMe, and NH_2 substituents, all of which are electron withdrawing by induction, but electron donating by resonance. The Cl substituent is also electron withdrawing by induction and electron donating by resonance, however when compared to the aforementioned substituents, the resonance effect is much lower, and the inductive effect is much higher. This would explain why the 5-chloro substituted 3-oxidopyridinium was faster than the unsubstituted 3-oxidopyridinium, but not the fastest tested pyridinium. The slowest reactions were observed with NO_2 and CF_3 substituents, both of which are electron withdrawing by induction and resonance. Of the most used substituents, trimethylsilyl substituents are electron donating by induction and electron withdrawing by resonance – the opposite of OH, OMe, and NH_2 substituents, which if the proposed reaction mechanism is true, would offer significantly slower reaction rates. Further work with a wider range of substituents including trimethylsilyl would be required to confirm that the reaction between DIBO and 3-oxidopyridiniums are dominated by resonance effects.

2.3.6 Comparison to Computational Work

3-oxidopyridiniums in the literature have been shown to react with 2π dipolarophiles typically along the 2,6 position in [3+2] cycloaddition, but also along the 2,O or 4,O position in a [7+2] cycloaddition (Scheme 2.2). At the start of this project, the mode of the cycloaddition was key to determining whether the reaction can be used in a bioorthogonal setting as adducts from [7+2]

cycloadditions have been shown to hydrolyze in water[10,11] (Scheme 2.12). While the NMR data confirms the formation of the [3+2] cycloaddition, computational data can be used to determine how well the observed results correlated with the calculated theoretical.

The distortion/interaction (D/I) model has been commonly used to analyze, describe, and predict reaction rates and selectivity of reactions. In this model, the potential energy of a reaction is broken down into distortion energy (energy required to distort the reactant into its transition state configuration) and interaction energy (attractive and repulsive electrostatic interactions) and is analyzed over the course of a reaction. Density functional theory (DFT) calculations in combination with the D/I model have been successfully used for reaction prediction in bioorthogonal chemistry[29,30], and was also conducted herein to model the cycloadditions of 5-substituted 3-OXPs with dipolarophiles. The [3+2] and [7+2] cycloadditions of DIBO with 4a-h in AcN have been modelled using Gaussian 16, and geometry optimizations were done at the M06-2X level of theory with the 6-31+G(d,p) basis set. D/I energies were also calculated for each cycloaddition along with the energy of the reaction (ΔE), activation energy ($\Delta E^{\ddagger}$), Gibbs reaction energy (ΔG), and Gibbs activation energy ($\Delta G^{\ddagger}$) of each cycloaddition and are summarized in Table 2.9.

Table 2.9: Summary of the D/I energies of the two modes of cycloaddition along with the calculated energies of activation, free energy of activation, the experimental k_2, and $\Delta G^{\ddagger}$ calculated using the Arrhenius equation. Calculations for [3+2] cycloadditions were done for 2 both stereoisomers, a (N-methyl pointed toward the plane of DIBO) and b (N-methyl pointed away from the plane DIBO).

N-Me-3-OXP	Rxn	Exp. k_2 (M^{-1} s^{-1})	Exp. $\Delta G^{\ddagger}$ (kcal/mol)	Calculated Energies (kcal/mol)							
				$\Delta E^{\ddagger}$	ΔE	$\Delta G^{\ddagger}$	ΔG	Distortion DIBO	Distortion N-Me-3-OXP	Distortion Total	Interaction
5-CF_3	[3+2] a	0.000331	21.235	10.3195	-24.9447	27.3608	-4.8725	7.2116	19.2773	26.4889	-16.1695
	[3+2] b			9.7210	-26.0582	26.6556	-5.9440	7.1620	18.6402	25.8023	-16.0812
	[7+2]			18.0985	-30.8272	33.6928	-12.3684	8.7147	8.9946	17.7093	0.3892
5-NO_2	[3+2] a	slow	large	10.2863	-30.4991	26.4102	-12.6916	7.2957	19.4953	26.7910	-16.5047
	[3+2] b			10.2208	-26.0508	26.3710	-6.5271	7.2405	18.9843	26.2248	-16.0040
	[7+2]			16.9141	-37.0054	31.9047	-19.0066	8.2746	9.3134	17.5880	-0.6739
5-Me	[3+2] a	0.00884	20.290	8.2686	-27.5842	25.3833	-7.4192	7.0334	17.5531	24.5865	-16.3179
	[3+2] b			7.4222	-28.8303	24.3757	-8.6515	6.9711	16.4913	23.4625	-16.0403
	[7+2]			19.6857	-23.6036	35.5968	-4.7651	9.7586	7.8325	17.5911	2.0946
5-Cl	[3+2] a	0.0133	20.013	8.6326	-32.6003	24.4176	-14.7226	6.8554	17.8807	24.7361	-16.1035
	[3+2] b			8.1228	-28.5919	23.9568	-9.7051	6.7877	17.2694	24.0571	-15.9343
	[7+2]			20.1783	-25.3500	34.9756	-7.8638	9.4609	9.3106	18.7715	1.4068
5-H	[3+2] a	0.00370	20.771	8.5500	-29.9050	24.2698	-12.1434	6.7465	17.1071	23.8536	-15.3036
	[3+2] b			8.5965	-26.7998	24.3006	-8.0887	6.7306	16.9996	23.7303	-15.1337
	[7+2]			19.5417	-24.4688	34.3848	-6.9130	9.7118	8.2177	17.9295	1.6122
5-OH	[3+2] a	0.163	18.528	5.6089	-36.3171	21.8809	-17.7366	6.0792	15.2308	21.3101	-15.7011
	[3+2] b			5.6174	-32.7284	21.7137	-13.2593	6.0581	15.0778	21.1359	-15.5185
	[7+2]			22.0902	-20.0112	36.6773	-2.6223	10.6287	8.8675	19.4962	2.5940
5-NH_2	[3+2] a	1.07	17.413	5.6891	-39.5122	20.9966	-21.2573	6.5634	15.0623	21.6257	-15.9366
	[3+2] b			5.4195	-35.3340	21.1719	-16.1742	6.2101	15.1898	21.3999	-15.9804
	[7+2]			21.5314	-19.5758	36.0400	-2.2452	10.4303	7.8508	18.2811	3.2503
5-OMe	[3+2] a	0.506	17.857	4.8760	-38.0434	20.7420	-19.9410	5.9427	14.6195	20.5622	-15.6862
	[3+2] b			4.9101	-34.2540	20.5690	-15.1821	5.9163	14.4520	20.3683	-15.4582
	[7+2]			22.5533	-19.1369	36.8486	-2.6233	11.1338	8.6941	19.8279	2.7254

The computational work shows that the [3+2] cycloadditions across the 2, 6 positions are thermodynamically and kinetically favoured over the [7+2] cycloadditions based on the largest free energies of the reaction and lowest free energy of activation respectively. Between the two stereoisomers, their free energies of activation are relatively similar, consistent with the experimental data showing the equal preference of both stereoisomers. (Figure 2.16a).

Thermodynamically however, diastereomer A is favoured over B, especially for the more electron donating pyridiniums based on the free energy of the reaction (Figure 2.16b).

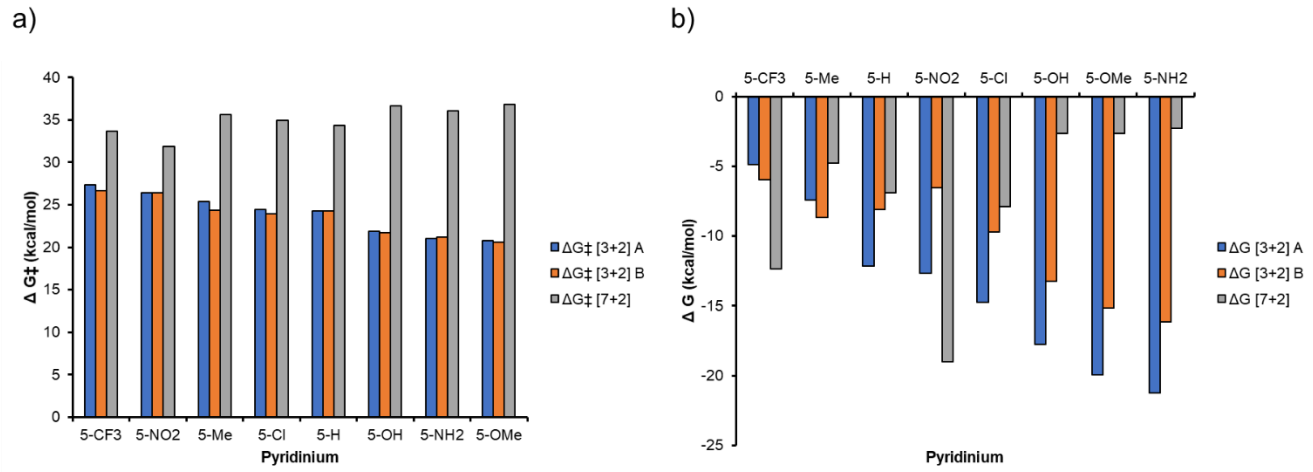

Figure 2.16: Calculated free energies of activation (a) and free energies of the reaction for the cycloadditions of pyridiniums with DIBO in [3+2] and [7+2] cycloadditions.

The D/I energies for the two different modes of cycloaddition show that the distortion energy for required for DIBO is lower for the [3+2] cycloadditions than for [7+2] cycloadditions (Figure 2.17a), indicating that the structure of DIBO at its ground state is most similar to its transition state configuration in the [3+2] cycloaddition rather than the [7+2]. Distortion energies for the pyridiniums in [7+2] cycloadditions were lower than the [3+2] cycloadditions again indicating that the structure of the pyridiniums at their ground states is similar to the transition state configuration of the [7+2] cycloaddition rather than the [3+2] cycloaddition (Figure 2.17b). Interaction energies are typically stabilizing energies, and this was found to be the case for the [3+2] cycloadditions as they are much lower than the [7+2] cycloadditions (Figure 2.17c). This results in an overall much smaller activation energy for the [3+2] cycloadditions, favouring it over the [7+2] cycloaddition. D/I graphs of each mode of cycloaddition is found in Appendix A.

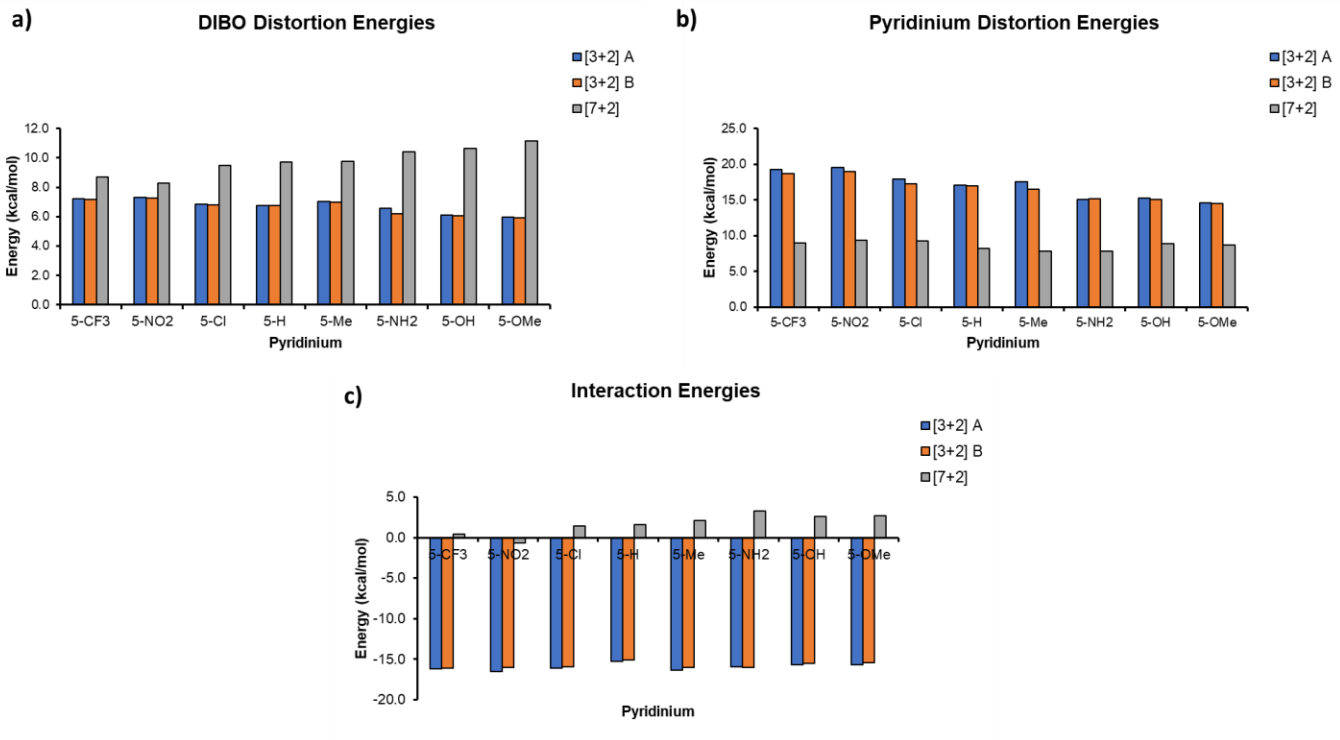

Figure 2.17: D/I energies calculated for each cycloadditions [3+2]A, [3+2]B, and [7+2] for each of the pyridiniums tested with DIBO.

The calculated energies are plotted as a function of the negative ln of the bimolecular rates determined in Section 2.3.3 (Figure 2.18) in order to compare them. In transition state theory, reaction rate constants are related to the energetic reaction barriers (Eyring and Arrhenius equations) and the subsequent graph establishes linear free energy relationships with the Gibbs free energy of activation and the distortion energy of the pyridiniums. The distortion energies of the pyridiniums in [3+2] cycloadditions correspond well with the reaction rate constants, indicating that the distortion of the pyridiniums play a significant role in determining the relative reaction barriers. The D/I model has shown to predict the relative reactivities of the cycloadditions of 5-substituted N-methyl-3-OXPs with DIBO and can be applied to future investigations of 3-oxidopyridiniums in bioorthogonal chemistry. Graphs plotted for [3+2]B and [7+2] cycloadditions are located in Appendix A.

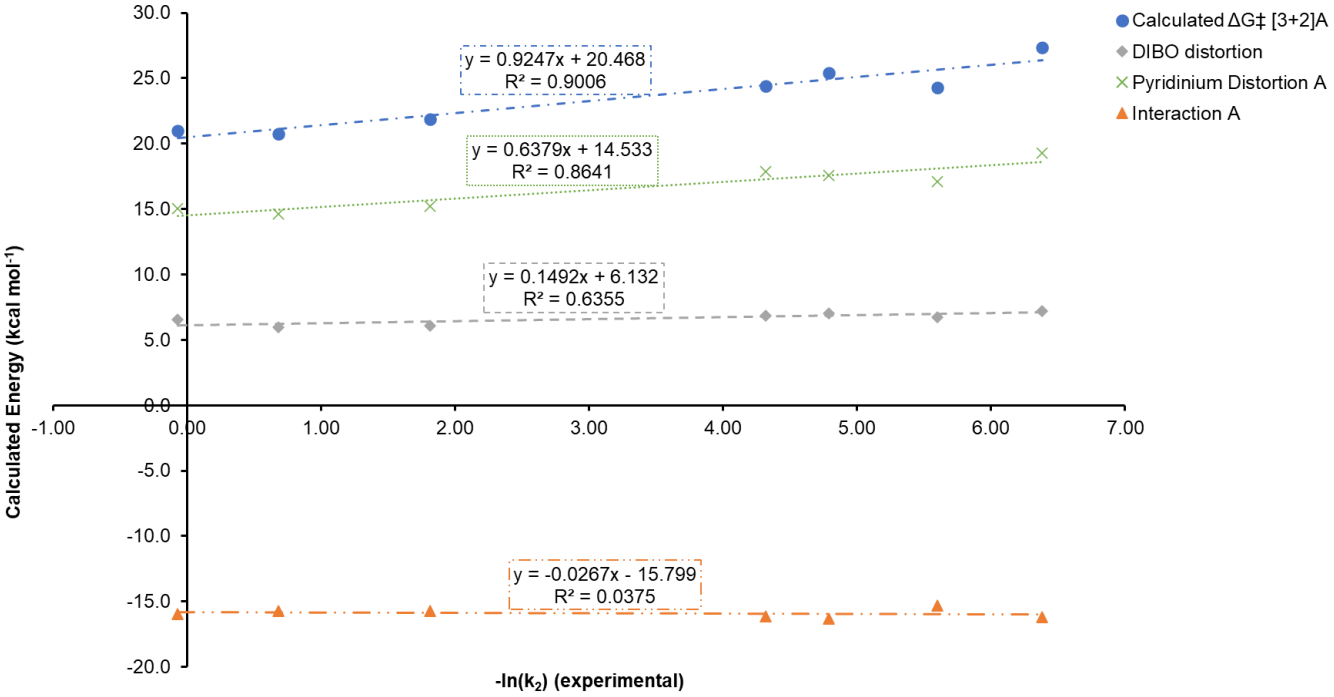

Figure 2.18: Calculated energies for [3+2] A cycloadditions as a function of -ln(k_2). The data shows that the experimentally determined rate constants correspond well with both the Gibbs free energy of activation and the distortion energies of the pyridiniums.

2.4 Future Directions

2.4.1 Bioorthogonal Labelling of Peptidoglycans using Pyridinium Modified D-Lysine

The application of 3-oxidopyridinium cycloadditions in biological applications is key to establishing it as a viable bioorthogonal reaction. While 3-oxidopyridiniums haven't been used in biological applications previously and have been mainly used to synthesize the 7 membered ring scaffold of tropolones and tropone containing natural products, pyridinium salts have been used in a wide range of both industrial (cosmetics, pharmaceuticals, surfactants, polymers, solvents) and biological applications[31]. Natural products containing pyridiniums are commonly found in marine sponges and have been shown to exhibit antimicrobial properties[32,33]. N-alkylated pyridinium salts have been used as disinfectants and surfactants[34] and have also been used to form liposomes and micelles for gene transfer.[35] This information is useful because not only does it corroborate what was

observed in the lab in terms of water solubility, but it also indicates that it can be readily used in a biological setting.

Unnatural amino acids (UAAs) have been used to incorporate bioorthogonal reporters into proteins at both the site-specific and residue-specific level. Residue-specific incorporation of an UAA involves supplementing auxotrophic organisms (i.e.: some strains of *E. coli*) with the UAA so that the native aminoacyl-tRNA-synthetase incorporates it over the native amino acid. Site-specific incorporation uses genetic code expansion with an orthogonal aminoacyl tRNA/tRNA pair has been evolved to specifically only recognize the UAA. The UAA is inserted into the peptide when the translation machinery encounters an amber stop codon, which controls the specific site of UAA incorporation[36].

N-substituents onto 3-hydroxypyridine are commonly synthesized in 2 separate ways (Scheme 2.17), allowing for the synthesis of various UAAs that can contain pyridiniums. The primary amine of the lysine side chain can react with furfural (Scheme 2.17b) or can be swapped for a halogen to react with 3-hydroxypyridine in an S_N2 reaction (Scheme 2.17a). Based on solely the kinetic data, the ideal UAA would include a substituent on the 5-position of the pyridinium which would make the synthetic route that involves furfural less convenient since the amino group would either have to be added onto the labelled carbon on furfural in Scheme 2.17b to end up in the appropriate place or added on to an intermediate or the product. As a result, the more convenient synthetic route would be a halogenated D-lysine derivative (Scheme 2.17a).

While the kinetic data would suggest that the UAA should be made using 5-amino-3-hydroxypyridine, the cycloadduct of DIBO and 5-amino-N-methyl-3-oxidopyridinium did display evidence of degradation and in order to ensure product stability and bioorthogonality, faster kinetics may have to be sacrificed by using 5-methoxy-3-hydroxypyridine to synthesize the UAA.

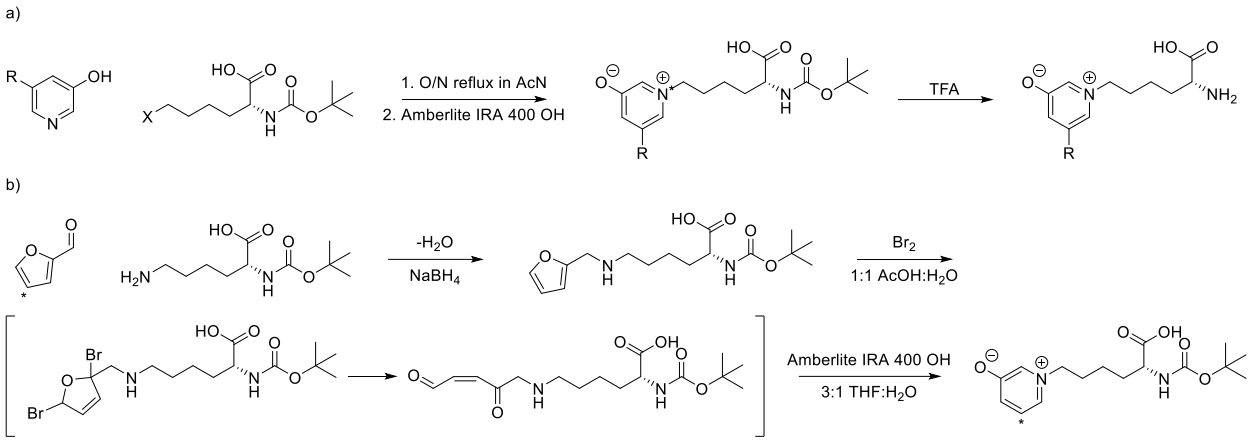

*Scheme 2.17: Synthetic routes for 3-oxidopyridinium functionalized unnatural amino acids derived from D-lysine. R = 5-substituent, X = halogen, * = location of substituent on furfural and final product.*

The synthesized UAA would then be used to label the peptidoglycan layer of bacteria. Lysine derived UAA containing cyclic nitrones have been previously shown to incorporate into the peptidoglycan layer of Gram-positive *Listeria innocua* readily and efficiently[37].

2.4.2 Second Addition of DIBO and Double Labeling

As mentioned in Section 2.1, when N-methyl-3OXP reacted with benzynes, a double addition of benzyne was observed[21]. The proposed mechanism for the second addition (Scheme 2.18) involves a nucleophilic attack from the bridged nitrogen toward the second equivalent of benzyne. The NMR product tracking experiments (Section 2.3.4) were conducted in 1:1 molar ratio of DIBO and pyridinium, however on the trials where slightly extra DIBO is added due to weighing errors, there doesn't seem to be any evidence of a second addition, nor do the found masses for any of the products indicate the formation of a second addition. However, this rationale isn't sufficient to completely disregard the potential for a second addition of DIBO and future work should properly investigate the feasibility of a second addition. Similar to how the Katritzky group changed ring substituents on their tested 3-oxidopyridinums (Scheme 2.6) to assist in synthesizing more diverse troponoids, perhaps the addition of a substituent on the ring could promote a second addition of dipolarophile.

The products also clearly show a Michael acceptor making the enone susceptible to nucleophilic attack. The reactivity of the Michael acceptor should be investigated further to determine if it can be taken advantage of to not just add another dipolarophile (DIBO or a second dipolarophile) but to also prevent the degradation seen in product 6.

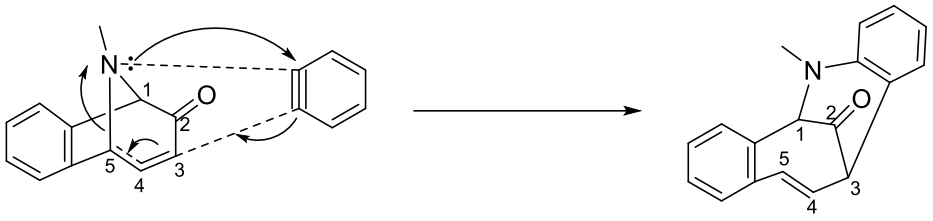

Scheme 2.18: Mechanism proposed by N. Dennis et. al for a second addition of benzyne.[9]

A recent trend in bioorthogonal chemistry is investigating the ability to simultaneously target multiple chemical reporters without any cross reactivity. The investigated pyridiniums herein were most reactive with DIBO, indicating that it would preferentially react with a functionalized DIBO probe should it be used in a multiplex labelling experiment with other dipolarophiles or dipoles. This can potentially be tested with other bioorthogonal reacting partners once the unnatural amino acid is synthesized and applied in bacterial peptidoglycan labelling.

2.5 Conclusions

3-oxidopyridiniums have been demonstrated to show, on a chemical level, that they can be adapted for bioorthogonal applications. [3+2] cycloadditions of 5-substituted-N-methyl-3-oxidopyridiniums with DIBO have been observed to form 4 isomers, 2 regio- and 2 stereoisomers. Electron donating 5-substituents have been shown to significantly increase the rate of the reaction, with bimolecular rate constants ranging from 3.31^{x} 10^{-4} with 5-trifluoromethyl-N-methyl-3-oxidopyridinium with to 1.07 M^{-1} s^{-1} with 5-amino-N-methyl-3-oxidopyridinium. These cycloadditions significantly widen the scope of bioorthogonal reactions and have the potential to be readily used in a variety of biological applications as an UAA. The preference of DIBO over other

dipolarophiles indicates that 3-oxidopyridiniums have the potential to be successfully used in multiplex labelling applications with other bioorthogonal reacting pairs.

2.6 Materials and Experimental Details

Commercially available reagents were purchased from CombiBlocks, Sigma-Aldrich, or Alfa Aesar and used without further purification. Bicyclo[6.1.0]nonyne (BCN) was purchased from Conju-Probe and used without further purification. Deuterated solvents were purchased from Cambridge Isotopes with the exception of deuterated acetonitrile which was purchased from Sigma-Aldrich and were used as received. Thin layer chromatography was performed on SiliaPlate™ silica gel (aluminum backed, 60 Å, F_{254}, layer thickness 200 μm), analytical preparative chromatography was performed on MilliporeSigma silica gel (glass backed, 60 Å, F_{254}, layer thickness 250 μm). Flash chromatography was conducted with silica gel (60 Å, particle size 40-63 μm), and basic aluminum oxide (Brockmann I, 40-300μm, 60 Å). Silica gel was neutralized by the addition of 1% v/m triethylamine to the aforementioned silica gel in a slurry with hexanes for even distribution. Hexanes were evaporated by reduced pressure on a rotary evaporator. Preparative HPLC was conducted on a Waters 2695 using XBridge preparatory column (19x50 mm, 5 μm OBD). Absorbances at wavelength of 260 nm was monitored for eluting compounds.

^{1}H NMR spectra were obtained using 300 MHz, 400 MHz, and 600 MHz Bruker NMR spectrometers. ^{13}C, ^{13}C DEPT 90, ^{13}C DEPT 135, 2D ^{1}H-^{1}H COSY, 2D ^{1}H-^{1}H NOSY, and 2D ^{1}H-^{13}C HSQC NMR spectra were obtained using 400 MHz and 600 MHz Bruker NMR spectrometers. All spectra were processed using Bruker TopSpin 4.0.6 software. NMR spectra peaks are measured in ppm and referenced from the residual deuterated solvent peak. Abbreviations for the multiplicity of peaks are as follows: s = singlet, d = doublet, t = triplet, m = multiplet or unresolved, br = broad and J = coupling constants are reported in Hz.

2.6.1 Synthesis of Reagents and Product Elucidation

4-dibenzocyclooctynol (DIBO)

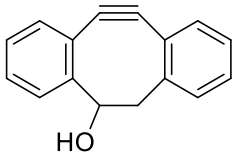

Synthesized according to previously reported procedures[38]. Spectral data was consistent with what was reported in the literature. Product was obtained as an off-white/yellow powder in a 9.5% yield over 4 steps. ^{1}H NMR (300 MHz, d_3-AcN) δ 7.53 (m, 8H), 4.44 (br s, 1H), 3.77 (d, *J* = 5.0 Hz, 1H), 3.09 (dd, *J* = 14.6, 2.2, 1H), 2.81 (dd, *J* = 14.6, 3.7, 1H)

General Synthesis of 5-substituted-3-oxidopyridiniums unless otherwise stated:

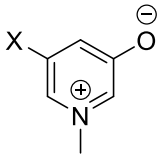

300 mg of 5-substituted 3-hydroxypyridine was added to a dry 50 mL round bottom flask with 10 mL of reagent grade acetonitrile. After the addition of 1 mole equivalent of MeI, the reaction was heated under reflux overnight. The solvent was then removed by reduced pressure on a rotary evaporator and dissolved in 80 mL of a 3:1 solution of THF:water and neutralized with 40 g of Amberlite® IRN78 resin (OH form). After 30 minutes of stirring the resin was filtered off and the filtrate was concentrated using reduced pressure on a rotary evaporator. The crude product was purified by recrystallization from methanol and ethyl acetate or flash column chromatography.

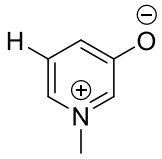

***N*-methyl-3-oxidopyridinium.** The pyridinium was synthesized as described in the general synthesis. Purification with column chromatography (neutralized silica, 5% MeOH in DCM) resulted in a dark oil in 72% yield. ^{1}H NMR (600 MHz, d_3-AcN): δ 7.34 (t, *J* = 2.1 Hz, 1H), 7.28 – 7.17 (m, 2H), 7.08 (dd, *J* = 8.9, 2.6 Hz, 1H), 3.94 (s, 3H); ^{13}C NMR (151 MHz, d_3-AcN): δ 169.9, 135.6, 133.4, 127.8, 124.6, 47.9; HRMS (EI) m/z calculated for C_6H_7NO: 109.05276 [M], found 109.05288.

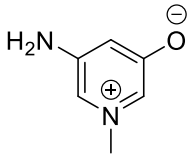

5-amino-*N*-methyl-3-oxidopyridinium. The pyridinium was synthesized as described in the general synthesis. Purification by crystallization resulted in brown crystals in 59% yield. ^{1}H NMR (600 MHz, d_3-AcN): δ 6.81 (t, *J* = 1.9 Hz, 1H), 6.69 (t, *J* = 1.8 Hz, 1H), 6.33 (t, *J* = 2.0 Hz, 1H), 3.81 (s, 3H); ^{13}C NMR (151 MHz, d_3-AcN): δ 169.6, 149.1, 127.8, 115.3, 114.0, 47.9; HRMS (EI) m/z calculated for $C_6H_8N_2O$: 124.06366 [M], found 124.06471.

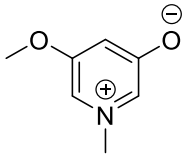

5-methoxy-*N*-methyl-3-oxidopyridinium. The pyridinium was synthesized as described in the general synthesis. Purification by crystallization resulted in beige crystals in 84% yield. ^{1}H NMR (600 MHz, d_3-AcN): δ 7.08 (br s, 1H), 6.97 (br s, 1H), 6.66 (br s, 1H), 3.88 (s, 3H), 3.74 (s, 3H); ^{13}C NMR (151 MHz, d_3-AcN): δ 170.7, 160.4, 130.5, 115.7, 114.7, 49.8, 48.1; Spectral data was consistent with what was reported in the literature[40].

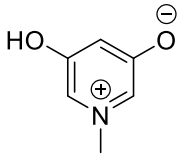

5-hydroxy-*N*-methyl-3-oxidopyridinium. The pyridinium was synthesized as described in the general synthesis. Purification by crystallization resulted in off-white/brown flakes in 65% yield. ^{1}H NMR (600 MHz, d_3-AcN): δ 7.89 (d, *J* = 1.8 Hz, 2H), 7.76 (t, *J* = 1.8 Hz, 1H), 4.13 (s, 3H); ^{13}C NMR (151 MHz, d_3-AcN): δ 158.2, 127.2, 118.0, 49.3; HRMS (ESI+) m/z calculated for $C_6H_8NO_2$ [M+H] 126.0555, found 126.0561.

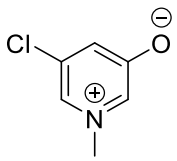

5-chloro-*N*-methyl-3-oxidopyridinium. The pyridinium was synthesized as described in the general synthesis. Purification by crystallization resulted in off-white/green-blue

powder in 86% yield. ^{1}H NMR (600 MHz, d_3-AcN): δ 6.81 (t, *J* = 1.9 Hz, 1H), 6.69 (t, *J* = 1.8 Hz, 1H), 6.33 (t, *J* = 2.0 Hz, 1H), 3.81 (s, 3H); ^{13}C NMR (151 MHz, d_3-AcN): δ 169.8, 135.8, 134.7, 132.0, 122.0, 48.1; HRMS (ESI+) m/z calculated for $C_6H_6ClN_2ONa$ [M+Na] 166.0048, found 166.0036.

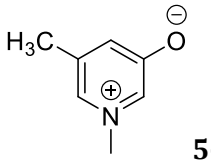

5-methyl-*N*-methyl-3-oxidopyridinium. The pyridinium was synthesized as described in the general synthesis. Purification by crystallization resulted in off-white/brown crystals in 58% yield. ^{1}H NMR (600 MHz, d_3-AcN): δ 6.81 (t, *J* = 1.9 Hz, 1H), 6.69 (t, *J* = 1.8 Hz, 1H), 6.33 (t, *J* = 2.0 Hz, 1H), 3.81 (s, 3H); ^{13}C NMR (151 MHz, d_3-AcN): δ 169.6, 149.1, 127.8, 115.3, 114.0, 47.9; HRMS (EI) m/z calculated for C_7H_9NO [M] 123.06841, found 123.06762.

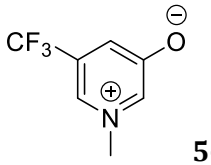

5-trifluoromethyl-*N*-methyl-3-oxidopyridinium. The pyridinium was synthesized as described in the general synthesis with the following modifications: after solvent removal, the crude product is purified by column chromatography (basic alumina, 5% MeOH in DCM) which resulted in a pale-yellow oil in 42% yield. ^{1}H NMR (600 MHz, d_3-AcN): δ 7.61 (br s, 1H), 7.55 (br s), 7.28 (br s, 1H), 4.01 (s, 3H); ^{13}C NMR (151 MHz, d_3-AcN): δ 169.2, 139.8, 129.1, 128.7, 128.7, 114.9, 48.6; HRMS (EI) m/z calculated for $C_7H_6F_3NO$ [M] 177.04015, found 177.04053.

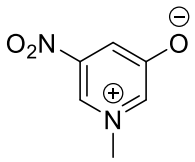

5-nitro-*N*-methyl-3-oxidopyridinium. The pyridinium was synthesized as described in the general synthesis with the following modifications: after solvent removal, the crude product is purified by column chromatography (basic alumina, 5% MeOH in DCM) which resulted in an orange/yellow oil in 38% yield. ^{1}H NMR (600 MHz, d_3-AcN): δ 8.06 (br s, 1H), 7.70 (br s), 7.67 (br

s, 1H), 4.07 (s, 3H); ^{13}C NMR (151 MHz, d_3-AcN): δ 169.2, 139.8, 129.1, 128.7, 120.7 48.6; HRMS (ESI +) m/z calculated for $C_7H_6N_2O_3Na$ [M+Na] 177.0276, found 177.0280.

2.6.2 Kinetics Studies Procedure

Data Collection:

Absorbances were monitored for kinetic measurements using the Agilent Cary 60 UV-vis spectrophotometer. 1.5 mL Quartz screw cap cuvettes (10 mm pathlength) were used and were rinsed with acetone 3 times, then with methanol 3 times and dried for an hour before each experiment. Kimwipes were used to remove outside residue on the cuvettes. Prior to each experiment a 25 mM and 4 mM stock solution of DIBO and pyridine, respectively are prepared in 20 mL screw cap vials with Optima or HPLC grade AcN and MeOH. Any unused stock solution was concentrated under reduced pressure on a rotary evaporator. For pyridiniums that don't dissolve well in AcN, the 4 mM solution was prepared with a 5% solution of methanol in AcN.

1 mL of the corresponding solvent was used to blank the spectrophotometer prior to reaction monitoring. AcN, DIBO, and pyridinium were added in that order. The volumes used are summarized in Table 2.10. Upon the addition of the pyridinium, the cuvette is stoppered and quickly inverted three times before inserting it for absorbance monitoring. The absorbance of the reaction was measured over a range of 200 nm to 600 nm in duplicate and was used to track the disappearance of the pyridinium. The reaction was deemed complete when the change in absorbance plateaus.

Table 2.10: Volumes of stock solutions used for pseudo-first order kinetics experiments of 5-substituted-N-methyl-3-oxidopyridiniums with dipolarophiles.

Reaction	***Volume of solvent (uL)***	***Volume of 25 mM Dipolarophile stock (uL)***	***Volume of 4 mM pyridinium stock (uL)***	***Total Volume (uL)***
12.5 mM DIBO 100 uM pyridinium	475	500	25	1000
10 mM DIBO 100 uM pyridinium	575	400	25	1000
7.5 mM DIBO 100 uM pyridinium	675	300	25	1000
5 mM DIBO 100 uM pyridinium	775	200	25	1000

Data Analysis:

All data analysis was conducted using Microsoft Excel, version 2201. Pseudo-first order kinetic constants were determined using non-linear regression fitted to the first-order integrated rate law. Second order rate constants, k_2 ($M^{-1}\,s^{-1}$) were determined by the slope of the line of best fit on a plot of k_{obs} as a function of the concentration of dipolarophile (M).

2.7 References

(1) Devaraj, N. K. The Future of Bioorthogonal Chemistry. *ACS Cent. Sci.* **2018**, *4* (8), 952–959. https://doi.org/10.1021/acscentsci.8b00251.

(2) Deb, T.; Tu, J.; Franzini, R. M. Mechanisms and Substituent Effects of Metal-Free Bioorthogonal Reactions. *Chem. Rev.* **2021**, *121* (12), 6850–6914. https://doi.org/10.1021/acs.chemrev.0c01013.

(3) Ramil, C. P.; Lin, Q. Bioorthogonal Chemistry: Strategies and Recent Developments. *Chem. Commun.* **2013**, *49* (94), 11007–11022. https://doi.org/10.1039/c3cc44272a.

(4) Nguyen, S. S.; Prescher, J. A. Developing Bioorthogonal Probes to Span a Spectrum of Reactivities. *Nat. Rev. Chem.* **2020**, *4* (9), 476–489. https://doi.org/10.1038/s41570-020-0205-0.

(5) Smeenk, M. L. W. J.; Agramunt, J.; Bonger, K. M. Recent Developments in Bioorthogonal Chemistry and the Orthogonality Within. *Current Opinion in Chemical Biology*. Elsevier Current Trends February 1, 2021, pp 79–88. https://doi.org/10.1016/j.cbpa.2020.09.002.

(6) Tu, J.; Svatunek, D.; Parvez, S.; Liu, A. C.; Levandowski, B. J.; Eckvahl, H. J.; Peterson, R. T.; Houk, K. N.; Franzini, R. M. Stable, Reactive, and Orthogonal Tetrazines: Dispersion Forces Promote the Cycloaddition with Isonitriles. *Angew. Chemie* **2019**, *131* (27), 9141–9146. https://doi.org/10.1002/ANGE.201903877.

(7) Bird, R. E.; Lemmel, S. A.; Yu, X.; Zhou, Q. A. Bioorthogonal Chemistry and Its Applications. *Bioconjug. Chem.* **2021**, *32* (12), 2457–2479. https://doi.org/10.1021/ACS.BIOCONJCHEM.1C00461.

(8) Scinto, S. L.; Bilodeau, D. A.; Hincapie, R.; Lee, W.; Nguyen, S. S.; Xu, M.; am Ende, C. W.; Finn, M. G.; Lang, K.; Lin, Q.; Pezacki, J. P.; Prescher, J. A.; Robillard, M. S.; Fox, J. M. Bioorthogonal Chemistry. *Nat. Rev. Methods Prim. 2021 11* **2021**, *1* (1), 1–23. https://doi.org/10.1038/s43586-021-00028-z.

(9) Dennis, N.; Katritzky, A. R.; Takeuchi, Y. Synthetic Applications of Heteroaromatic Betaines with Six-Membered Rings. *Angew. Chemie Int. Ed. English* **1976**, *15* (1), 1–9. https://doi.org/10.1002/anie.197600011.

(10) Ishag, C. Y.; Fisher, K. J.; Ibrahim, B. E.; Iskander, G. M.; Katritzky, A. R. 1,3-Dipolar Character of Six-Membered Aromatic Rings. Part LVI The Cycloadditions of Acetylenes and 3-Oxidopyridinium Betaines. *J. Chem. Soc. Perkin Trans. 1* **1988**, No. 4, 917–920.

(11) Ren, H.; Wu, C.; Ding, X.; Chen, X.; Shi, F. Aryne Cycloaddition with 3-Oxidopyridinium Species. *Org. Biomol. Chem.* **2012**, *10* (45), 8975–8984. https://doi.org/10.1039/c2ob26519b.

(12) Katritzky, A. R.; Dennis, N. Cycloaddition Reactions of Heteroaromatic Six-Membered Rings. *Chem. Rev.* **1989**, *89* (4), 827–861. https://doi.org/10.1021/cr00094a006.

(13) Katritzky, A. R.; Takeuchi, Y. 1,3-Dipolar Character of Six-Membered Aromatic Rings. Part I. 1-Methyl-3-Oxidopyridinium. *J. Chem. Soc. C Org.* **1971**, 874–877.

(14) Guiheneuf, G.; Laurence, C.; Katritzky, A. R. 1,3-Dipolar Character of Six-Membered Aromatic

Rings. Part XXIX. Kinetic Rates and Equilibria for the Addition of 2π-Electron Addends to 3-Oxidopyridinium Betaines. *J. Chem. Soc. - Perkin Trans. 1* **1976**, 1829–1831.

(15) Dennis, N.; Ibrahim, B.; Katritzky, A. R. The Dimer of 1-(5-Nitro-2-Pyridyl)-3-Oxidopyridinium and Its Reactions. *J. Chem. Soc. Chem. Commun.* **1974**, No. 13, 500–501. https://doi.org/10.1039/C39740000500.

(16) Dennis, N.; Ibrahim, B.; Katritzky, A. R.; Sciences, C. 1,3-Dipolar Character of Six-Membered Aromatic Rings. Part XXI. Thermal Cycloadditions of 1-(5-Nitro-Z-PyridyI)- and 1-(4,6-Dimethyl- Pyrimidin-2-Yl)-3-Oxidopyridinium with 2, 4, and 6 n-Electron Components. *J. Chem. Soc. Perkin Trans. 1* **1976**, 2307–2328.

(17) Katritzky, A. R.; Dennis, N.; Chaillet, M.; Larrieu, C.; El Mouhtadi, M. 1,3-Dipolar Character of Six-Membered Aromatic Rings. Part XXXVIII. FMO Treatment of Peri-, Site, Regio, and Stereo-Selectivity, and Relative Reaction Rates of Cycloaddition Reactions. *J. Chem. Soc. Perkin Trans. 1* **1979**, *0* (0), 408–417. https://doi.org/10.1039/P19790000408.

(18) Dennis, N.; Katritzky, A. R.; Rittner, R. *1,3-Dipolar Character of Six-Membered Aromatic Rings. Part XXV. 5-Aryl-1 -Methyl-3-Oxidopyrid Iniums*; 1976.

(19) Tamura, Y.; Akita, M.; Kiyokawa, H.; Chen, L. C.; Ishibashi, H. 1,3-Dipolar Cycloaddition of 5-Methoxy-1-Methyl-3-Oxidopyridinium. *Tetrahedron Lett.* **1978**, *19* (20), 1751–1752. https://doi.org/10.1016/0040-4039(78)80034-3.

(20) Katritzky, A. R.; Banerji, J.; Dennis, N.; Ellison, J.; Sabongi, G. J.; Würthwein, E. U. 1,3-Dipolar Character of Six-Membered Aromatic Rings. Part XLIV. Further Examples of Troponoid Synthesis. *J. Chem. Soc. Perkin Trans. 1* **1979**, 2528–2534. https://doi.org/10.1039/P19790002528.

(21) Dennis, N.; Katritzky, A. R.; Parton, S. K. 1,3-Dipolar Character of Six-Membered Aromatic Rings. Part XVI. Reactions of Benzyne with 3-Hydroxypyridine, 1-Methyl-3-Oxidopyridinium, and Related Compounds. *J. Chem. Soc. Perkin Trans. 1* **1976**, 2285–2288. https://doi.org/10.1039/P19760002285.

(22) Katritzky, A. R.; Takeuchi, Y. 1,3-Dipolar Character of Six-Membered Aromatic Rings. Part II. A Novel Route to Tropones and Tropolones. *J. Chem. Soc. C Org. Chem.* **1971**, *55* (2), 878–880. https://doi.org/10.1039/J39710000878.

(23) Kirchhecker, S.; Tröger-Müller, S.; Bake, S.; Antonietti, M.; Taubert, A.; Esposito, D. Renewable Pyridinium Ionic Liquids from the Continuous Hydrothermal Decarboxylation of Furfural-Amino Acid Derived Pyridinium Zwitterions. *Green Chem.* **2015**, *17* (8), 4151–4156. https://doi.org/10.1039/c5gc00913h.

(24) Mackenzie, D. A.; Pezacki, J. P. Kinetics Studies of Rapid Strain-Promoted [3+2] Cycloadditions of Nitrones with Bicyclo[6.1.0]Nonyne. *Can. J. Chem.* **2014**, *92* (4), 337–340. https://doi.org/10.1139/cjc-2013-0577.

(25) Sherratt, A. R.; Chigrinova, M.; McKay, C. S.; Beaulieu, L. P. B.; Rouleau, Y.; Pezacki, J. P. Copper-Catalysed Cycloaddition Reactions of Nitrones and Alkynes for Bioorthogonal Labelling of Living Cells. *RSC Adv.* **2014**, *4* (87), 46966–46969. https://doi.org/10.1039/c4ra07851a.

(26) Jaffé, H. H. A Reëxamination of the Hammett Equation. *Chem. Rev.* **2002**, *53* (2), 191–261. https://doi.org/10.1021/CR60165A003.

(27) Carey, F. A.; Sundberg, R. J. *Advanced Organic Chemistry Part A: Structure and Mechanisms*; 2007. https://doi.org/10.1021/ed065pA139.2.

(28) Um, I. H.; Han, J. Y.; Hwang, S. J. Analysis of Linear Free-Energy Relationships Combined with Activation Parameters Assigns a Concerted Mechanism to Alkaline Hydrolysis of X-Substituted Phenyl Diphenylphosphinates. *Chem. – A Eur. J.* **2008**, *14* (24), 7324–7330. https://doi.org/10.1002/CHEM.200800553.

(29) Nakajima, M.; Bilodeau, D. A.; Pezacki, J. P. Predicting Reactivity for Bioorthogonal Cycloadditions Involving Nitrones. *RSC Adv.* **2020**, *10* (49), 29306–29310. https://doi.org/10.1039/D0RA05092J.

(30) Liu, F.; Liang, Y.; Houk, K. N. Bioorthogonal Cycloadditions: Computational Analysis with the Distortion/Interaction Model and Predictions of Reactivities. *Acc. Chem. Res.* **2017**, *50* (9), 2297–2308. https://doi.org/10.1021/ACS.ACCOUNTS.7B00265.

(31) Sowmiah, S.; Esperança, J. M. S. S.; Rebelo, L. P. N.; Afonso, C. A. M. Pyridinium Salts: From Synthesis to Reactivity and Applications. *Organic Chemistry Frontiers*. Royal Society of Chemistry February 7, 2018, pp 453–493. https://doi.org/10.1039/c7qo00836h.

(32) Laville, R.; Genta-Jouve, G.; Urda, C.; Fernández, R.; Thomas, O. P.; Reyes, F.; Amade, P. Njaoaminiums A, B, and C: Cyclic 3-Alkylpyridinium Salts from the Marine Sponge Reniera Sp. *Molecules* **2009**, *14* (11), 4716. https://doi.org/10.3390/MOLECULES14114716.

(33) Laville, R.; Thomas, O. P.; Berrue, F.; Reyes, F.; Amade, P. Pachychalines A–C: Novel 3-Alkylpyridinium Salts from the Marine Sponge Pachychalina Sp. *European J. Org. Chem.* **2008**, *2008* (1), 121–125. https://doi.org/10.1002/EJOC.200700741.

(34) Dolezal, R.; Soukup, O.; Malinak, D.; Savedra, R. M. L.; Marek, J.; Dolezalova, M.; Pasdiorova, M.; Salajkova, S.; Korabecny, J.; Honegr, J.; Ramalho, T. C.; Kuca, K. Towards Understanding the Mechanism of Action of Antibacterial N-Alkyl-3-Hydroxypyridinium Salts: Biological Activities, Molecular Modeling and QSAR Studies. *Eur. J. Med. Chem.* **2016**, *121*, 699–711. https://doi.org/10.1016/J.EJMECH.2016.05.058.

(35) Zhu, L.; Lu, Y.; Miller, D. D.; Mahato, R. I. Structural and Formulation Factors Influencing Pyridinium Lipid-Based Gene Transfer. *Bioconjug. Chem.* **2008**, *19* (12), 2499–2512. https://doi.org/10.1021/BC8004039.

(36) Lang, K.; Chin, J. W. Cellular Incorporation of Unnatural Amino Acids and Bioorthogonal Labeling of Proteins. *Chem. Rev.* **2014**, *114* (9), 4764–4806. https://doi.org/10.1021/CR400355W.

(37) MacKenzie, D. A.; Sherratt, A. R.; Chigrinova, M.; Kell, A. J.; Pezacki, J. P. Bioorthogonal Labelling of Living Bacteria Using Unnatural Amino Acids Containing Nitrones and a Nitrone Derivative of Vancomycin. *Chem. Commun.* **2015**, *51* (62), 12501–12504. https://doi.org/10.1039/c5cc04901f.

(38) Zheng, J.; Liu, K.; Reneker, D. H.; Becker, M. L. Post-Assembly Derivatization of Electrospun Nanofibers via Strain-Promoted Azide Alkyne Cycloaddition. *J. Am. Chem. Soc.* **2012**, *134* (41), 17274–17277. https://doi.org/10.1021/JA307647X/SUPPL_FILE/JA307647X_SI_001.PDF.

(39) Dommerholt, J.; Schmidt, S.; Temming, R.; Hendriks, L. J. A.; Rutjes, F. P. J. T.; van Hest, J. C. M.; Lefeber, D. J.; Friedl, P.; van Delft, F. L.; van Hest, J. C. M.; Schmidt, S.; Lefeber, D. J.;

Dommerholt, J.; Hendriks, L. J. A.; Friedl, P.; Temming, R.; Rutjes, F. P. J. T.; van Delft, F. L. Readily Accessible Bicyclononynes for Bioorthogonal Labeling and Three-Dimensional Imaging of Living Cells. *Angew. Chemie Int. Ed.* **2010**, *49* (49), 9422–9425. https://doi.org/10.1002/anie.201003761.

(40) Tamura, Y.; Saito, T.; Kiyokawa, H.; Chen, L. C.; Ishibashi, H. Syntheses of Stipitatic Acid and Hinokitiol. *Tetrahedron Lett.* **1977**, *18* (47), 4075–4078. https://doi.org/10.1016/S0040-4039(01)83430-4.

Chapter 3

Use of Nitrones to probe RNA secondary structure using SPANC

3.1 Introduction

Up until the discovery of catalytic RNA in the 1980's[1], research into RNA function mainly focused on messenger, transfer, and ribosomal RNA (mRNA, tRNA, rRNA, respectively) and their roles in gene and protein expression[2]. Since then, research into non-coding RNA (ncRNAs)function determined that they are crucial in a wide range of cellular processes and account for roughly 98% of transcriptional output in humans in comparison to the roughly 2% transcriptional output of coding RNA[3]. Eukaryotic ncRNAs are typically grouped into two main categories: housekeeping and regulatory non-coding RNA. Housekeeping ncRNAs are ubiquitous, highly abundant, and constitutively expressed as they regulate and maintain basic cellular function. They are typically small (50 to 500 nucleotides (nt)) and include not only essential rRNA and tRNA for protein synthesis but also small nuclear RNA (snRNA) and small nucleolar RNA (snoRNA), which are responsible for RNA splicing and modifications respectively[4]. Regulatory ncRNAs are responsible for regulating gene expression at the epigenetic, transcription, and post-transcriptional levels and are further classified as either small non-coding RNA (sncRNA, transcripts less than 200 nt) or long non-coding RNA (lncRNA, transcripts greater than 200 nt)[5]. Small ncRNAs are broadly further categorized as microRNAs (miRNA), small interfering RNAs (siRNA), and piwi-interacting RNAs (piRNA) that play various roles in regulating gene expression and for piRNA specifically, offer transposon defense[4]. lncRNAs are found to have an expanding number of biological functionality and include chromatin, transcription and post-transcription regulation, and play a role in the function and assembly of nuclear condensates[6]. Figure 3.1 shows the functional roles of non-coding RNA in both the nucleus and the cytoplasm.

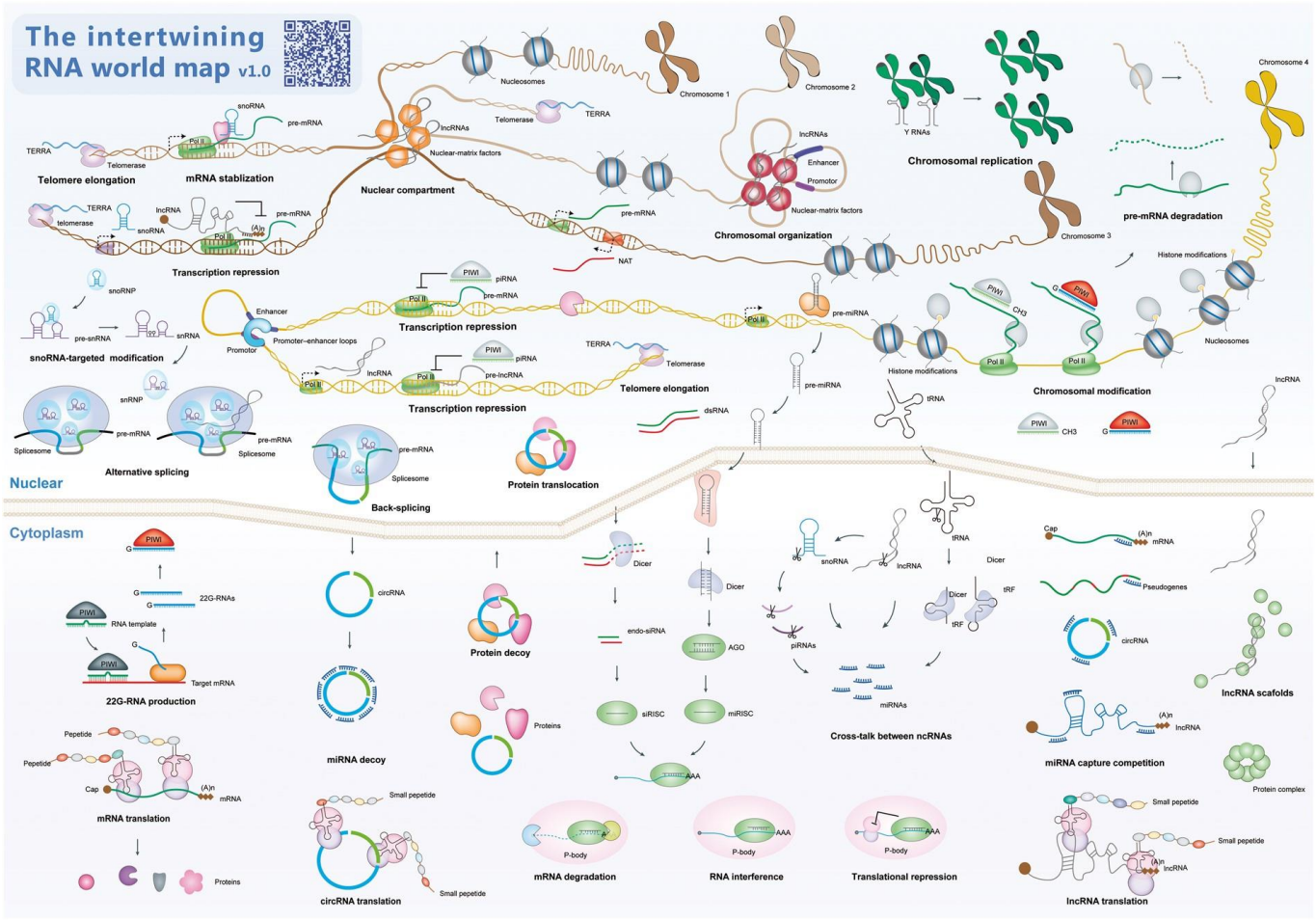

Figure 3.1: Functionality of non-coding RNA in the nucleus (top panel) and the cytoplasm (lower panel). Figure was reprinted from the literature with permission from Chen, Qi et al., Versatile interactions and bioinformatics analysis of noncoding RNAs, Briefings in Bioinformatics, 2019, 20, 5, 1781-1794, by permission of Oxford University Press [4].

Even though the mapping of the human genome in the early 2000s resulted in the discovery of a wide variety of ncRNA transcripts, determining the function of each gene and its specific role in cellular processes is still an on-going area of research. Since ncRNA can interact with mRNAs, other ncRNAs, DNA, and protein, the structure of an RNA transcript can shed more light on the nature of these interactions. ncRNA structures span a range of structural diversity and complexity that can be as simple as a hairpin loop that will be processed into a miRNA or have complex protein binding sites or act as a catalytic site[7]. An important factor to the structural diversity of RNAs in comparison to DNA is in part due to its ability to readily tolerate alternative base pairings, allowing for secondary and tertiary structure stabilization[8]. This arises from the three edges of each nucleic acid base from

which hydrogen bonding can occur (Figure 3.2). The non-Watson-Crick hydrogen bonds are what stabilize a variety of RNA tertiary structures beyond the double helix, such as quadruplexes, triplexes, and coaxial stacking motifs. Hydrogen bonding explains the stability of these motifs, but what gives RNA the ability to be dynamic and flexible is the 2' hydroxyl group (2'-OH) on the ribose sugar of the nucleotides as it can both accept and donate a hydrogen bond. Each 2'-OH can make up to two hydrogen bonds which allows for interactions and motifs that wouldn't be feasible with a deoxyribose in its place, explaining the scope of RNA structural diversity.

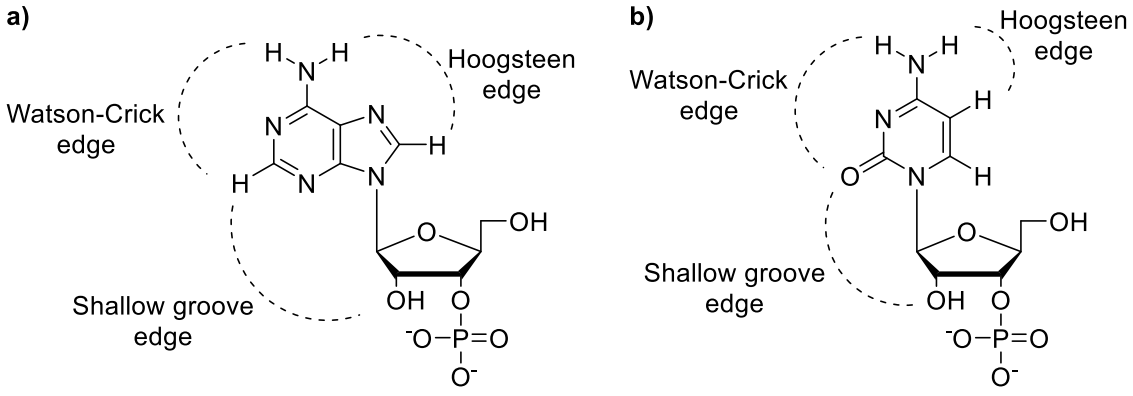

Figure 3.2: The three edges of (a) a purine base and (b) a pyrimidine base for hydrogen bonding. Figure adapted from E. Westhof et. al[8].

Since the 1980s, chemical methods have been used to determine RNA structure[9]. Chemical probing for RNA characterization *in vitro* either induces RNA backbone cleavage (Figure 3.3) or covalently modifies the RNA (Figure 3.4). In general, for both probing techniques, the RNA is first folded and then treated. The cleavage or covalent modification site is read by reverse transcription and cDNA synthesis which is then resolved by denaturing gel electrophoresis[9]. RNA backbone cleavage for probing RNA structure can be induced by taking advantage of the nucleophilic behaviour of the 2' OH group on the ribose. In slightly basic conditions, the 2' OH group can attack the 3' phosphate, resulting in cleaving the phosphodiester bond between the two nucleotides and forming intramolecular phosphodiester and 5'-hydroxyl products (Figure 3.3a). Scission can also be induced

by hydroxyl radicals that abstract a proton from the C5' on the backbone, resulting in its cleavage with 3'-phosphate and 5'-aldehyde products (Figure 3.3b).

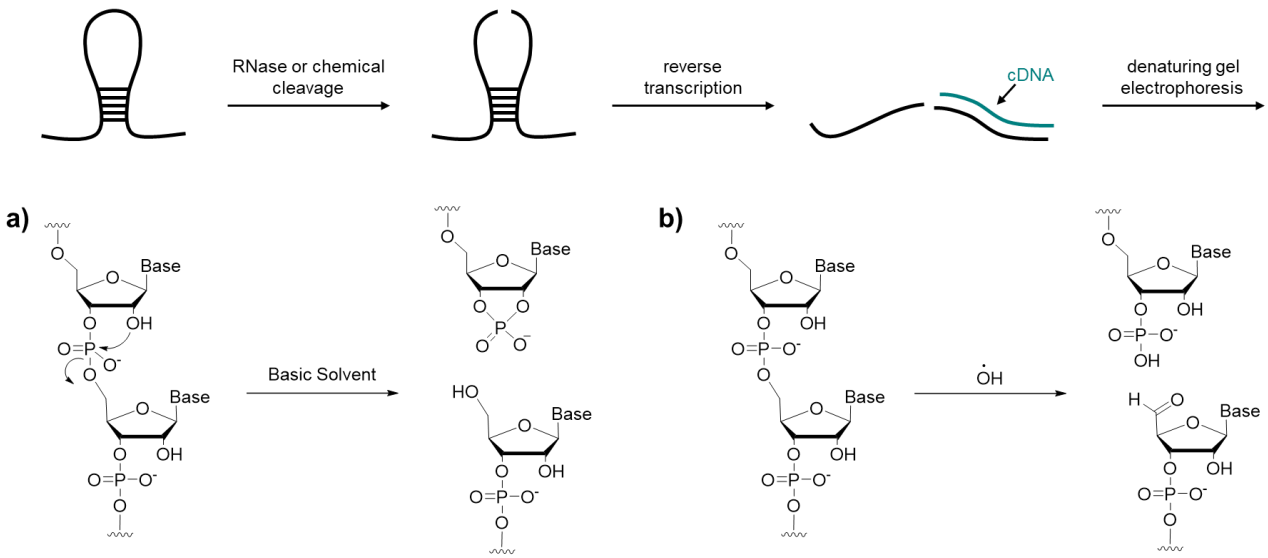

Figure 3.3: Induced chemical cleavage of RNA by 2' OH nucleophilic attack (a) or hydroxy radical abstraction (b). Figure adapted from M. Kubota et. al[9].

The first covalent modification of RNA structure for *in vitro* probing was using dimethylsulfate (DMS) to alkylate nucleophilic endocyclic atoms on the bases of the nucleotides (Figure 3.4a). Alkylation occurs on the N7 position of guanosine, N1 position of adenosine, and the N3 position of cytidine. Selective hydroxyl acylation analyzed by primer extension (SHAPE, Figure 3.4b) takes advantage of the inherent nucleophilicity of the 2' OH group of the ribose and is able to attack an activated electrophilic carbonyl resulting in its covalent modification.

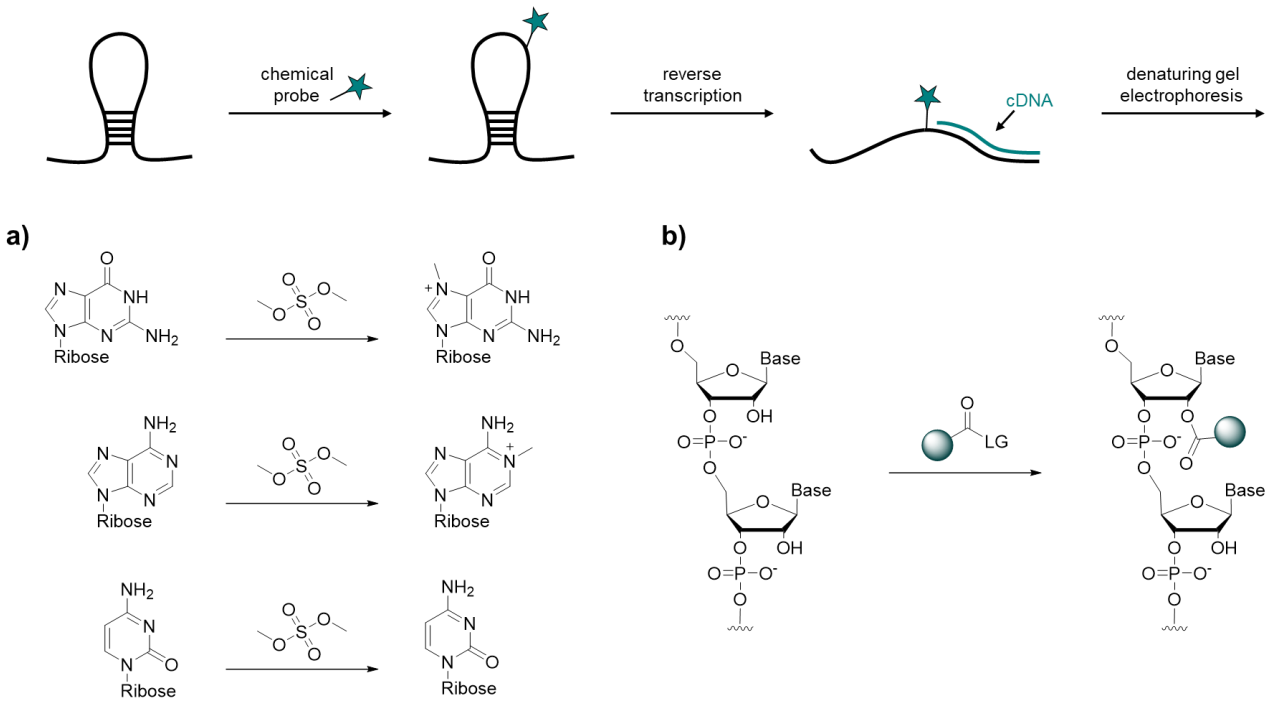

Figure 3.4: Chemical probing of RNA using dimethylsulfate (DMS) (a) or SHAPE (selective hydroxyl acylation analyzed by primer extension) with an activated electrophilic carbonyl (b). Figure adapted from M. Kubota et. al[9].

There are many contributing factors to the observed nucleophilicity of 2' OH group of RNA. Since chemical modification of RNA is conducted in water, the nucleophilicity of any alcohol, at neutral pH, is in direct competition with water. The pKa of alcohols is roughly between 14-15 whereas water has a pKa of 14, but at 55 M, it significantly outcompetes any nucleophilicity from the alcohol. The 2' OH of RNA however, has an estimated pKa between 12 – 14[10] , indicating that its observed reactivity is effected by its acidity. This is due in part to the inductive effect of adjacent heteroatoms (Scheme 3.1a), pulling electron density away from the 2'C. The proposed mechanism of 2' OH acylation whereby the phosphate group acts as a base to transiently deprotonate the 2' OH to make it a better nucleophile (Scheme 3.1b), also suggests that the relative acidity of the 2' OH contributes to its ability as a nucleophile[11].

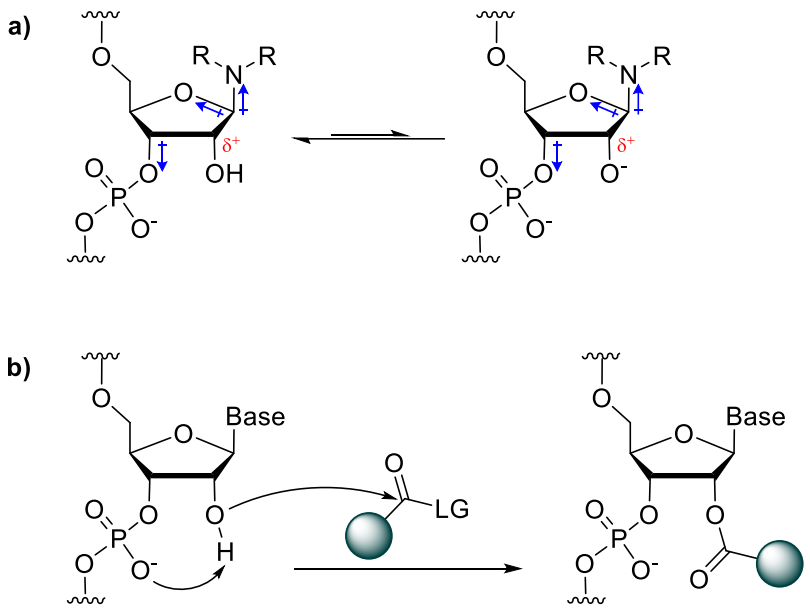

Scheme 3.1: (a) inductive effects of adjacent heteroatoms on the 2' OH of ribose. (b) the proposed mechanism of acylation for SHAPE probing. Adapted from W. A. Velema et. al[11].

Determining RNA secondary structure and its interactions *in vitro* using SHAPE (selective hydroxyl acylation analyzed by primer extension) takes advantage of RNA's flexibility and structural diversity (Figure 3.5). Acylating agents target the 2' OH of nucleotides that are flexible and accessible, typically in regions where the RNA is single stranded or the hydrogen bonds between two base pairs are relatively weak[7]. Positions where covalent modification occurred on the RNA are then detected by reverse transcriptase primer extension wherein DNA synthesis stops one nucleotide before the position of the adduct. The lengths of the complementary DNA strands indicate the site of RNA acylation, from which SHAPE reactivity is normalized as a function of nucleotide position. Positions with higher SHAPE reactivites are inferred to indicate regions on the RNA that are flexible.

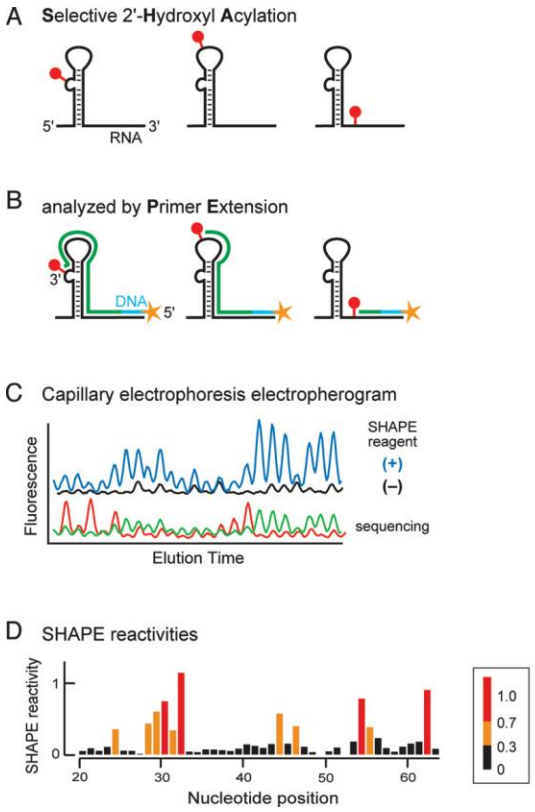

Figure 3.5: SHAPE experiment overview. (A) Selective covalent modification of RNA at single stranded/flexible regions of RNA. (B) Covalent adduct formation is detected by primer extension. (C) Primer extension products are resolved by capillary electrophoresis. (D) Normalized SHAPE reactivites indicate regions of RNA that are single stranded/flexible. Reprinted with permission from Acc. Chem. Res. 2011, 44 (12), 1280–1291. Copyright 2011. American Chemical Society[7].

For significant RNA labelling, the acylating agents used in SHAPE experiments (Figure 3.6) require an activated carbonyl for nucleophilic attack from the 2' OH group and should exhibit solubility in water while also being unreactive towards water. Satisfying these three requirements is challenging since highly reactive electrophiles tend to also hydrolyze in water, effectively decreasing the amount of electrophile available for RNA acylation. If the electrophile isn't reactive enough, insufficient RNA labelling will occur[12]. The half-life of the hydrolysis of various acylating reagents are typically associated with how efficient it is for RNA labelling and whether it can be reliably used for *in vivo* labelling. Shorter half-lives (seconds) have resulted in limited RNA acylation, as have much long half-lives (hours). Reagents with half-lives ranging from 30 minutes to 120 minutes was found to yield stoichiometrically higher levels of acylation[11]. The solubility of the reagents also plays a

major role in their applicability for either *in vivo* or *in vitro* use. For example 1M7 was not shown to modify RNA appreciably *in vivo*, presumably because its water solubility is relatively lower than other acylating agents, indicating that it may have gotten "stuck" in the lipid bilayer of cell membranes[12].

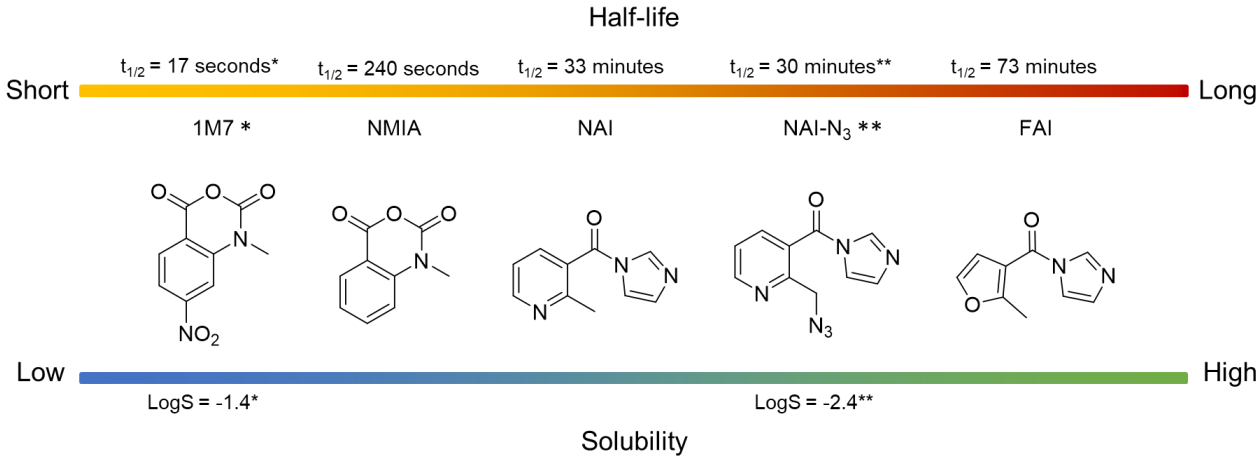

Figure 3.6: Most used SHAPE reagents for RNA structure elucidation arranged by half-life in water and their solubility in water. The marked reagents are representative of the lower (*) and higher (**) end of the spectrum in terms of efficient in vivo SHAPE labelling. 1M7 = 1-methyl-7-nitroisatoic anhydride, NMIA = N-methylisatoic anhydride, NAI = 2-methylnicotinic acid imidazolide, NAI-N_3 = 2-methylnicotinic acid imidazolide - azide, FAI = 2-methyl-3-furoic acid imidazolide. Figure adapted from B. Lee et. al.[12]

SHAPE *in vivo* was first demonstrated in 2013 by R. Spitale and coworkers[13] and significantly expanded SHAPE utility. New electrophilic acylation reagents were selected based on their how reactive they are to hydroxyl groups, their solubility at high concentrations, and whether sufficient RNA labelling is achieved. Acylimidazoles FAI (2-methyl-3-furoic acid imidazolide) and NAI (2-methylnicotinic acid imidazolide) were synthesized and were found to have much longer half-lives than previously used acylating reagents at 73 and 33 minutes, respectively. FAI and NAI were both used for *in vitro* SHAPE labelling of mouse embryonic stem cell (mESC) 5S rRNA and it was determined that NAI showed greater RNA modification than FAI. This also held true for *in vivo* labelling of live cells, and upon comparing SHAPE reactivity with the literature reported crystal structure of 5S rRNA, the majority of residues in flexible regions and involved in non-canonical Watson-Crick base pairing were labelled with NAI, resulting in researchers directing their focus on

using NAI for more complex *in vivo* use. In addition to cytosolic RNA, NAI was also found to modify nuclear RNA, suggesting that it is robust enough to label RNAs of lower abundance and permeable to the nuclear envelope. *In vivo* SHAPE labelling shows it can take advantage of the dynamic and flexible nature of RNA and shed light on tertiary structure and RNA interactions with other biomolecules (Figure 3.7). In the same seminal paper, *in vivo* and *in vitro* SHAPE reactivity profiles were compared to deduce RNA structural differences in its native environment and the location of RNA-protein interactions[13].

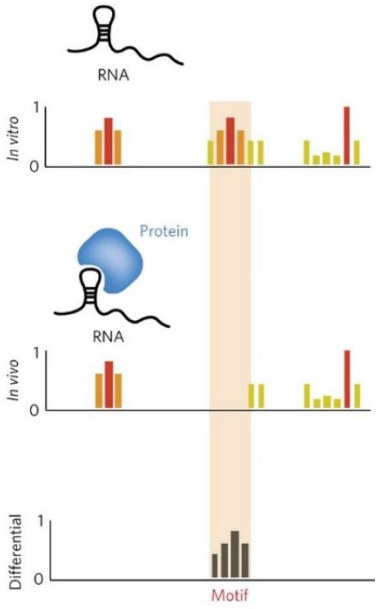

Figure 3.7: Schematic of differential RNA structure probing wherein the SHAPE reactivity as a function of nucleotide position indicates RNA-protein interactions. Reprinted by permission from Springer Nature, Nature Chemical Biology, Progress and challenges for chemical probing of RNA structure inside living cells, Miles Kubota et al, Copyright 2015 [9].

A few years later, Spitale and colleagues expanded on the applicability of SHAPE labelling overcoming concerns of low signal-to-noise ratios of *in vivo* SHAPE labelling, by using an azide modified NAI (NAI-N_3)[14], dubbed icSHAPE (*in vivo clicl* selective hydroxyl acylation analyzed by primer extension). Upon treatment of mouse embryonic stem cells with NAI-N_3, the acylated RNAs were biotinylated using biotin functionalized DIBO (dibenzocyclooctyne) in a SPAAC (strain-promoted azide-alkyne cycloaddition) reaction. The resulting RNA fragments are used to generate

cDNA sequencing libraries by subjecting the fragments to 3'-end repair, adapter ligation, size selection, biotin enrichment, reverse transcription, and PCR. This ensures that only the fragments modified by NAI-N_3 are amplified. cDNA sequencing libraries generated are used to map the entire transcriptome[15].

It must be noted that while the acylating reagents in Figure 3.6 are presented to be on a spectrum of applicability and effectiveness, what is considered useful or sufficient labelling is highly dependent on the application of the acylating reagent[11]. For example, 1M7 has a very short hydrolysis half-life indicating that it might not be suitable for labelling. However, it's high reactivity was what allowed for RNA labelling at nucleotide resolution to determine RNA secondary and tertiary structure[16]. Highly reactive reagents are typically applied when sparse acylation is required, whereas milder reagents are typically used for stoichiometric levels of labelling. It is for this reason that the development of novel acylating reagents is required to ensure that the SHAPE methodology can be used in a wide range of applications.

3.2 Objective

Nitrones are an allyl class of 1,3-dipoles that have three modification sites that allow for stereoelectronically tuning to optimize its reactivity to a dipolarophile. SPANC (strain-promoted alkyne-nitrone cycloaddition) involves a [3+2] cycloaddition between the reacting partners, and demonstrates rates up to 59 times faster than the analogous reaction between DIBO and benzyl azide[17]. Table 3.1 compares SPANC kinetic rates of commonly studied cyclic nitrones and the fastest observed acyclic nitrone with the parallel SPAAC reaction with benzyl azide and they demonstrate that across the range of dipolarophiles nitrones exhibit faster kinetic rates, making them better suited for *in vivo* use.

Table 3.1: SPANC kinetic rates for commonly used cyclic nitrones and the fastest observed acyclic nitrone in comparison with the parallel SPAAC reaction with benzyl azide. Second-order reaction rates in M^{-1} s^{-1}. [a]d_3-AcN. [b]99:1 AcN/H_2O. [c]MeOH. [d]d_4-MeOH. [e]2:1 AcN/THF. [f]d_6-C_6H_6 with DIBO. Reprinted with permission from Chem. Rev. 2021, 121, 12, 6699–6717. Copyright 2021. American Chemical Society[18].

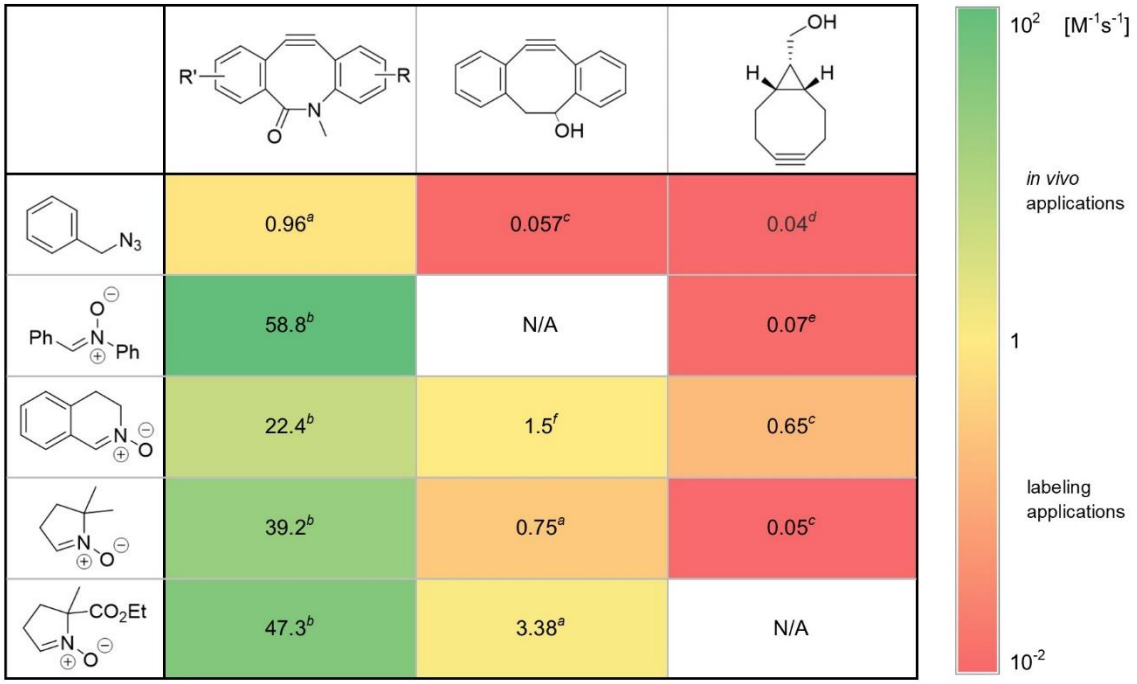

This chapter will demonstrate the applicability of SPANC reactions using cyclic nitrone DMImO (2,2-dimethyl-5-oxo-3-oxy-2,5-dihydro-imidazole) for the icSHAPE method of probing RNA structure. The bioorthogonal toolbox is expanded by modifying DMImO to introduce an activated electrophilic carbonyl and testing its reactivity towards d-ATP as a proxy for RNA. This proof-of-concept experiment aims to demonstrate the adaptability of nitrones for a larger scope of biological applications.

3.3 Results and Discussion

3.3.1 Design and Synthesis of Probe

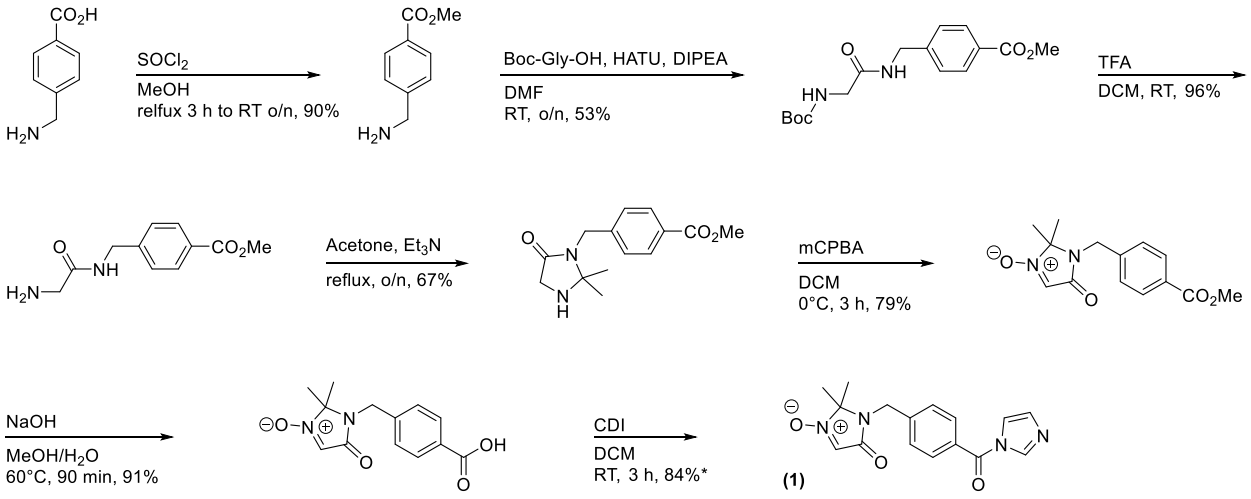

*Scheme 3.2: Synthetic procedure for preparing imidazole modified DMImO (DMImO-I, 1). Yields reflect the purified product. Overall yield of the carboxylic acid is 23% over 6 steps. *due to the rapid hydrolysis the yield reported is not an accurate representation of the purified product as it also includes the hydrolysis product. The actual yield would presumably be lower than what is reported.*

To design a 2'OH acylating reagent, the probe has to have an activated carbonyl that makes it susceptible to nucleophilic attack, while keeping in mind that the probe must be water soluble and that the leaving group must be benign to the biological environment. Our previous work demonstrates that DMImO can be modified into an efficient unnatural amino acid for peptidoglycan labelling[19], proving that DMImO moiety off the benzylic carbon is water soluble and amendable to biological environments. Of the 2' OH acylating reagents used for RNA labelling, the activated carbonyls most commonly used are either anhydrides or imidazole. The addition of the acylimidazole as the chosen activated carbonyl rather than the anhydride was based on previous literature findings where anhydrides were found to be too reactive and hydrolyzed too quickly for reliable RNA labelling[13].

The acylimidazole synthesized in the final step was done in two ways. The conditions reported in Scheme 3.2 were used for NMR and MS characterization experiments, while the stock solution prepared for labelling experiments was conducted by the dropwise addition of an equimolar amount of CDI in molecular biology grade DMSO to a solution of the carboxylic acid also in molecular biology grade DMSO. The synthesis of NAI–N_3 was carried out as reported in the literature and will be used for comparison with DMImO-I for future RNA labelling experiments.

3.3.2 Hydrolysis Rate and Half-Life Determination

The rate constant of the hydrolysis of DMImO-I was conducted in triplicate using UV-vis spectroscopy in a 100 mM HEPES buffer, pH 8.0, containing 6 mM MgCl2 and 100 mM NaCl at 25 $\pm$ 0.1 °C. 3 µL of a 100 mM solution of DMImO-I in molecular biology grade DMSO was added to 997 µL of reaction buffer and the reaction was continuously monitored for the decrease of absorbance at 265 nm. Rate of hydrolysis was determined by non-linear regression of the relative absorption values as a function of time (in seconds) to fit the first order integrated rate law $[A] = [A]_0 e^{-kt}$ by only changing the k value. Once the hydrolysis rate was determined, the half-life of the first order decay was determined using the equation $t_{\frac{1}{2}} = \frac{ln(2)}{k}$. The kinetic data is summarized in Table 3.2.

Table 3.2: Observed first order decay constants for the hydrolysis of DMImO-I along with its calculated half-life.

	$k_{observed}$ (s^{-1})	Half Life (s)
Trial 1	8.45E-04	821
Trial 2	8.12E-04	854
Trial 3	8.39E-04	826
Average	8.32E-04	834
Standard Deviation	1.45E-05	15

The observed half-life of 834 ± 15 seconds (13.9 minutes), is under the ideal range previously reported (30 – 120 min[11]), however that doesn't necessarily mean that DMImO-I will prove to be ineffective at labeling RNA *in vivo*. Of the reported half-lives of acylating reagents (Figure 3.6), there is a significant jump between the half-life of NMIA (4 minutes, ineffective for *in vivo* use) and NAI-N_3 (30 minutes, most effective for *in vivo* labelling), nor is there a probe that has a similar half-life. This indicates that *in vivo* RNA labelling can still occur at levels high enough for icSHAPE structure probing.

3.3.3 Product Formation Detected by Mass Spectrometry

The shorter half-life of DMImO-I in comparison to NAI-N_3 was evident when tracking the reaction of the two probes with d-ATP. Tracking the reactions using UV-Vis spectroscopy was challenging since the max absorbance peaks of both probes and d-ATP were in the 250 to 270 nm range resulting in badly resolved peaks, preventing proper absorbance tracking and so TLC was used to track the formation of product instead. The NAI-N_3 and DMImO-I probes both reacted in a 10:1 molar ratio with d-ATP in SHAPE reaction buffer and were tracked by TLC (eluting solvent 3:2:1 $ClCH_3$:EtOAc:MeOH) which are included in Appendix B. 25 µL of 100 mM solutions of probe in molecular grade DMSO, and 125 µL of a 2 mM solution of d-ATP in reaction buffer were added to an additional 350 µL of reaction buffer (total volume 500 µL). Product formation tracked by TLC showed that the DMImO-I probe reacted faster than the azide probe evidenced by the product spot first appearing after 5 minutes from when the reaction first started for DMImO-I vs 15 minutes for the azide probe. While this qualitative data indicates that the acylation reaction with d-ATP is faster with DMImO-I, future work will focus on acquiring more quantitative evidence of product formation rate (Section 3.4).

To confirm product formation, the reaction with DMImO-I and d-ATP was repeated and let to react for about 3 half-lives (45 minutes), after which, it was directly loaded onto a TOF Synapt Mass

Spectrometer in ES+ mode. The resulting ion of 534 was found, corresponding to the mass of the expected product with 3 phosphate groups cleaved off and the addition of a molecule of phosphate. (Scheme 3.3 and 3.4)

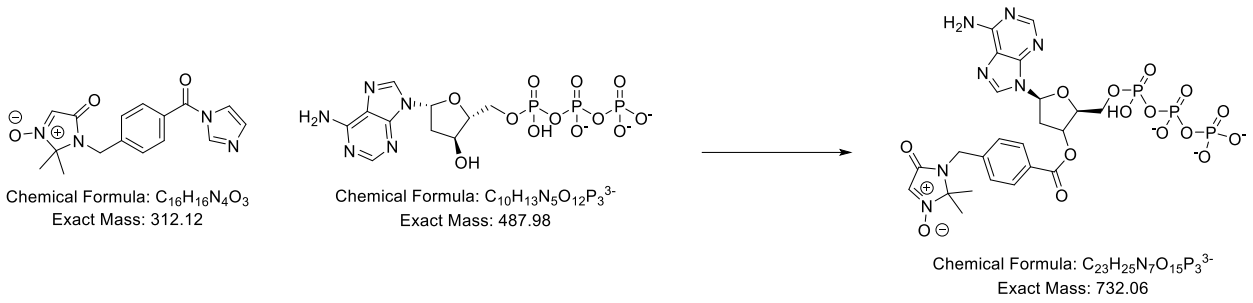

Scheme 3.3: Proposed reaction between DMImO-I and d-ATP.

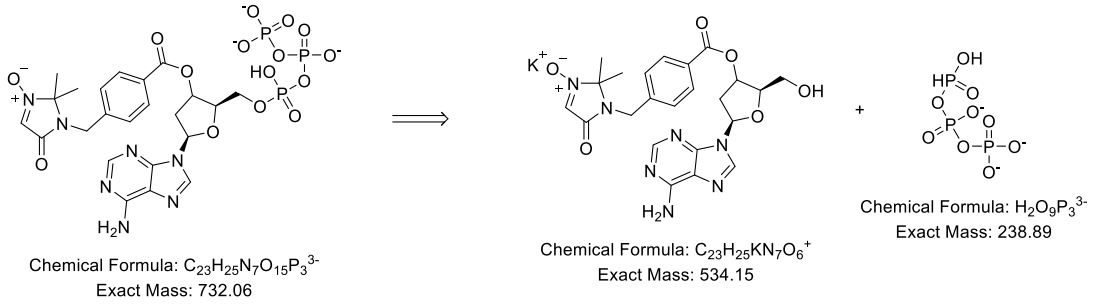

Scheme 3.4: Expected fragmentation of the final product resulting in the observed ion.

3.3.4 RNA Labelling

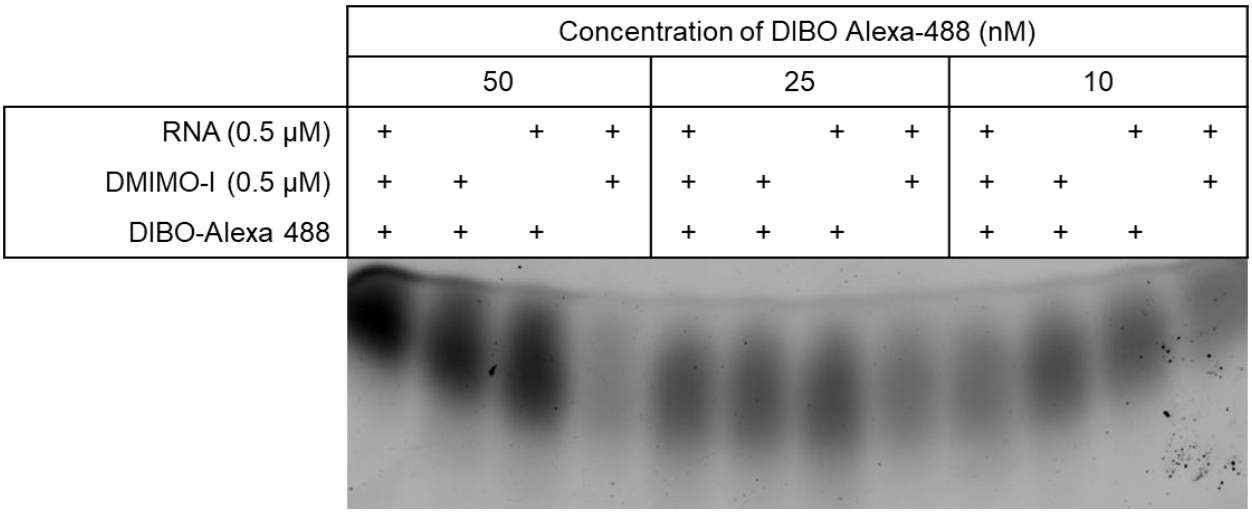

Figure 3.8: Gel shift of RNA labelling using DMImO-I and Alexa 488 functionalized DIBO.

The initial gel showed very broad bands indicating that there could be signal interference from unreacted DIBO-Alexa488. The band for column 1 using 50 nM of DIBO-Alexa488 is more condensed and brighter than the other bands, consistent with the amount of DIBO-Alexa 488 that was added. Since the band is condensed, this could mean that the SPANC reaction relatively in column 1 occurred more efficiently than the SPANC reaction for column 2 (DMImO-I and DIBO-Alexa488 only), potentially caused by DMImO-I labelling but this cannot be said for certain. Any unreacted DIBO and probe would have to be removed to be for certain.

The same guide strand RNA was also available as a Cy3 functionalized RNA, and although the signals of Cy3 and Alexa488 overlap, it may still offer some insight on whether labelling can be observed especially if unreacted probe or DIBO can be removed prior to gel loading. For the next gel, the same protocol was used with the exception of using P6 Microspin columns to remove excess probe and DIBO-Alexa488 prior to gel loading. NAI-N_3 was also used to compare its labelling with DMImO-I. (Figure 3.9). The amounts used are summarized in Appendix B.

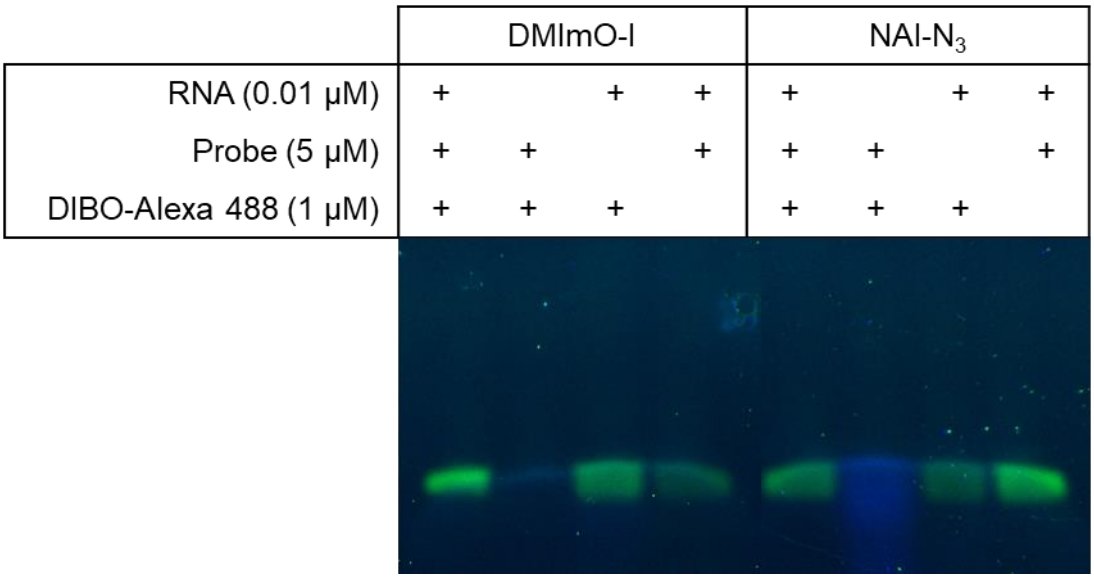

Figure 3.9: Imaged gel for in vitro Cy3- RNA labelling using DMImO-I, NAI-N_3 and Alexa 488 functionalized DIBO. Blue: Alexa-488, Green = Cy3 RNA.

These results were similar to the results in Figure 3.8 in the sense that the first control (with all reagents) appears to be the brightest for labelling with the nitrone probe. However, this again doesn't definitively indicate probe labelling even with excess probe and DIBO removal since the signals of both fluorophores can overlap. The increased brightness in lane one could be the misattributed to signal overlap rather than labelling. Future experiments would have to utilize a Cy5 functionalized DIBO or another more red-shifted fluorophore that wouldn't overlap with the Cy3 signal of the RNA.

In collaboration with the Sagan Lab at McGill university, a prepared solution of DMImO-I in DMSO was sent to confirm *in vitro* and *in vivo* labelling and compare its applicability for icSHAPE labelling with NAI-N_3. Preliminary results from the Sagan lab indicate similar *in vitro* and *in vivo* icSHAPE labelling of 5S rRNA using both probes (Figure 3.10 and 3.11, respectively), which is encouraging and offers more definitive evidence of effective labelling of RNA by DMImO-I.

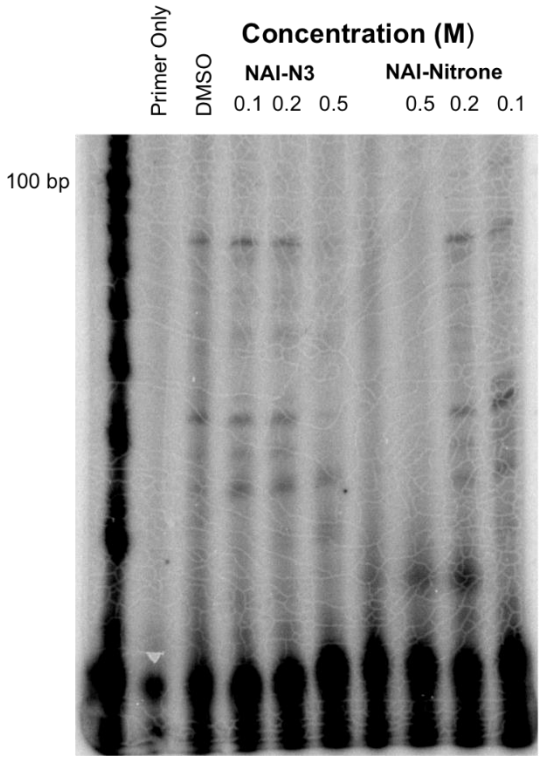

Figure 3.10: Concentration gradients of NAI-N_3 and DMImO-I (referred to here as NAI-Nitrone) used to label 5S rRNA extracted from A549 cells following procedure reported in the literature[13]. (Note: this experiment was conducted by Quinn Abram of the Sagan Lab at McGill University, following procedure previously reported in the literature[13]. The figure was also created by Abram.)

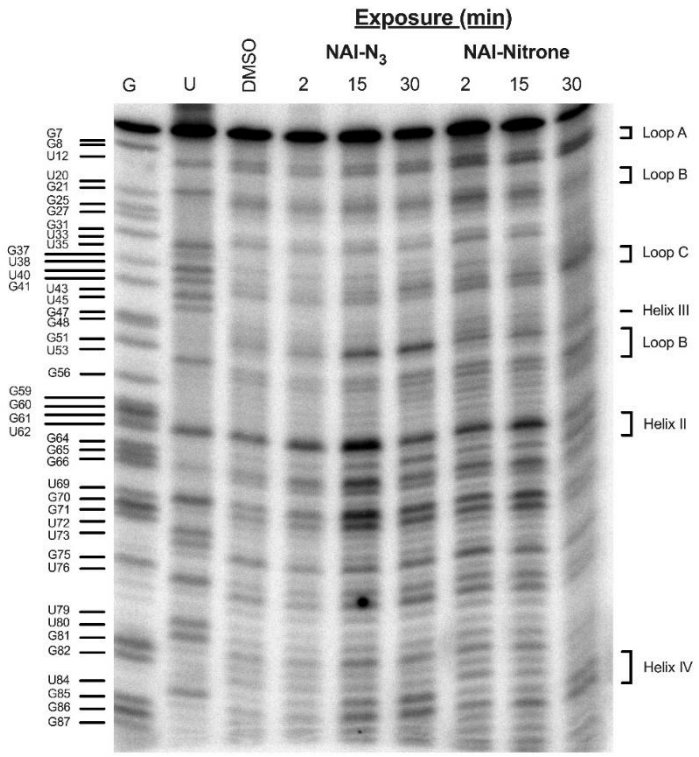

Figure 3.11: Denaturing gel electrophoresis of icSHAPE used to label 5S rRNA extracted from live A549 cells using NAI-N_3 and DMImO-I (referred to here as NAI-Nitrone) as probes. The resulting SHAPE profile was used to map out its sequence and annotate secondary structures. (Note: this experiment was conducted by Quinn Abram of the Sagan Lab at McGill University, following procedure previously reported in the literature[13]*. The figure was also created by Abram.)*

3.4 Future Directions

Based on how quickly the nitrone probe hydrolyzes, determining its reaction rate using d-ATP has been difficult especially since d-ATP only dissolves in water. Using MS could be used to get a more accurate representation of the reaction. A mixture of d-ATP and DMImO-I can be continuously injected by a syringe pump into a mass spectrometer that can detect peak intensities of selected masses over a period of time. This technique has been previously used in the lab to track a fast-reacting SPANC reaction (K. Margison, unpublished data) and has the potential to be used effectively to determine the reaction rate between DMImO-I and d-ATP.

Future experiments should also take into consideration the strained alkyne used. Previous work indicates that electron poor alkynes preferably react with electron rich nitrones and vice versa[20] (Figure 3.12). Since DMImO preferentially reacts with BCN rather than DIBO, using BCN with DMiMO-I may be even more favourable since BCN is smaller and more hydrophilic than DIBO, reducing steric hindrance and making SPANC better suited for *in vivo* SHAPE labelling.

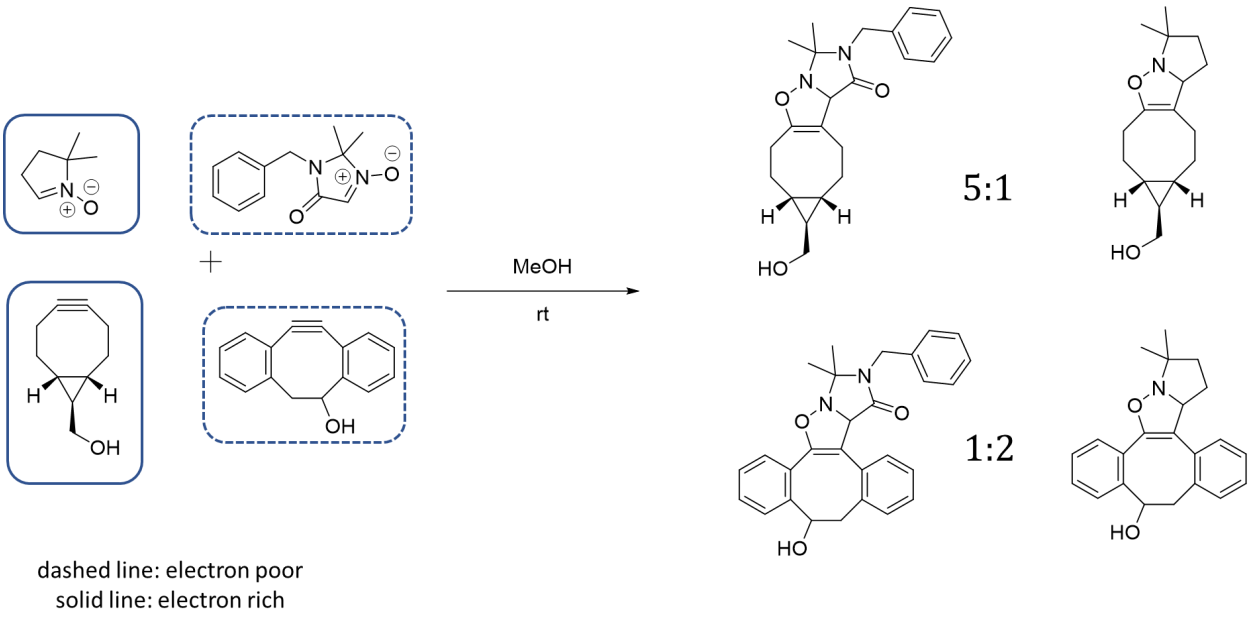

Figure 3.12: Product ratios from a one pot experiment with electron poor (dashed box) or electron rich (solid box). The electron rich nitrone reacted with electron poor DIBO and vice versa for BCN. Figure adapted from D. A. MacKenzie[20].

3.5 Conclusion

Preliminary data shows that DMImO-I can sufficiently label RNA *in vitro* based on the MS data using d-ATP as a proxy for RNA and preliminary RNA labelling data from the Sagan Lab at McGill University and shows similar reactivity to the azide probe. The rates of the reaction between d-ATP and the nitrone probe will be determined using MS and will shed more insight onto the reactivity of the probe. GL2 guide strand RNA labelling will also have to be repeated with a red-shifted fluorophore to confirm *in vitro* DMImO-I labelling.

3.6 Methods and Experimental Details

Commercially available reagents were purchased from Sigma-Aldrich, or Alfa Aesar and used without further purification. 2'-deoxyadenosine-5'-triphosphate (d-ATP) was purchased from CombiBlocks as a trisodium salt and was used without further purification. Deuterated solvents were purchased from Cambridge Isotopes with the exception of deuterated acetonitrile which was purchased from Sigma-Aldrich and were used as received. Thin layer chromatography was performed on SiliaPlate™ silica gel (aluminum backed, 60 Å, F_{254}, layer thickness 200 µm), analytical preparative chromatography was performed on MilliporeSigma silica gel (glass backed, 60 Å, F_{254}, layer thickness 250 µm). Flash chromatography was conducted with silica gel (60 Å, particle size 40-63 µm).

^{1}H NMR spectra were obtained using 300 MHz, 400 MHz, and 600 MHz Bruker NMR spectrometers. ^{13}C, ^{13}C DEPT 90, ^{13}C DEPT 135, 2D ^{1}H-^{1}H COSY, 2D ^{1}H-^{1}H NOSY, and 2D ^{1}H-^{13}C HSQC NMR spectra were obtained using 400 MHz and 600 MHz Bruker NMR spectrometers. All spectra were processed using Bruker TopSpin 4.0.6 software. NMR spectra peaks are measured in ppm and referenced from the residual deuterated solvent peak. Abbreviations for the multiplicity of peaks are as follows: s = singlet, d = doublet, t = triplet, m = multiplet or unresolved, br = broad and J = coupling constants are reported in Hz.

3.6.1 Synthesis of Reagents

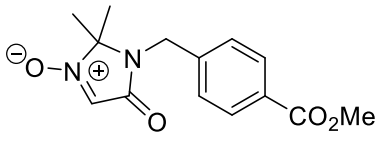

1-[(*p*-Methoxycarbonylphenyl)methyl]-2,2-dimethyl-5-oxo-3-imidazolin-3-ium-3-olate (DMImO) Synthesized according to previously reported procedures[21]. ^{1}H NMR (300 MHz; d-$CDCl_3$): δ 8.02 (d, *J* = 8.34 Hz, 2H), 7.40 (d, *J* = 8.34 Hz, 2H), 7.10 (s, 1H), 4.71 (s,

2H), 3.92 (s, 3H), 1.49 (s, 6H). Spectral data was consistent with what was reported in the literature. Product was obtained as an off-white powder in a 24% yield over 5 steps.

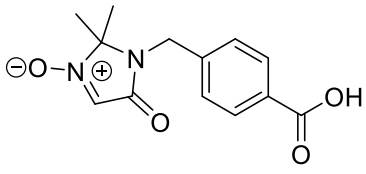

1-[(*p*-Carboxyphenyl)methyl]-2,2-dimethyl-5-oxo-3-imidazolin-3-ium-3-olate DMImO (500 mg, 1.8 mmol) was added to a 15 mL 1:1 MeOH:H_2O solution of 0.5 M NaOH. The reaction was heated to 60°C and was stirred for 30 minutes. An additional 15 mL of water was added, the reaction was acidified to a pH of 4 using a resin (AmberChrom, 50WX4 hydrogen form, Sigma-Aldrich) and was filtered through a Celite pad. The solution was washed using EtOAC 5 times, dried using Na_2SO_4, and concentrated. Crude product was purified using column chromatography (silica, 5% MeOH in DCM) resulting in an off-white powder in 91% yield. ^{1}H NMR (300 MHz; d-D_3COD): δ 7.93 (m, 2H), 7.38 (m, 3H), 4.76 (s, 2H), 1.51 (s, 6H). Spectral data was consistent with what was reported in the literature. HRMS (ESI+) m/z calculated for $C_{13}H_{14}N_2O_4Na$ [M + Na] 285.0851, found 285.0874.

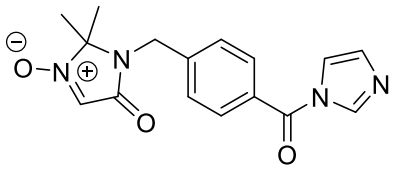

1-({*p*-[(1-Imidazolyl)carbonyl]phenyl}methyl)-2,2-dimethyl-5-oxo-3-imidazolin-3-ium-3-olate (DMImO-I): The carboxylic acid (420 mg, 1.6 mmol) was dissolved in 0.4 mL of anhydrous molecular grade DMSO. A solution of N,N'-carbonyldiimidazole (260 mg, 1.6 mmol) in 0.4 mL of anhydrous molecular grade DMSO was added drop-wise, creating gas. The reaction was left to react for 1 hour resulting in a 2 M stock solution of the probe that was used as is for RNA labeling experiments. For structure confirmation and elucidation 2 smaller scale reactions (final concentrations of 40 mM) were done. One was done in anhydrous d_6-DMSO for NMR elucidation and the second was done in anhydrous DCM for MS analysis which was purified using column chromatography (silica, EtOAc). ^{1}H NMR (400 MHz; d_6-DMSO): δ 7.79 (m, 2H), 7.66 (m, 4H),

7.59 (m, 2H), 4.77 (s, 2H), 1.50 (s, 6H). ^{13}C NMR (100 MHz, d_6-DMSO) δ 165.85, 162.25, 143.60, 138.45, 135.16 , 130.56, 130.47, 130.14, 129.48, 127.91, 123.80, 121.71, 118.46, 89.85, 42.32, 24.15. MS (ESI+) m/z calculated for $C_{16}H_{16}N_4O_3Na$ [M + Na] 335.1, found 335.1.

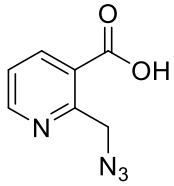

2-(azidomethyl)nicotinic acid: Synthesized according to previously reported procedures[14]. ^1H NMR (300 MHz; d-$CDCl_3$): δ 8.85 (dd, *J* = 4.8, 1.6 Hz, 1H), 8.44 (dd, *J* = 7.9, 1.6 Hz, 1H), 7.45 (dd, *J* =7.9, 4.8 Hz, 1H), 4.96 (s, 2H). Spectral data was consistent with what was reported in the literature. Carboxylic acid was obtained as a pale brown powder in 78% yield over 3 steps. MS (ESI+) m/z calculated for $C_7H_6N_4O_2Na_2$ [M + 2 Na] 228.2, found 228.2.

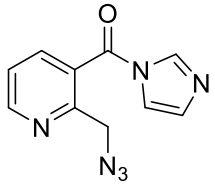

2-(azidomethyl)nicotinic acid acyl imidazole: Synthesized according to previously reported procedures[14]. ^1H NMR (300 MHz; d-$CDCl_3$): δ 8.84 (dd, *J* = 4.9, 1.7 Hz, 1H), 7.95 (s, 1H), 7.84 (dd, *J* = 7.8, 1.7 Hz, 1H), 7.47 (dd, *J* = 7.8, 4.9 Hz, 2H), 7.21 (m, 1H), 4.68 (s, 2H). Spectral data was consistent with what was reported in the literature. MS (EI) m/z calculated for $C_{10}H_8N_6O$ [M] 228.2, found 228.2.

3.6.2 Hydrolysis Rate Determination

Absorbances were monitored for kinetic measurements using the Agilent Cary 60 UV-vis spectrophotometer. 1.5 mL Quartz screw cap cuvettes (10 mm pathlength) were used and were rinsed with acetone 3 times, then with methanol 3 times and dried for an hour before each experiment. Kimwipes were used to remove outside residue on the cuvettes. 997 µL of SHAPE buffer (100 mM HEPES, 6 mM $MgCl_2$ and 100 mM NaCl, pH 7.5), and 3 µL of anhydrous molecular grade DMSO was used to blank the spectrophotometer prior to reaction monitoring. To a cuvette, 997 µL

of SHAPE buffer and 3 µL of a 100 mM solution of DMImO-I probe in anhydrous DMSO was added. Upon the addition of probe, the cuvette is stoppered and quickly inverted three times before inserting it for absorbance monitoring. The absorbance of the reaction was measured over a range of 200 nm to 600 nm in triplicate and was used to track the disappearance of the probe. The reaction was deemed complete when the change in absorbance plateaus. Data analysis was conducted using Microsoft Excel, version 2201. First order decay kinetic constants were determined using non-linear regression fitted to the first-order integrated rate law.

3.6.3 RNA Labelling

In vitro RNA labelling was done on either a 21-mer GL2 guide strand RNA (5'-CGU ACG CGG AAU ACU UCG AUU-3') or a 5' Cy3 functionalized 21-mer GL2 guide strand RNA (5'-Cy3-CGU ACG CGG AAU ACU UCG AUU-3'). RNA was incubated in the reaction buffer with probe for approximately 5 half-lives (1.5 h) at room temperature, after which an Alexa 488 functionalized DIBO was added and left to react for 20 minutes. TBE loading buffer was added and the samples were loaded onto a 20% TBE native gel, was run for 1.5 h at 95V, and was imaged using a ChemiDoc. The concentrations and amounts used are summarized in Appendix B.

3.6.3.1 *in vitro* and *in vivo* labelling of 5S rRNA (note: methodology provided as is by PhD candidate, Quinn Abram, of the Sagan Lab at McGill University)

3x10E5 A549 (lung carcinoma) cells seeding in 6-well plates for 16 h, and then exposed to 0.1 M NAI-N3 or NAI-Nitrone in 250 µL PBS for 2, 15, or 30 minutes. 10% DMSO in PBS was used as treatment control. Samples were then Trizol extracted to quench the labelling reaction. 6 µg of each RNA sample was then used in primer extension reactions with P32-labelled oligos that bind human 5S rRNA (5' - AAA GCC TAC AGC ACC CGG TAT - 3'). Samples were then denatured at 95ºC for 10 min and run on a 15% UREA-PAGE gel for 3 h at 30 W to resolve cDNA extensions. Sequencing ladders

were generated using corresponding ddNTP in the extension reaction with RNA from DMSO-treated control cells.

For total RNA, 6 µg of RNA extracted from A549 cells was denatured at 95ºC for 3 minutes and then flash-cooled on ice for 5 min. 3× SHAPE buffer (333 mM HEPES, pH 8.0, 20 mM MgCl2 and 333 mM NaCl) was added, and RNA was allowed to equilibrate at 37 °C for 10 min. RNA was then exposed to 0.1 M NAI-N3 or NAI-Nitrone for 1, 15, or 30 minutes, and then Trizol extracted to quench the labelling reaction. All extracted RNA was used in subsequent PE reactions and analyzed as described for live-cell experiments.

3.7 References

(1) Guerrier-Takada, C.; Gardiner, K.; Marsh, T.; Pace, N.; Altman, S. The RNA Moiety of Ribonuclease P Is the Catalytic Subunit of the Enzyme. *Cell* **1983**, *35* (3), 849–857. https://doi.org/10.1016/0092-8674(83)90117-4.

(2) Cech, T. R.; Steitz, J. A. The Noncoding RNA Revolution - Trashing Old Rules to Forge New Ones. *Cell*. Elsevier March 27, 2014, pp 77–94. https://doi.org/10.1016/j.cell.2014.03.008.

(3) Mattick, J. S. Non-Coding RNAs: The Architects of Eukaryotic Complexity. *EMBO Rep.* **2001**, *2* (11), 986–991. https://doi.org/10.1093/embo-reports/kve230.

(4) Chen, Q.; Meng, X.; Liao, Q.; Chen, M. Versatile Interactions and Bioinformatics Analysis of Noncoding RNAs. *Brief. Bioinform.* **2019**, *20* (5), 1781–1794. https://doi.org/10.1093/BIB/BBY050.

(5) Zhang, P.; Wu, W.; Chen, Q.; Chen, M. Non-Coding RNAs and Their Integrated Networks. *J. Integr. Bioinform.* **2019**, *16* (3). https://doi.org/10.1515/JIB-2019-0027.

(6) Statello, L.; Guo, C. J.; Chen, L. L.; Huarte, M. Gene Regulation by Long Non-Coding RNAs and Its Biological Functions. *Nature Reviews Molecular Cell Biology*. Nature Publishing Group December 22, 2021, pp 96–118. https://doi.org/10.1038/s41580-020-00315-9.

(7) Weeks, K. M.; Mauger, D. M. Exploring RNA Structural Codes with SHAPE Chemistry. *Acc. Chem. Res.* **2011**, *44* (12), 1280–1291. https://doi.org/10.1021/AR200051H.

(8) Westhof, E.; Fritsch, V. RNA Folding: Beyond Watson–Crick Pairs. *Structure* **2000**, *8* (3), R55–R65. https://doi.org/10.1016/S0969-2126(00)00112-X.

(9) Kubota, M.; Tran, C.; Spitale, R. C. Progress and Challenges for Chemical Probing of RNA Structure inside Living Cells. *Nat. Chem. Biol.* **2015**, *11* (12), 933–941. https://doi.org/10.1038/nchembio.1958.

(10) Velikyan, I.; Acharya, S.; Trifonova, A.; Földesi, A.; Chattopadhyaya, J. The PKa's of 2′-Hydroxyl Group in Nucleosides and Nucleotides. *J. Am. Chem. Soc.* **2001**, *123* (12), 2893–2894. https://doi.org/10.1021/JA0036312/SUPPL_FILE/JA0036312_S.PDF.

(11) Velema, W. A.; Kool, E. T. The Chemistry and Applications of RNA 2′-OH Acylation. *Nat. Rev. Chem.* **2020**, *4* (1), 22–37. https://doi.org/10.1038/s41570-019-0147-6.

(12) Lee, B.; Flynn, R. A.; Kadina, A.; Guo, J. K.; Kool, E. T.; Chang, H. Y. Comparison of SHAPE Reagents for Mapping RNA Structures inside Living Cells. *RNA* **2017**, *23* (2), 169–174. https://doi.org/10.1261/RNA.058784.116.

(13) Spitale, R. C.; Crisalli, P.; Flynn, R. A.; Torre, E. A.; Kool, E. T.; Chang, H. Y. RNA SHAPE Analysis in Living Cells. *Nat. Chem. Biol.* **2013**, *9* (1), 18–20. https://doi.org/10.1038/nchembio.1131.

(14) Spitale, R. C.; Flynn, R. A.; Zhang, Q. C.; Crisalli, P.; Lee, B.; Jung, J.-W. W.; Kuchelmeister, H. Y.; Batista, P. J.; Torre, E. A.; Kool, E. T.; Chang, H. Y. Structural Imprints in Vivo Decode RNA Regulatory Mechanisms. *Nature* **2015**, *519* (7544), 486–490. https://doi.org/10.1038/nature14263.

(15) Flynn, R. A.; Zhang, Q. C.; Spitale, R. C.; Lee, B.; Mumbach, M. R.; Chang, H. Y. Transcriptome-Wide Interrogation of RNA Secondary Structure in Living Cells with IcSHAPE. *Nat. Protoc.* **2016**, *11* (2), 273–290. https://doi.org/10.1038/nprot.2016.011.

(16) Mortimer, S. A.; Weeks, K. M. A Fast-Acting Reagent for Accurate Analysis of RNA Secondary

and Tertiary Structure by SHAPE Chemistry. *J. Am. Chem. Soc.* **2007**, *129* (14), 4144–4145. https://doi.org/10.1021/JA0704028/SUPPL_FILE/JA0704028SI20070301_105055.PDF.

(17) McKay, C. S.; Blake, J. A.; Cheng, J.; Danielson, D. C.; Pezacki, J. P. Strain-Promoted Cycloadditions of Cyclic Nitrones with Cyclooctynes for Labeling Human Cancer Cells. *Chem. Commun.* **2011**, *47* (36), 10040–10042. https://doi.org/10.1039/c1cc13808a.

(18) Bilodeau, D. A. D. A.; Margison, K. D. K. D.; Serhan, M.; Pezacki, J. P. J. P. Bioorthogonal Reactions Utilizing Nitrones as Versatile Dipoles in Cycloaddition Reactions. *Chem. Rev.* **2021**, *121* (12), 6699–6717. https://doi.org/10.1021/acs.chemrev.0c00832.

(19) MacKenzie, D. A.; Sherratt, A. R.; Chigrinova, M.; Kell, A. J.; Pezacki, J. P. Bioorthogonal Labelling of Living Bacteria Using Unnatural Amino Acids Containing Nitrones and a Nitrone Derivative of Vancomycin. *Chem. Commun.* **2015**, *51* (62), 12501–12504. https://doi.org/10.1039/c5cc04901f.

(20) Mackenzie, D. A.; Pezacki, J. P. Kinetics Studies of Rapid Strain-Promoted [3+2] Cycloadditions of Nitrones with Bicyclo[6.1.0]Nonyne. *Can. J. Chem.* **2014**, *92* (4), 337–340. https://doi.org/10.1139/cjc-2013-0577.

(21) Margison, K. D.; Bilodeau, D. A.; Mahmoudi, F.; Pezacki, J. P. Cycloadditions of Trans-Cyclooctenes and Nitrones as Tools for Bioorthogonal Labelling. *ChemBioChem* **2020**, *21* (7), 948–951. https://doi.org/10.1002/CBIC.201900627.

Appendix A: Kinetic Analysis for Chapter 2

Preliminary Testing of Dipolarophiles

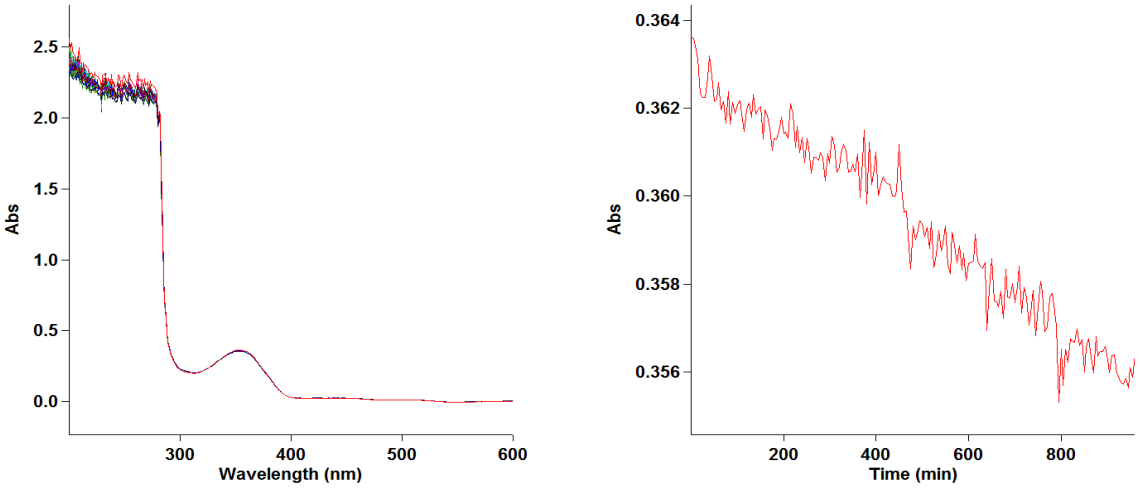

Figure 13: UV trace of the reaction between 1-methyl-3-oxidopyridinium and phenylacetylene in Kinugasa reaction conditions. The disappearance of the absorbance of the pyridinium was tracked over time at wavelength 365 nm.

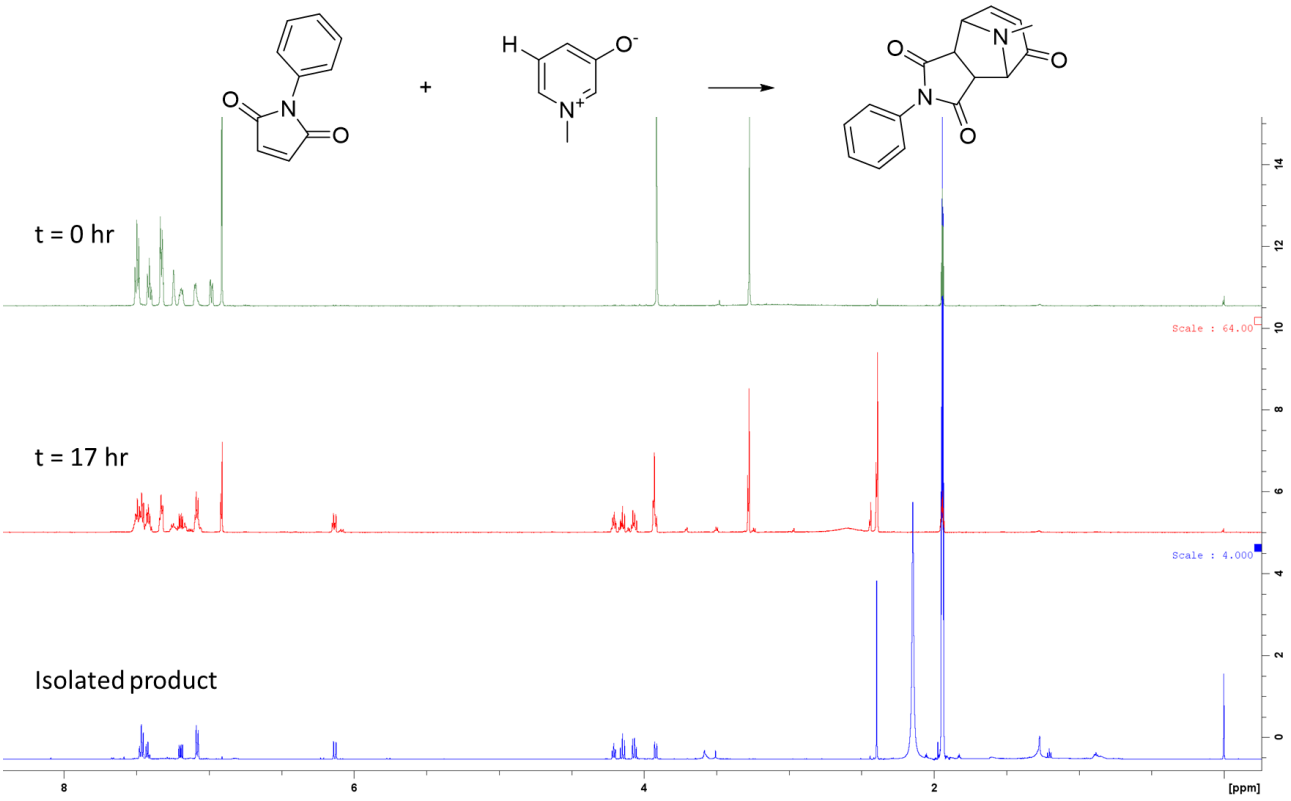

Figure 14: NMR kinetic experiment (d_3 – AcN, 600 MHz) of N-phenylmaleimide and 1-methyl-3-oxidopyridinium at t = 0 hr and t = 17 hr along with the isolated product after product purification.

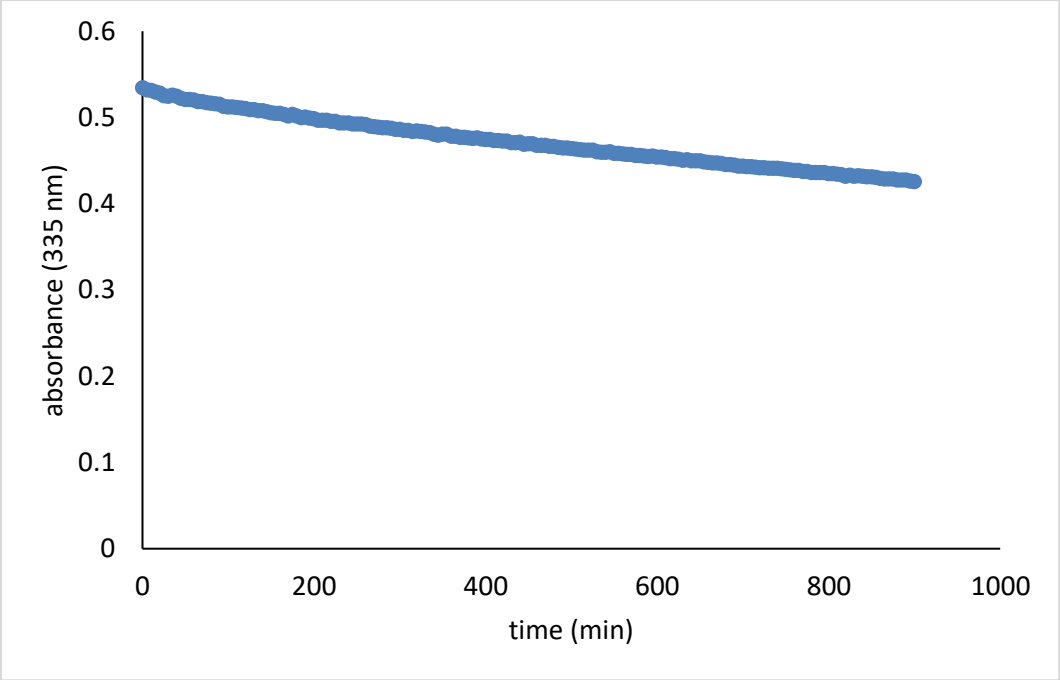

Figure 15: Disappearance of absorbance of 1-methyl-3-oxidopyridinium when reacted with BCN in 10% MeOH in AcN, tracked by UV vis spectroscopy.

UV-vis pseudo first-order kinetic analysis:

Table 3: Observed rate constants of the cycloadditions of DIBO with unsubstituted N-methyl-3-oxidopyridinium across a range of DIBO concentrations. Reaction conducted in acetonitrile at 25°C

[DIBO] (M)	[5-H NM3OXP] (μM)	k_{obs} (s^{-1})
0.01	100	5.85293E-05
0.008	100	5.06006E-05
0.006	100	4.29512E-05
0.004	100	3.64218E-05

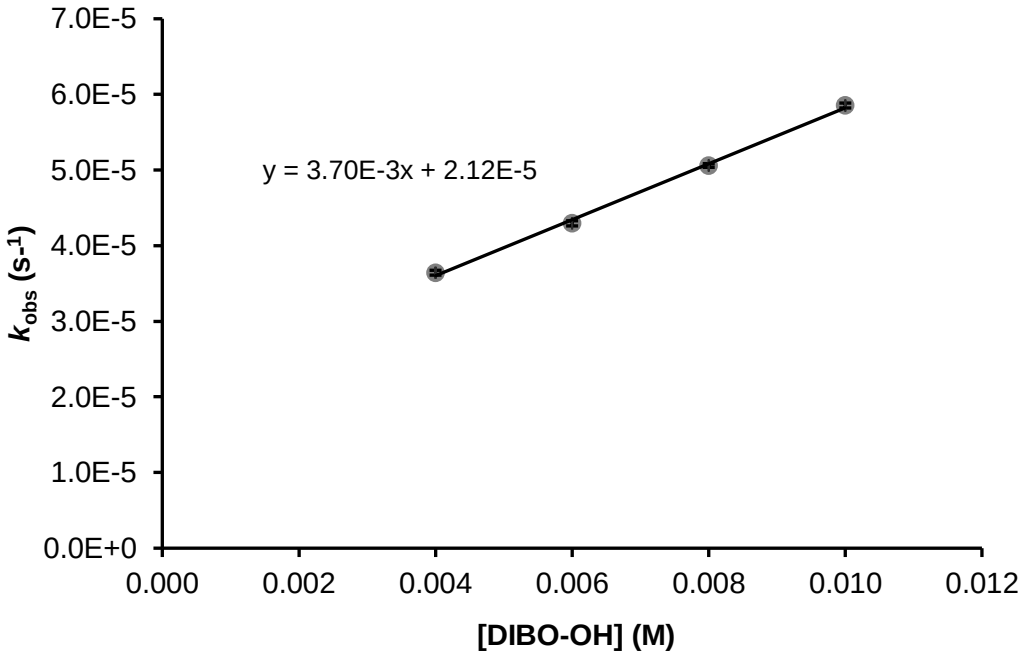

Figure 16: Plot of observed rate constants of the cycloadditions of DIBO with unsubstituted N-methyl-3-oxidopyridinium as a function of DIBO concentration. The slope indicates the reaction rate constant k_2 ($M^{-1}s^{-1}$). R^2 = 0.9981.

Table 4: Observed rate constants of the cycloadditions of DIBO with 5-OMe-N-methyl-3-oxidopyridinium across a range of DIBO concentrations. Reaction conducted in acetonitrile at 25°C

[DIBO] (M)	[5-OMe NM3OXP] (μM)	k_{obs} (s^{-1})
0.01	100	0.005492692
0.008	100	0.004522069
0.006	100	0.003494269
0.004	100	0.002458717

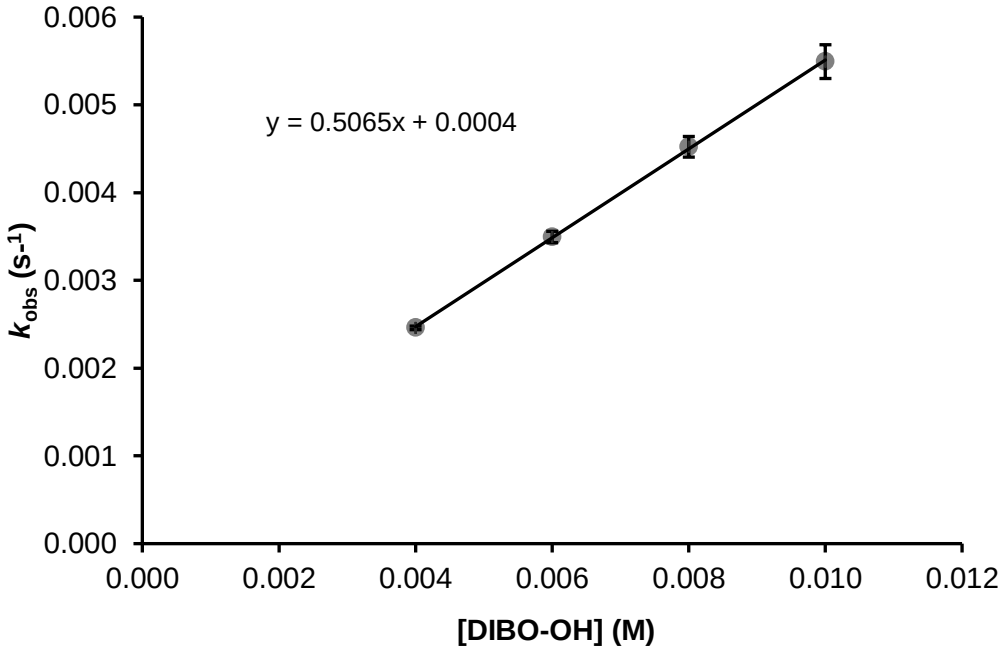

Figure 17: Plot of observed rate constants of the cycloadditions of DIBO with 5-OMe-N-methyl-3-oxidopyridinium as a function of DIBO concentration. The slope indicates the reaction rate constant k_2 ($M^{-1}s^{-1}$). R^2 = 0.9998.

Table 5: Observed rate constants of the cycloadditions of DIBO with 5-NH_2-N-methyl-3-oxidopyridinium across a range of DIBO concentrations. Reaction conducted in acetonitrile at 25°C

[DIBO] (M)	[5-NH_2 NM3OXP] (μM)	k_{obs} (s^{-1})
0.01	100	0.012079784
0.008	100	0.010015418
0.006	100	0.008058713
0.004	100	0.005579809

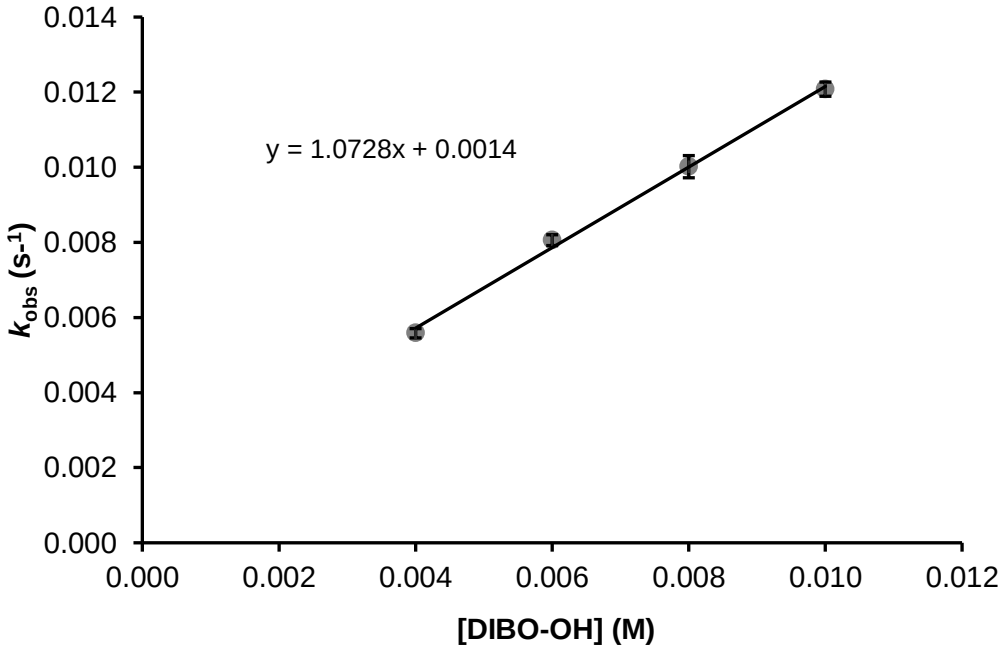

Figure 18: Plot of observed rate constants of the cycloadditions of DIBO with 5-NH_2-N-methyl-3-oxidopyridinium as a function of DIBO concentration. The slope indicates the reaction rate constant k_2 ($M^{-1}s^{-1}$). R^2 = 0.9973.

Table 6: Observed rate constants of the cycloadditions of DIBO with 5-OH-N-methyl-3-oxidopyridinium across a range of DIBO concentrations. Reaction conducted in acetonitrile at 25°C

[DIBO] (M)	[5-OH NM3OXP] (μM)	k_{obs} (s^{-1})
0.0125	100	0.00210225
0.01	100	0.00168335
0.0075	100	0.001265326
0.005	100	0.000872564

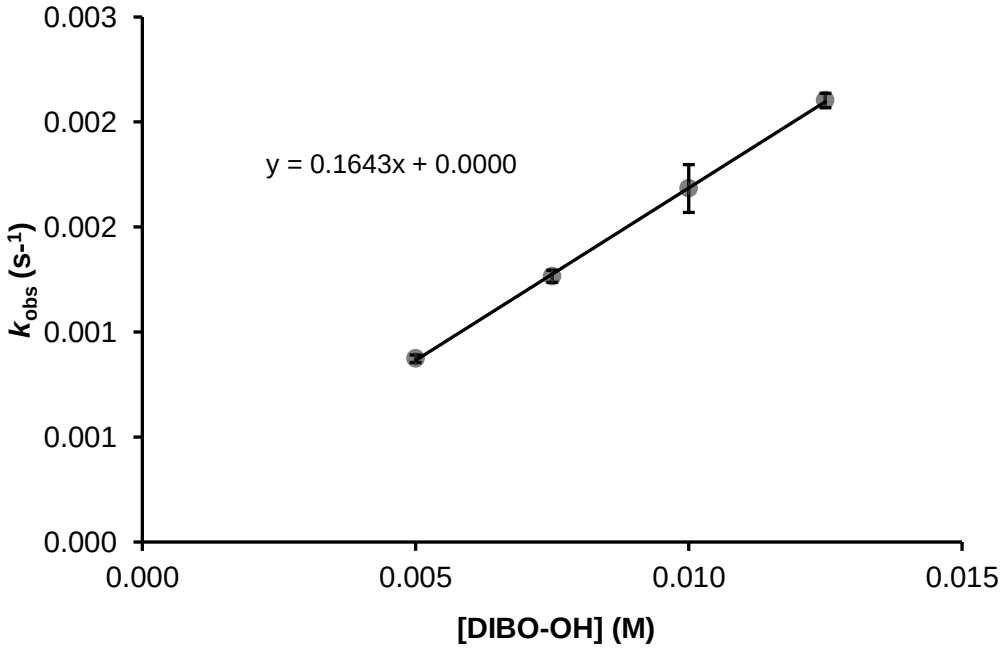

Figure 19: Plot of observed rate constants of the cycloadditions of DIBO with 5-OH-N-methyl-3-oxidopyridinium as a function of DIBO concentration. The slope indicates the reaction rate constant k_2 ($M^{-1}s^{-1}$). R^2 = 0.9998.

Table 7: Observed rate constants of the cycloadditions of DIBO with 5-CF_3-N-methyl-3-oxidopyridinium across a range of DIBO concentrations. Reaction conducted in acetonitrile at 25°C

[DIBO] (M)	[5-CF_3 NM3OXP] (μM)	k_{obs} (s^{-1})
0.025	100	3.66191E-05
0.02	100	3.48911E-05
0.015	100	3.35501E-05
0.01	100	3.15556E-05

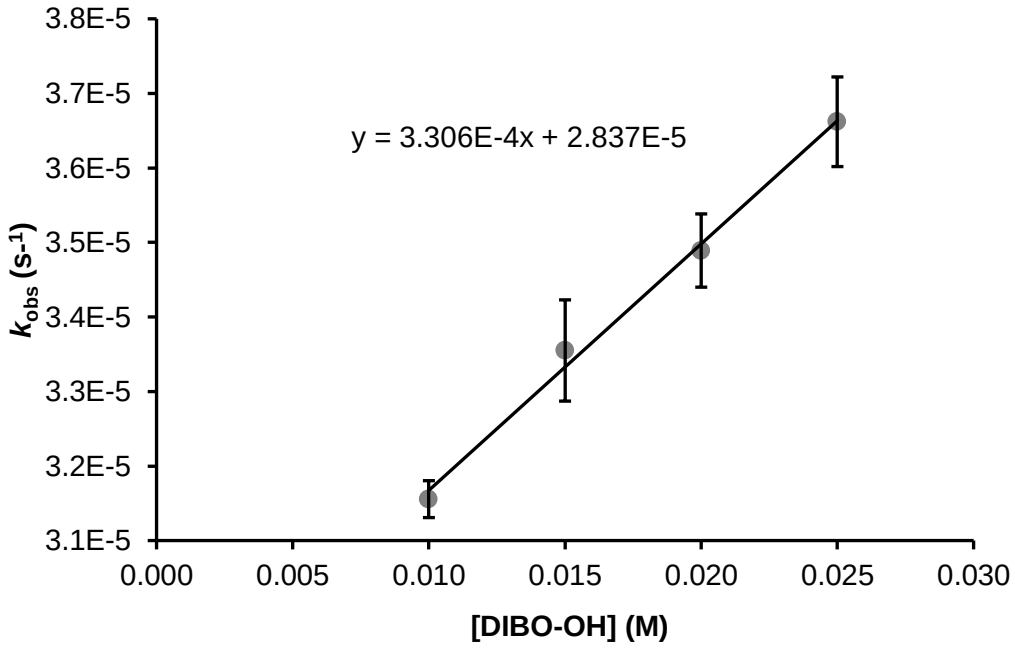

Figure 20: Plot of observed rate constants of the cycloadditions of DIBO with 5-CF_3-N-methyl-3-oxidopyridinium as a function of DIBO concentration. The slope indicates the reaction rate constant k_2 ($M^{-1}s^{-1}$). R^2 = 0.9948.

Table 8: Observed rate constants of the cycloadditions of DIBO with 5-Cl-N-methyl-3-oxidopyridinium across a range of DIBO concentrations. Reaction conducted in acetonitrile at 25°C

[DIBO] (M)	[5-Cl NM3OXP] (μM)	k_{obs} (s^{-1})
0.01	100	0.000150447
0.0075	100	0.0001148
0.005	100	8.09175E-05
0.0025	100	5.09341E-05

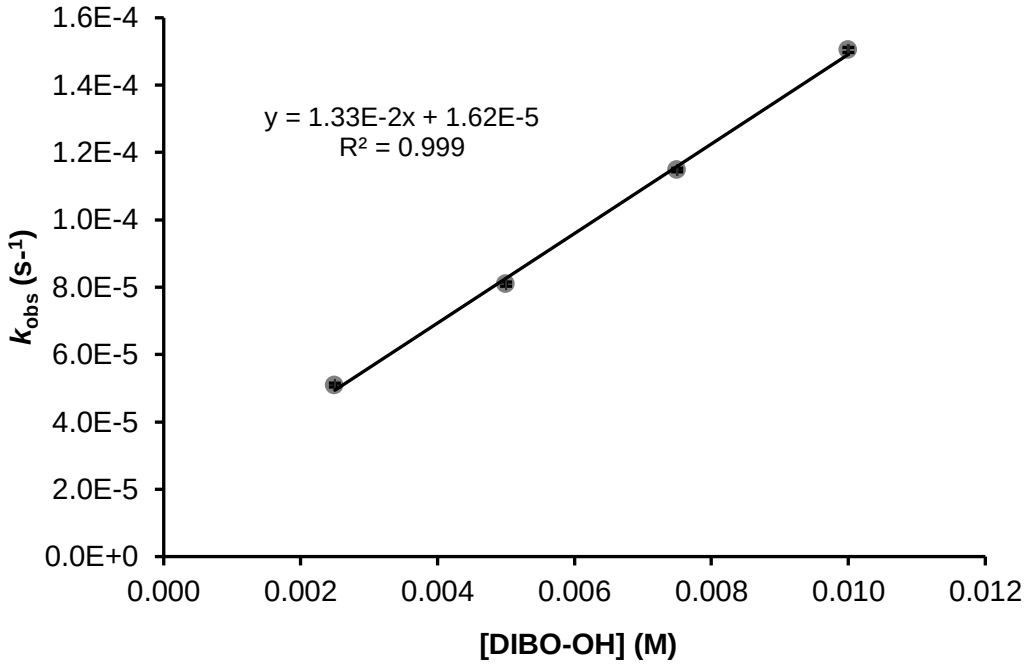

Figure 21: Plot of observed rate constants of the cycloadditions of DIBO with 5-Cl-N-methyl-3-oxidopyridinium as a function of DIBO concentration. The slope indicates the reaction rate constant k_2 ($M^{-1}s^{-1}$). R^2 = 0.9985

Table 9: Observed rate constants of the cycloadditions of DIBO with 5-CH_3-N-methyl-3-oxidopyridinium across a range of DIBO concentrations. Reaction conducted in acetonitrile at 25°C

[DIBO] (M)	[5-CH_3 NM3OXP] (μM)	k_{obs} (s^{-1})
0.0125	100	0.000129514
0.01	100	0.000103794
0.0075	100	8.47189E-05
0.005	100	6.21828E-05

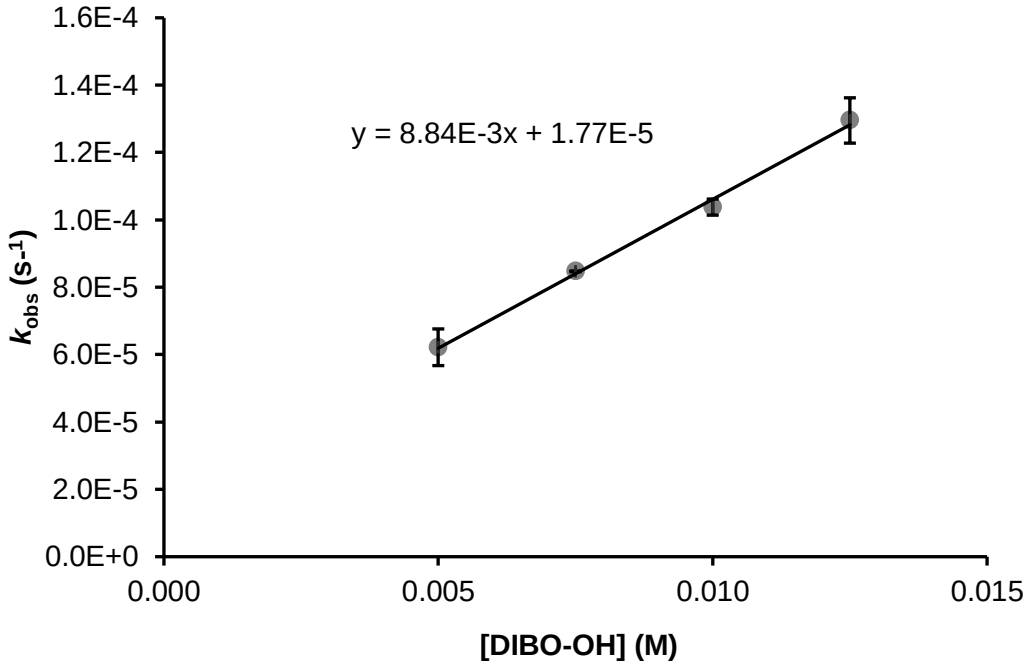

Figure 22: Plot of observed rate constants of the cycloadditions of DIBO with 5-CH_3-N-methyl-3-oxidopyridinium as a function of DIBO concentration. The slope indicates the reaction rate constant k_2 ($M^{-1}s^{-1}$). R^2 = 0.9969

Table 10: Observed rate constants of the cycloadditions of BCN with 5-NO_2-N-methyl-3-oxidopyridinium across a range of BCN concentrations. Reaction conducted in acetonitrile at 25°C

[BCN] (M)	[5-NO_2 NM3OXP] (μM)	k_{obs} (s^{-1})
0.0125	100	0.000274264
0.01	100	0.000231631
0.0075	100	0.000197621
0.005	100	0.000137705

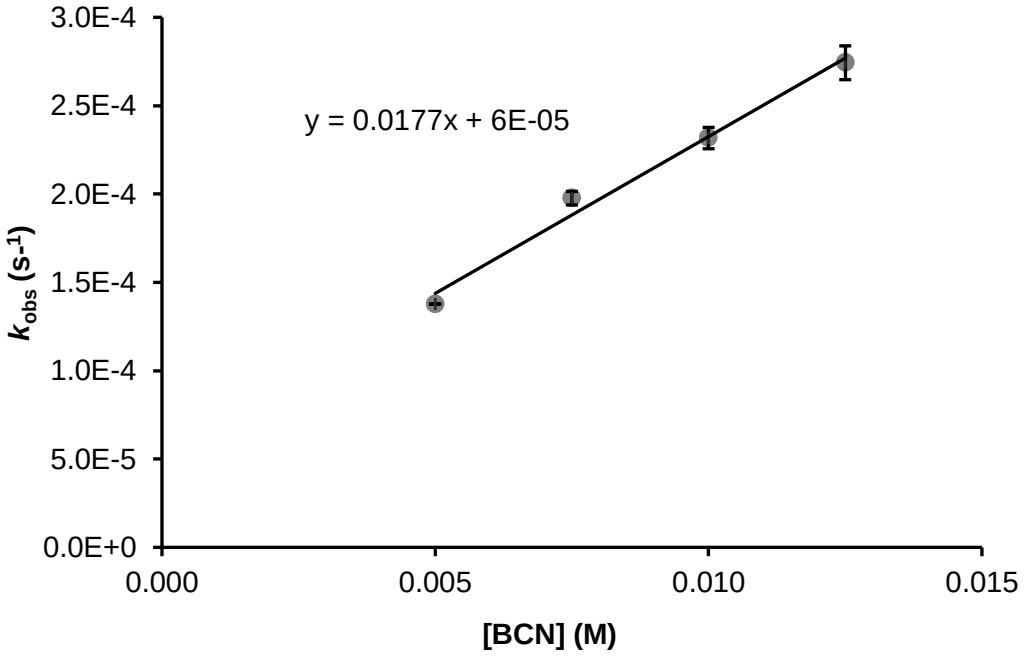

Figure 23: Plot of observed rate constants of the cycloadditions of BCN with 5-NO_2-N-methyl-3-oxidopyridinium as a function of BCN concentration. The slope indicates the reaction rate constant k_2 ($M^{-1}s^{-1}$). R^2 = 0.9865

^{13}C NMR shifts of 5-substituted 3-oxidopyridiniums as a function of sigma values for Hammett plots

5-Substituent	σ^+	*C2* ^{13}C *ppm*	*C3* ^{13}C *ppm*	*C4* ^{13}C *ppm*	*C5* ^{13}C *ppm*	*C6* ^{13}C *ppm*	*N-methyl* ^{13}C *ppm*
CF_3	0.61	139.36	168.87	130.54	128.68	130.76	48.16
CH_3	-0.31	133.41	169.4	124.59	138.13	133.03	47.29
Cl	0.11	135.38	169.42	131.63	134.32	131.8	47.65
H	0	135.25	169.48	133	127.43	124.15	47.5
NH_2	-1.3	127.88	169.66	115.45	149.12	112.29	47.96
NO_2	0.79	141.05	168.96	125.67	148.6	119.18	48.53
OH	-0.92	127.17	158.13	117.98	158.13	127.17	49.3
OMe	-0.78	129.29	167.07	115.71	160.15	129.29	49.57

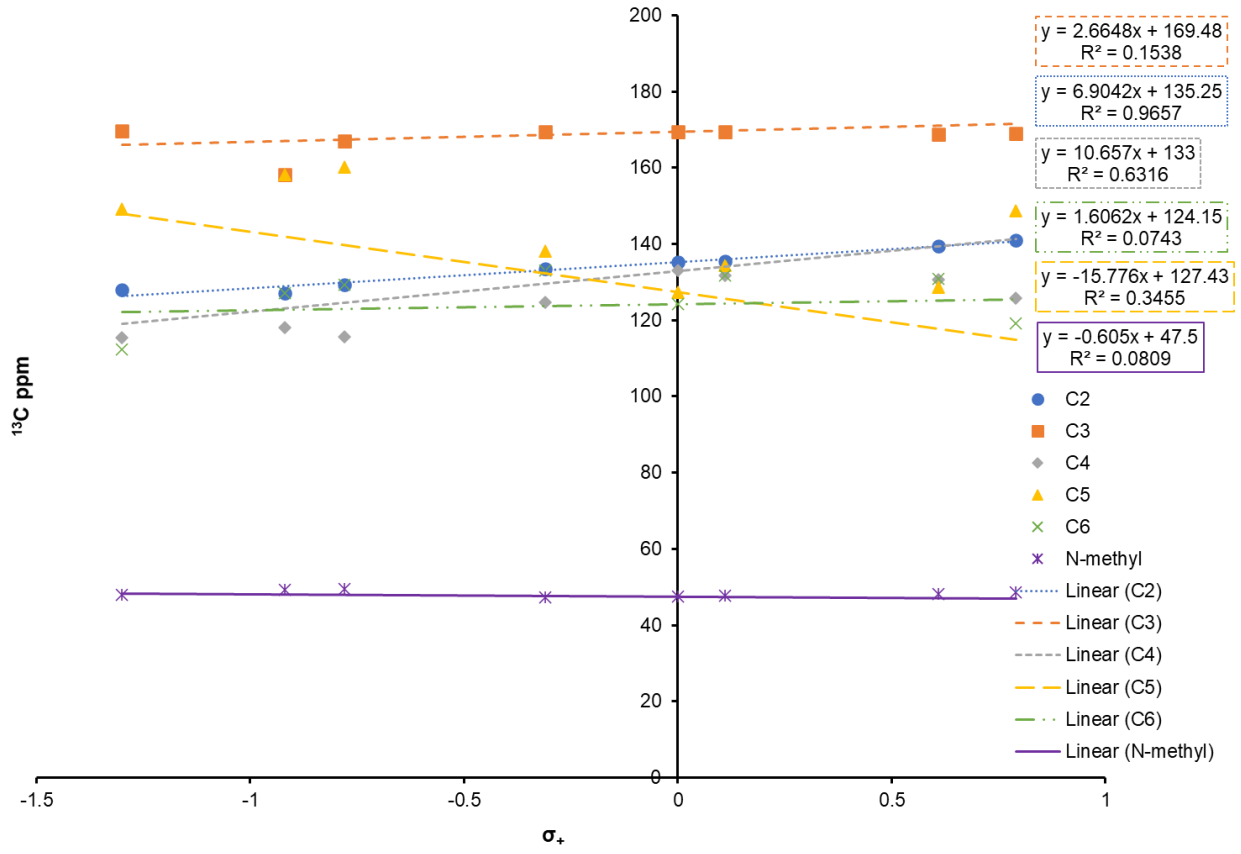

Figure 24: The linear trend between ^{13}C NMR chemical shifts and published σ^+. Graphs were plotted using Excel, and the y-intercept was set to the 13C ppm of the unsubstituted N-methyl-3-oxidopyridinium.

5-Substituent	σ_p	C2 ^{13}C ppm	C3 ^{13}C ppm	C4 ^{13}C ppm	C5 ^{13}C ppm	C6 ^{13}C ppm	N-methyl ^{13}C ppm
NH_2	-0.66	127.88	169.66	115.45	149.12	112.29	47.96
OH	-0.37	127.17	158.13	117.98	158.13	127.17	49.3
OMe	-0.268	129.29	167.07	115.71	160.15	129.29	49.57
CH_3	-0.17	133.41	169.4	124.59	138.13	133.03	47.29
H	0	135.25	169.48	133	127.43	124.15	47.5
Cl	0.227	135.38	169.42	131.63	134.32	131.8	47.65
CF_3	0.54	139.36	168.87	130.54	128.68	130.76	48.16
NO_2	0.778	141.05	168.96	125.67	148.6	119.18	48.53

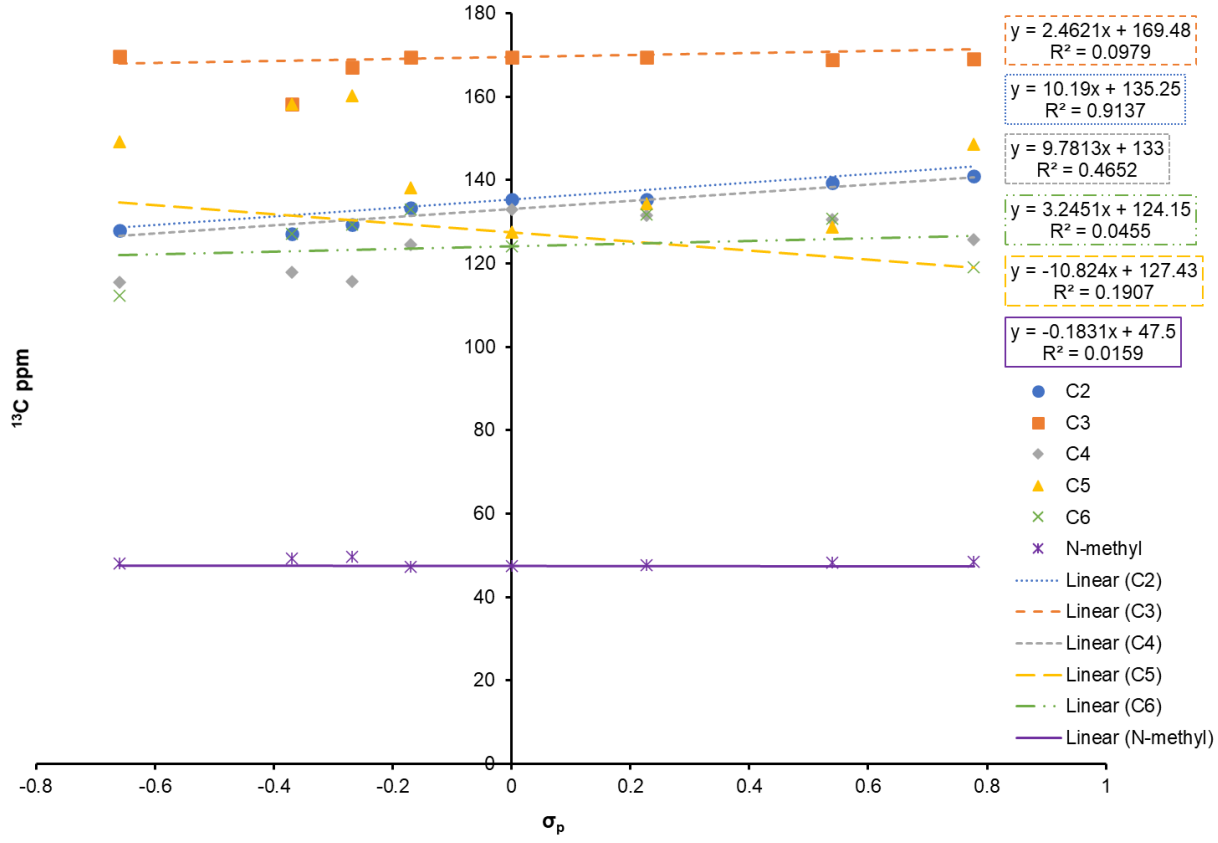

Figure 25: The linear trend between ^{13}C NMR chemical shifts and published σ_p. Graphs were plotted using Excel, and the y-intercept was set to the ^{13}C ppm of the unsubstituted N-methyl-3-oxidopyridinium.

5-Substituent	σ_R	C2 ^{13}C ppm	C3 ^{13}C ppm	C4 ^{13}C ppm	C5 ^{13}C ppm	C6 ^{13}C ppm	N-methyl ^{13}C ppm
CF_3	0.11	139.36	168.87	130.54	128.68	130.76	48.16
CH_3	-0.16	133.41	169.4	124.59	138.13	133.03	47.29
Cl	-0.25	135.38	169.42	131.63	134.32	131.8	47.65
H	0	135.25	169.48	133	127.43	124.15	47.5
NH_2	-0.8	127.88	169.66	115.45	149.12	112.29	47.96
NO_2	0.1	141.05	168.96	125.67	148.6	119.18	48.53
OH	-0.62	127.17	158.13	117.98	158.13	127.17	49.3
OMe	-0.58	129.29	167.07	115.71	160.15	129.29	49.57

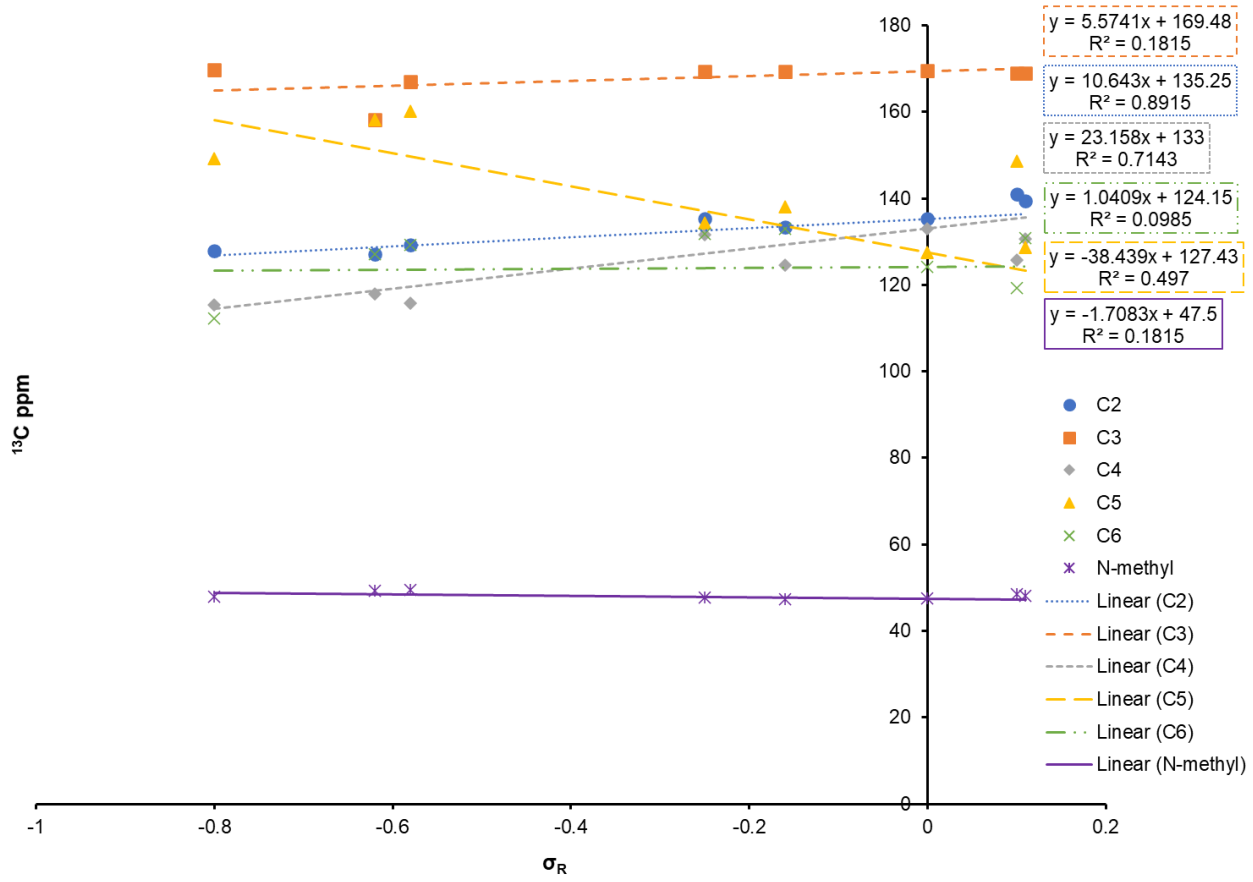

Figure 26: The linear trend between ^{13}C NMR chemical shifts and published σ_R. Graphs were plotted using Excel, and the y-intercept was set to the ^{13}C ppm of the unsubstituted N-methyl-3-oxidopyridinium.

5-Substituent	σ⁻	C2 ^{13}C ppm	C3 ^{13}C ppm	C4 ^{13}C ppm	C5 ^{13}C ppm	C6 ^{13}C ppm	N-methyl ^{13}C ppm
NO_2	1.27	141.05	168.96	125.67	148.6	119.18	48.53
CF_3	0.65	139.36	168.87	130.54	128.68	130.76	48.16
Cl	0.19	135.38	169.42	131.63	134.32	131.8	47.65
H	0	135.25	169.48	133	127.43	124.15	47.5
CH_3	-0.17	133.41	169.4	124.59	138.13	133.03	47.29
OMe	-0.26	129.29	167.07	115.71	160.15	129.29	49.57
NH_2	-0.15	127.88	169.66	115.45	149.12	112.29	47.96
OH	-0.37	127.17	158.13	117.98	158.13	127.17	49.3

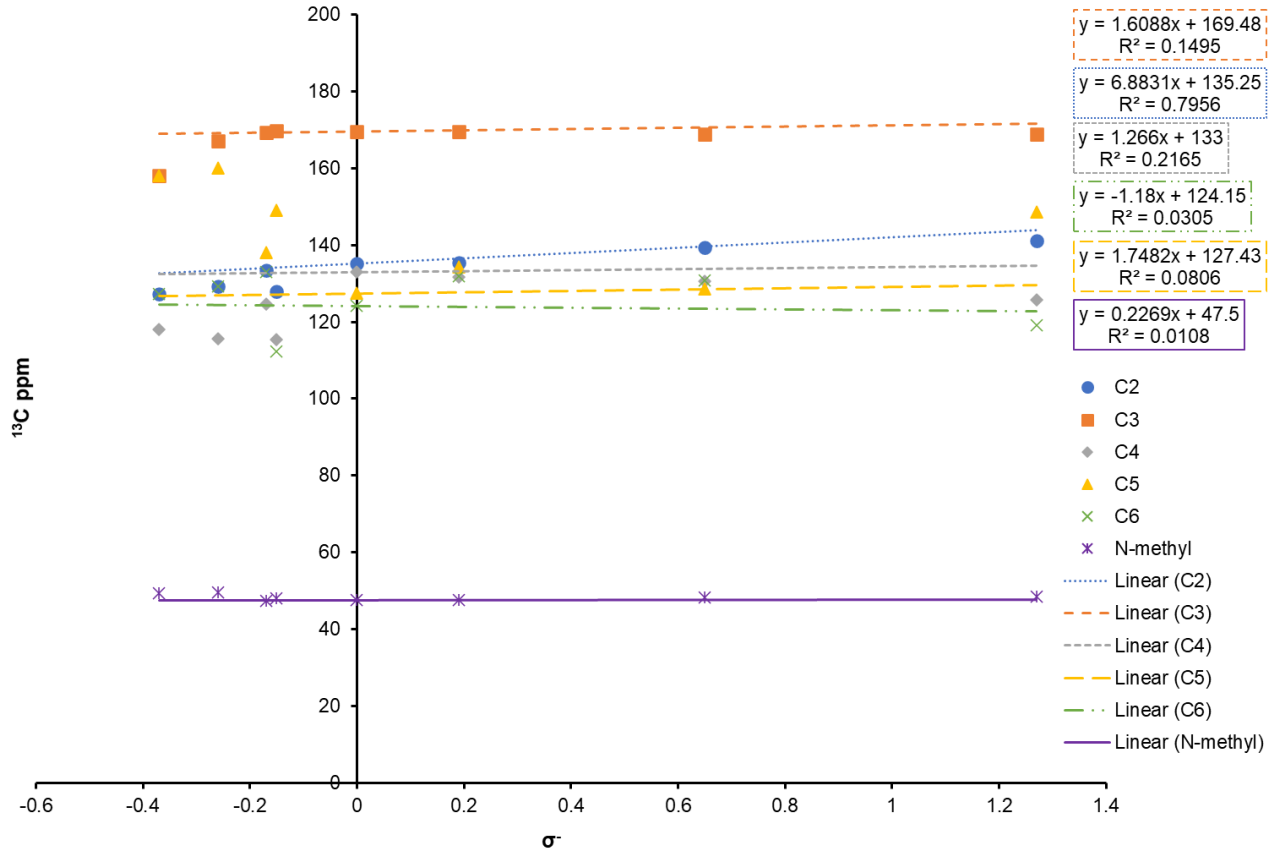

Figure 27: The linear trend between ^{13}C NMR chemical shifts and published σ⁻. Graphs were plotted using Excel, and the y-intercept was set to the ^{13}C ppm of the unsubstituted N-methyl-3-oxidopyridinium.

5-Substituent	σ_m	C2 ^{13}C ppm	C3 ^{13}C ppm	C4 ^{13}C ppm	C5 ^{13}C ppm	C6 ^{13}C ppm	N-methyl ^{13}C ppm
OH	0.12	127.17	158.13	117.98	158.13	127.17	49.3
NH_2	-0.161	127.88	169.66	115.45	149.12	112.29	47.96
OMe	0.115	129.29	167.07	115.71	160.15	129.29	49.57
CH_3	-0.069	133.41	169.4	124.59	138.13	133.03	47.29
H	0	135.25	169.48	133	127.43	124.15	47.5
Cl	0.373	135.38	169.42	131.63	134.32	131.8	47.65
CF_3	0.43	139.36	168.87	130.54	128.68	130.76	48.16
NO_2	0.71	141.05	168.96	125.67	148.6	119.18	48.53

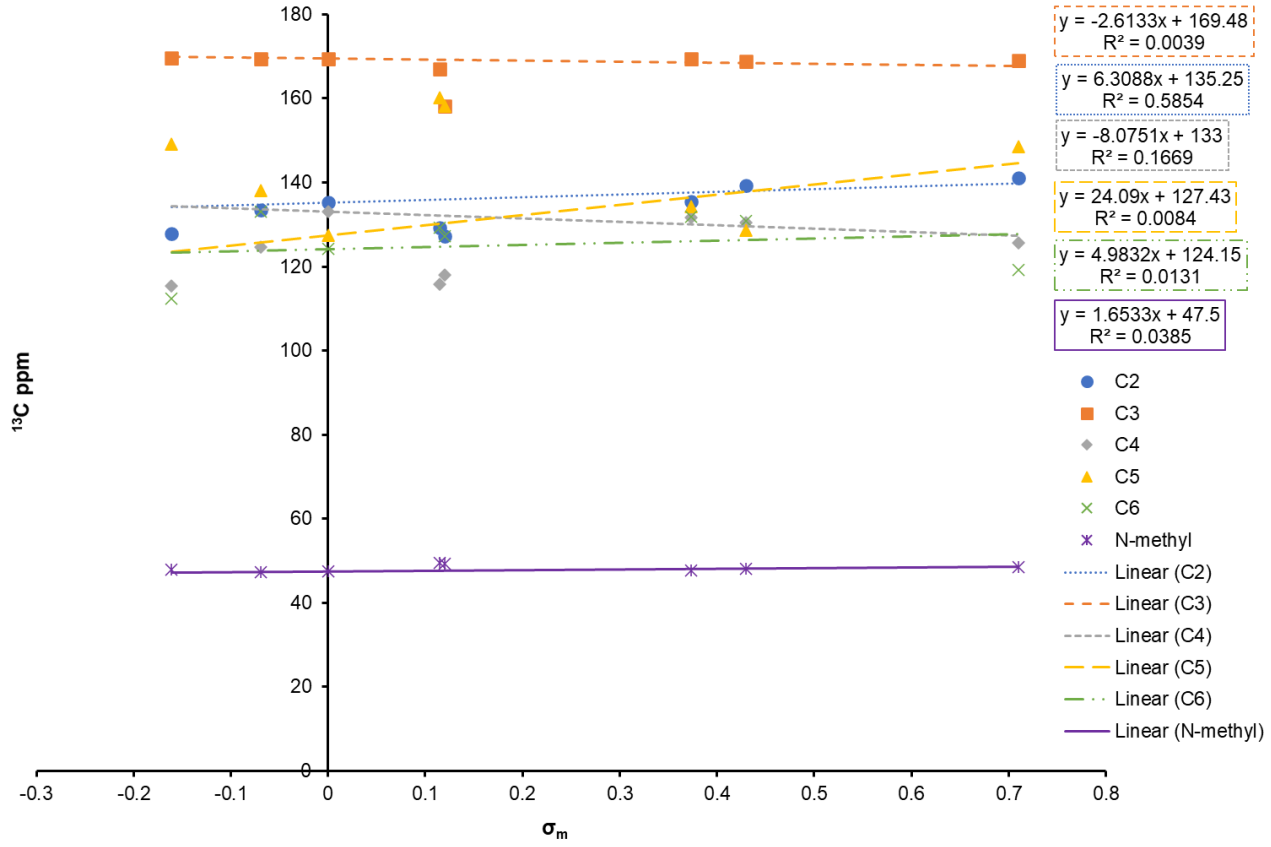

Figure 28: The linear trend between ^{13}C NMR chemical shifts and published σ_m. Graphs were plotted using Excel, and the y-intercept was set to the ^{13}C ppm of the unsubstituted N-methyl-3-oxidopyridinium.

5-Substituent	σ_I	C2 ^{13}C ppm	C3 ^{13}C ppm	C4 ^{13}C ppm	C5 ^{13}C ppm	C6 ^{13}C ppm	N-methyl ^{13}C ppm
NO_2	0.67	141.05	168.96	125.67	148.6	119.18	48.53
CF_3	0.4	139.36	168.87	130.54	128.68	130.76	48.16
Cl	0.47	135.38	169.42	131.63	134.32	131.8	47.65
H	0	135.25	169.48	133	127.43	124.15	47.5
CH_3	-0.01	133.41	169.4	124.59	138.13	133.03	47.29
OMe	0.3	129.29	167.07	115.71	160.15	129.29	49.57
NH_2	0.17	127.88	169.66	115.45	149.12	112.29	47.96
OH	0.24	127.17	158.13	117.98	158.13	127.17	49.3

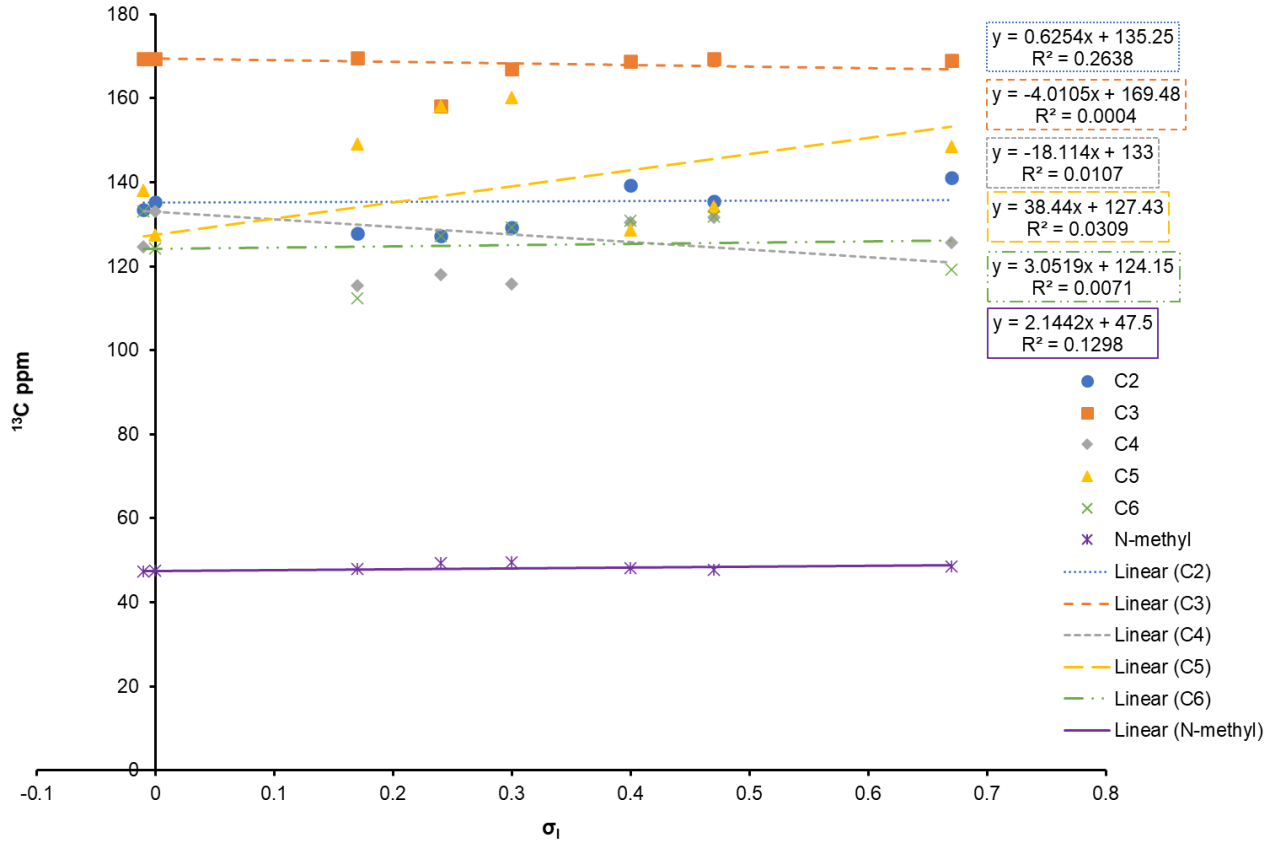

Figure 29: The linear trend between ^{13}C NMR chemical shifts and published σ_I. Graphs were plotted using Excel, and the y-intercept was set to the ^{13}C ppm of the unsubstituted N-methyl-3-oxidopyridinium.

*Table 11: Summary of slope and R^2 values of the linear trend between ^{13}C NMR chemical shifts and published sigma values. Graphs were plotted using Excel, and the y-intercept was set to the ^{13}C ppm of the unsubstituted N-methyl-3-oxidopyridinium. *The best correlation was identified based on the R^2 values and σ^+ was selected to construct the initial Hammett plot.*

	C_2		
σ	slope	R^2	Spearman correlation coefficient r_s
σ_m	6.31	0.584	0.6905
σ_p	10.19	0.914	0.9762
σ^+	6.90	0.966*	0.9762
σ^-	6.88	0.796	0.9286
σ_R	10.64	0.892	0.8810
σ_I	0.62	0.264	0.5952

Hammett Plots constructed using different sigma values:

5-Substituent	σ_R	k_2 (M^{-1} s^{-1})	k_x/k_H	$log(k_x/k_h)$
NH_2	-0.80	1.07	289.30	2.46134641
OMe	-0.58	0.506	136.81	2.13611315
OH	-0.62	0.163	44.07	1.64415024
Cl	-0.25	1.33E-02	3.60	0.55581428
CH_3	-0.16	8.84E-03	2.25	0.35260764
H	0	3.70E-03	1.00	0
CF_3	0.11	3.31E-04	0.09	-1.04869511

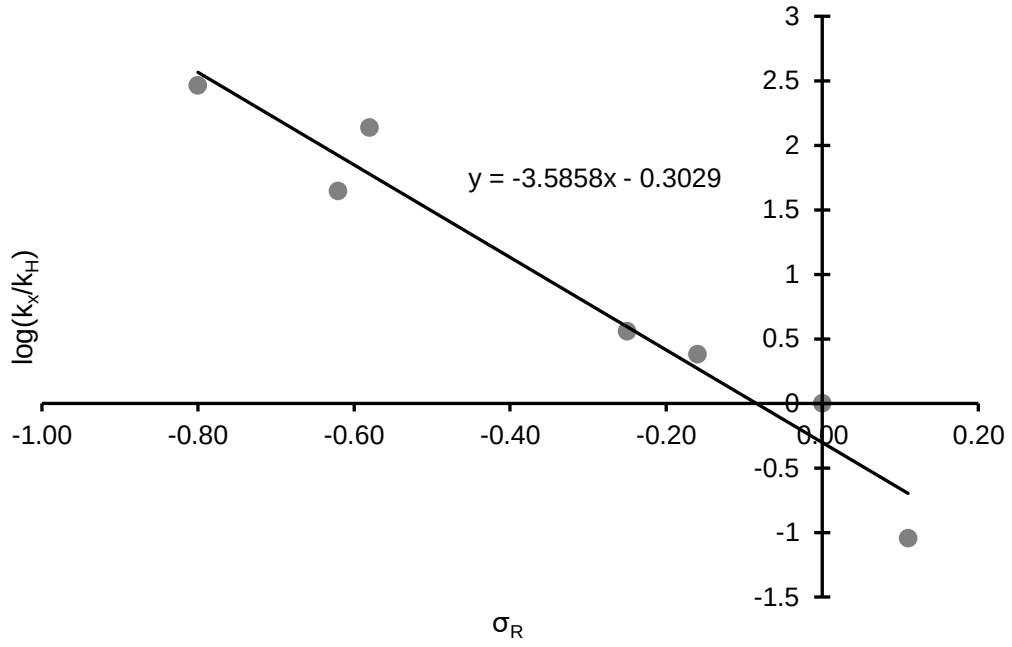

Figure 30: Hammett plot depicting substituent effects on the cycloadditions of 5-substituted-N-methyl-3-oxidopyridiniums with DIBO using σ_R constants. R^2= 0.9533

5-Substituent	σ^+	k_2 (M^{-1} s^{-1})	k_x/k_H	$log(k_x/k_h)$
NH_2	-1.30	1.07	289.30	2.46134641
OMe	-0.78	0.506	136.81	2.13611315
OH	-0.92	0.163	44.07	1.64415024
Cl	0.11	1.33E-02	3.60	0.55581428
CH_3	-0.31	8.84E-03	2.25	0.35260764
H	0	3.70E-03	1.00	0
CF_3	0.61	3.31E-04	0.09	-1.04869511

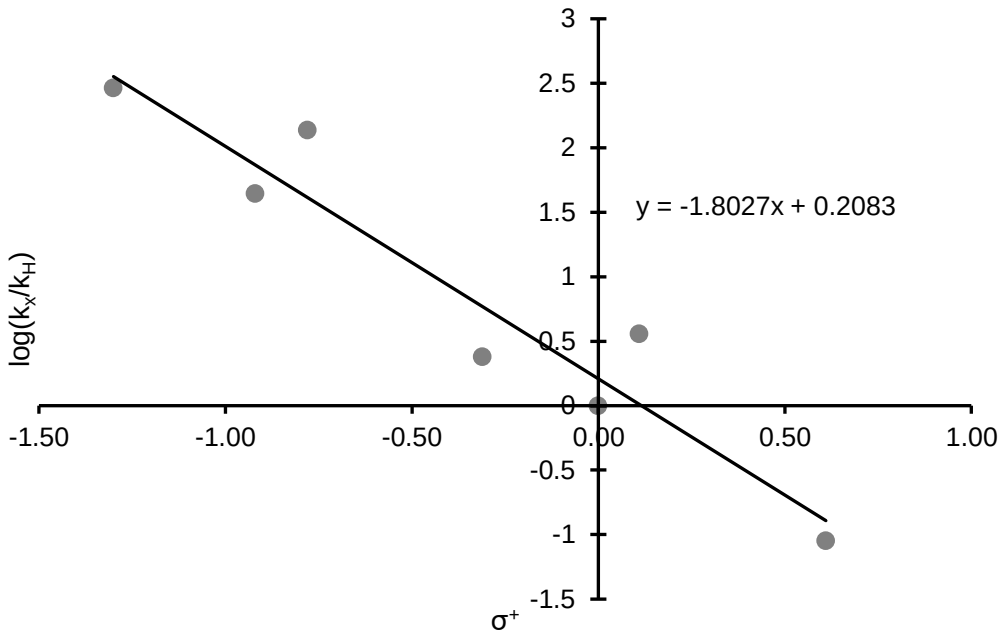

Figure 31: Hammett plot depicting substituent effects on the cycloadditions of 5-substituted-N-methyl-3-oxidopyridiniums with DIBO using σ^+ constants. R^2= 0.9110

5-Substituent	σ_p	k_2 (M^{-1} s^{-1})	k_x/k_H	$log(k_x/k_h)$
NH_2	-0.66	1.07	289.30	2.46134641
OMe	-0.27	0.506	136.81	2.13611315
OH	-0.37	0.163	44.07	1.64415024
Cl	0.23	1.33E-02	3.60	0.55581428
CH_3	-0.17	8.84E-03	2.25	0.35260764
H	0	3.70E-03	1.00	0
CF_3	0.54	3.31E-04	0.09	-1.04869511

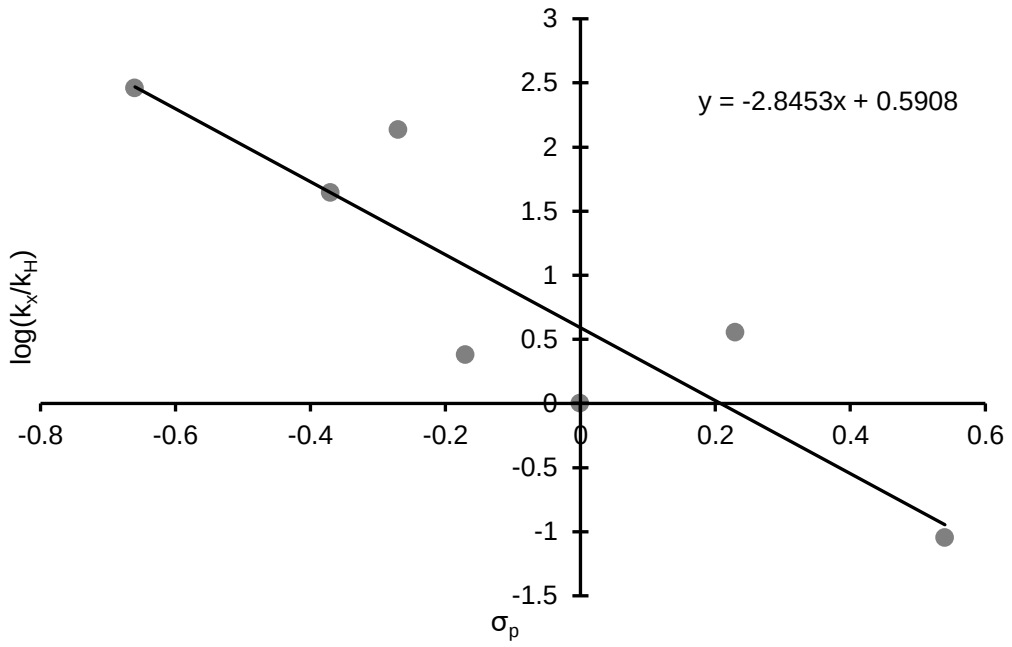

Figure 32: Hammett plot depicting substituent effects on the cycloadditions of 5-substituted-N-methyl-3-oxidopyridiniums with DIBO using σ_p constants. R^2= 0.8074.

5-Substituent	σ^-	k_2 (M^{-1} s^{-1})	k_x/k_H	$\log(k_x/k_h)$
NH_2	-0.15	1.07	289.30	2.46134641
OMe	-0.26	0.506	136.81	2.13611315
OH	-0.37	0.163	44.07	1.64415024
Cl	0.19	1.33E-02	3.60	0.55581428
CH_3	-0.17	8.84E-03	2.25	0.35260764
H	0	3.70E-03	1.00	0
CF_3	0.65	3.31E-04	0.09	-1.04869511

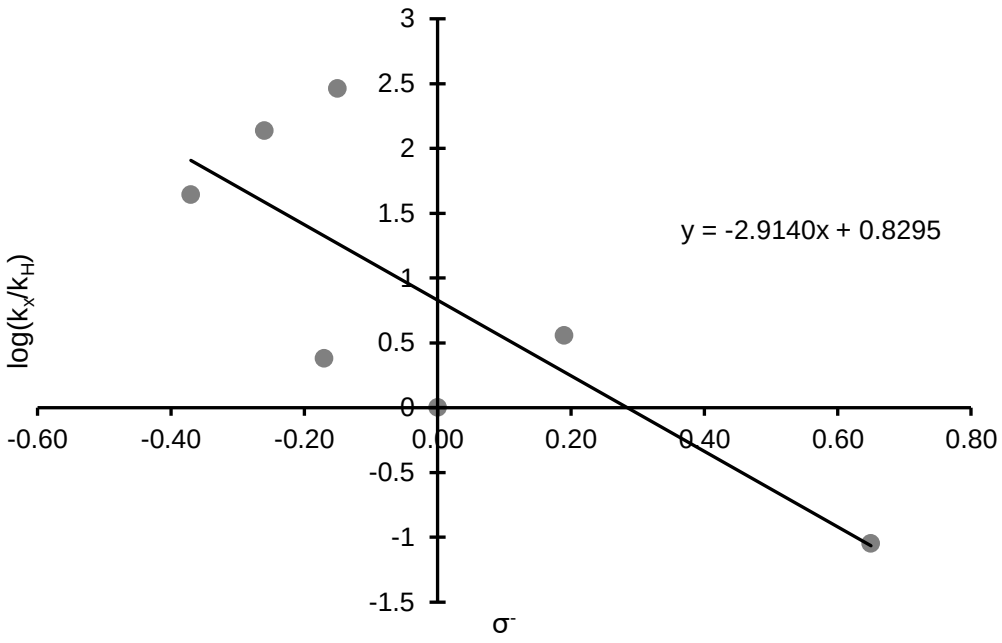

Figure 33: Hammett plot depicting substituent effects on the cycloadditions of 5-substituted-N-methyl-3-oxidopyridiniums with DIBO using σ^- constants. R^2= 0.6362.

5-Substituent	σ_m	k_2 (M^{-1} s^{-1})	k_x/k_H	$log(k_x/k_h)$
NH_2	-0.16	1.07	289.30	2.46134641
OMe	0.12	0.506	136.81	2.13611315
OH	0.12	0.163	44.07	1.64415024
Cl	0.37	1.33E-02	3.60	0.55581428
CH_3	-0.07	8.84E-03	2.25	0.35260764
H	0	3.70E-03	1.00	0
CF_3	0.43	3.31E-04	0.09	-1.04869511

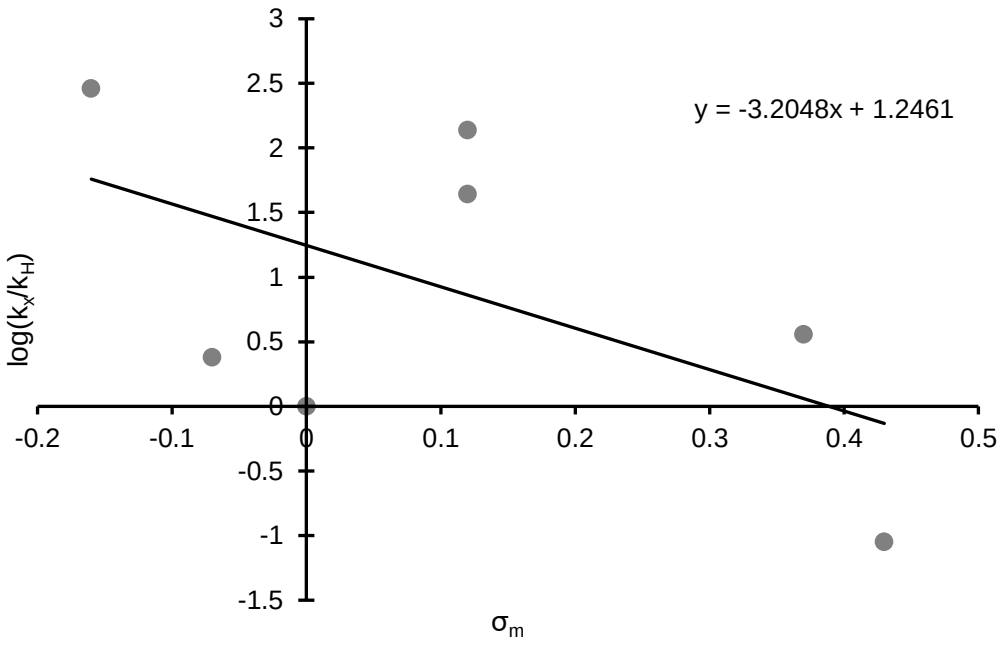

Figure 34: Hammett plot depicting substituent effects on the cycloadditions of 5-substituted-N-methyl-3-oxidopyridiniums with DIBO using σ_m constants. R^2= 0.3102.

5-Substituent	σ_I	k_2 (M^{-1} s^{-1})	k_x/k_H	$log(k_x/k_h)$
NH_2	0.17	1.07	289.30	2.46134641
OMe	0.30	0.506	136.81	2.13611315
OH	0.24	0.163	44.07	1.64415024
Cl	0.47	1.33E-02	3.60	0.55581428
CH_3	-0.01	8.84E-03	2.25	0.35260764
H	0	3.70E-03	1.00	0
CF_3	0.40	3.31E-04	0.09	-1.04869511

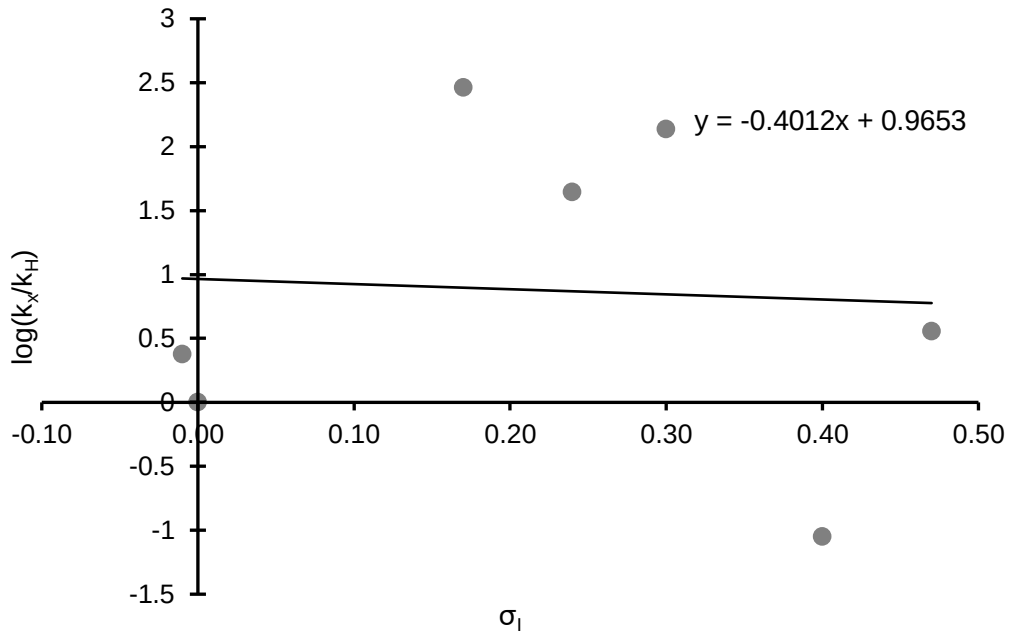

Figure 20: Hammett plot depicting substituent effects on the cycloadditions of 5-substituted-N-methyl-3-oxidopyridiniums with DIBO using σ_I constants. R^2= 0.0035.

Additional Computational Data Analysis:

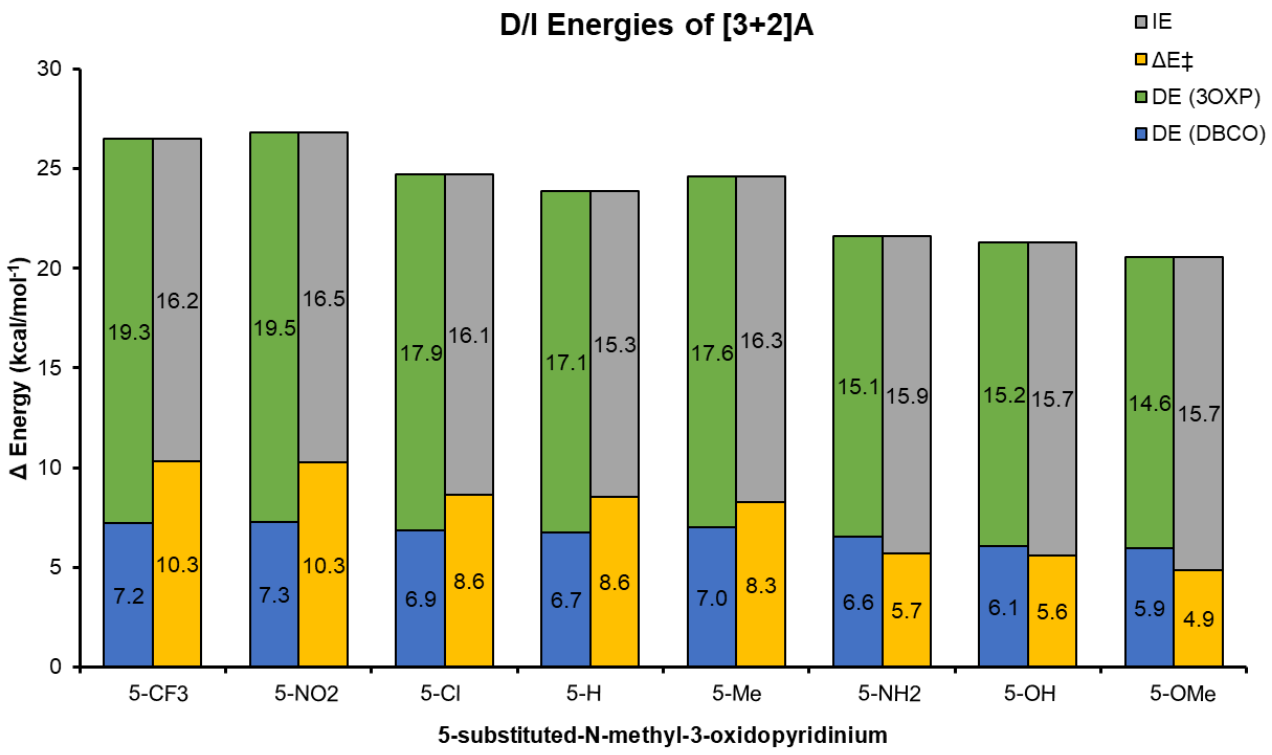

Figure 35: Calculated D/I energies of the [3+2]A cycloaddition of DIBO and 5-substituted 3-oxidopyridiniums.

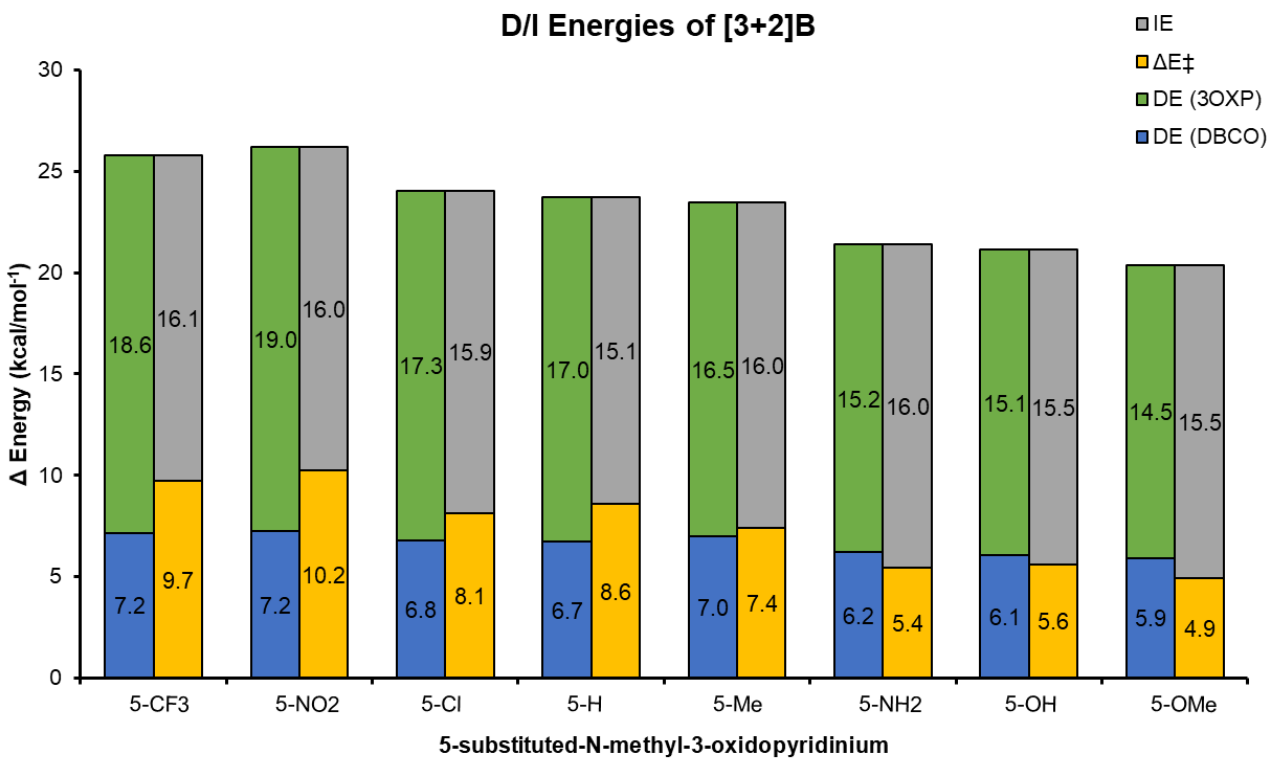

Figure 36: D/I energies of the [3+2]B cycloaddition of DIBO and 5-substituted 3-oxidopyridiniums.

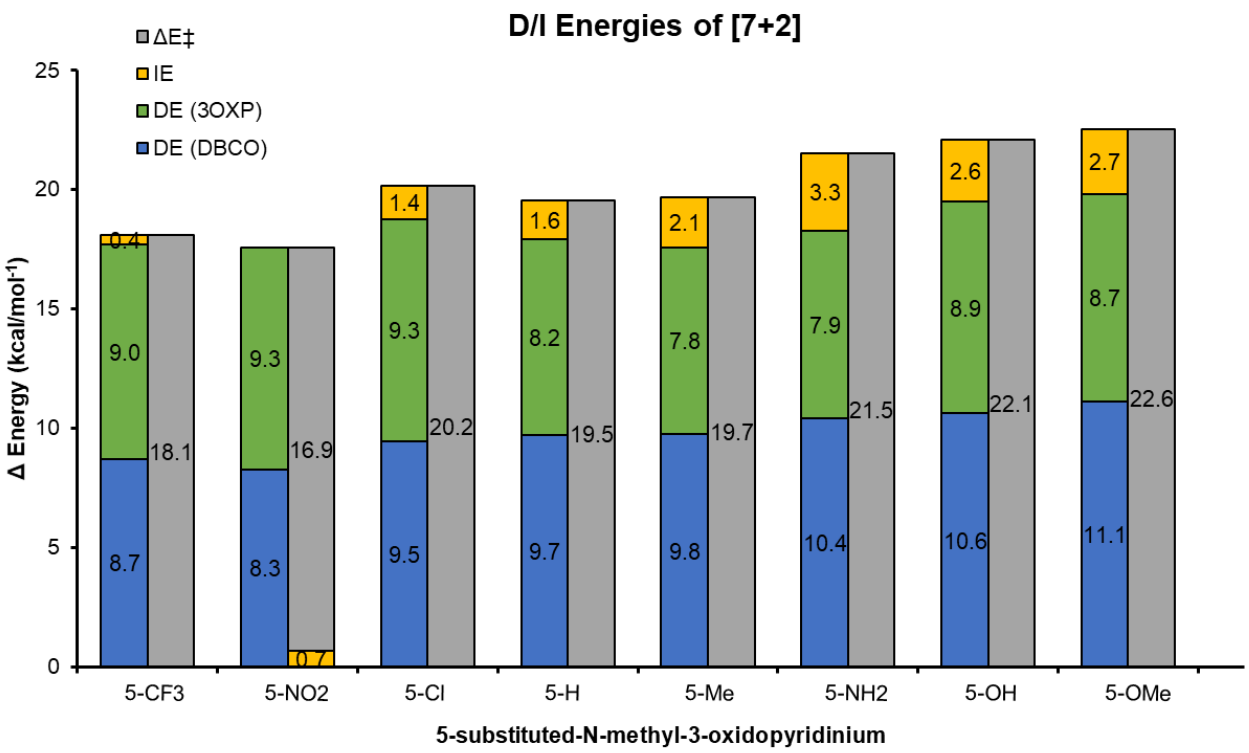

Figure 37: D/I energies of the [7+2] cycloaddition of DIBO and 5-substituted 3-oxidopyridiniums.

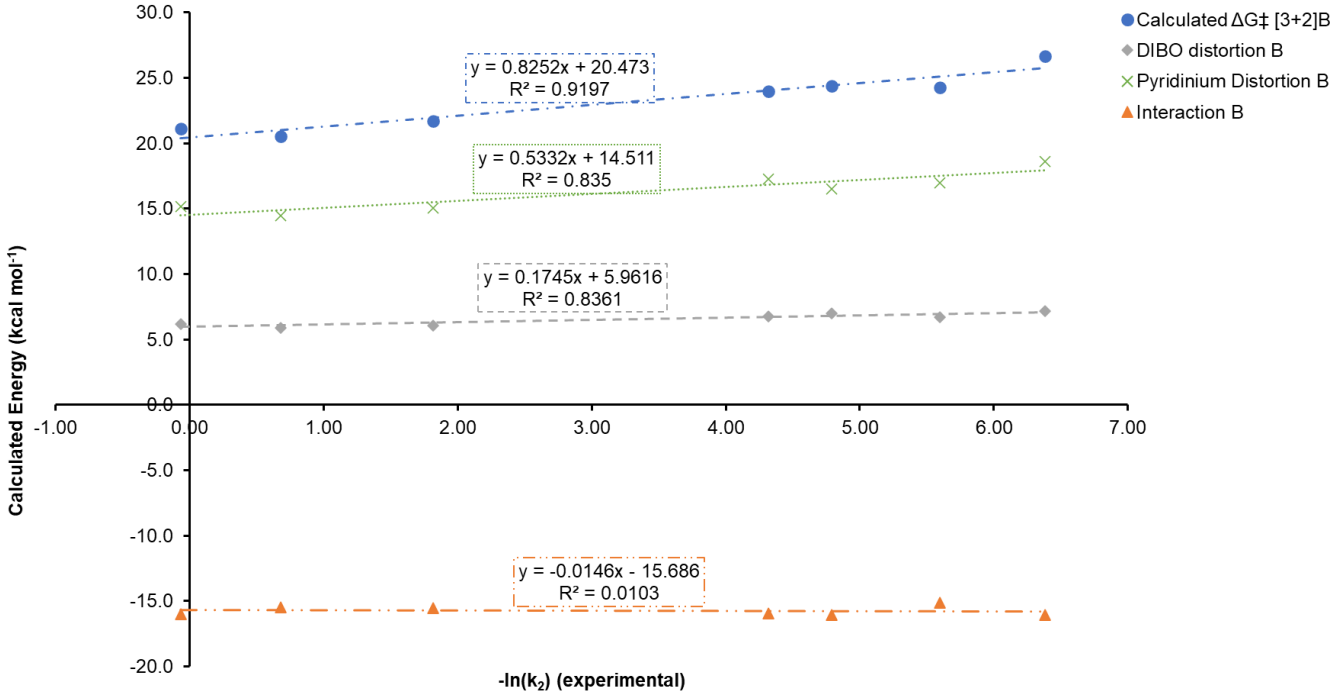

Figure 38: Calculated energies for [3+2]B cycloadditions as a function of -ln(k_2).

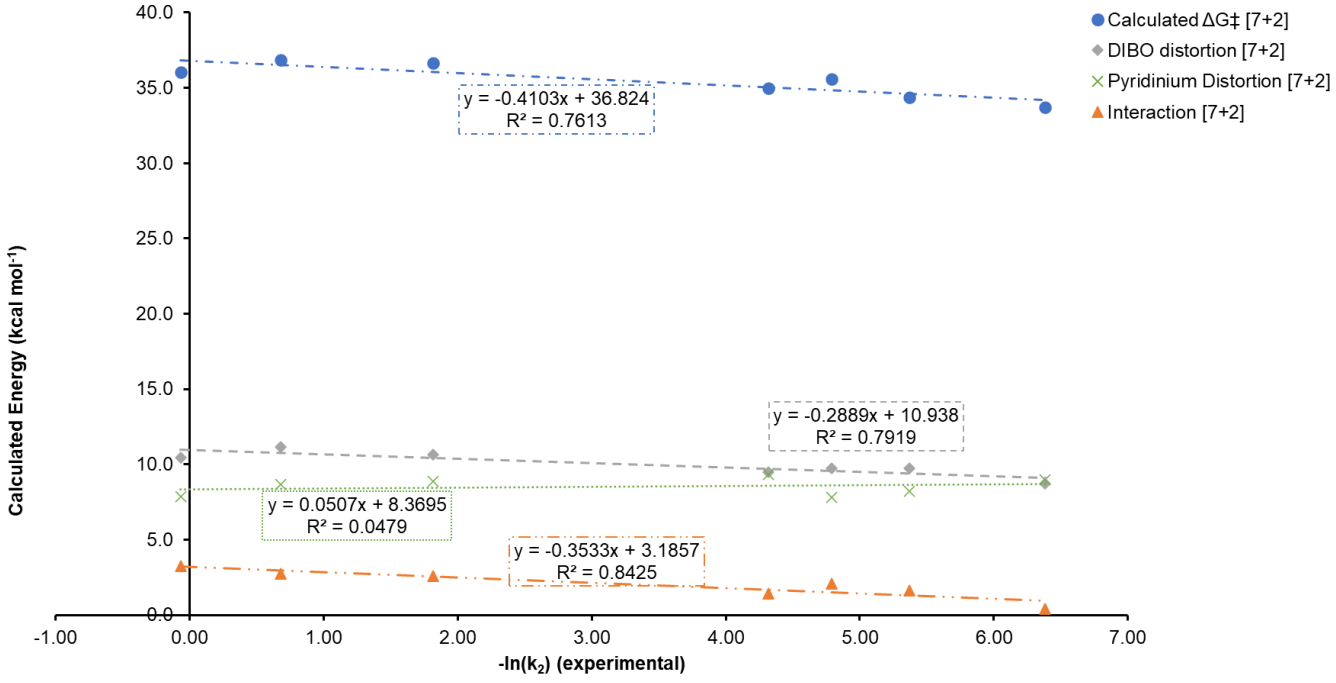

Figure 39: Calculated energies for [7+2] cycloadditions as a function of -ln(k_2).

Appendix B: Supplemental Data for Chapter 3

Table 0: Amounts used for in vitro labelling of a 21-mer GL2 guide strand RNA

Reagent (stock concentration)	***Conc.***	***Exp 1 amounts (µL)***	***Exp 2 amounts (µL)***	***Exp 3 amounts (µL)***	***Exp 4 amounts (µL)***
RNA (10 µM)	0.5 µM	2.5	0	2.5	2.5
Probe (100 µM)	0.5 µM	0.25	0.25	0	0.25
DIBO-Alexa 488 dye (10 µM)	**50 nM**	0.25	0.25	0.25	0
Buffer (10X)	1X	5	5	5	5
Water		42	44.5	42.25	42.25
RNA (10 µM)	0.5 µM	2.5	0	2.5	2.5
Probe (100 µM)	0.5 µM	0.25	0.25	0	0.25
DIBO-Alexa 488 dye (1 µM)	**25 nM**	1.25	1.25	1.25	0
Buffer (10X)	1X	5	5	5	5
Water		41	43.5	41.25	42.25
RNA (10 µM)	0.5 µM	2.5	0	2.5	2.5
Probe (100 µM)	0.5 µM	0.25	0.25	0	0.25
DIBO-Alexa 488 dye (100 nM)	**10 nM**	5	5	5	0
Buffer (10X)	1X	5	5	5	5
Water		37.25	37.75	37.5	42.25

Table 2: Amounts used for in vitro labelling of a 21-mer GL2 guide strand RNA functionalized by Cy3.

Reagent (stock concentration)	*Conc.*	*Exp 1 amounts (µL)*	*Exp 2 amounts (µL)*	*Exp 3 amounts (µL)*	*Exp 4 amounts (µL)*
Cy 3 RNA (0.2 µM)	0.01 µM	2.5	0	2.5	2.5
DMiMO-I probe (100 µM)	5 µM	2.5	2.5	0	2.5
DIBO-Alexa 488 dye (10 µM)	1 µM	5	5	5	0
Buffer (10X)	1X	5	5	5	5
Water		35	37.5	37.5	40
Cy 3 RNA (0.2 µM)	0.01 µM	2.5	0	2.5	2.5
NAI probe (100 µM)	5 µM	2.5	2.5	0	2.5
DIBO-Alexa 488 dye (10 µM)	1 µM	5	5	5	0
Buffer (10X)	1X	5	5	5	5
Water		35	37.5	37.5	40

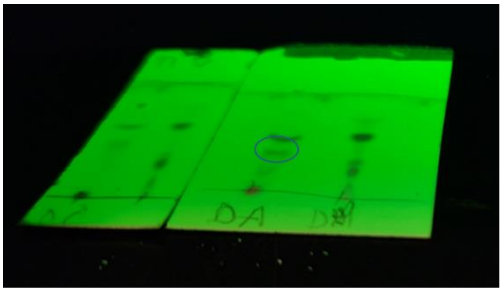

t = 0 min (left) 15 min (right)

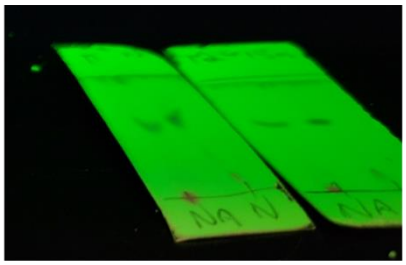

t = 0 min (left) 15 min (right)

All TLC Plates:
Column 1: d-ATP and probe
Column 2: probe

Eluted with: 3:2:1
$ClCH_3$:EtOAc:MeOH

Figure 40: Comparison of both the DMiMO-I (left) and NAI (right) probes when reacted with d-ATP. After 15 minutes, reactivity is observed with the DMiMO-I probe in comparison to the NAI probe.

Appendix C: Nuclear Magnetic Resonance and Mass Spectrometry Data

Spectra from Chapter 2:

^{1}H NMR of synthesized pyridiniums

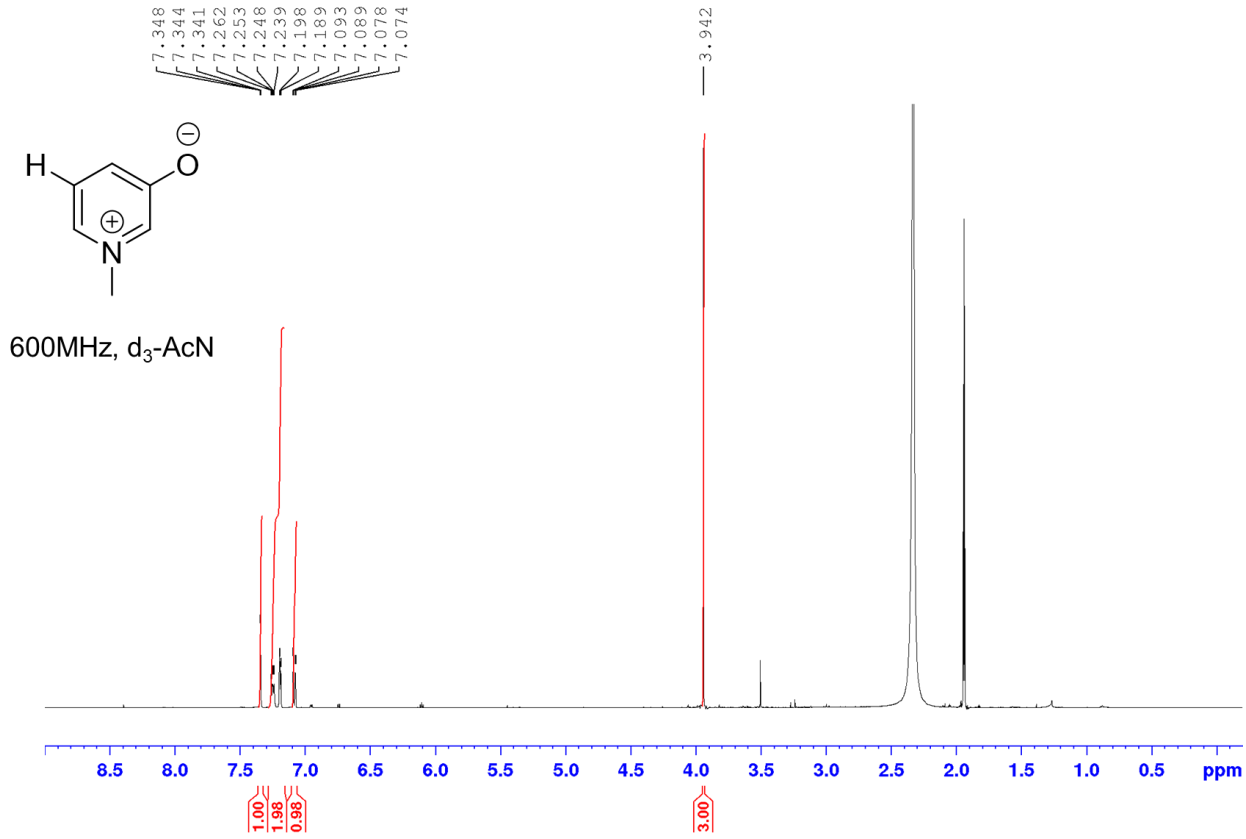

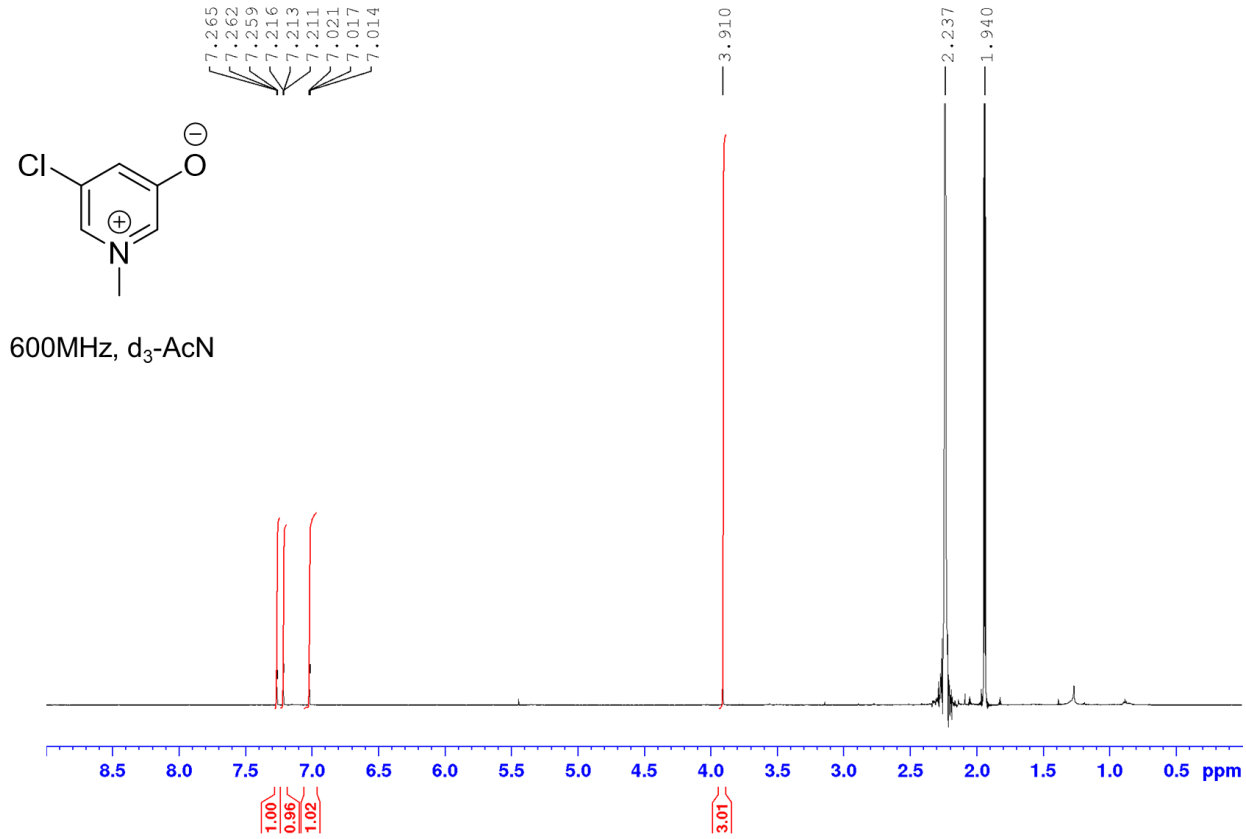
7.265
7.262
7.259
7.216
7.213
7.211
7.021
7.017
7.014
3.910
2.237
1.940
Cl
O
N
600MHz, d3-AcN
8.5 8.0 7.5 7.0 6.5 6.0 5.5 5.0 4.5 4.0 3.5 3.0 2.5 2.0 1.5 1.0 0.5 ppm
1.00
0.96
1.02
3.01

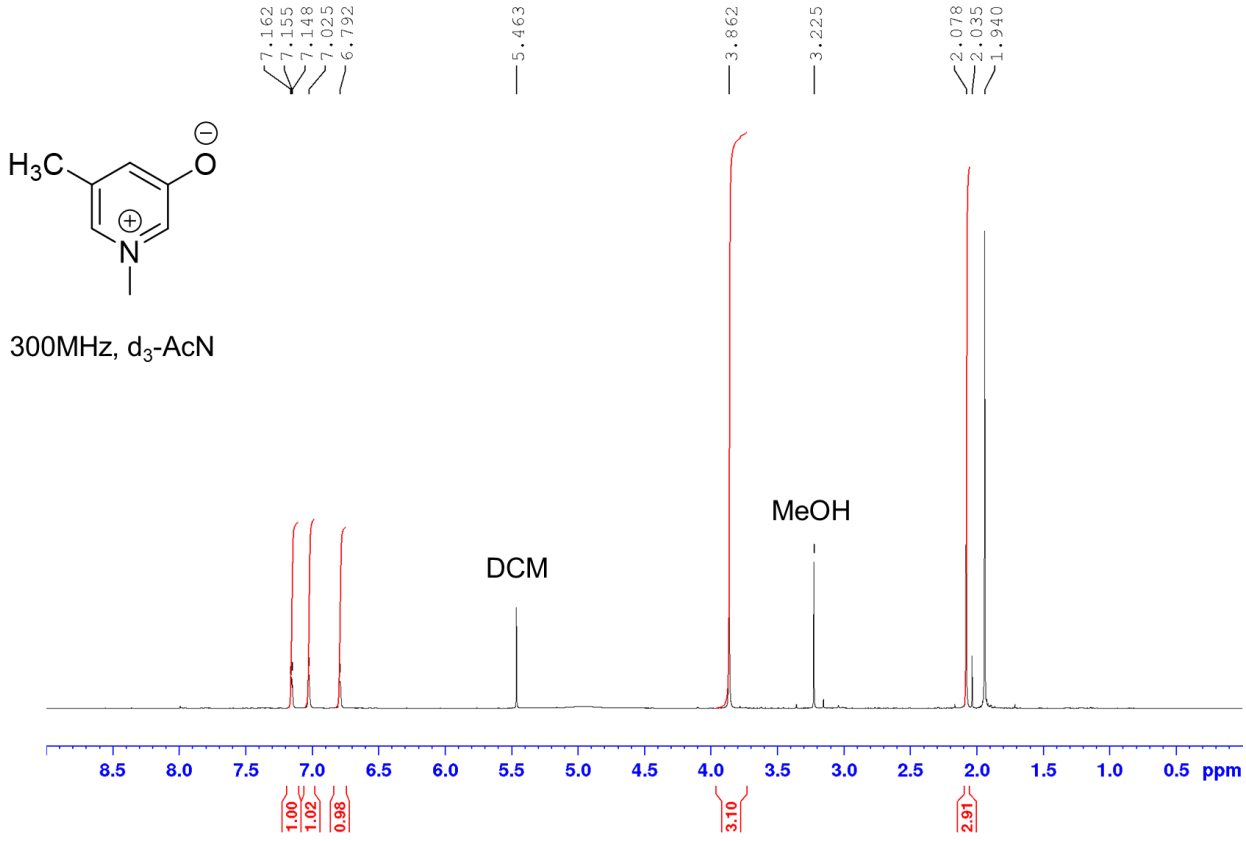
7.162
7.155
7.148
7.025
6.792
5.463
3.862
3.225
2.078
2.035
1.940
H3C
O
N
300MHz, d3-AcN
DCM
MeOH
8.5 8.0 7.5 7.0 6.5 6.0 5.5 5.0 4.5 4.0 3.5 3.0 2.5 2.0 1.5 1.0 0.5 ppm
1.00
1.02
0.98
3.10
2.91

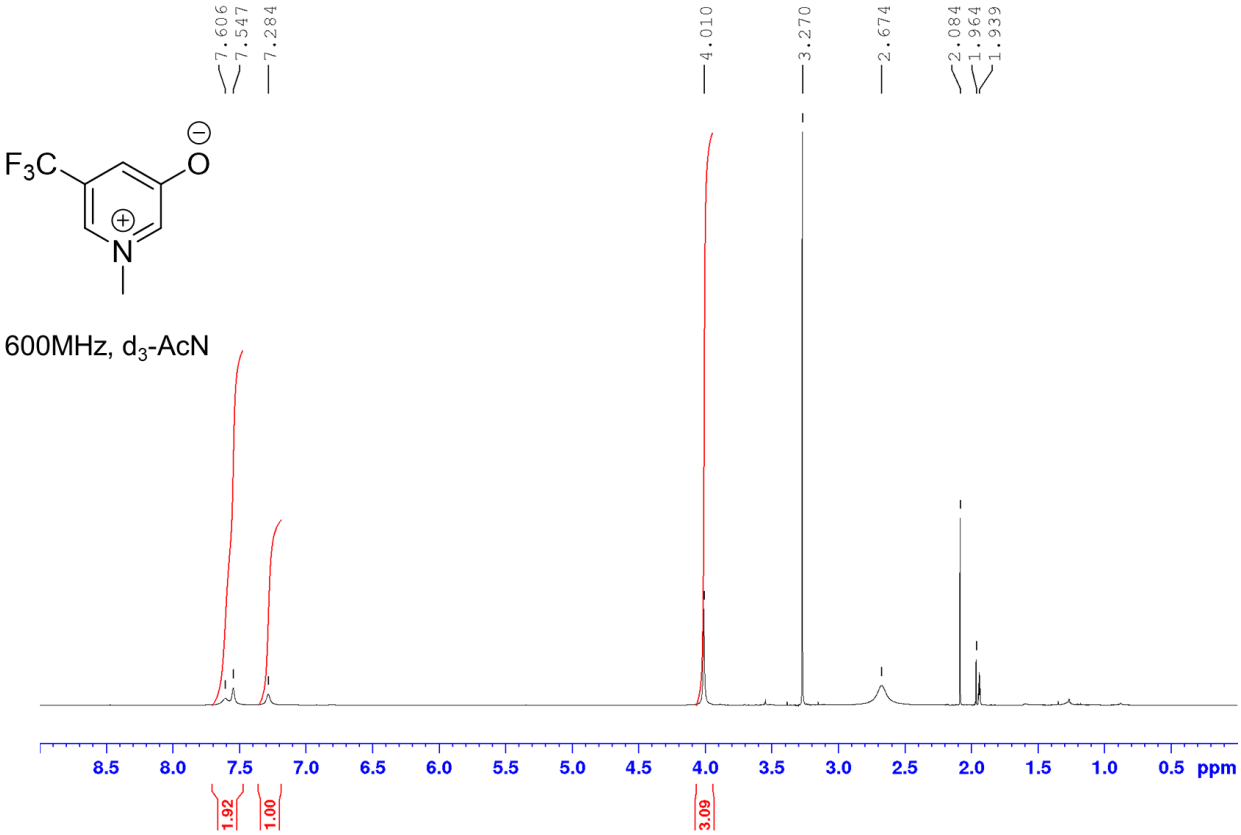
7.606
7.547
7.284
4.010
3.270
2.674
2.084
1.964
1.939
F3C
O
N
600MHz, d3-AcN
8.5 8.0 7.5 7.0 6.5 6.0 5.5 5.0 4.5 4.0 3.5 3.0 2.5 2.0 1.5 1.0 0.5 ppm
1.92
1.00
3.09

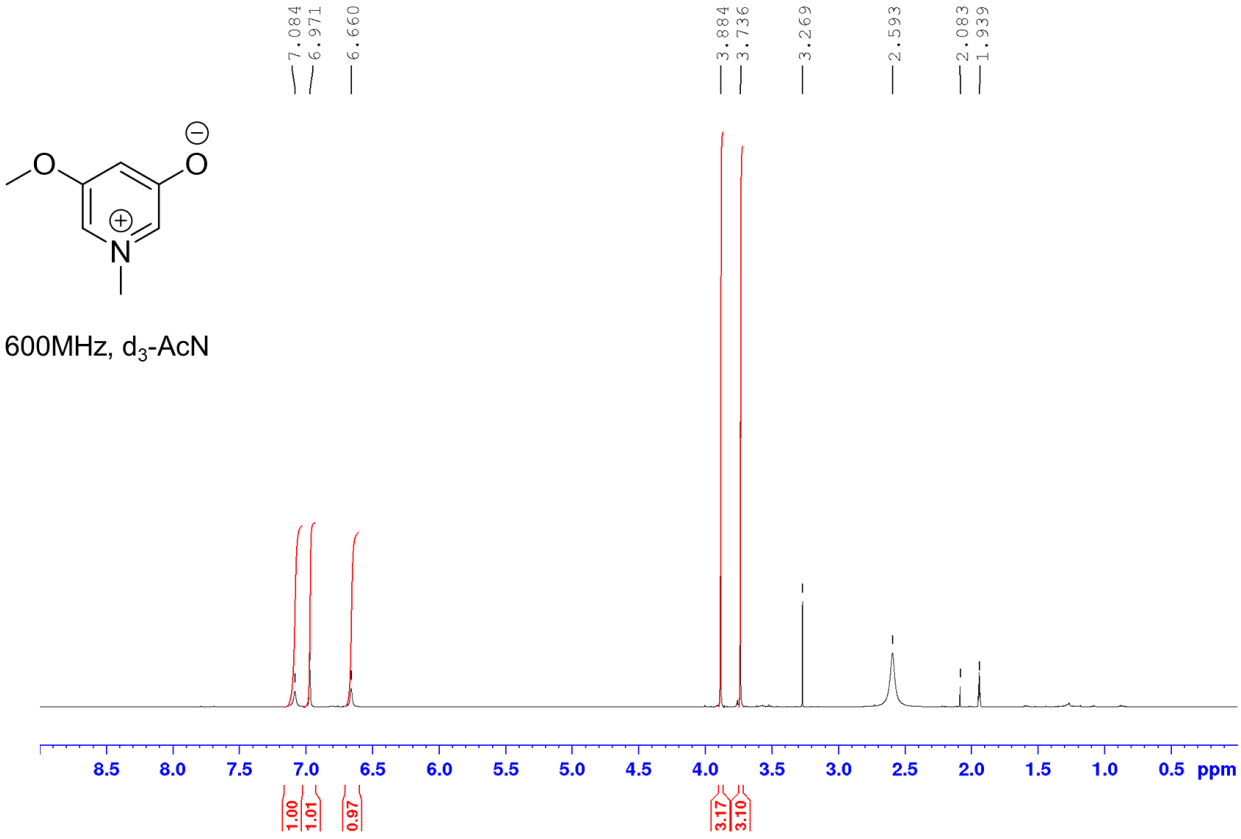
7.084
6.971
6.660
3.884
3.736
3.269
2.593
2.083
1.939
O
O
N
600MHz, d3-AcN
8.5 8.0 7.5 7.0 6.5 6.0 5.5 5.0 4.5 4.0 3.5 3.0 2.5 2.0 1.5 1.0 0.5 ppm
1.00
1.01
0.97
3.17
3.10

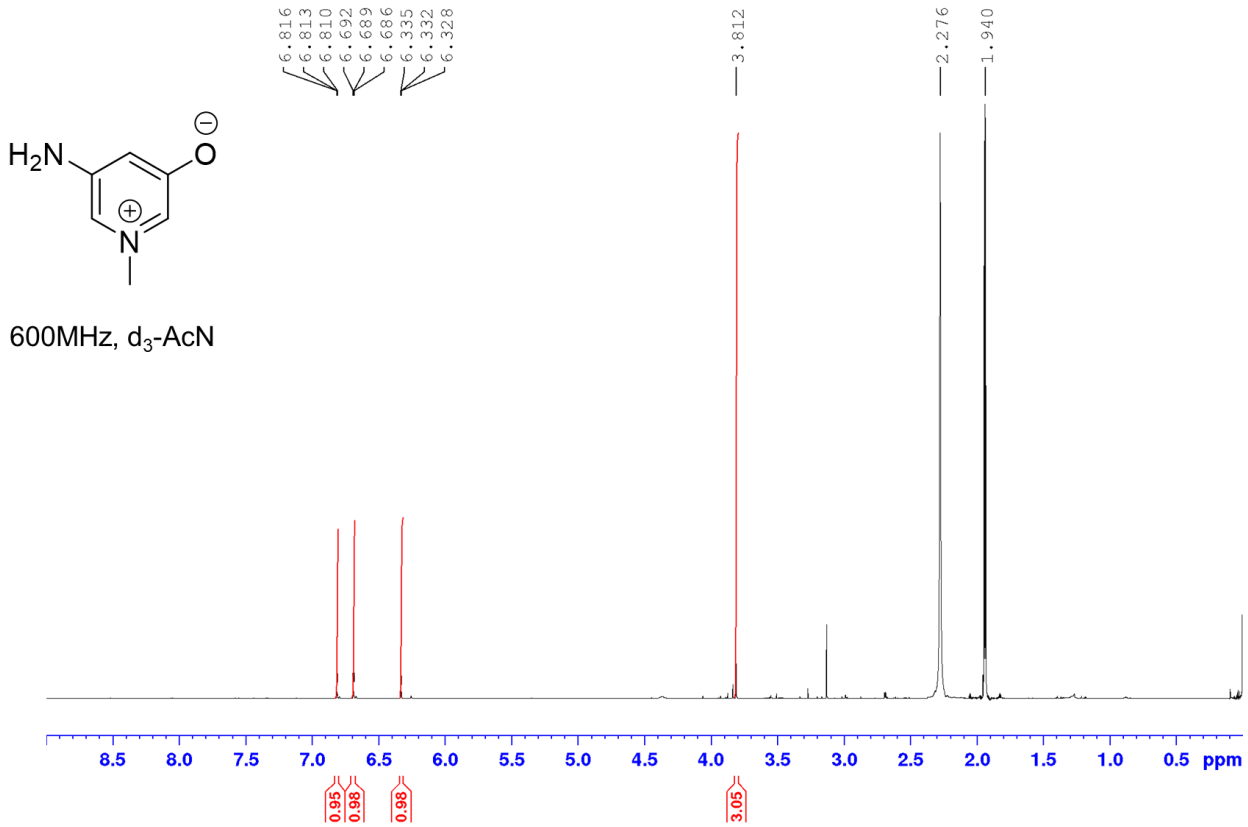
6.816
6.813
6.810
6.692
6.689
6.686
6.335
6.332
6.328
3.812
2.276
1.940
H2N
O
N
600MHz, d3-AcN
8.5 8.0 7.5 7.0 6.5 6.0 5.5 5.0 4.5 4.0 3.5 3.0 2.5 2.0 1.5 1.0 0.5 ppm
0.95
0.98
0.98
3.05

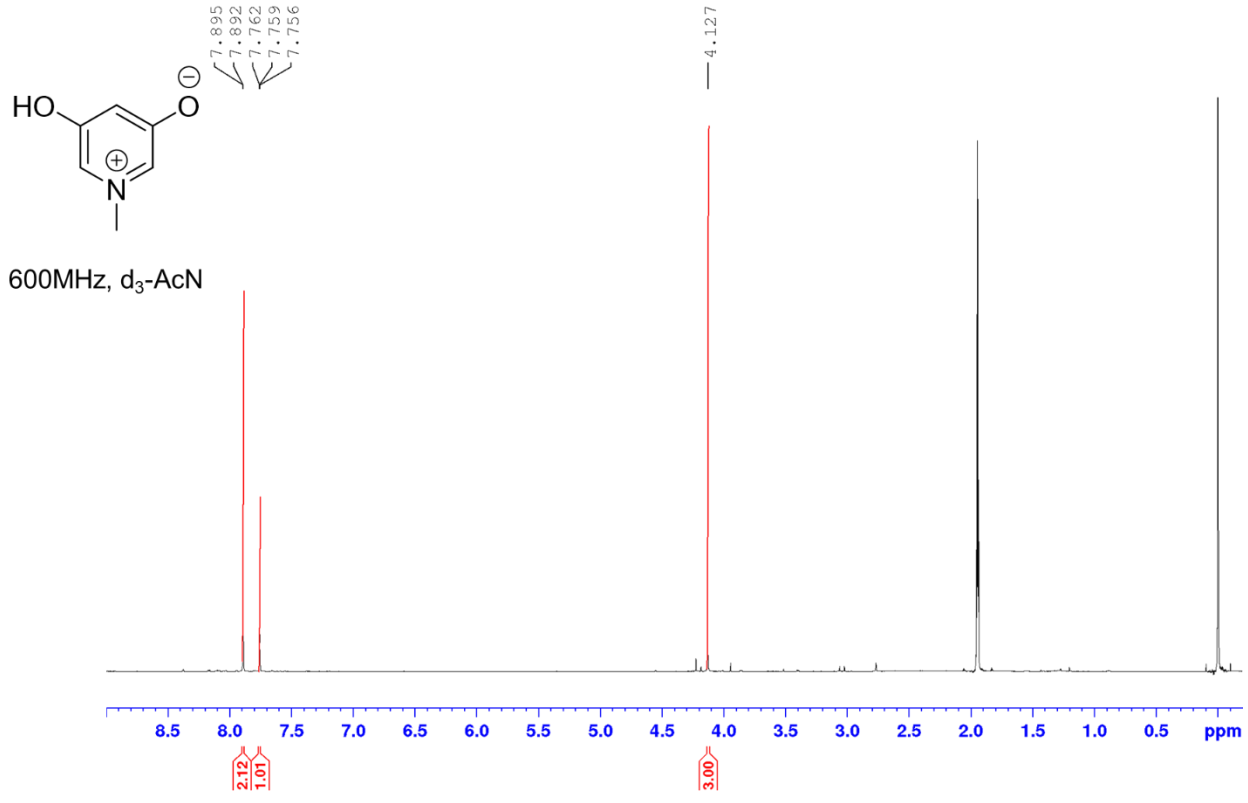
7.895
7.892
7.762
7.759
7.756
4.127
HO
O
N
600MHz, d3-AcN
8.5 8.0 7.5 7.0 6.5 6.0 5.5 5.0 4.5 4.0 3.5 3.0 2.5 2.0 1.5 1.0 0.5 ppm
2.12
1.01
3.00

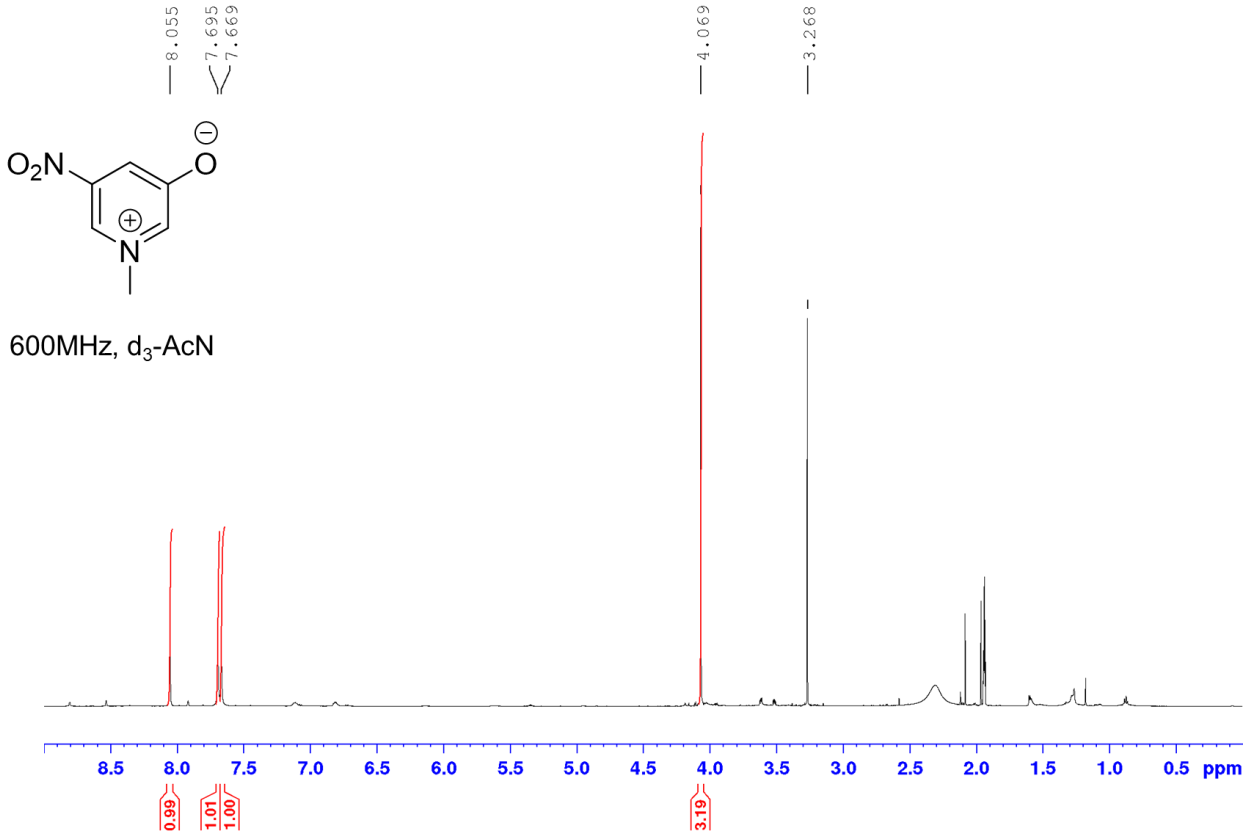
8.055
7.695
7.669
4.069
3.268
O2N
O
N
600MHz, d3-AcN
8.5
8.0
7.5
7.0
6.5
6.0
5.5
5.0
4.5
4.0
3.5
3.0
2.5
2.0
1.5
1.0
0.5
ppm
0.99
1.01
1.00
3.19

^{13}C NMR of synthesized pyridiniums

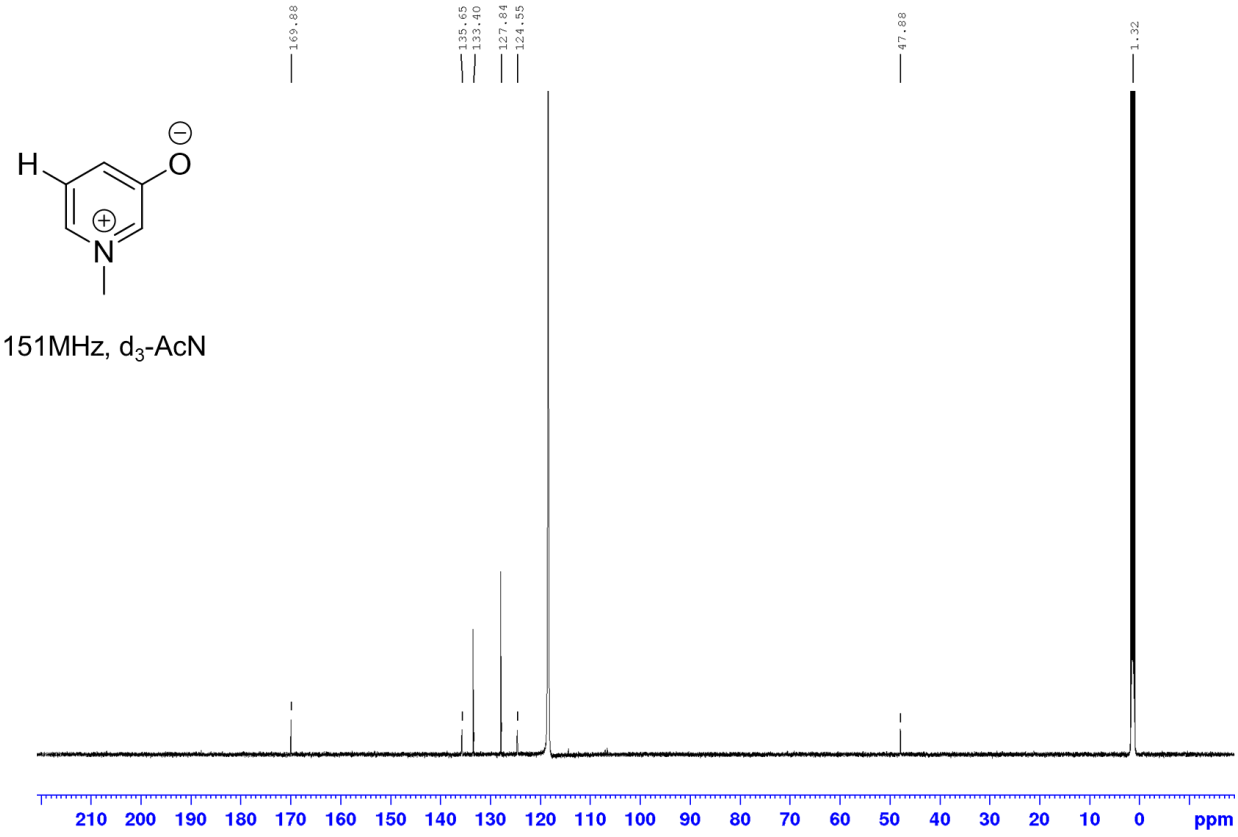

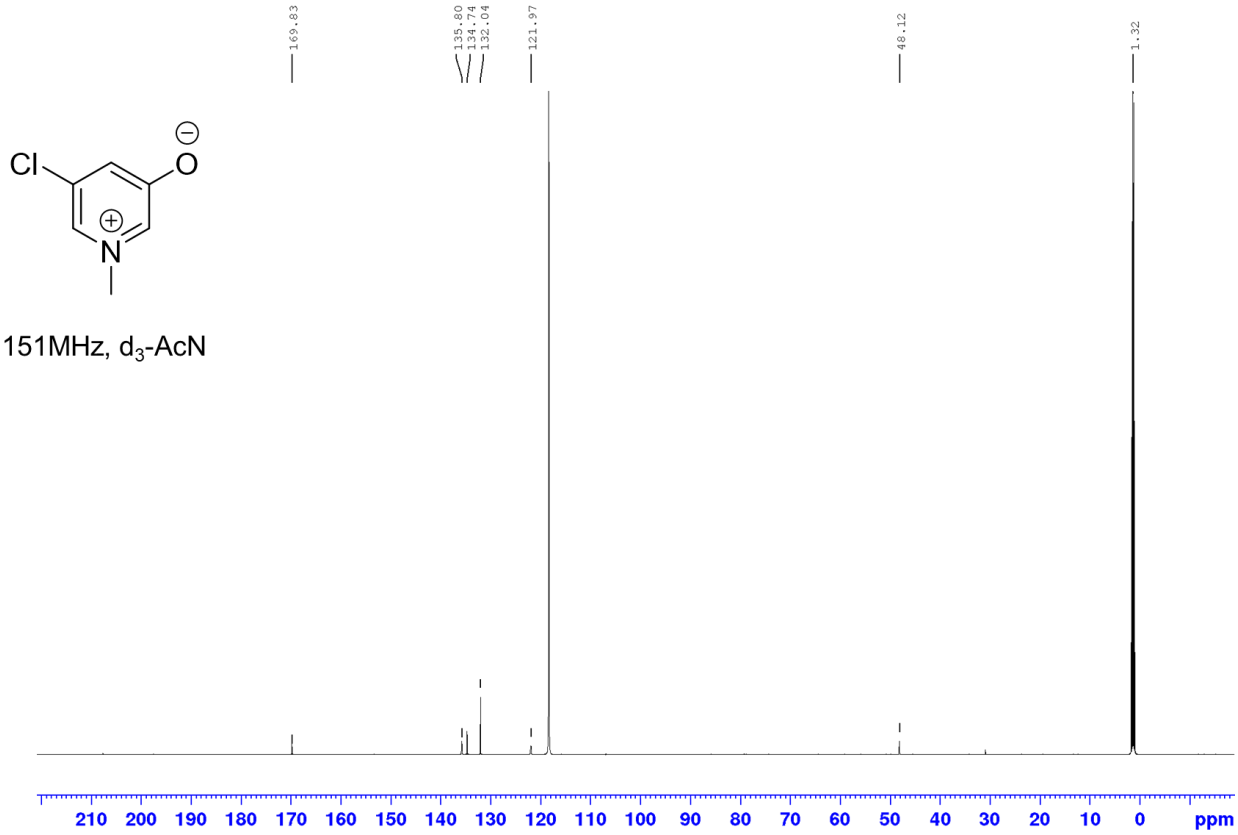

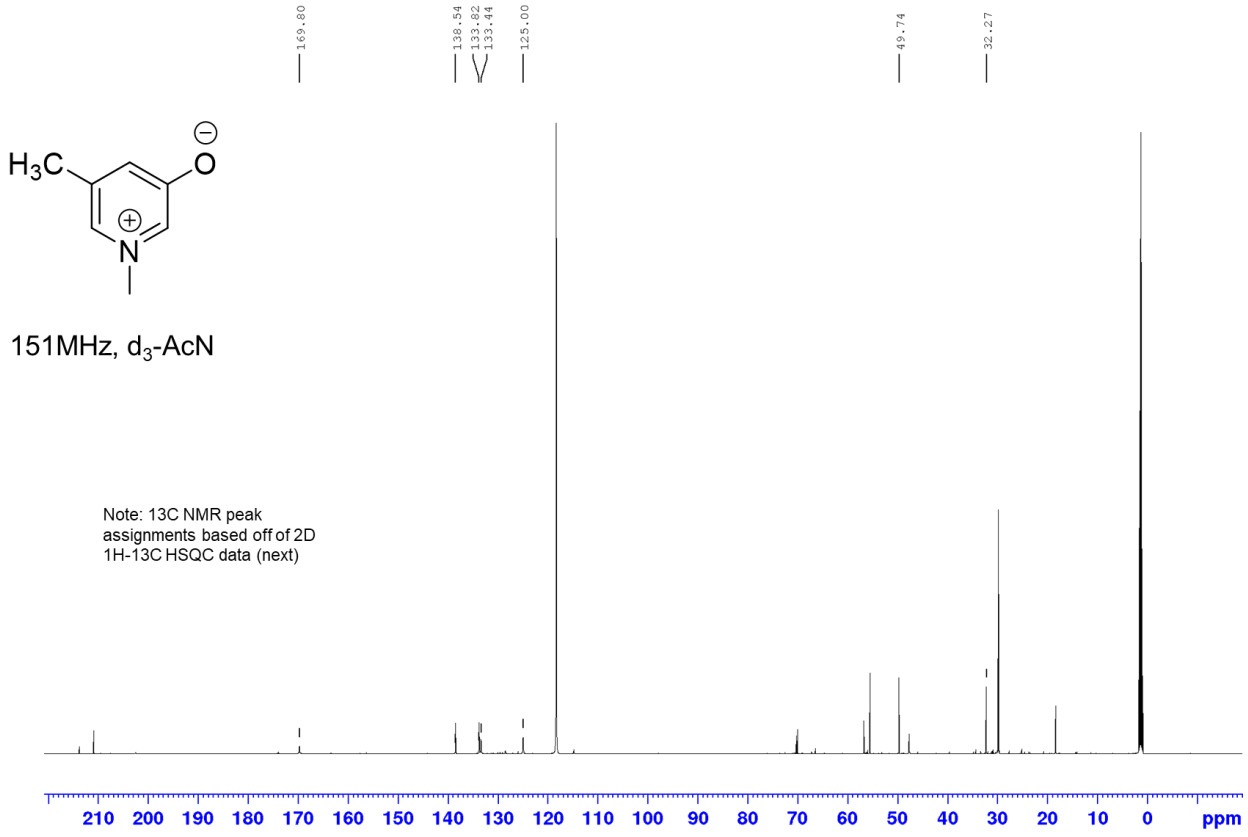
169.80
138.54
133.82
133.44
125.00
49.74
32.27
151MHz, d3-AcN
Note: 13C NMR peak assignments based off of 2D 1H-13C HSQC data (next)
210 200 190 180 170 160 150 140 130 120 110 100 90 80 70 60 50 40 30 20 10 0 ppm

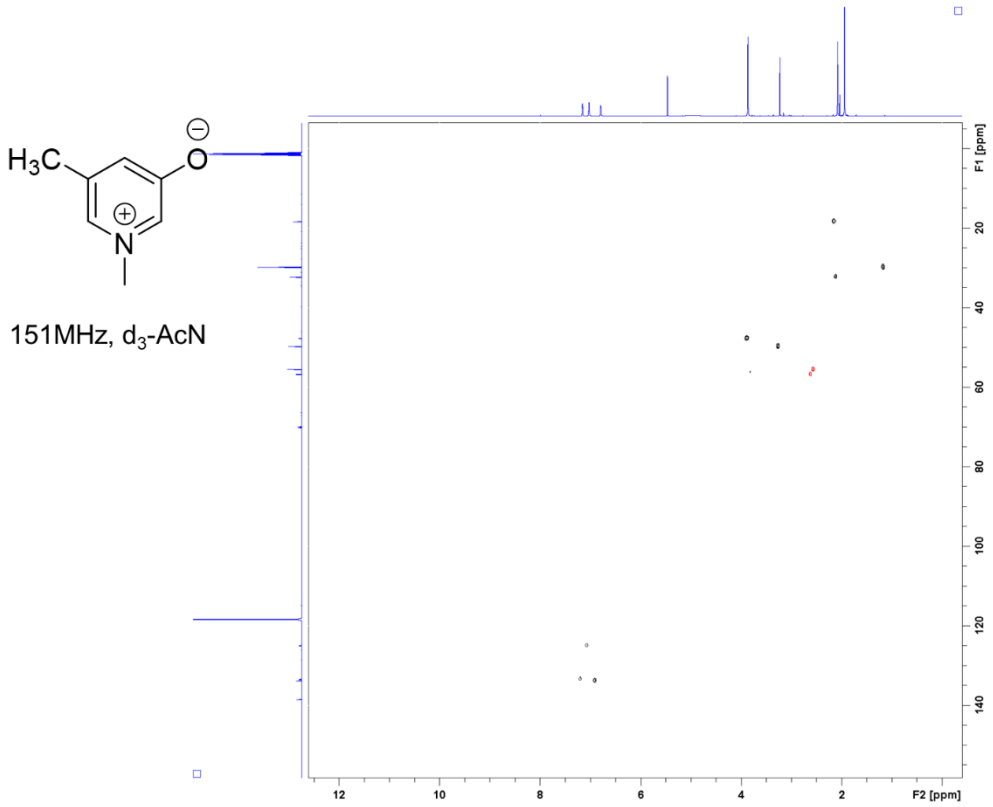
151MHz, d3-AcN
F1 [ppm]
20
40
60
80
100
120
140
12
10
8
6
4
2
F2 [ppm]

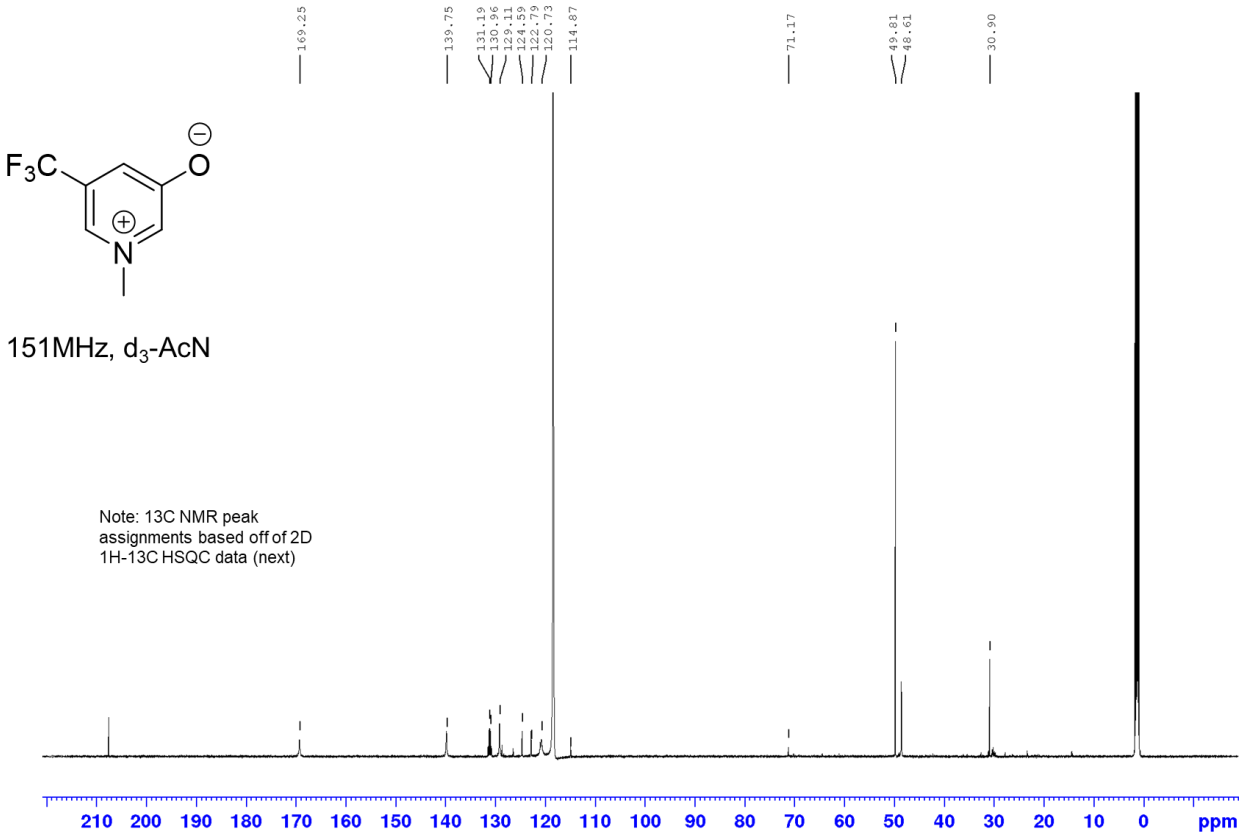
169.25
139.75
131.19
130.96
129.11
124.59
122.79
120.73
114.87
71.17
49.81
48.61
30.90
F3C
O
N
151MHz, d3-AcN
Note: 13C NMR peak
assignments based off of 2D
1H-13C HSQC data (next)
210 200 190 180 170 160 150 140 130 120 110 100 90 80 70 60 50 40 30 20 10 0 ppm

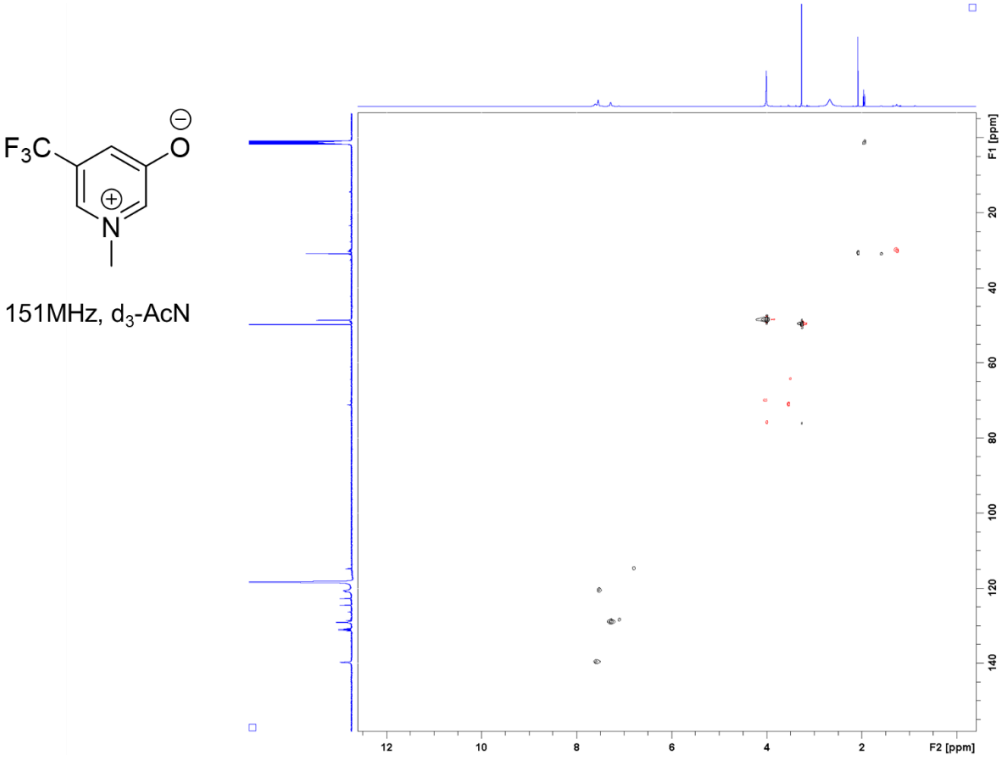
F3C
O
N
151MHz, d3-AcN
F1 [ppm]
20
40
60
80
100
120
140
12
10
8
6
4
2
F2 [ppm]

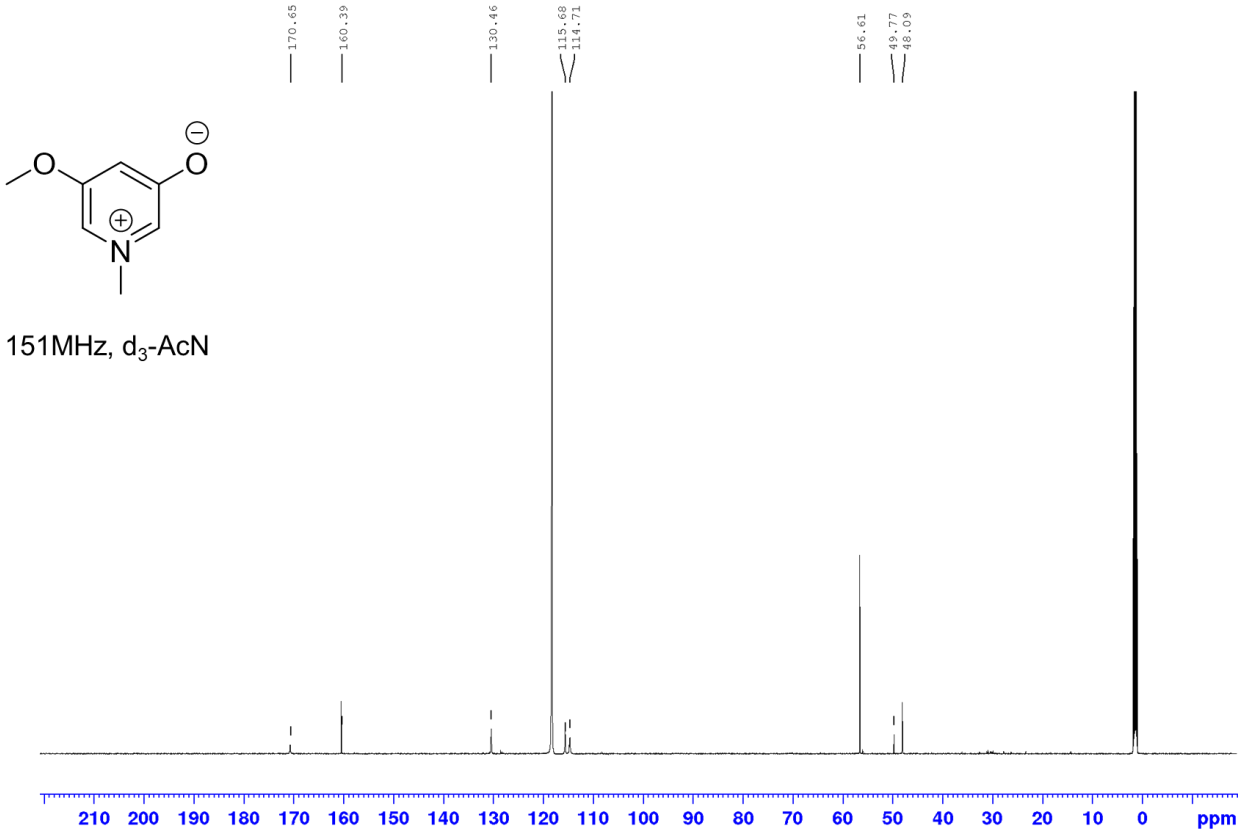

151MHz, d_3-AcN

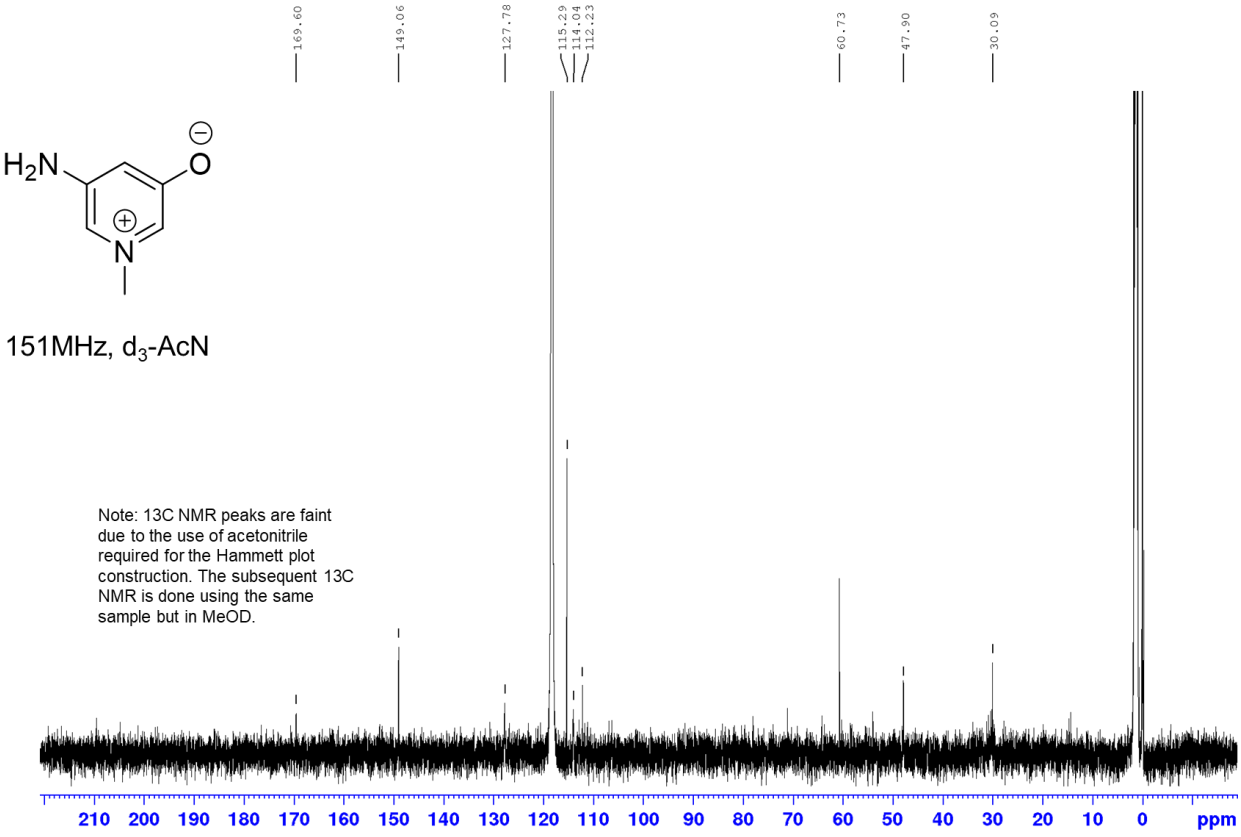

151MHz, d_3-AcN

Note: 13C NMR peaks are faint due to the use of acetonitrile required for the Hammett plot construction. The subsequent 13C NMR is done using the same sample but in MeOD.

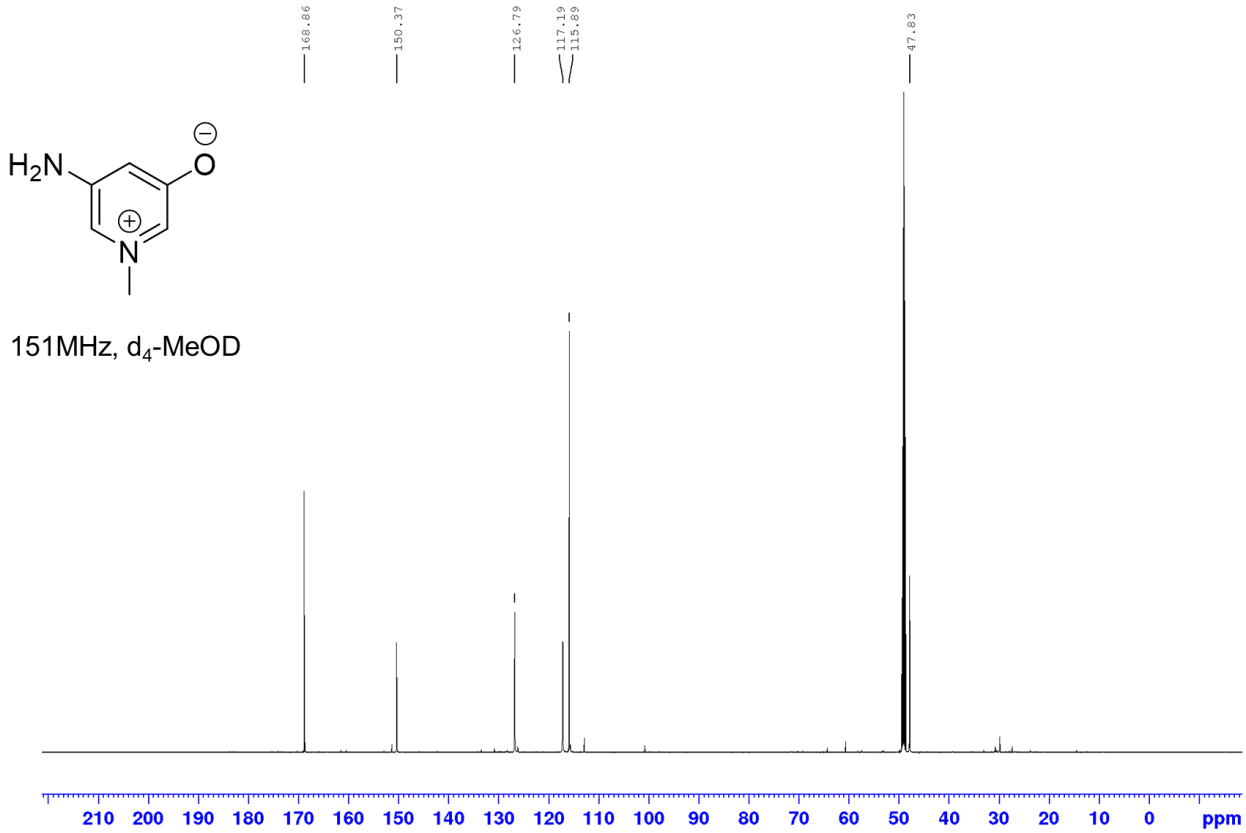

151MHz, d_4-MeOD

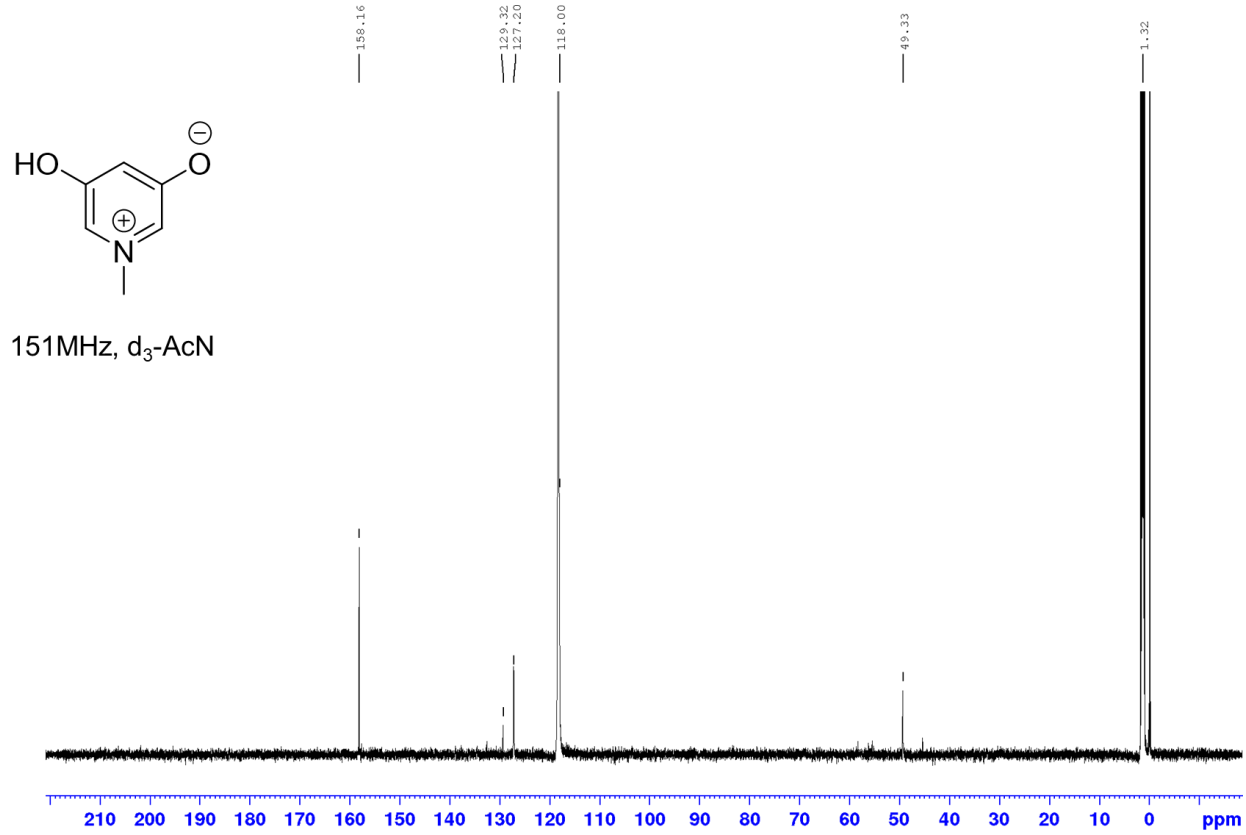

151MHz, d_3-AcN

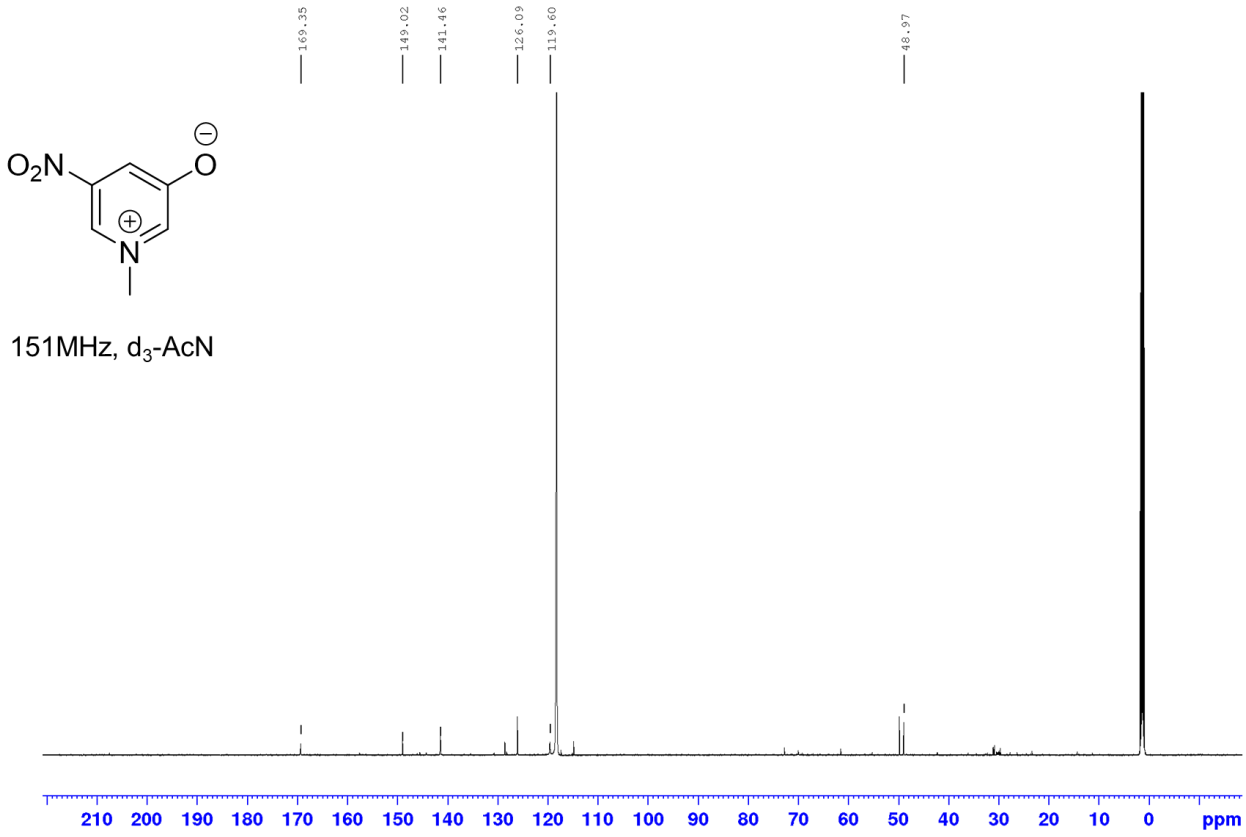
169.35
149.02
141.46
126.09
119.60
48.97
O2N
O
N
151MHz, d3-AcN
210 200 190 180 170 160 150 140 130 120 110 100 90 80 70 60 50 40 30 20 10 0 ppm

Spectra of Cycloaddition Product 5 (all isomers):

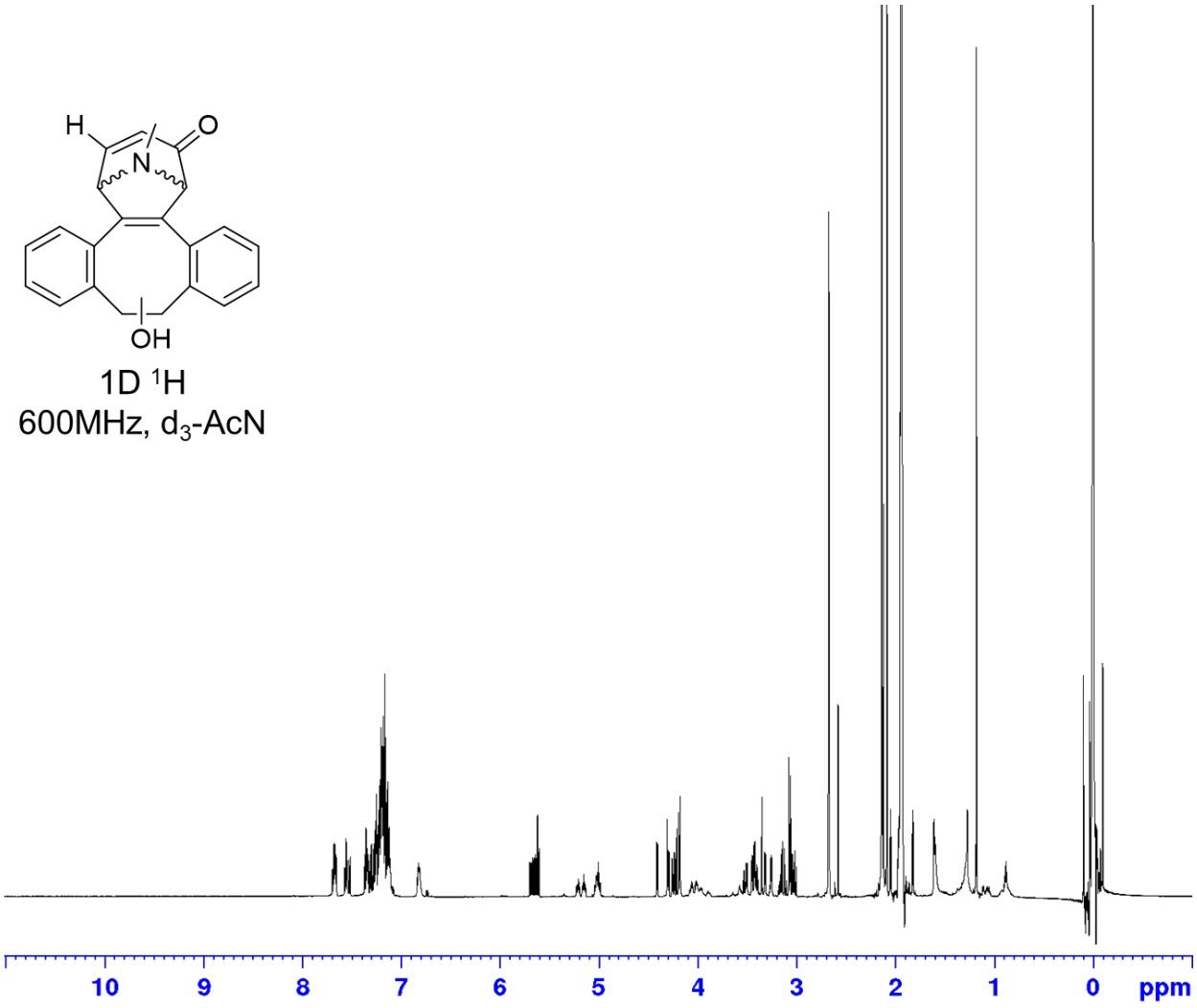

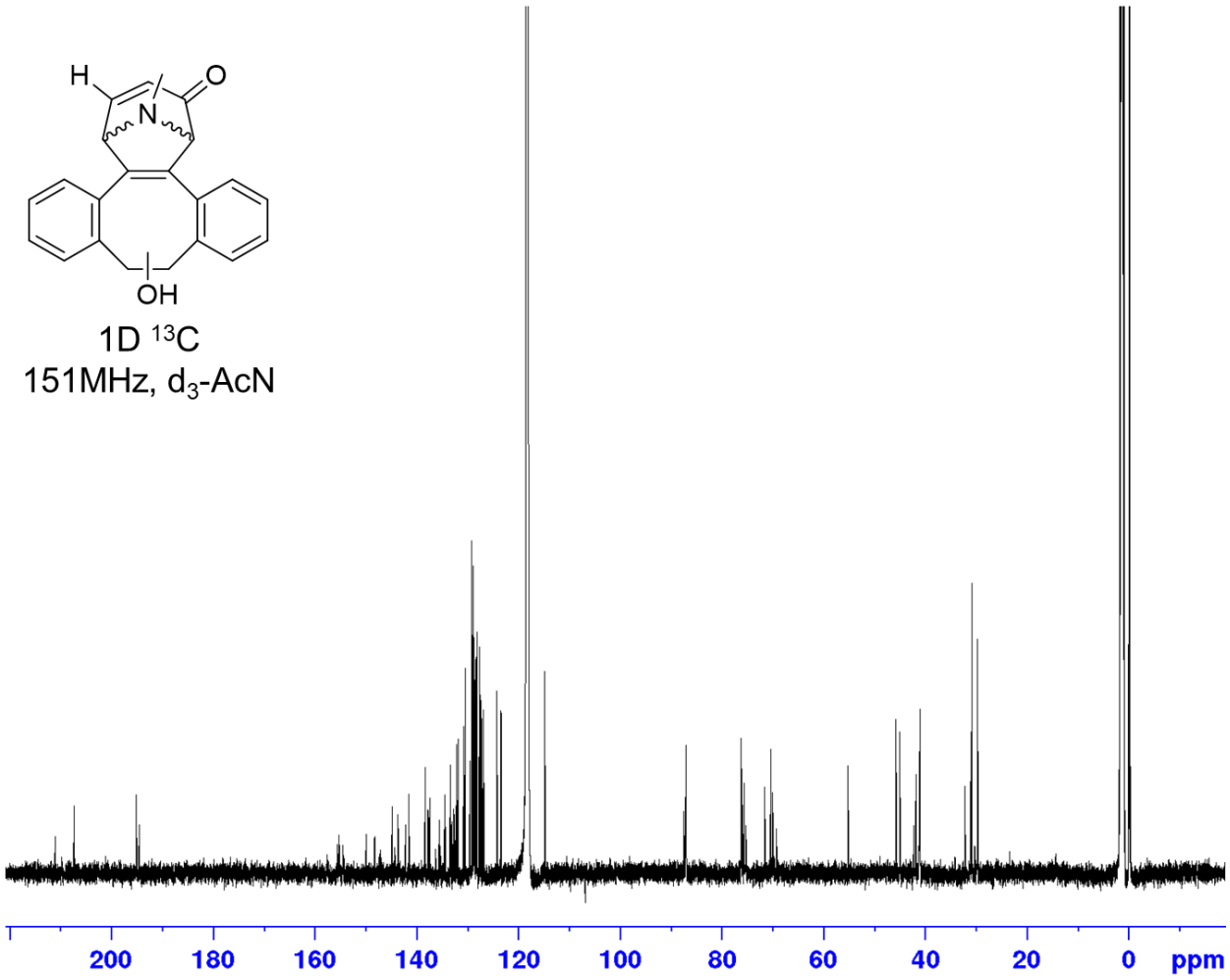
H
O
N
OH
1D ^{13}C
151MHz, d_3-AcN
200
180
160
140
120
100
80
60
40
20
0
ppm

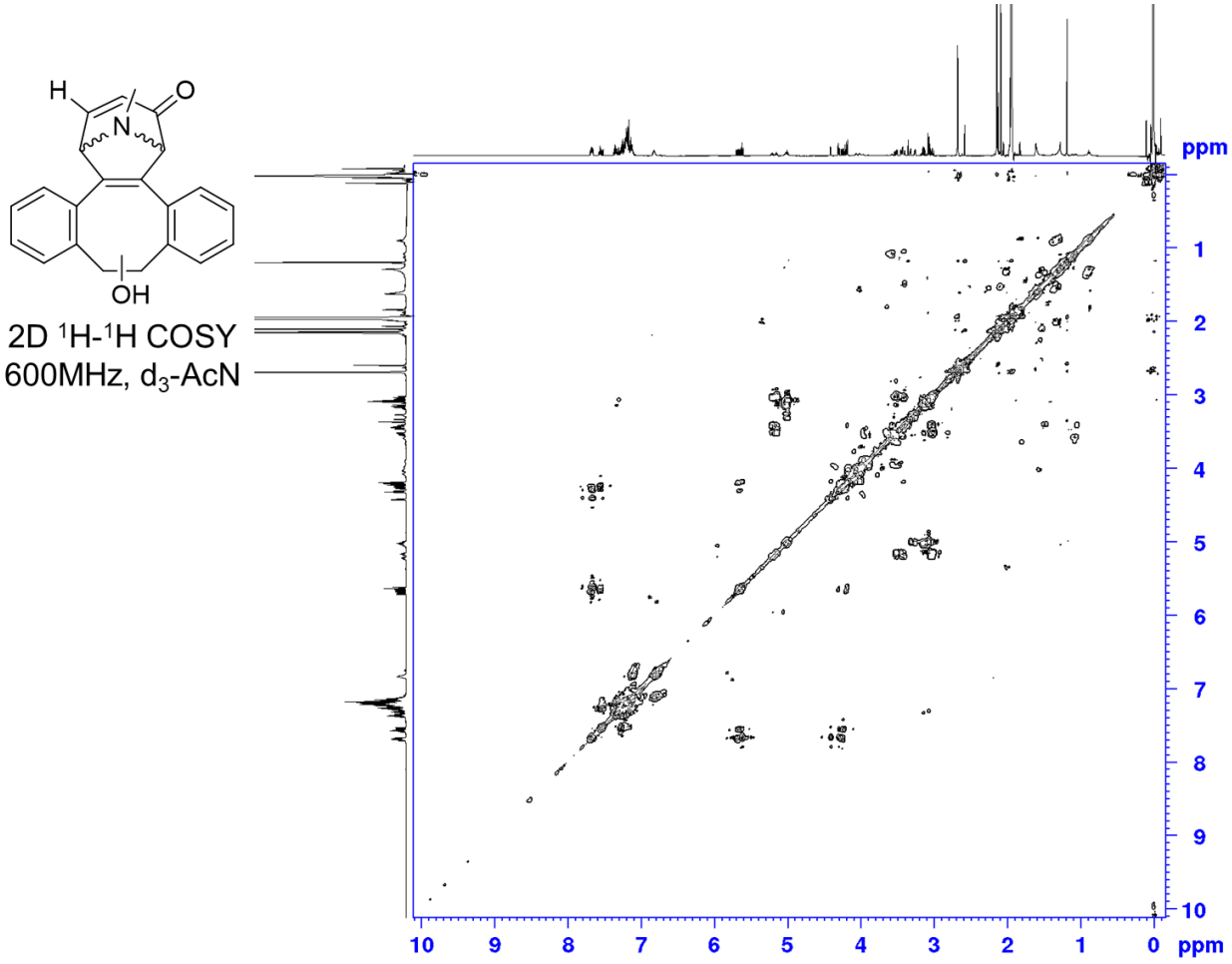
H
O
N
OH
2D ^{1}H-^{1}H COSY
600MHz, d_3-AcN
ppm
1
2
3
4
5
6
7
8
9
10
10 9 8 7 6 5 4 3 2 1 0 ppm

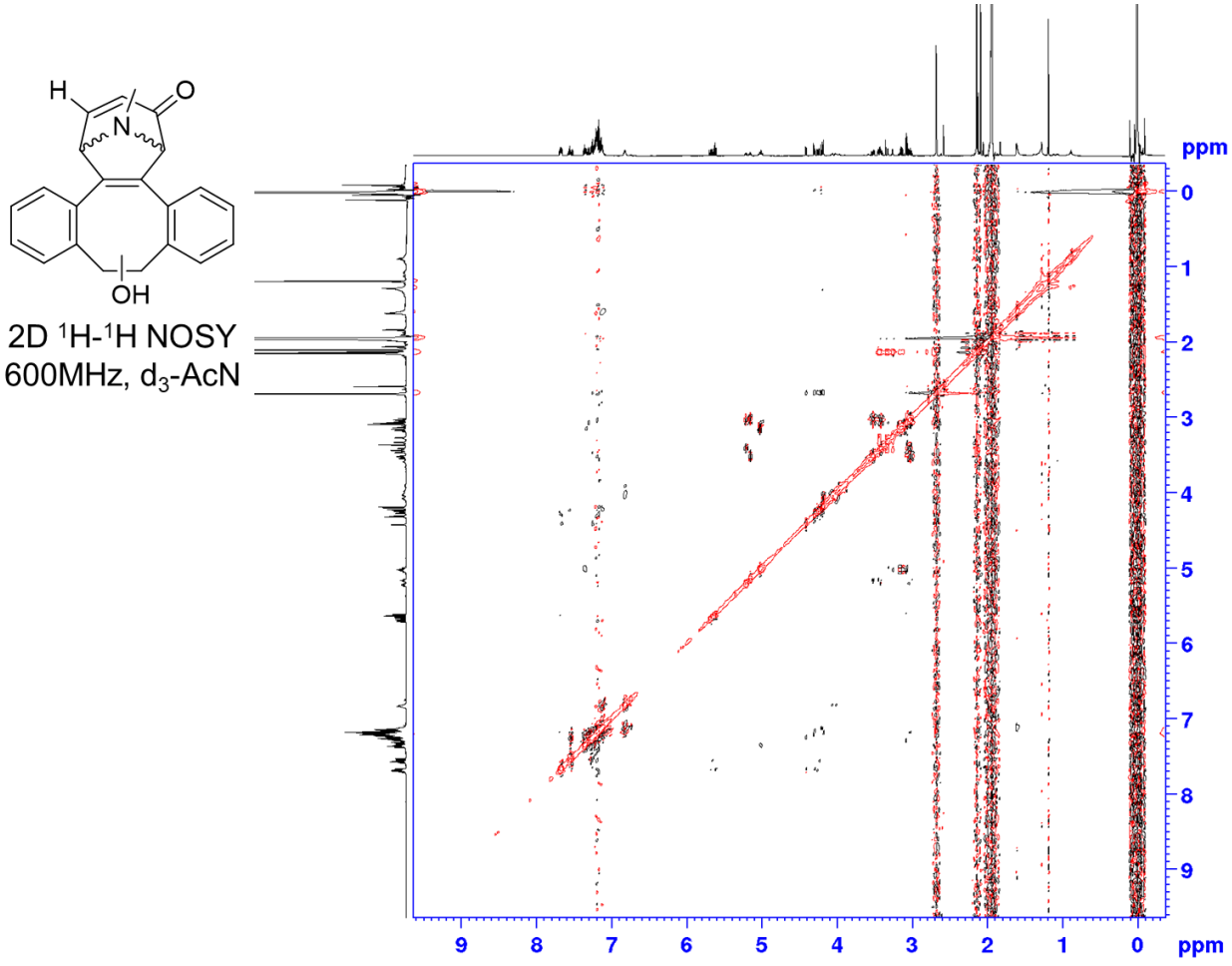
H
O
N
OH
2D ^{1}H-^{1}H NOSY
600MHz, d_3-AcN
ppm
0
1
2
3
4
5
6
7
8
9
ppm
9
8
7
6
5
4
3
2
1
0

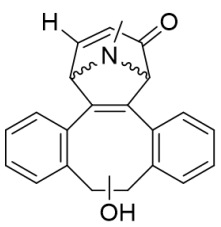

2D ^{1}H-^{13}C HSQC
600, 151MHz, d_3-AcN

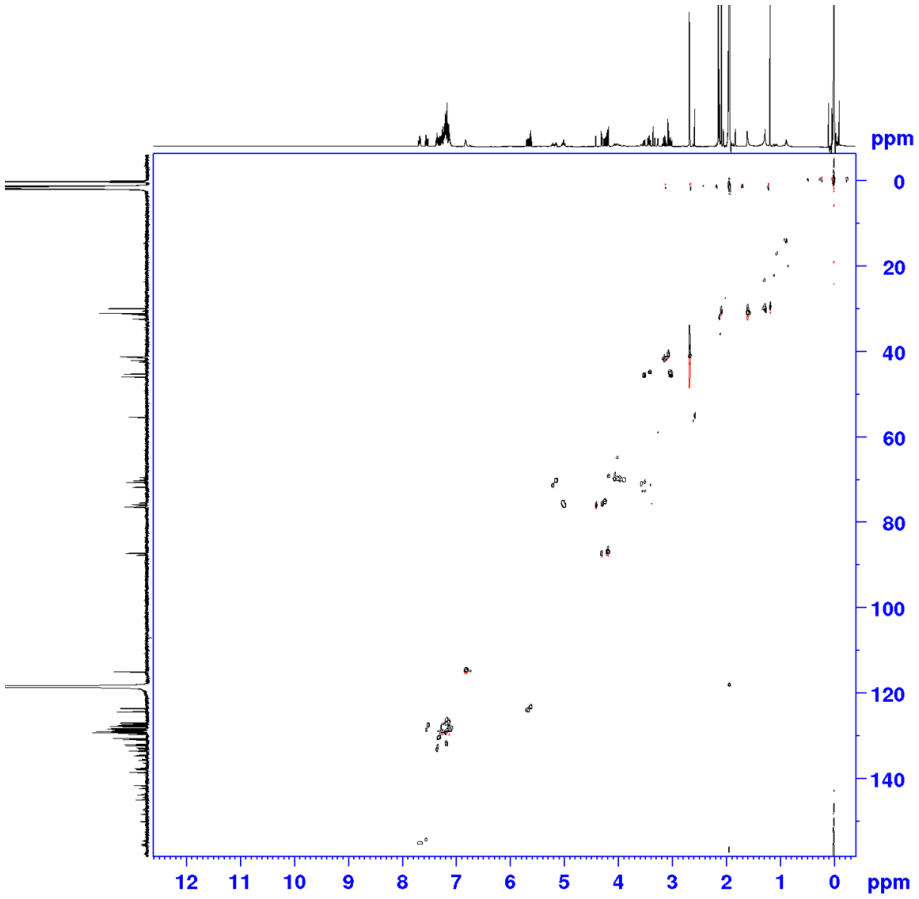

Spectra of Cycloaddition Product 5a:

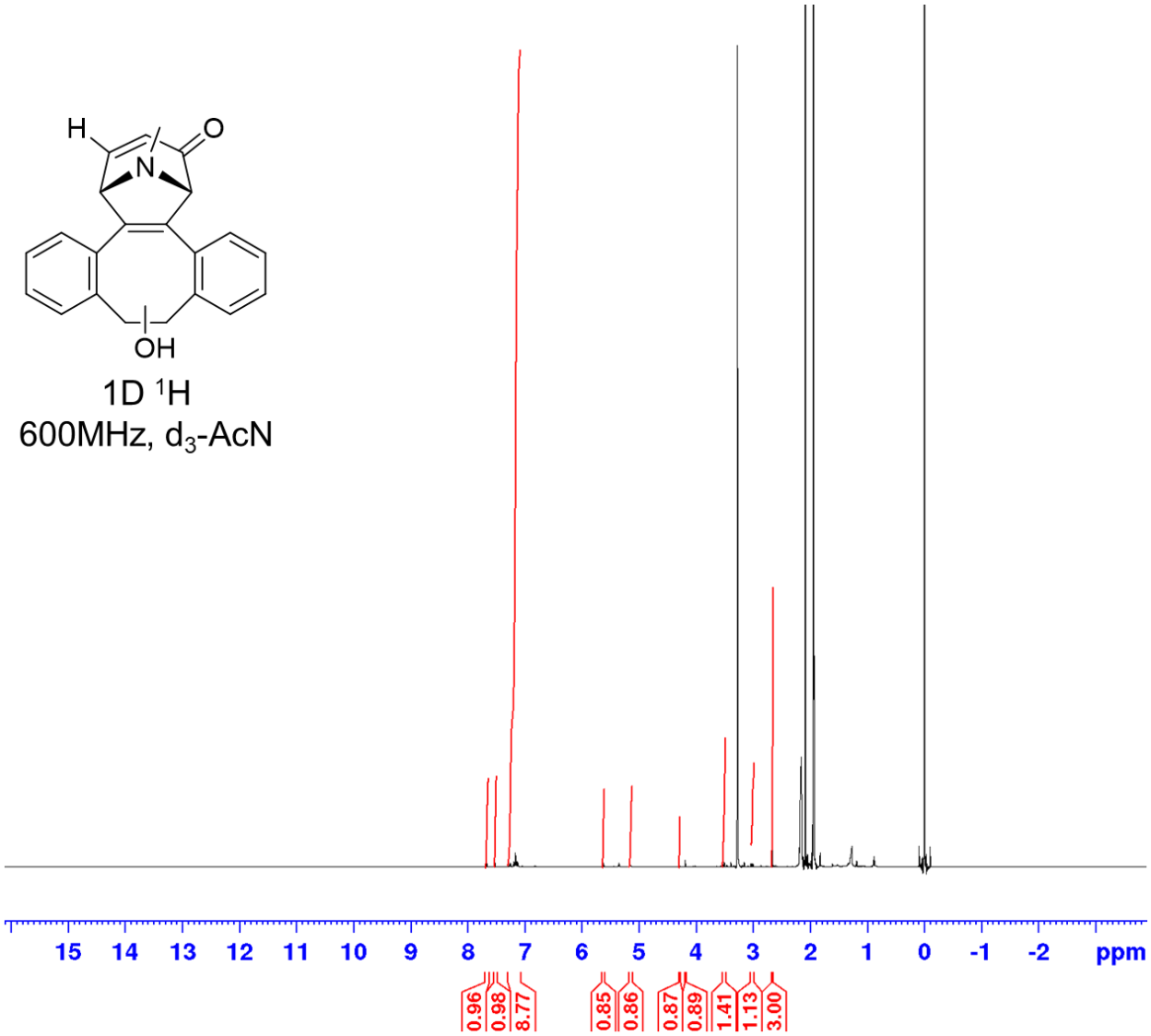

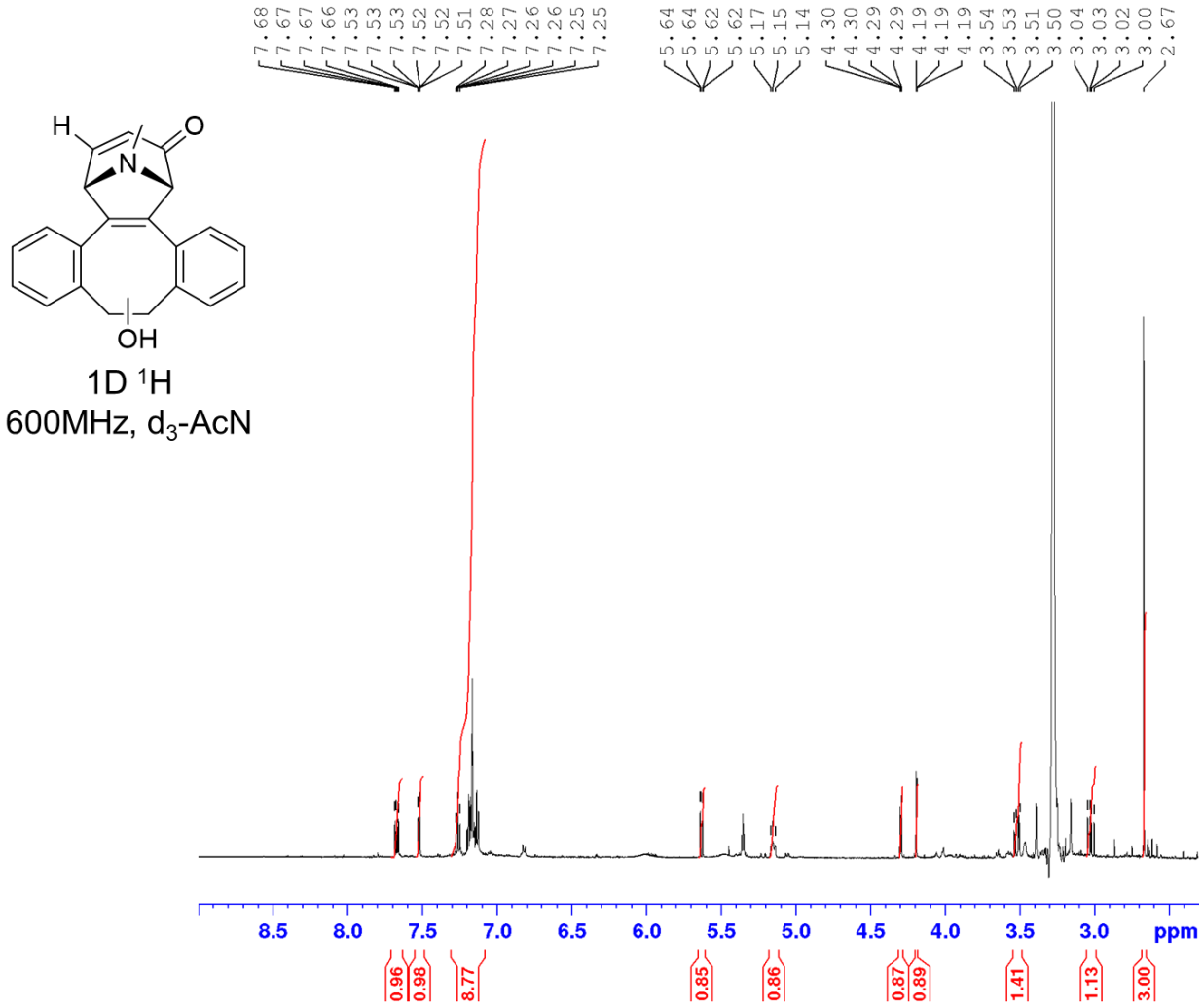
7.68
7.67
7.67
7.66
7.53
7.53
7.53
7.52
7.52
7.51
7.28
7.27
7.26
7.26
7.25
7.25
5.64
5.64
5.62
5.62
5.17
5.15
5.14
4.30
4.30
4.29
4.29
4.19
4.19
4.19
3.54
3.53
3.51
3.50
3.04
3.03
3.02
3.00
2.67
H
O
N
OH
1D ^{1}H
600MHz, d_3-AcN
8.5
8.0
7.5
7.0
6.5
6.0
5.5
5.0
4.5
4.0
3.5
3.0
ppm
0.96
0.98
8.77
0.85
0.86
0.87
0.89
1.41
1.13
3.00

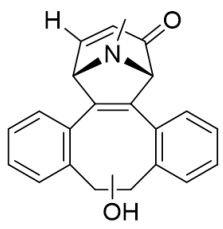

1D ^{13}C
151MHz, d_3-AcN

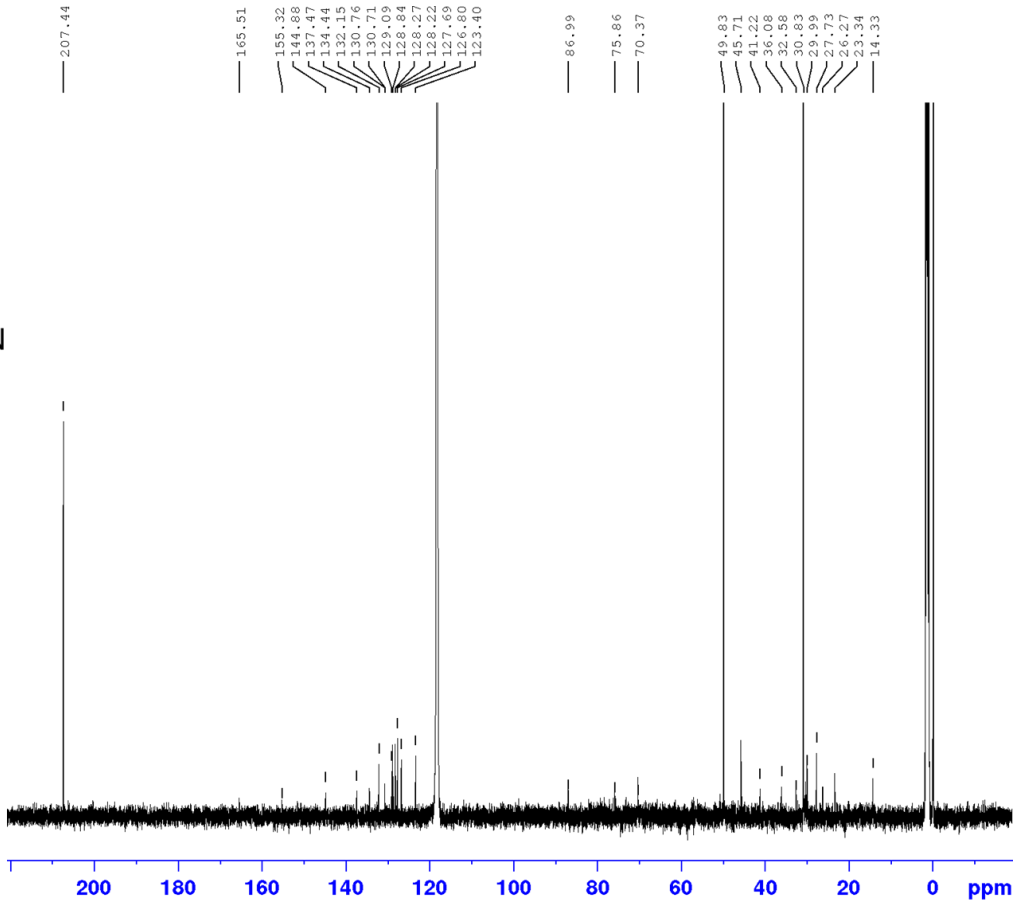

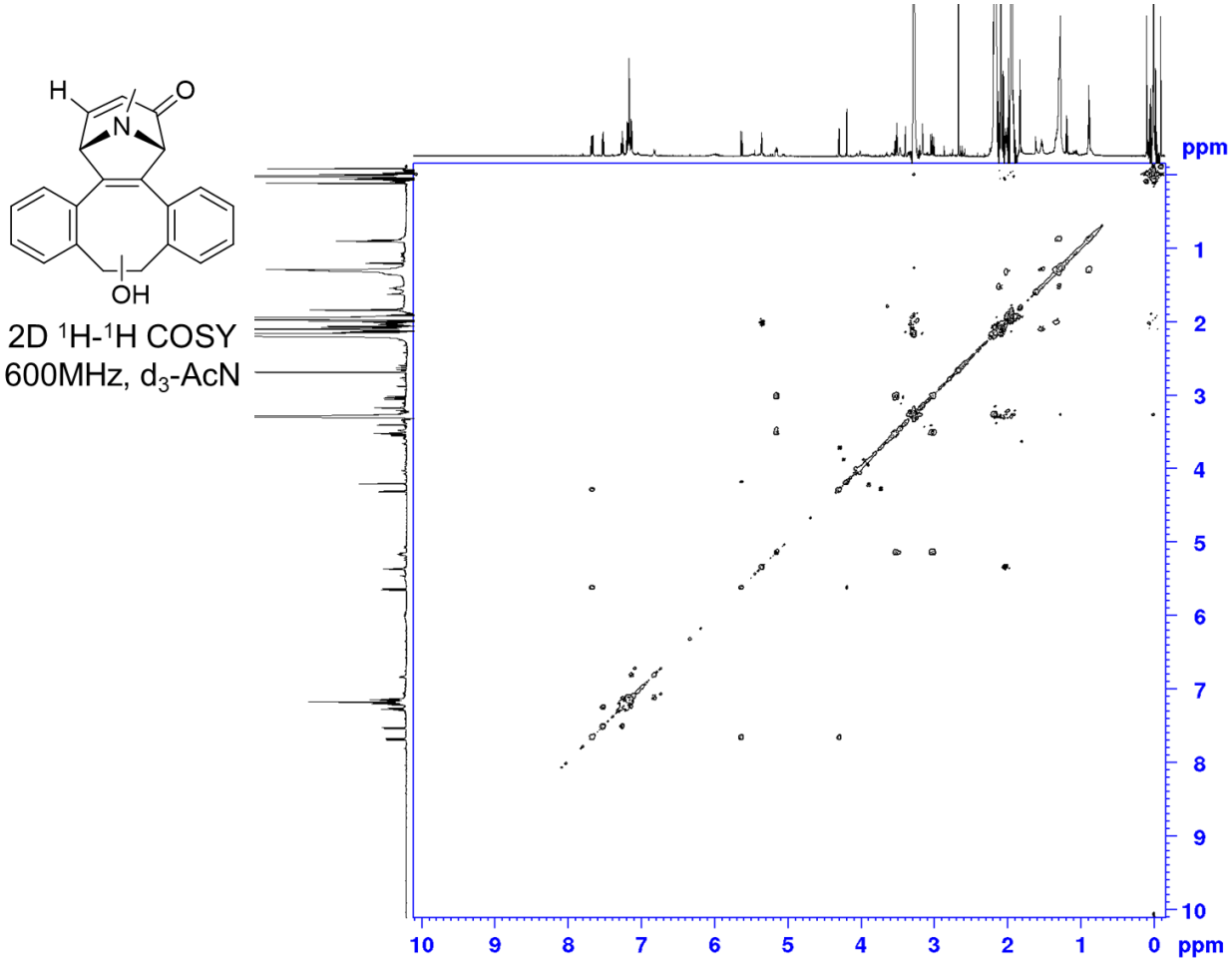
H
O
N
OH
2D ^{1}H-^{1}H COSY
600MHz, d_3-AcN
ppm
1
2
3
4
5
6
7
8
9
10
10
9
8
7
6
5
4
3
2
1
0
ppm

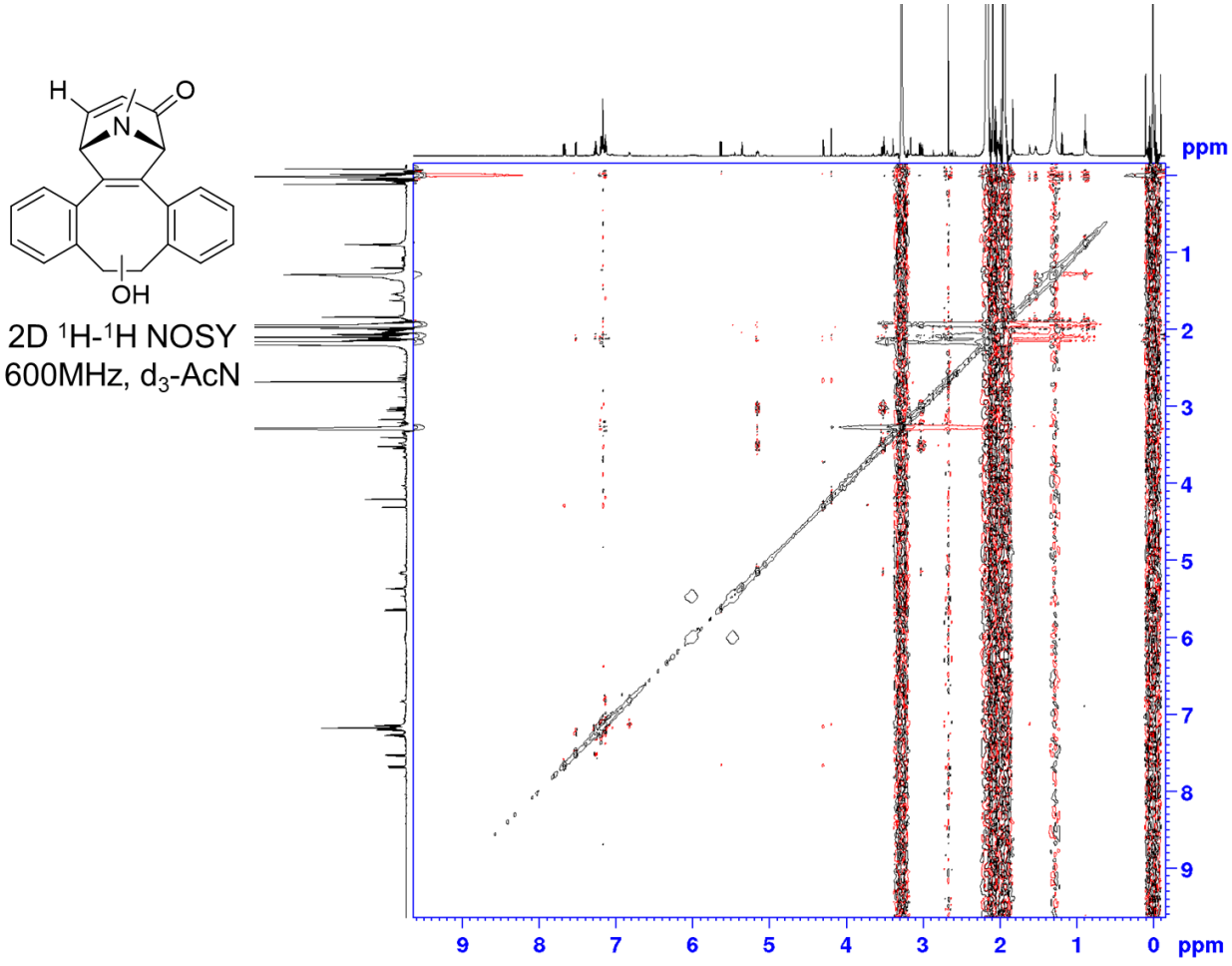
H
O
N
OH
2D ^{1}H-^{1}H NOSY
600MHz, d_3-AcN
ppm
1
2
3
4
5
6
7
8
9
9
8
7
6
5
4
3
2
1
0
ppm

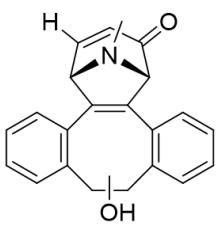

2D ^{1}H-^{13}C HSQC
600, 151MHz, d_3-AcN

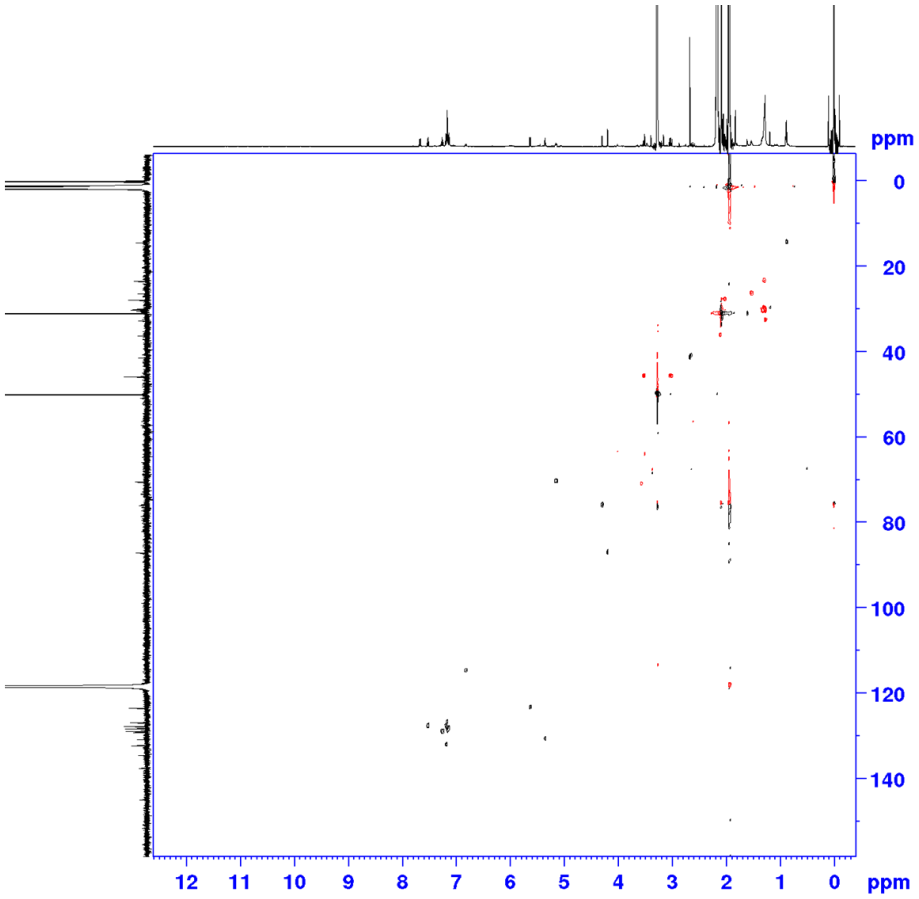

Spectra of Cycloaddition Product 5b:

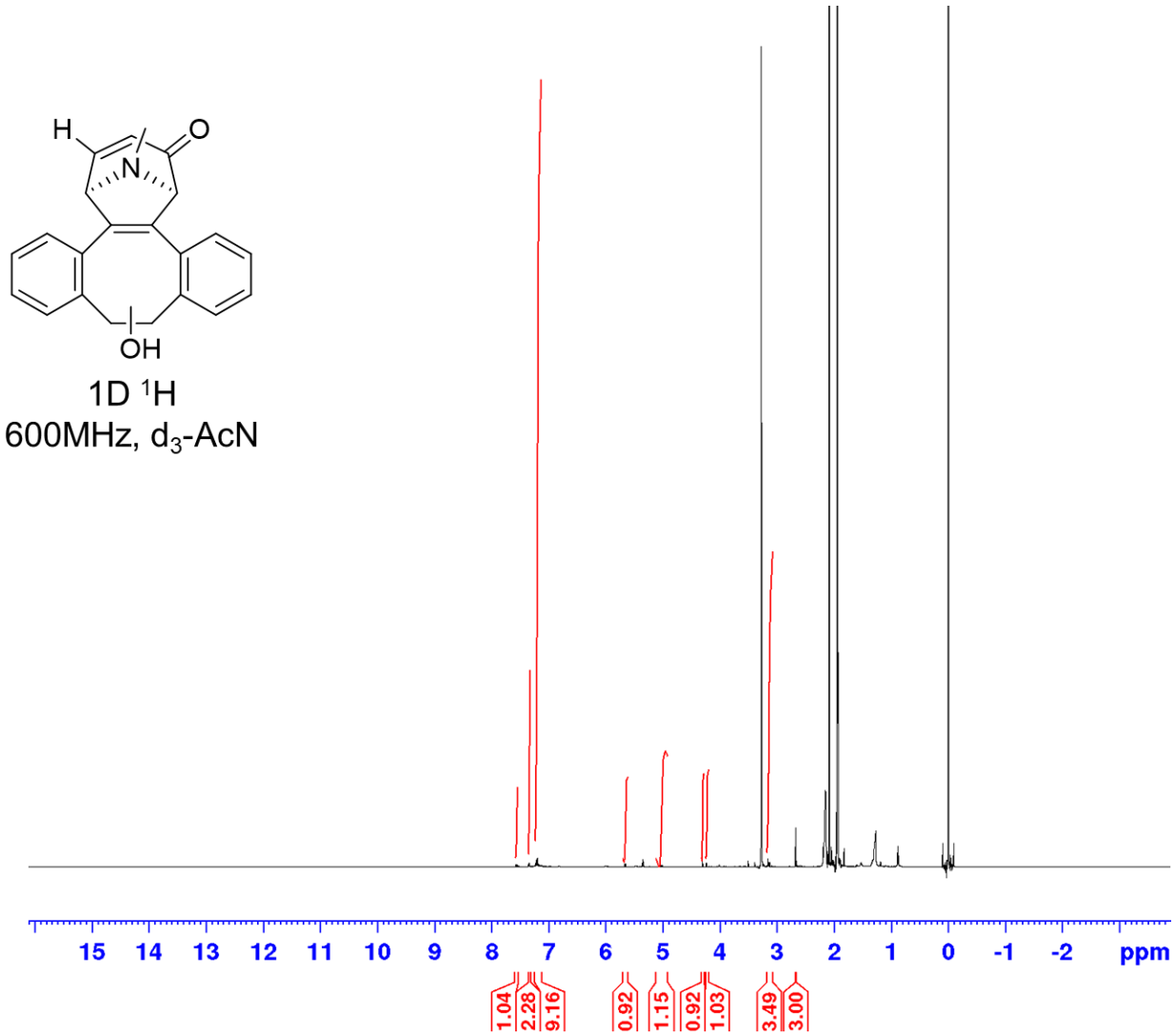

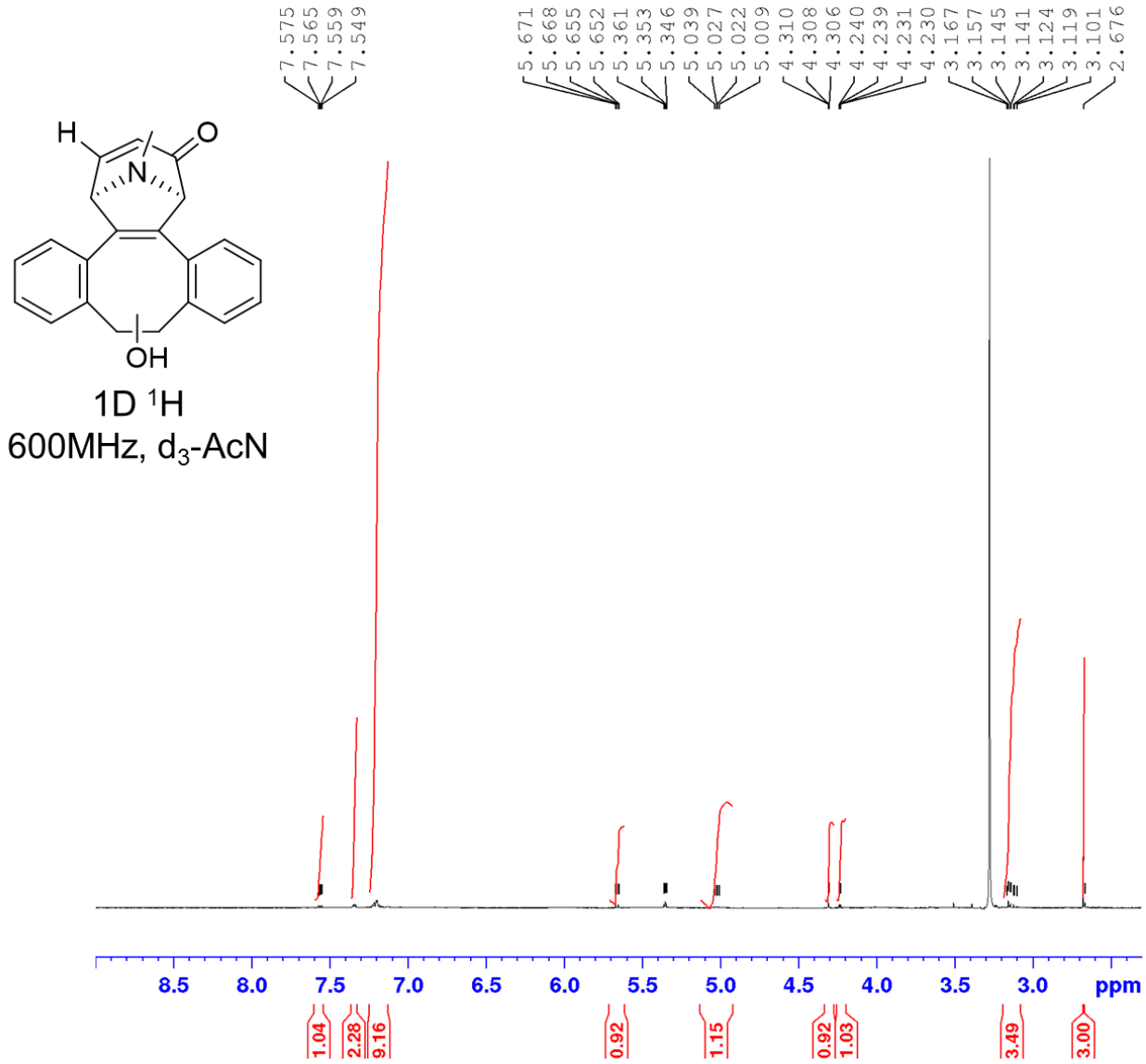
7.575
7.565
7.559
7.549
5.671
5.668
5.655
5.652
5.361
5.353
5.346
5.039
5.027
5.022
5.009
4.310
4.308
4.306
4.240
4.239
4.231
4.230
3.167
3.157
3.145
3.141
3.124
3.119
3.101
2.676
H
O
N
OH
1D ^{1}H
600MHz, d_3-AcN
8.5
8.0
7.5
7.0
6.5
6.0
5.5
5.0
4.5
4.0
3.5
3.0
ppm
1.04
2.28
9.16
0.92
1.15
0.92
1.03
3.49
3.00

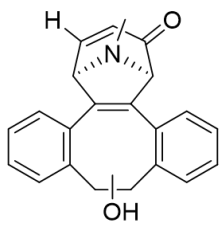

1D ^{13}C
151MHz, d_3-AcN

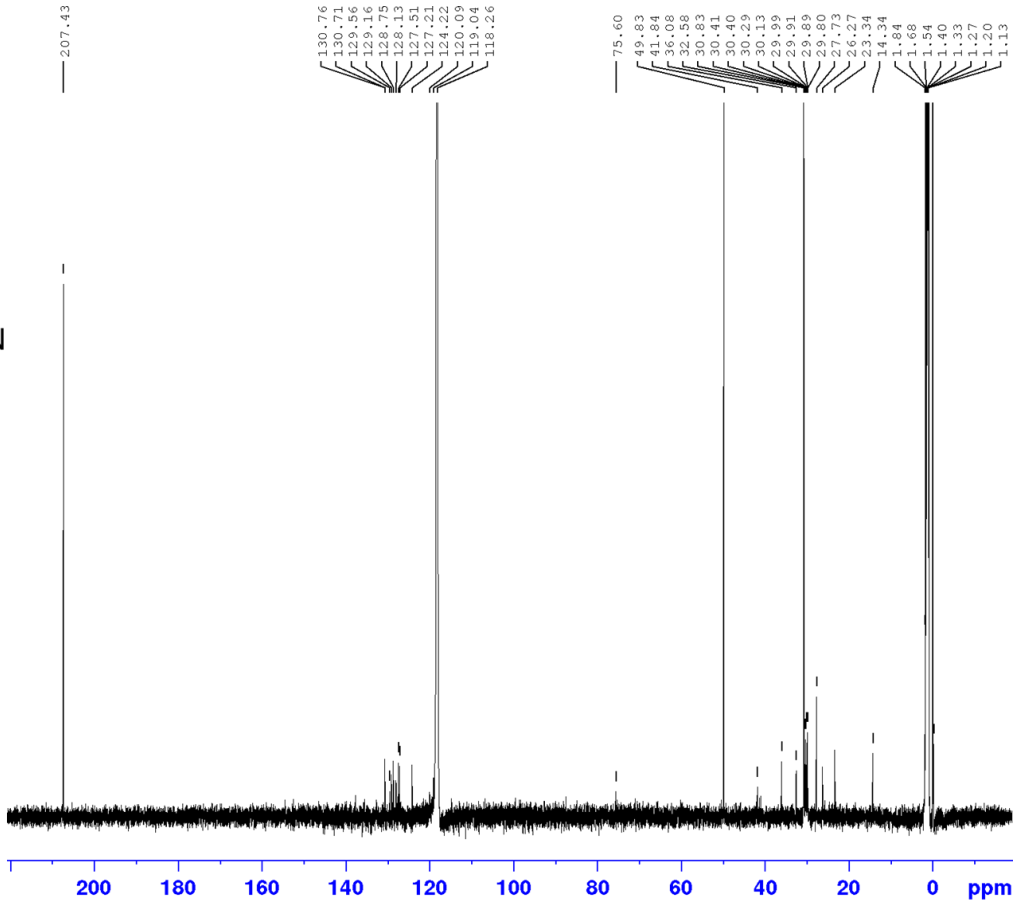

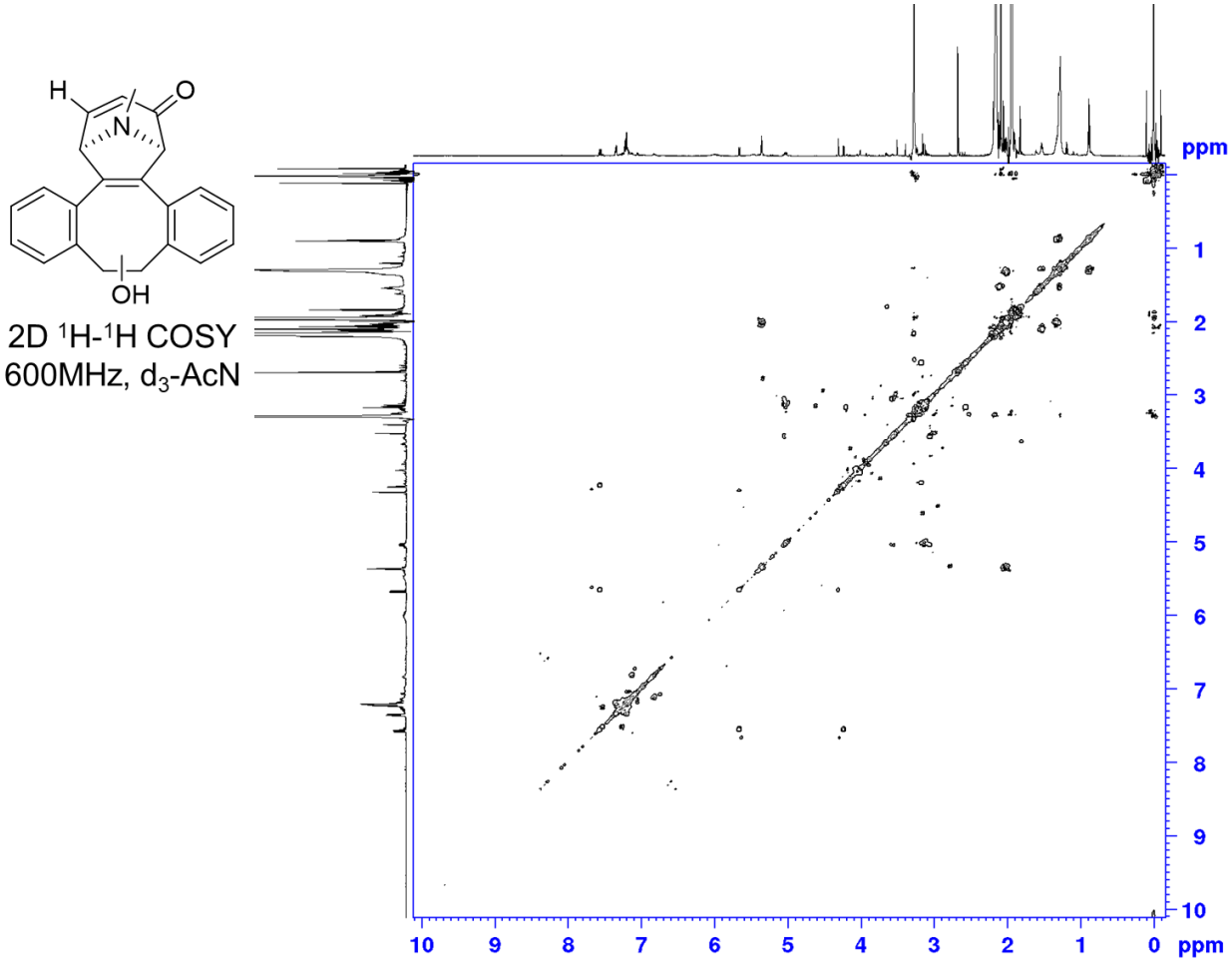
H
O
N
OH
2D ^{1}H-^{1}H COSY
600MHz, d_3-AcN
ppm
1
2
3
4
5
6
7
8
9
10
10 9 8 7 6 5 4 3 2 1 0 ppm

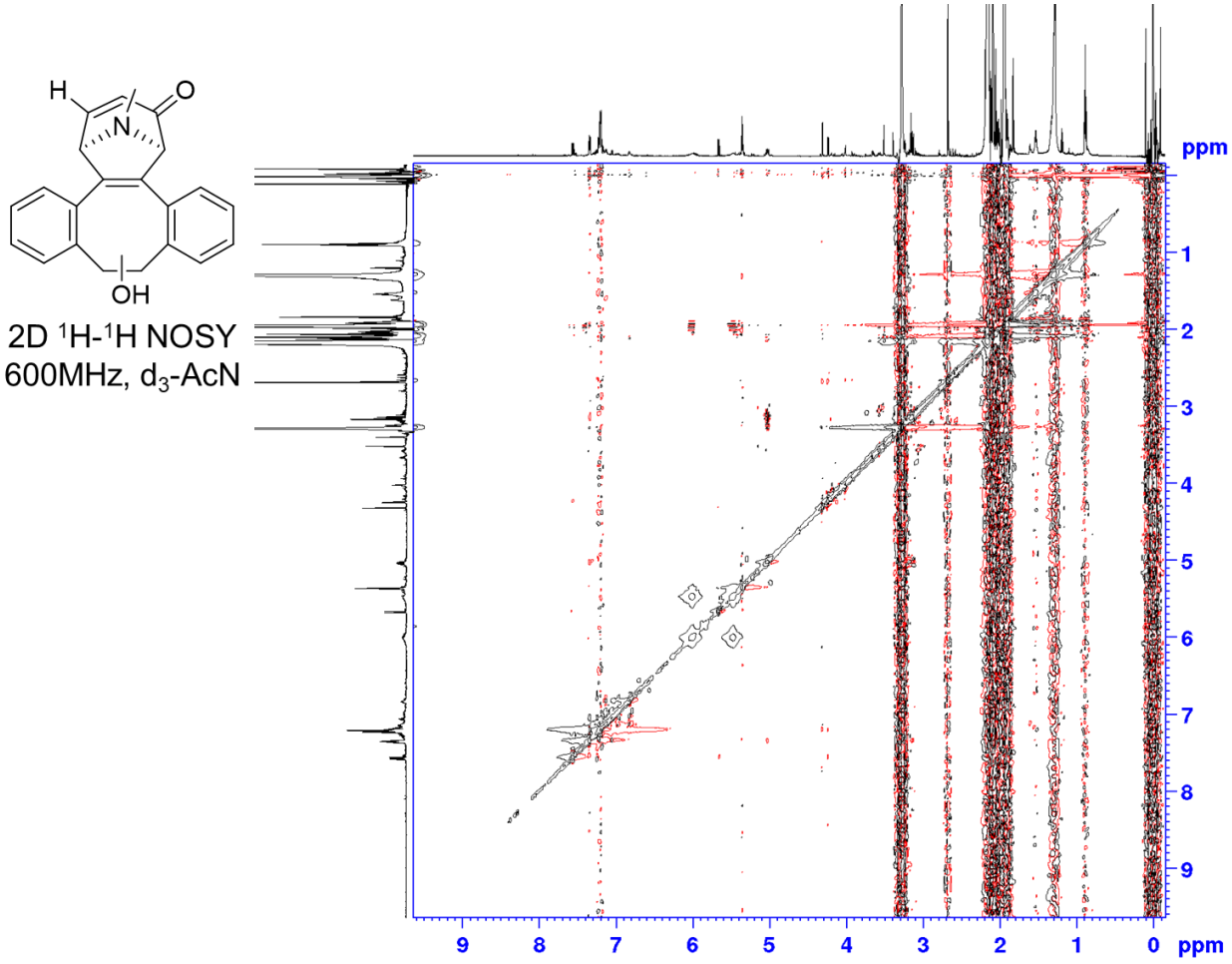
H
O
N
OH
2D ^{1}H-^{1}H NOSY
600MHz, d_3-AcN
ppm
1
2
3
4
5
6
7
8
9
9
8
7
6
5
4
3
2
1
0
ppm

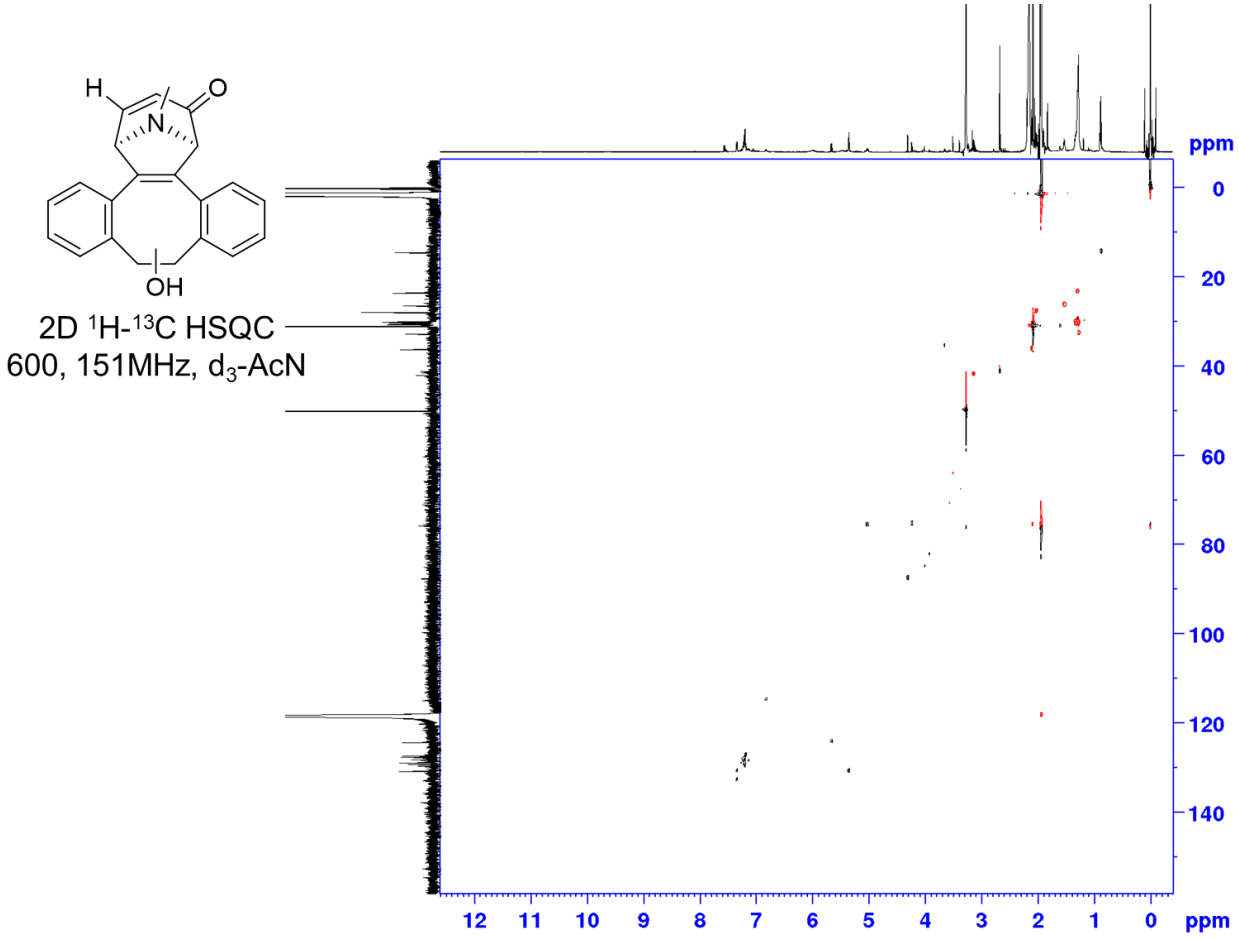
H
O
N
OH
2D ^{1}H-^{13}C HSQC
600, 151MHz, d_3-AcN
ppm
0
20
40
60
80
100
120
140
12
11
10
9
8
7
6
5
4
3
2
1
0
ppm

Spectra of Cycloaddition Product 5c:

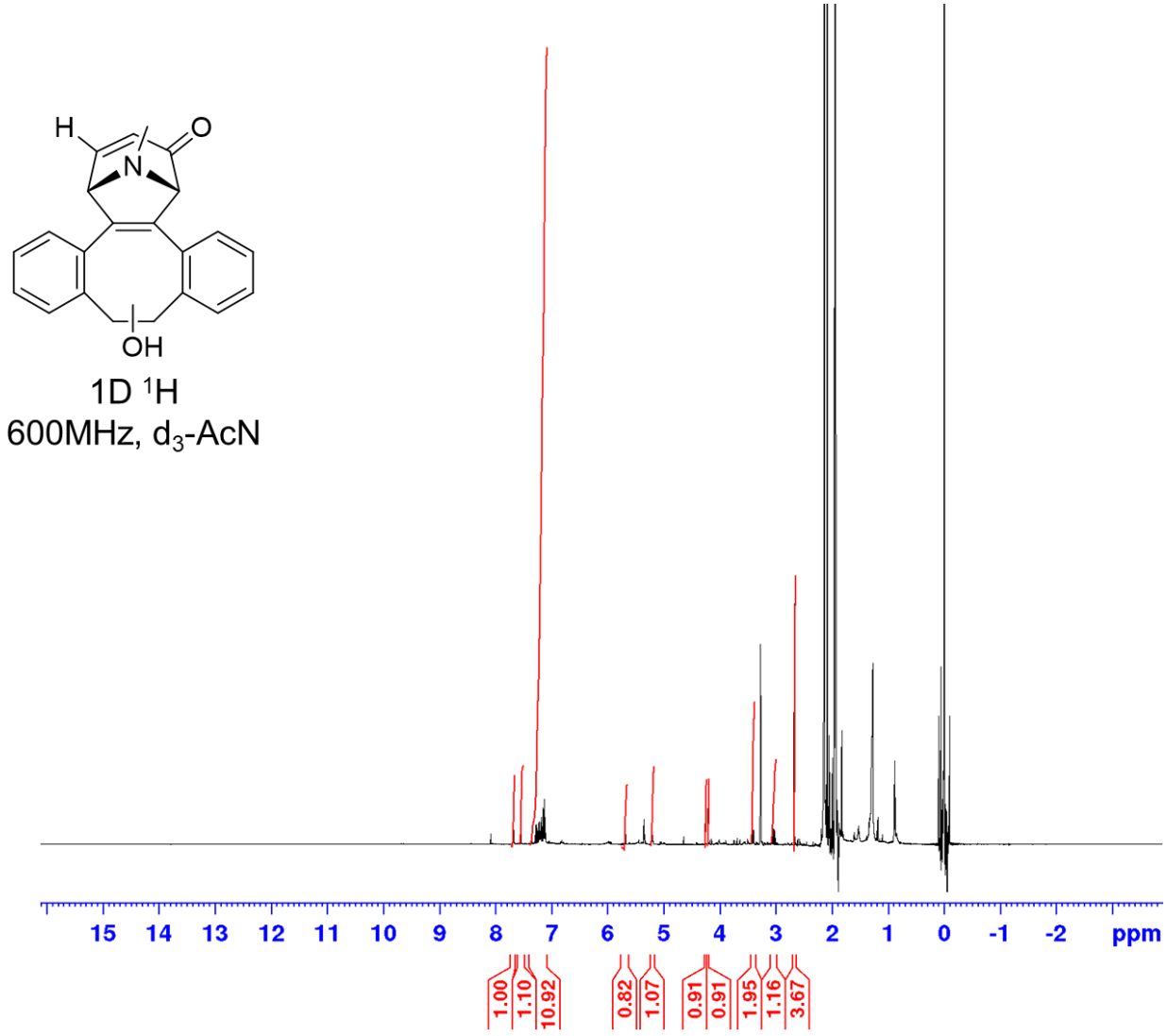

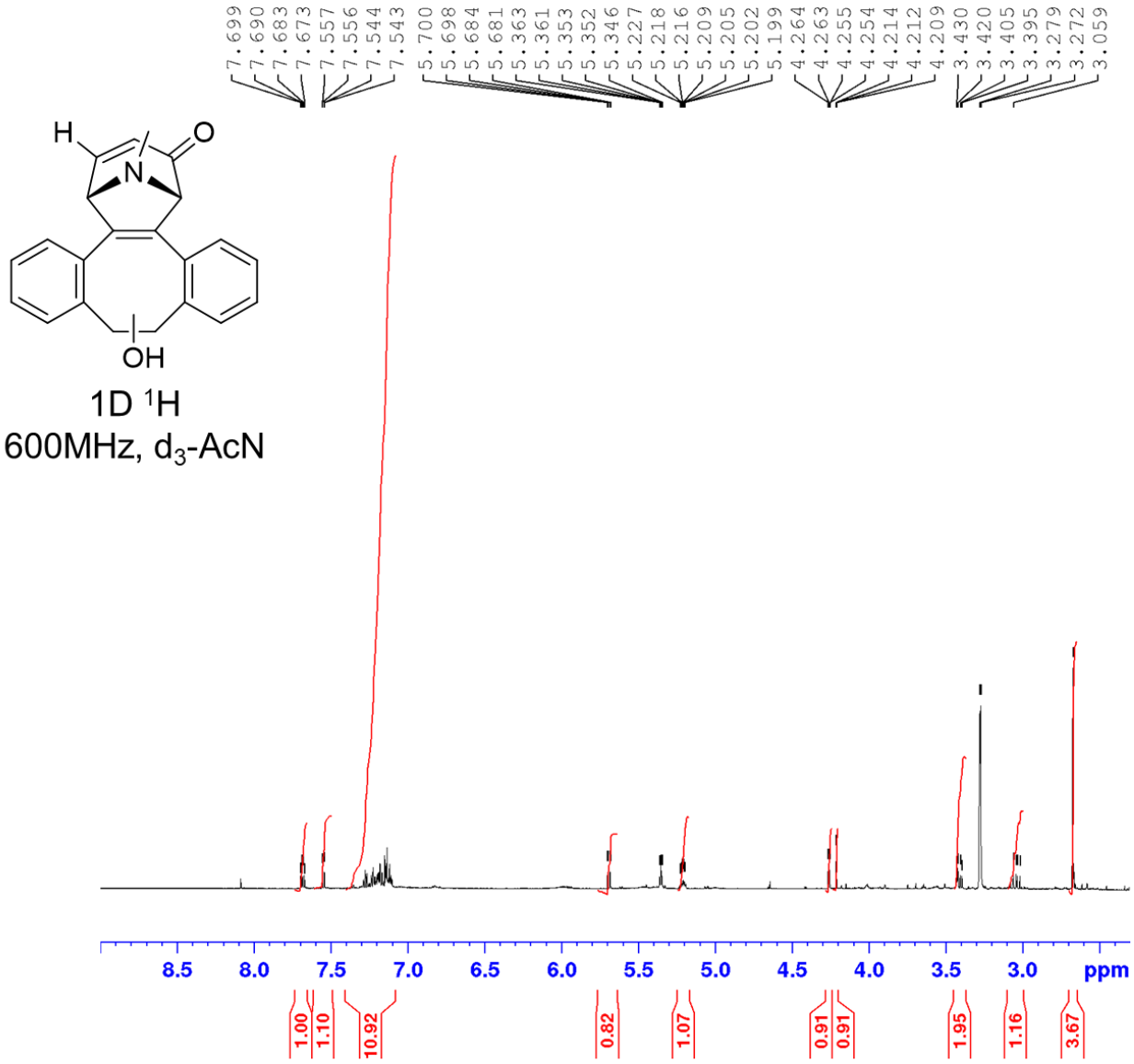
7.699
7.690
7.683
7.673
7.557
7.556
7.544
7.543
5.700
5.698
5.684
5.681
5.363
5.361
5.353
5.352
5.346
5.227
5.218
5.216
5.209
5.205
5.202
5.199
4.264
4.263
4.255
4.254
4.214
4.212
4.209
3.430
3.420
3.405
3.395
3.279
3.272
3.059
H
O
N
OH
1D ^{1}H
600MHz, d_3-AcN
8.5
8.0
7.5
7.0
6.5
6.0
5.5
5.0
4.5
4.0
3.5
3.0
ppm
1.00
1.10
10.92
0.82
1.07
0.91
0.91
1.95
1.16
3.67

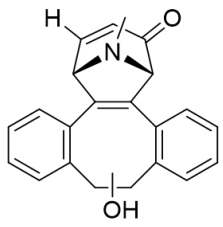

1D ^{13}C
151MHz, d_3-AcN

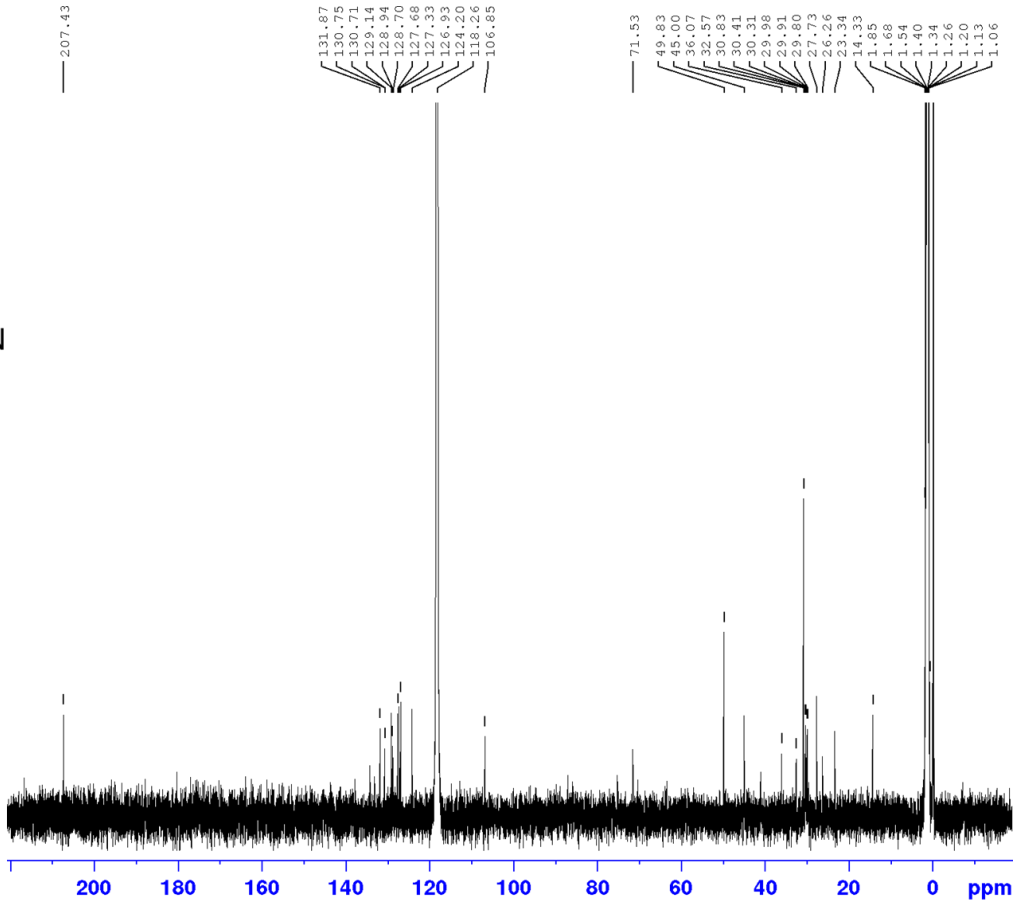

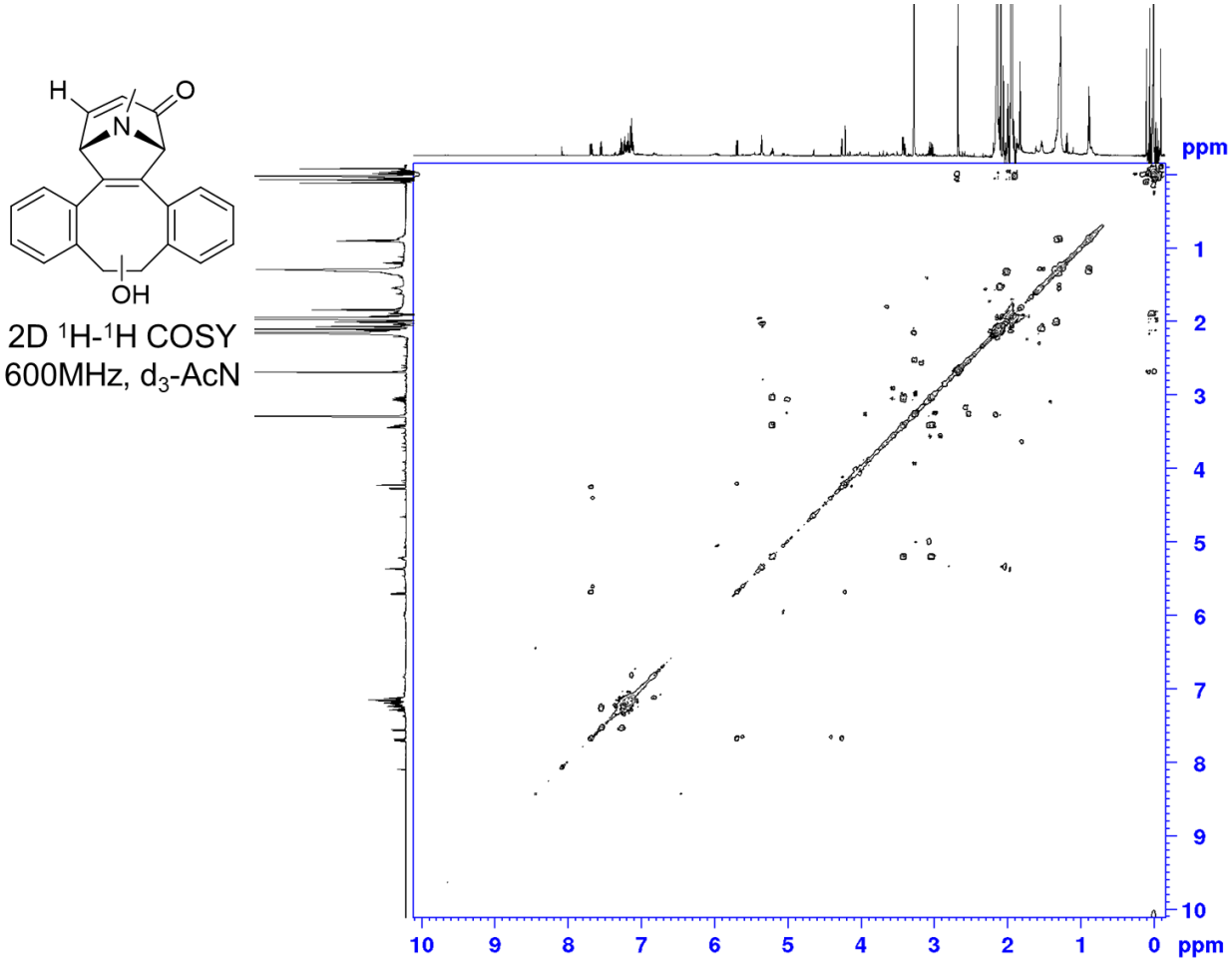
H
O
N
OH
2D ^{1}H-^{1}H COSY
600MHz, d_3-AcN
ppm
1
2
3
4
5
6
7
8
9
10
10 9 8 7 6 5 4 3 2 1 0 ppm

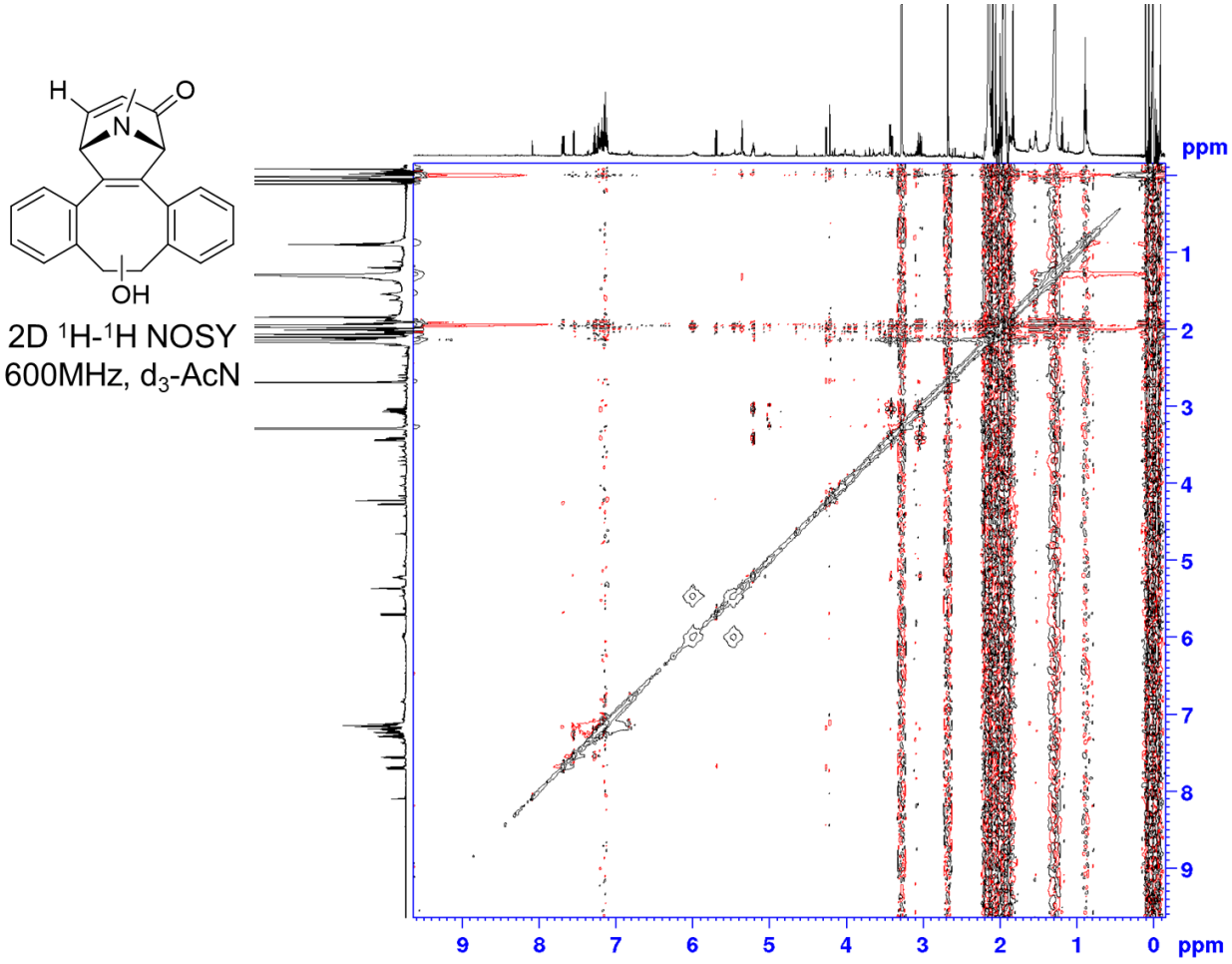
H
O
N
OH
2D ^{1}H-^{1}H NOSY
600MHz, d_3-AcN
ppm
1
2
3
4
5
6
7
8
9
9
8
7
6
5
4
3
2
1
0
ppm

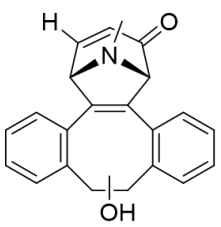

2D ^{1}H-^{13}C HSQC
600, 151MHz, d_3-AcN

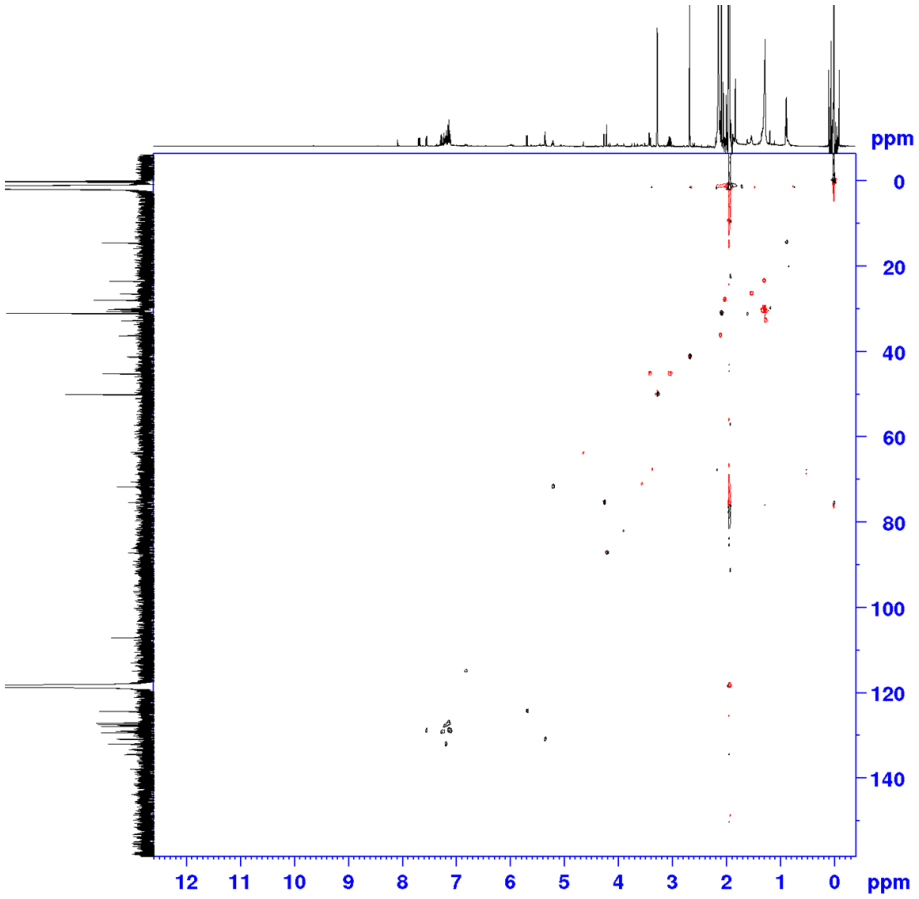

Spectra of Cycloaddition Product 5d:

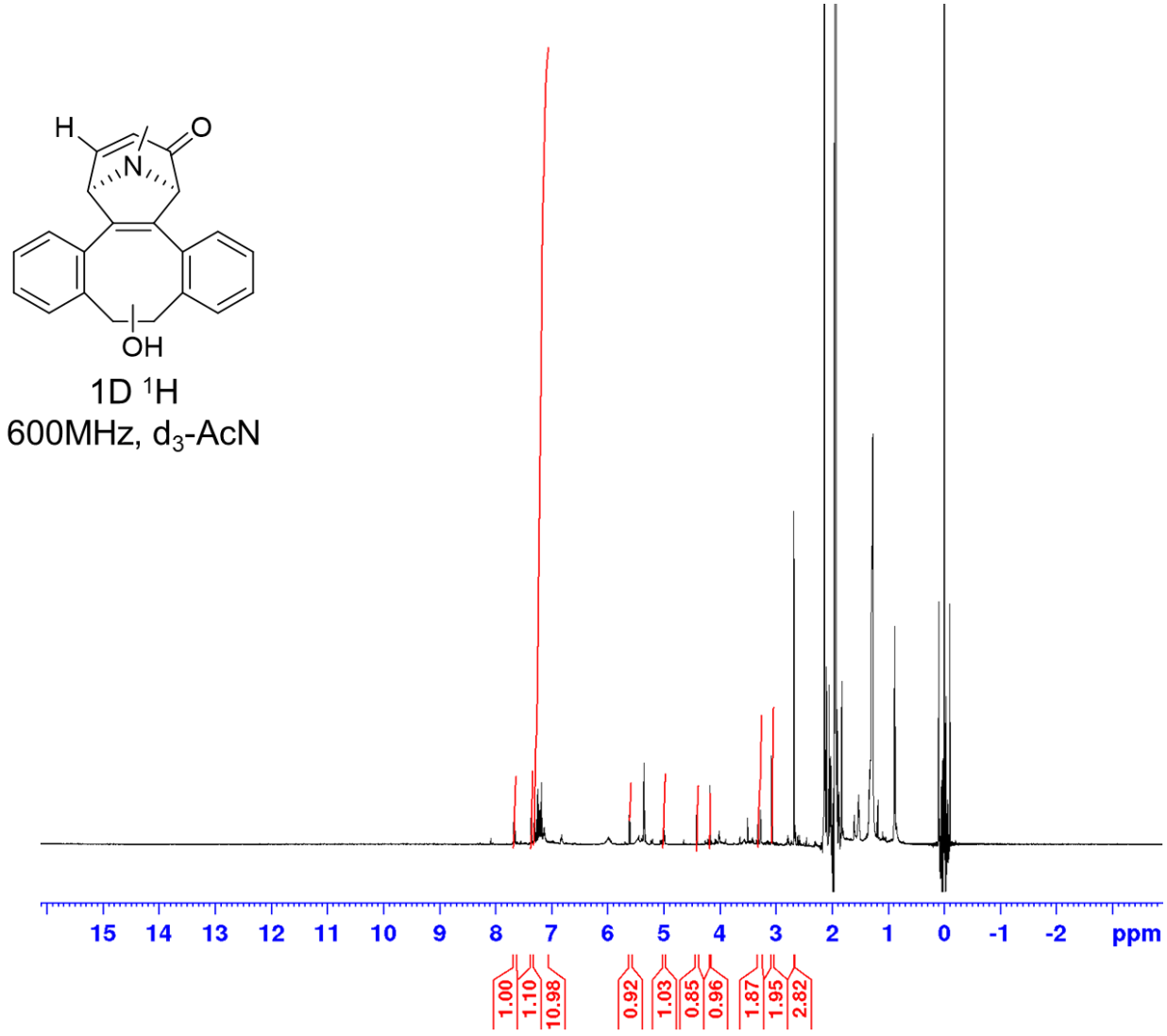

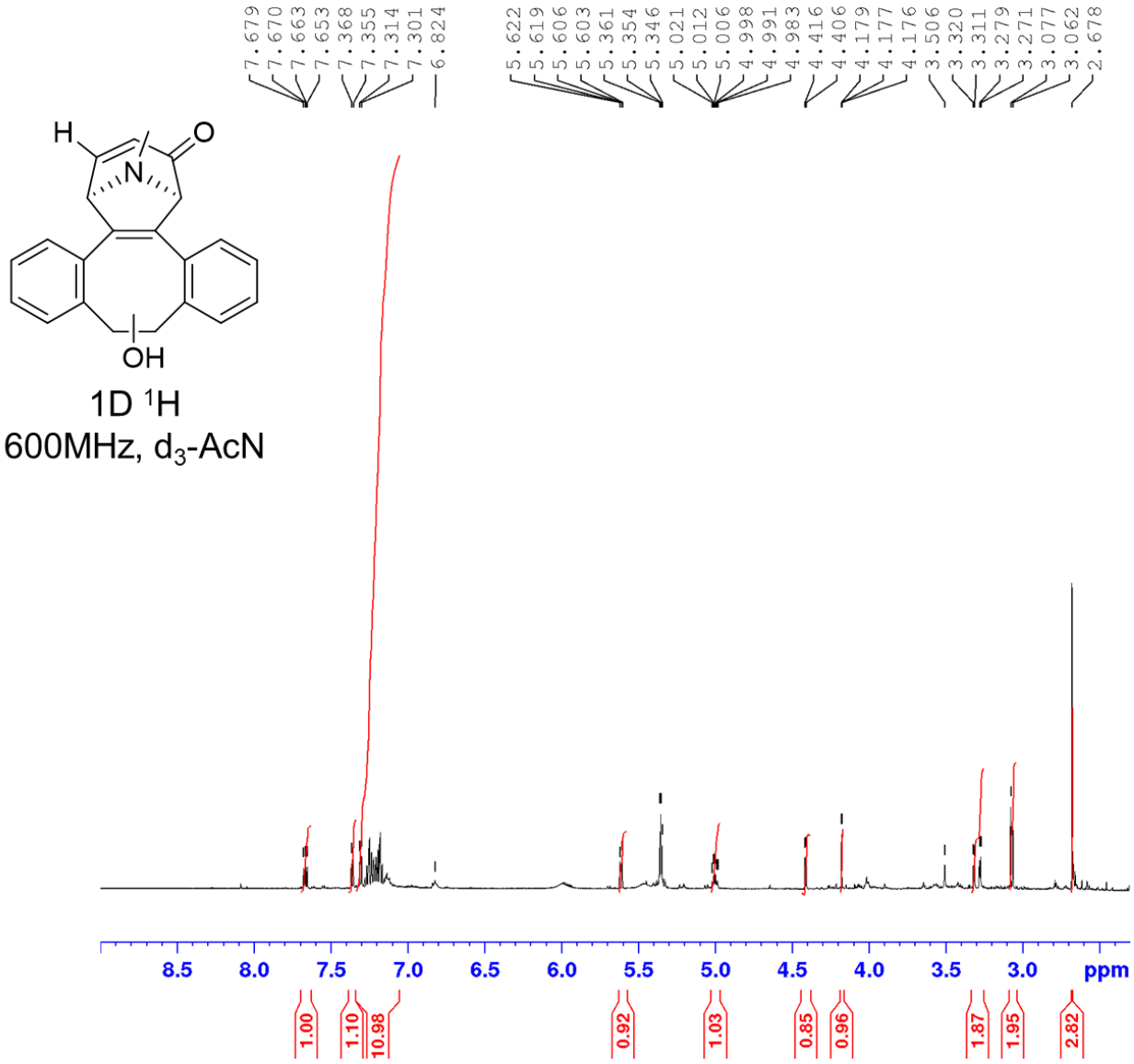
7.679
7.670
7.663
7.653
7.368
7.355
7.314
7.301
6.824
5.622
5.619
5.606
5.603
5.361
5.354
5.346
5.021
5.012
5.006
4.998
4.991
4.983
4.416
4.406
4.179
4.177
4.176
3.506
3.320
3.311
3.279
3.271
3.077
3.062
2.678
H
O
N
OH
1D ^{1}H
600MHz, d_3-AcN
8.5
8.0
7.5
7.0
6.5
6.0
5.5
5.0
4.5
4.0
3.5
3.0
ppm
1.00
1.10
10.98
0.92
1.03
0.85
0.96
1.87
1.95
2.82

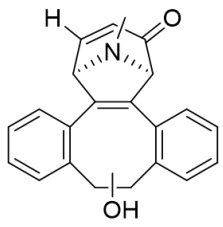

1D ^{13}C
151MHz, d_3-AcN

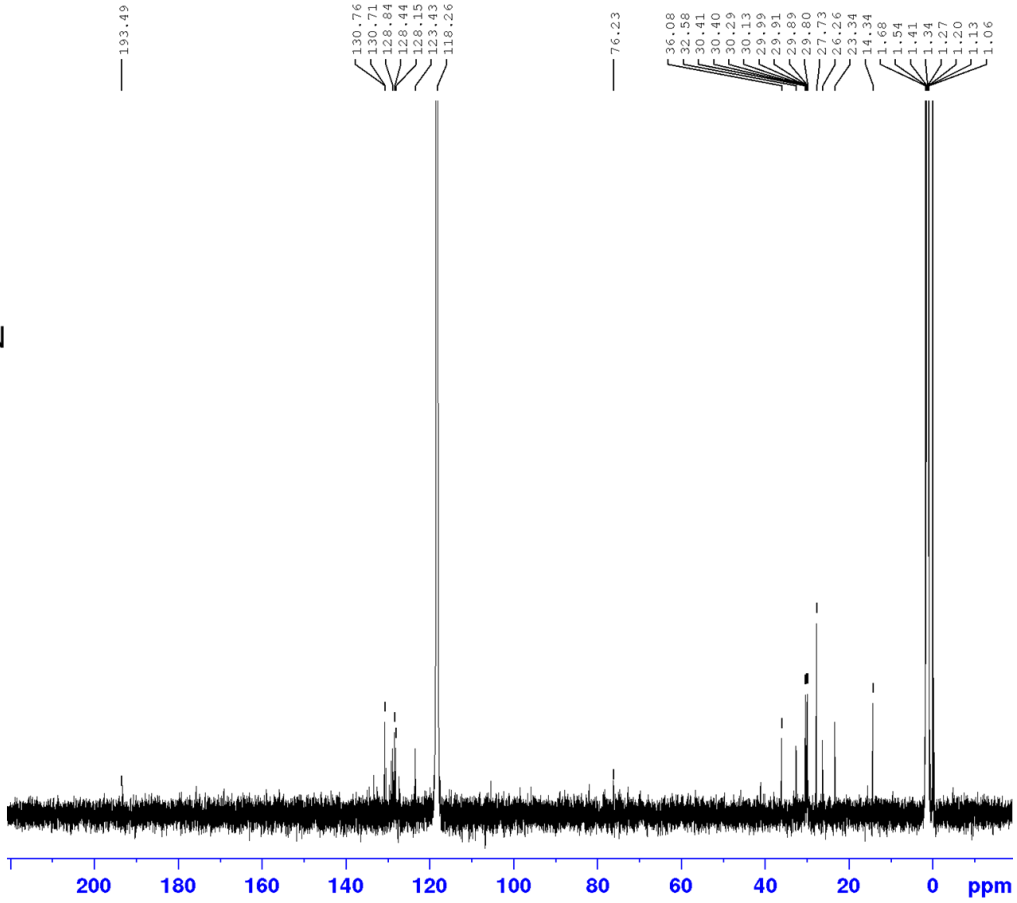

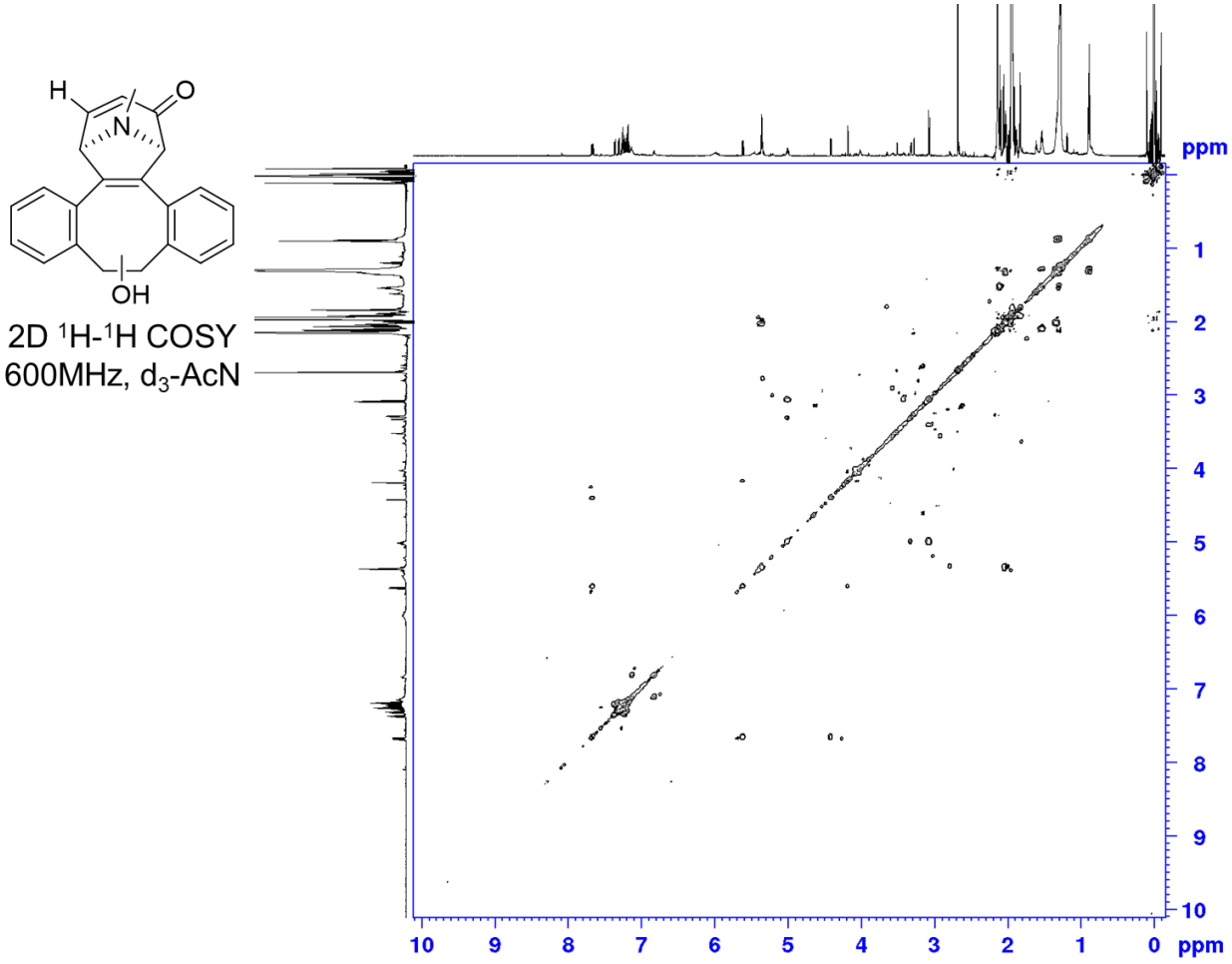
H
O
N
OH
2D ^{1}H-^{1}H COSY
600MHz, d_3-AcN
ppm
1
2
3
4
5
6
7
8
9
10
10
9
8
7
6
5
4
3
2
1
0
ppm

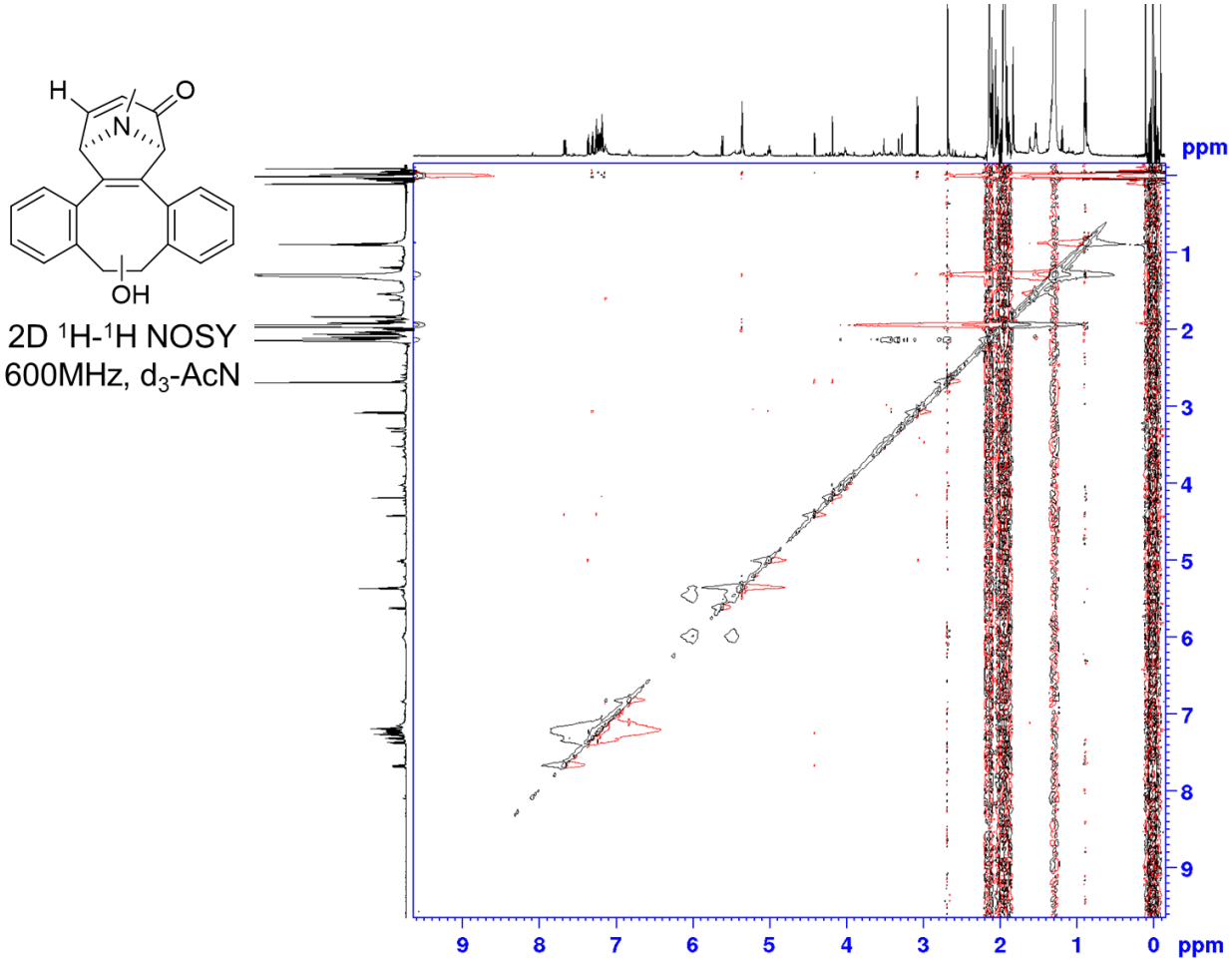
H
O
N
OH
2D ^{1}H-^{1}H NOSY
600MHz, d_3-AcN
ppm
1
2
3
4
5
6
7
8
9
9
8
7
6
5
4
3
2
1
0
ppm

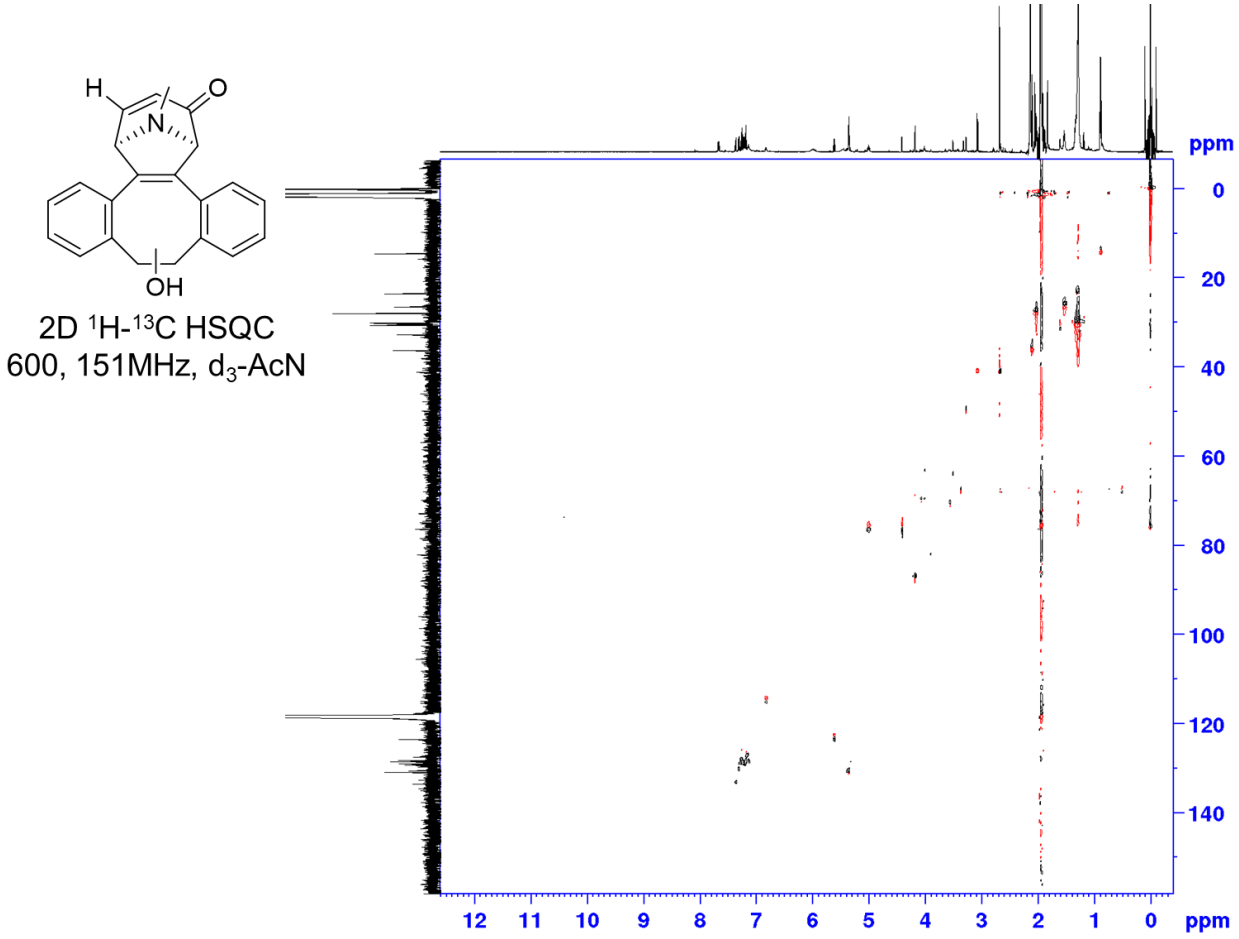
H
O
N
OH
2D ^{1}H-^{13}C HSQC
600, 151MHz, d_3-AcN
ppm
0
20
40
60
80
100
120
140
12
11
10
9
8
7
6
5
4
3
2
1
0
ppm

Spectra of Cycloaddition Product 7:

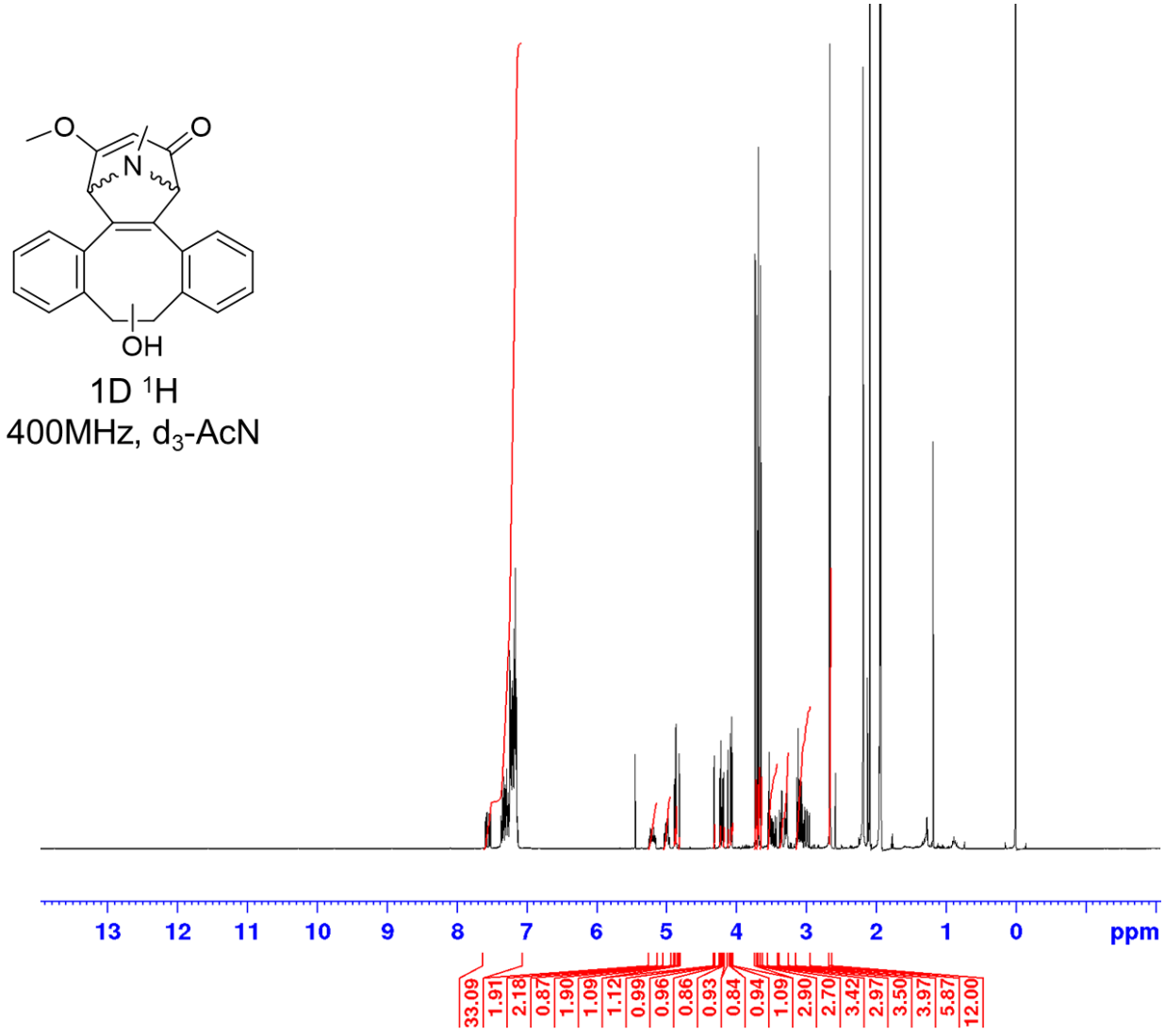

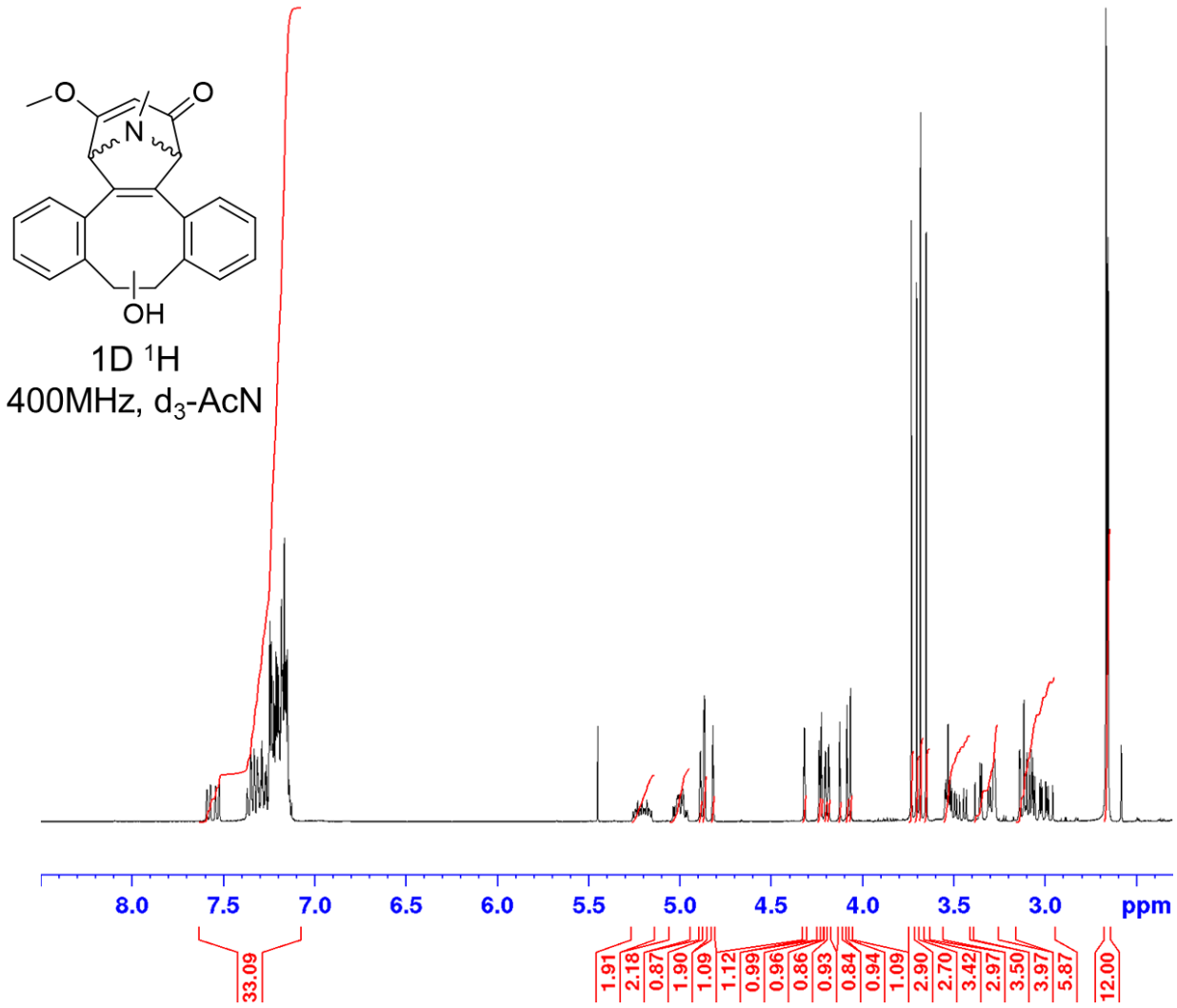
O
O
N
OH
1D ^{1}H
400MHz, d_3-AcN
8.0
7.5
7.0
6.5
6.0
5.5
5.0
4.5
4.0
3.5
3.0
ppm
33.09
1.91
2.18
0.87
1.90
1.09
1.12
0.99
0.96
0.86
0.93
0.84
0.94
1.09
2.90
2.70
3.42
2.97
3.50
3.97
5.87
12.00

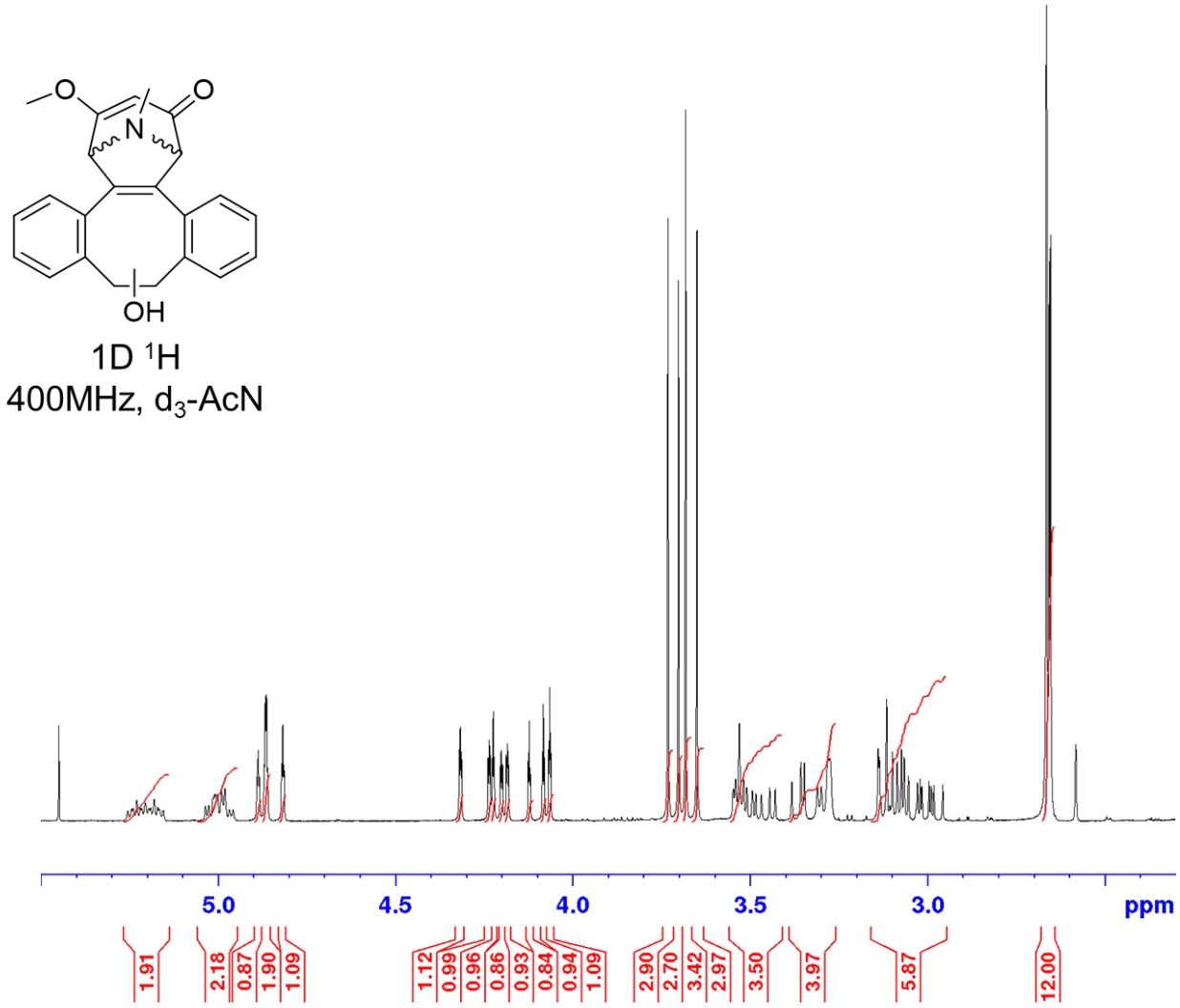
O
O
N
OH
1D ^{1}H
400MHz, d_3-AcN
5.0
4.5
4.0
3.5
3.0
ppm
1.91
2.18
0.87
1.90
1.09
1.12
0.99
0.96
0.86
0.93
0.84
0.94
1.09
2.90
2.70
3.42
2.97
3.50
3.97
5.87
12.00

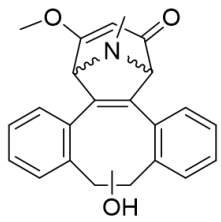

1D ^{13}C
100MHz, d_3-AcN

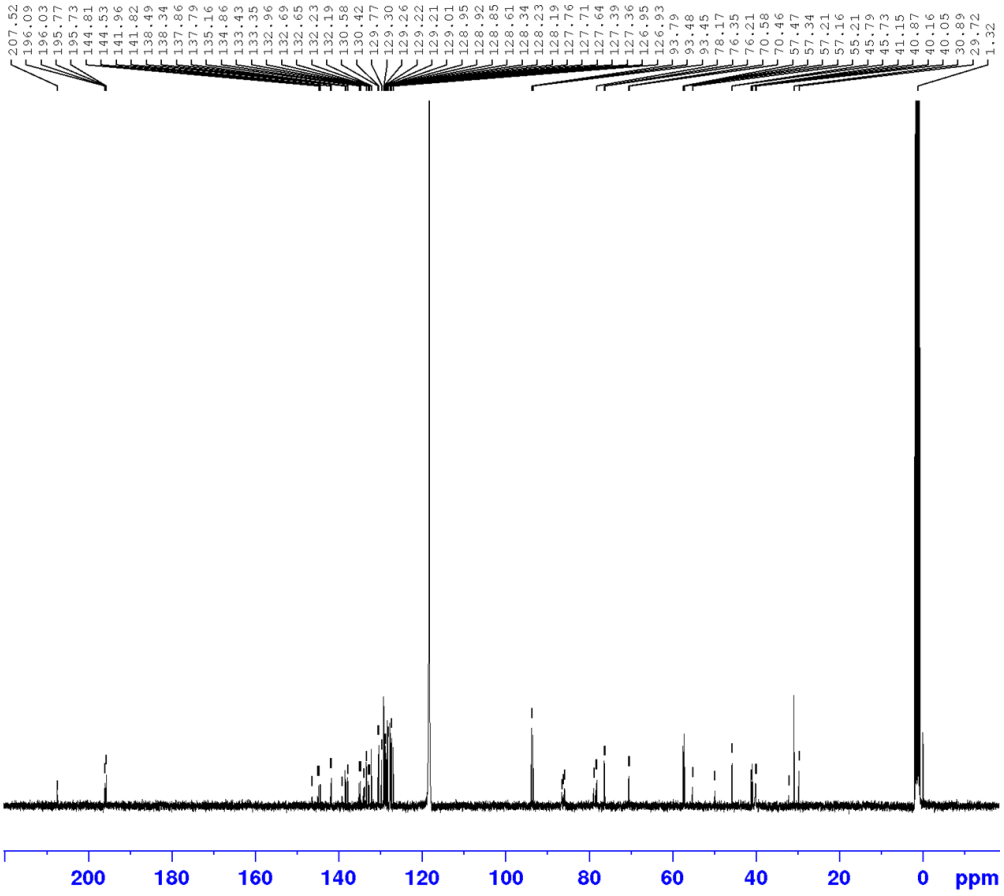

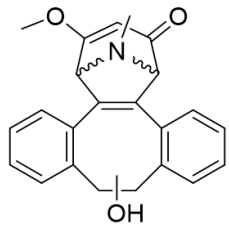

2D ^{1}H-^{1}H COSY
400MHz, d_3-AcN

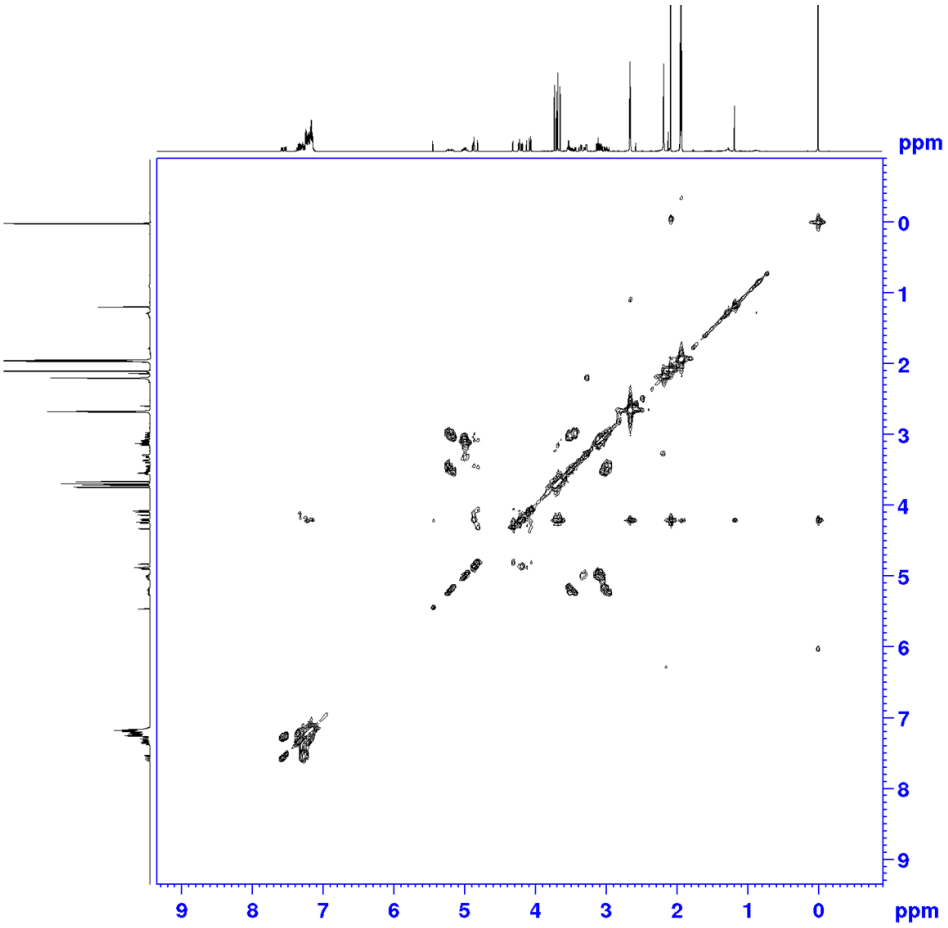

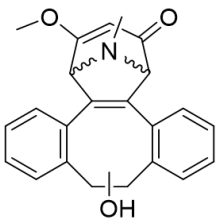

2D ^{1}H-^{13}C HSQC
400, 100 MHz, d_3-AcN

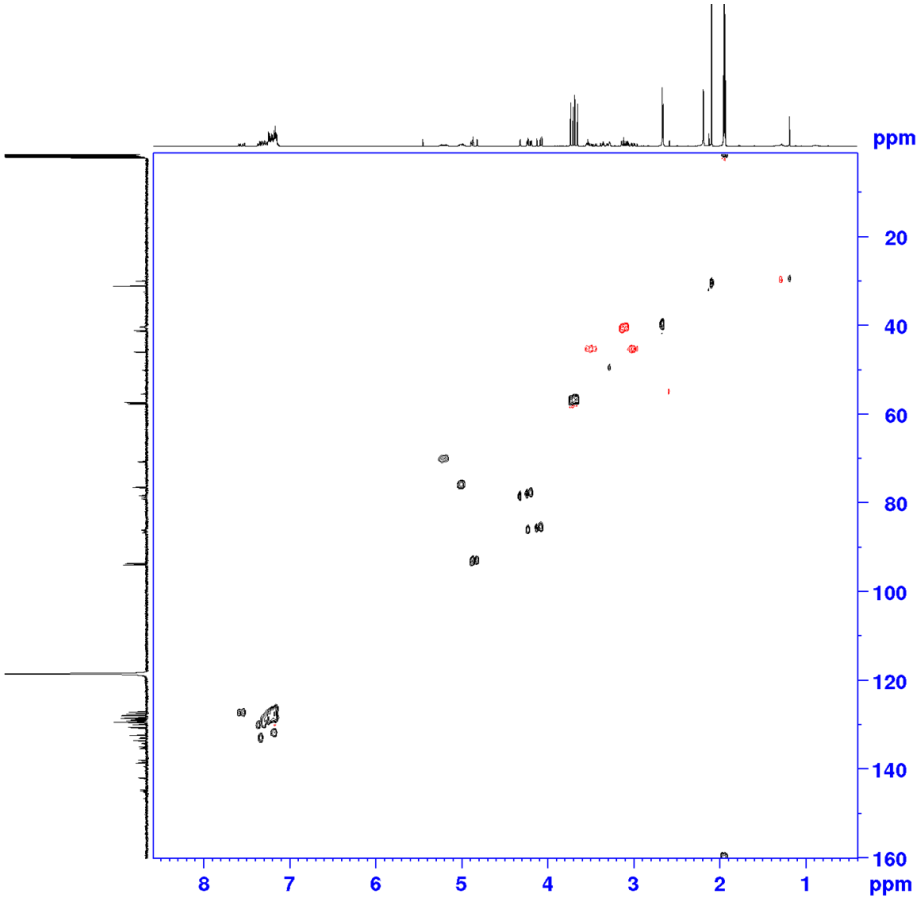

Spectra of Cycloaddition Product 8:

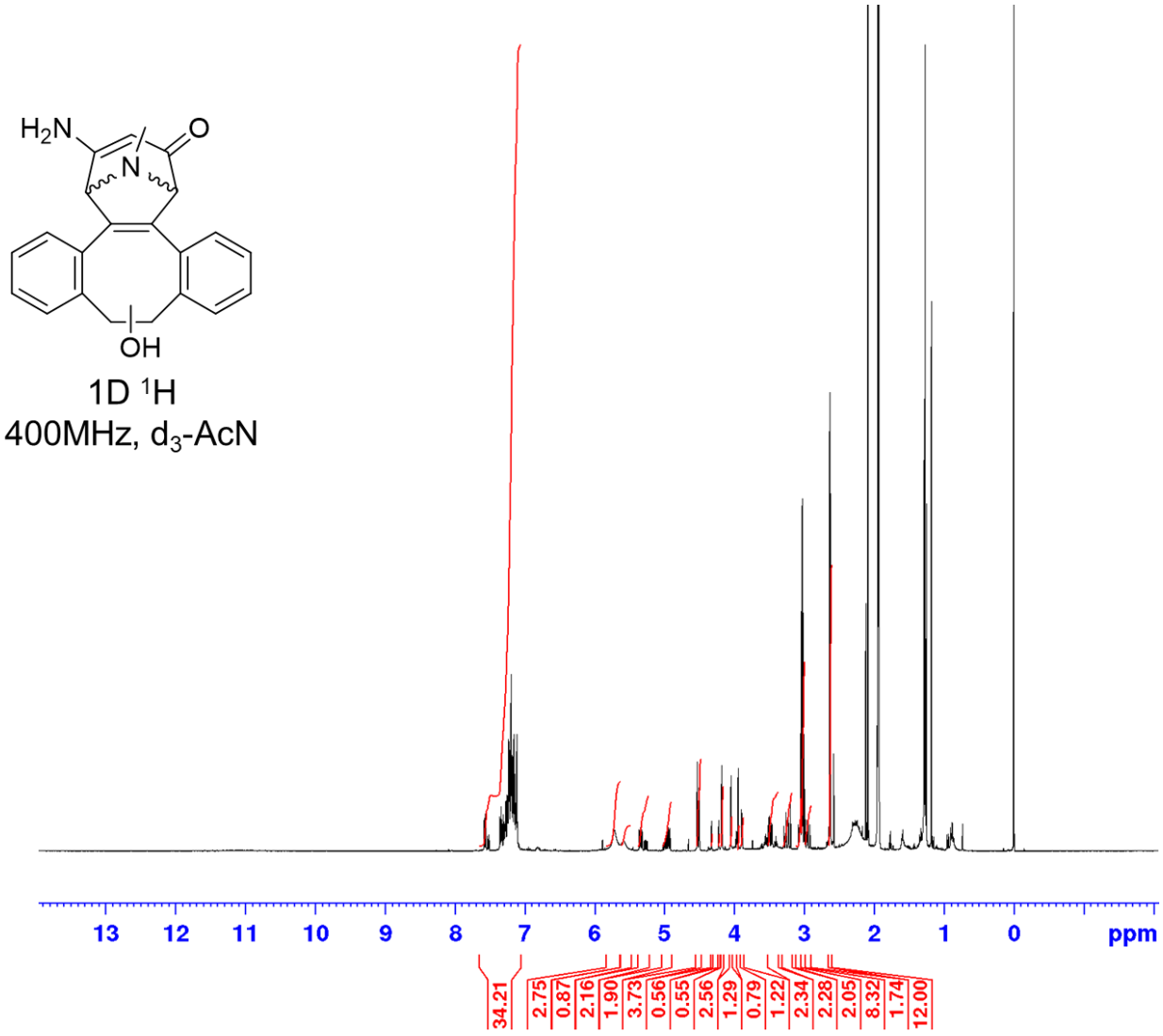

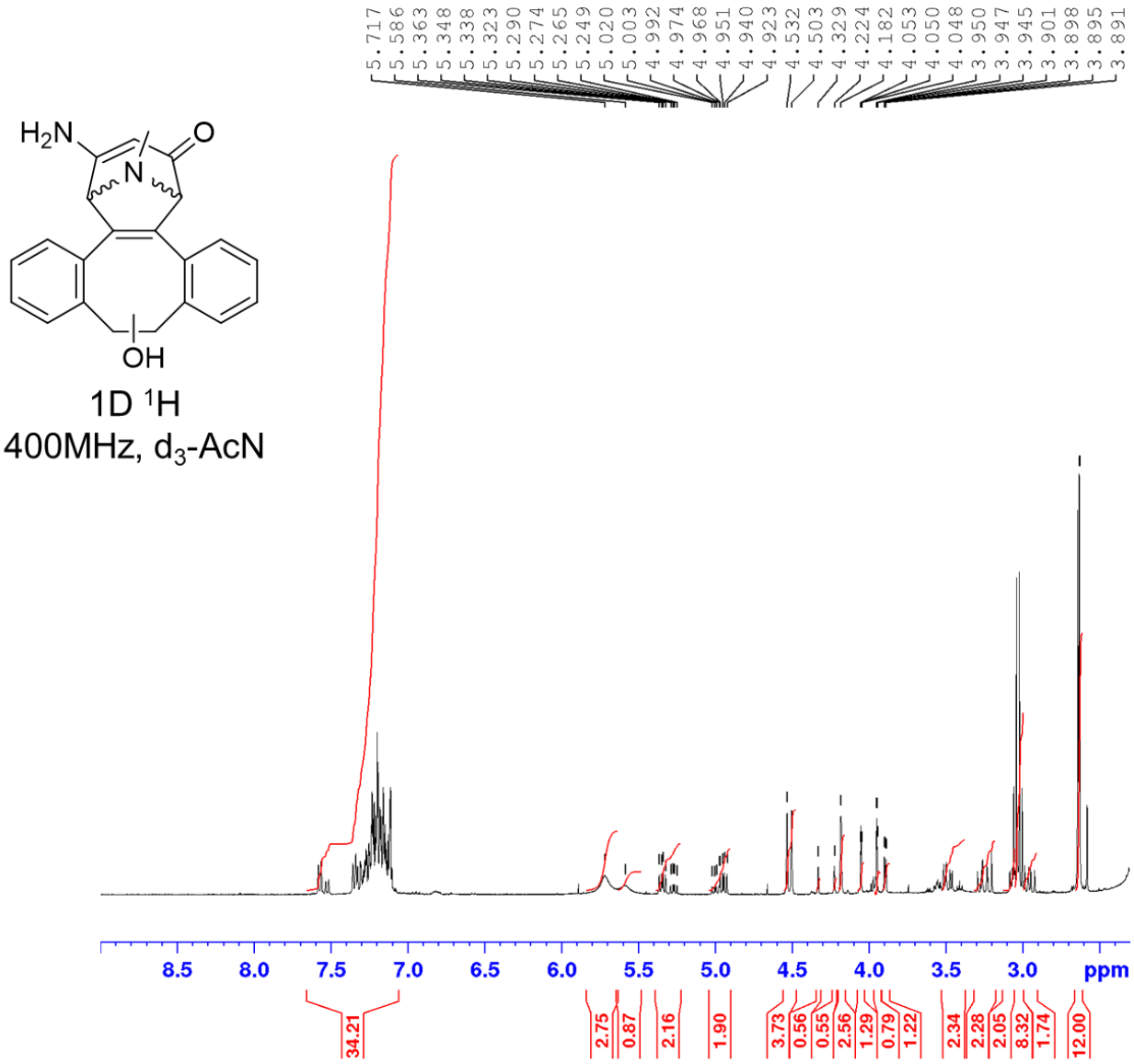
5.717
5.586
5.363
5.348
5.338
5.323
5.290
5.274
5.265
5.249
5.020
5.003
4.992
4.974
4.968
4.951
4.940
4.923
4.532
4.503
4.329
4.224
4.182
4.053
4.050
4.048
3.950
3.947
3.945
3.901
3.898
3.895
3.891
H2N
O
N
OH
1D 1H
400MHz, d3-AcN
8.5
8.0
7.5
7.0
6.5
6.0
5.5
5.0
4.5
4.0
3.5
3.0
ppm
34.21
2.75
0.87
2.16
1.90
3.73
0.56
0.55
2.56
1.29
0.79
1.22
2.34
2.28
2.05
8.32
1.74
12.00

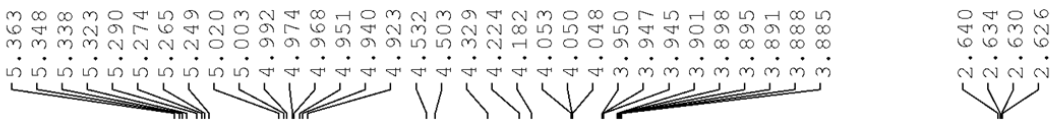

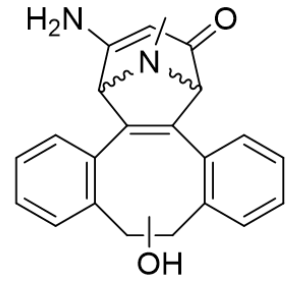

1D ^{1}H
400MHz, d_3-AcN

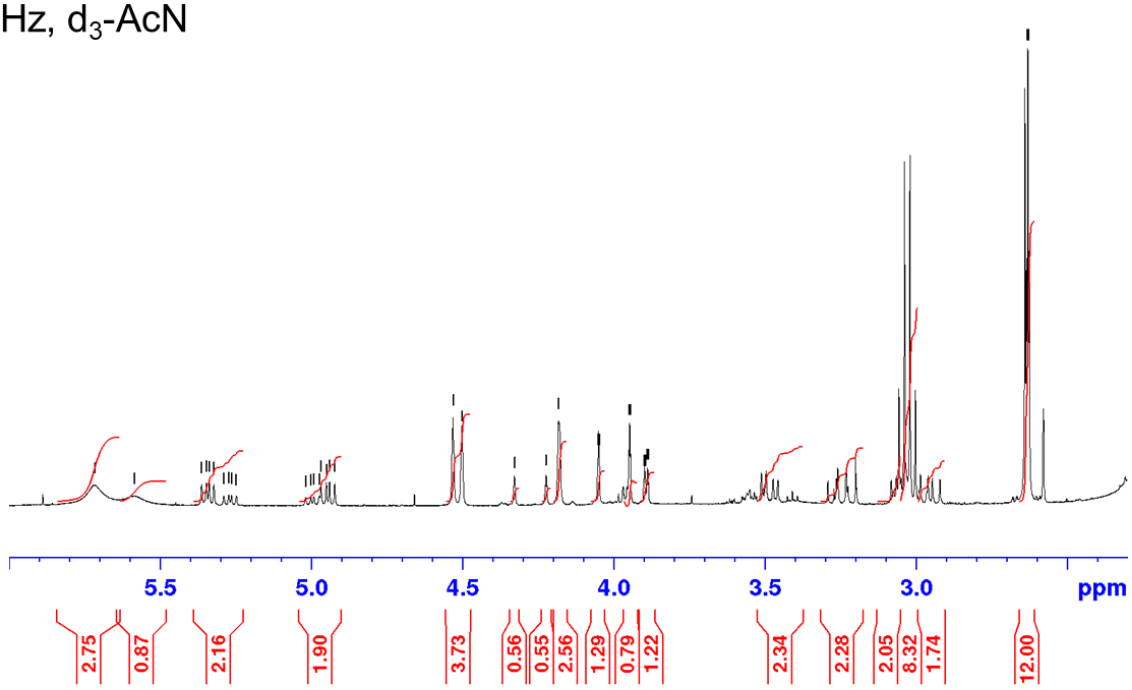

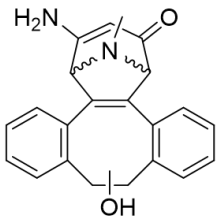

1D ^{13}C
100MHz, d_3-AcN

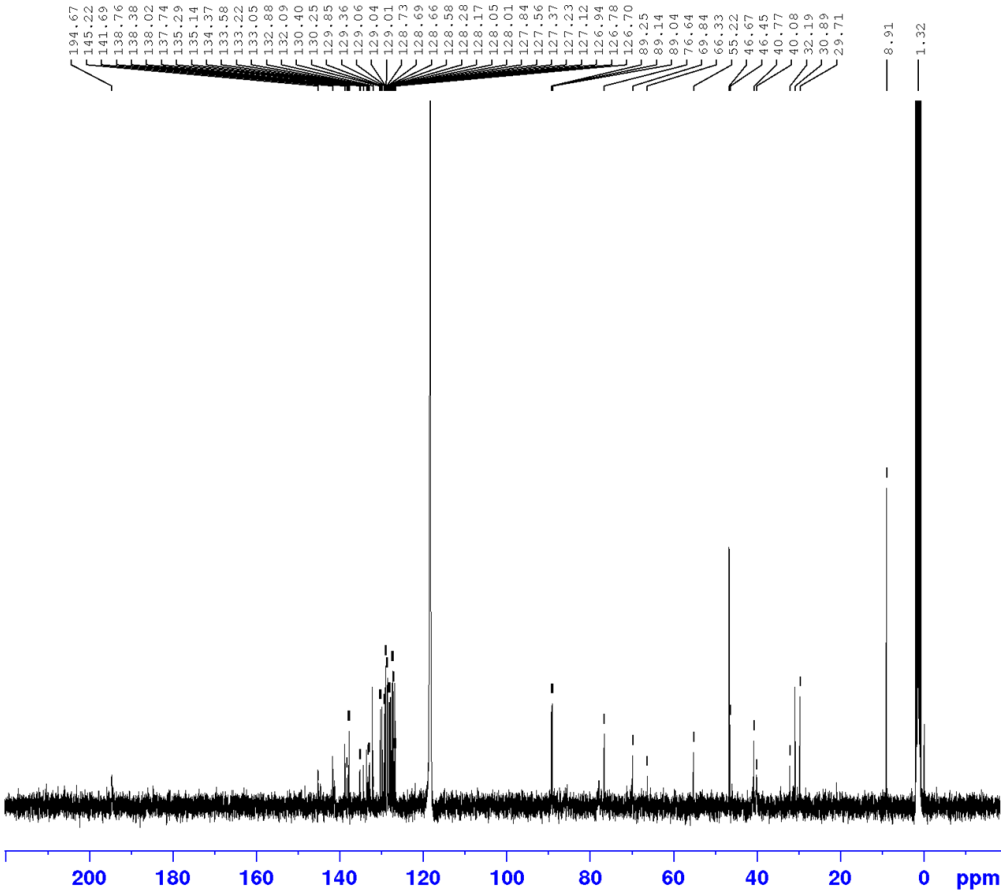

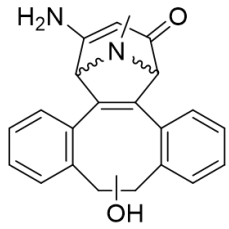

2D ^{1}H-^{1}H COSY
400MHz, d_3-AcN

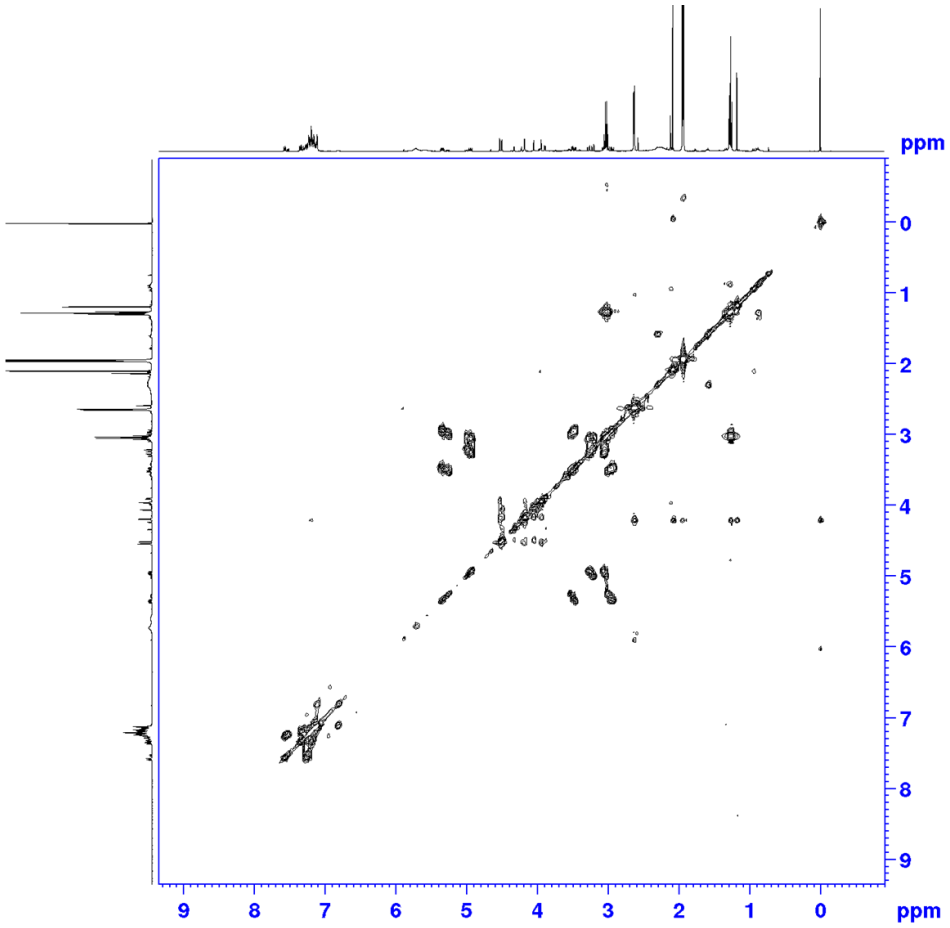

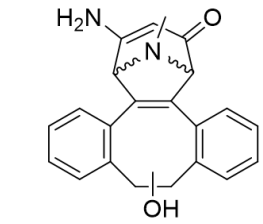

2D ^{1}H-^{13}C HSQC
400, 100 MHz, d_3-AcN

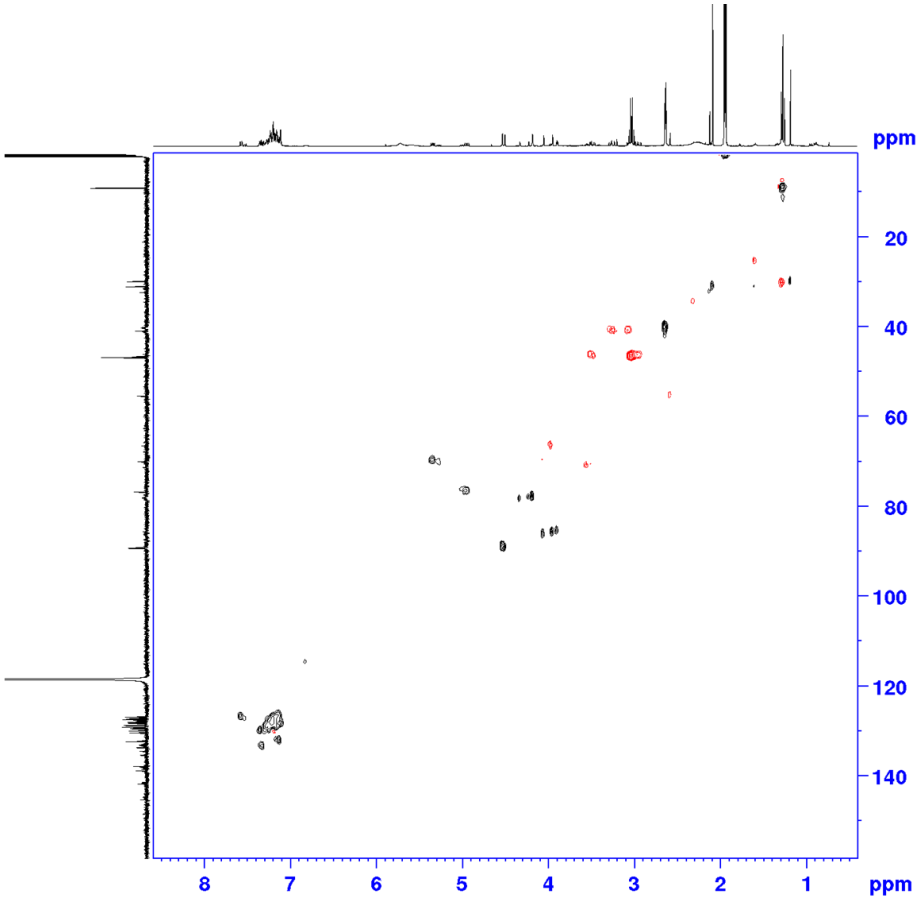

Spectra of Cycloaddition Product 6:

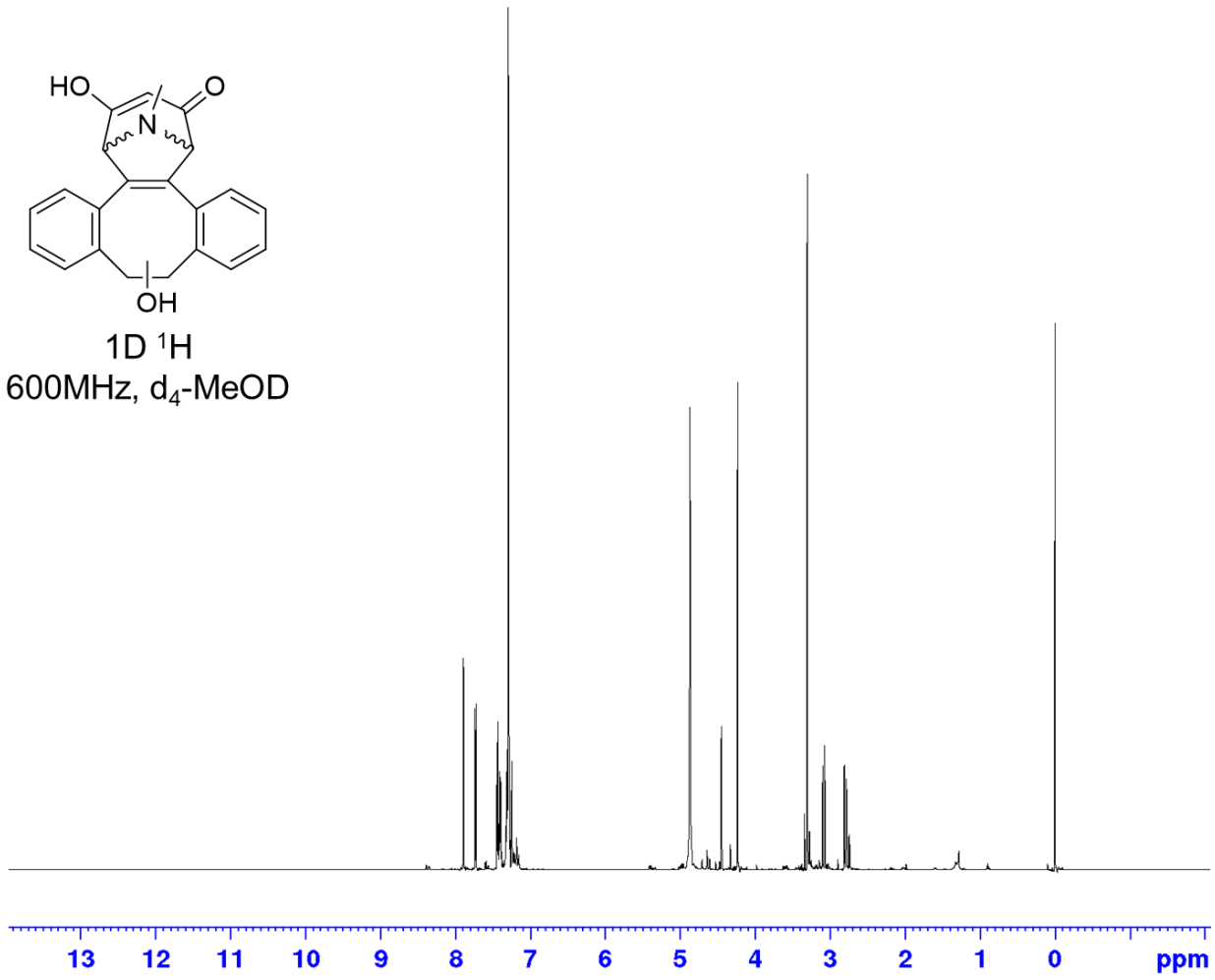

^{1}H spectrum taken automatically after NMR kinetics experiment.

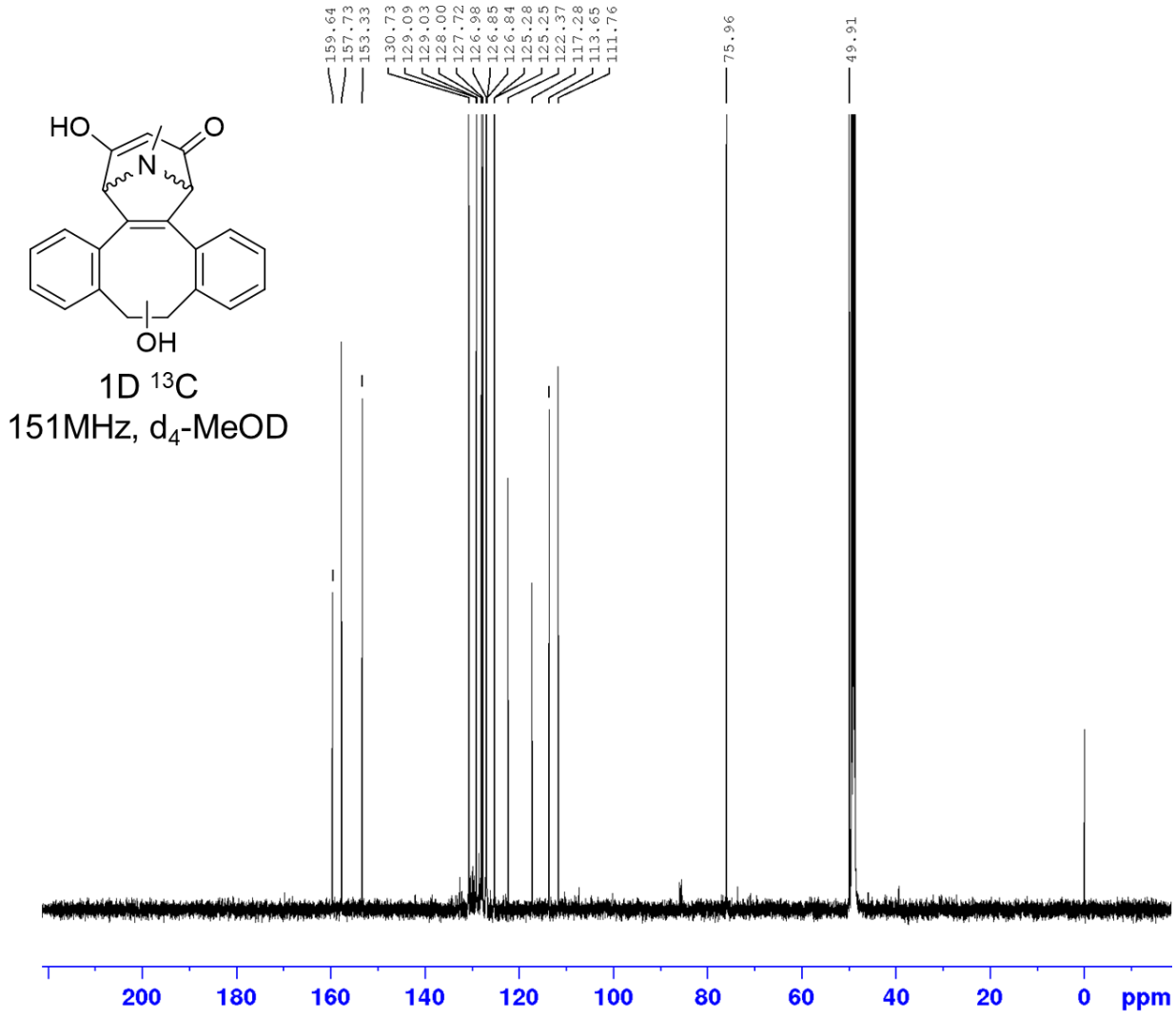

^{13}C spectrum taken automatically after NMR kinetics experiment.

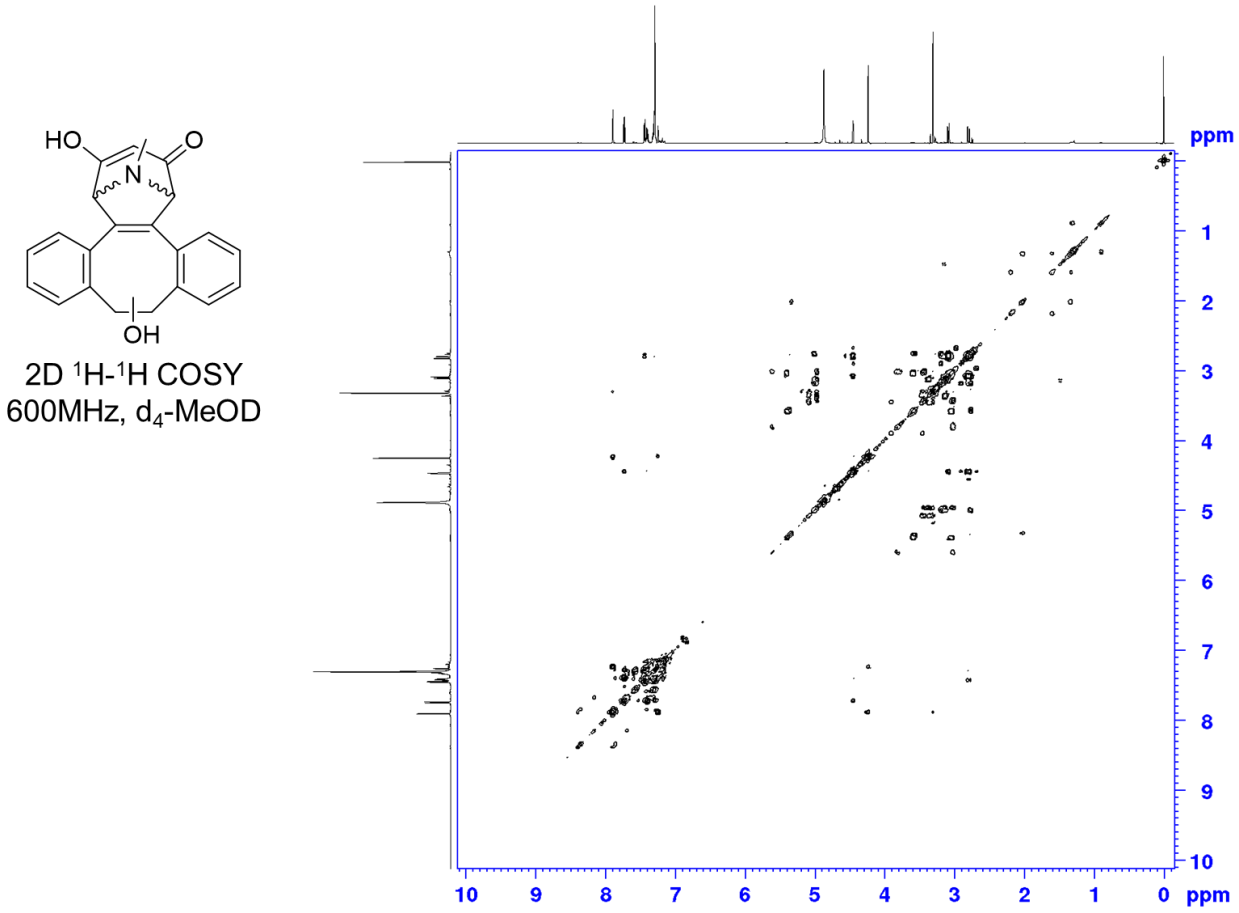

2D ^{1}H-^{1}H COSY spectrum taken automatically after NMR kinetics experiment.

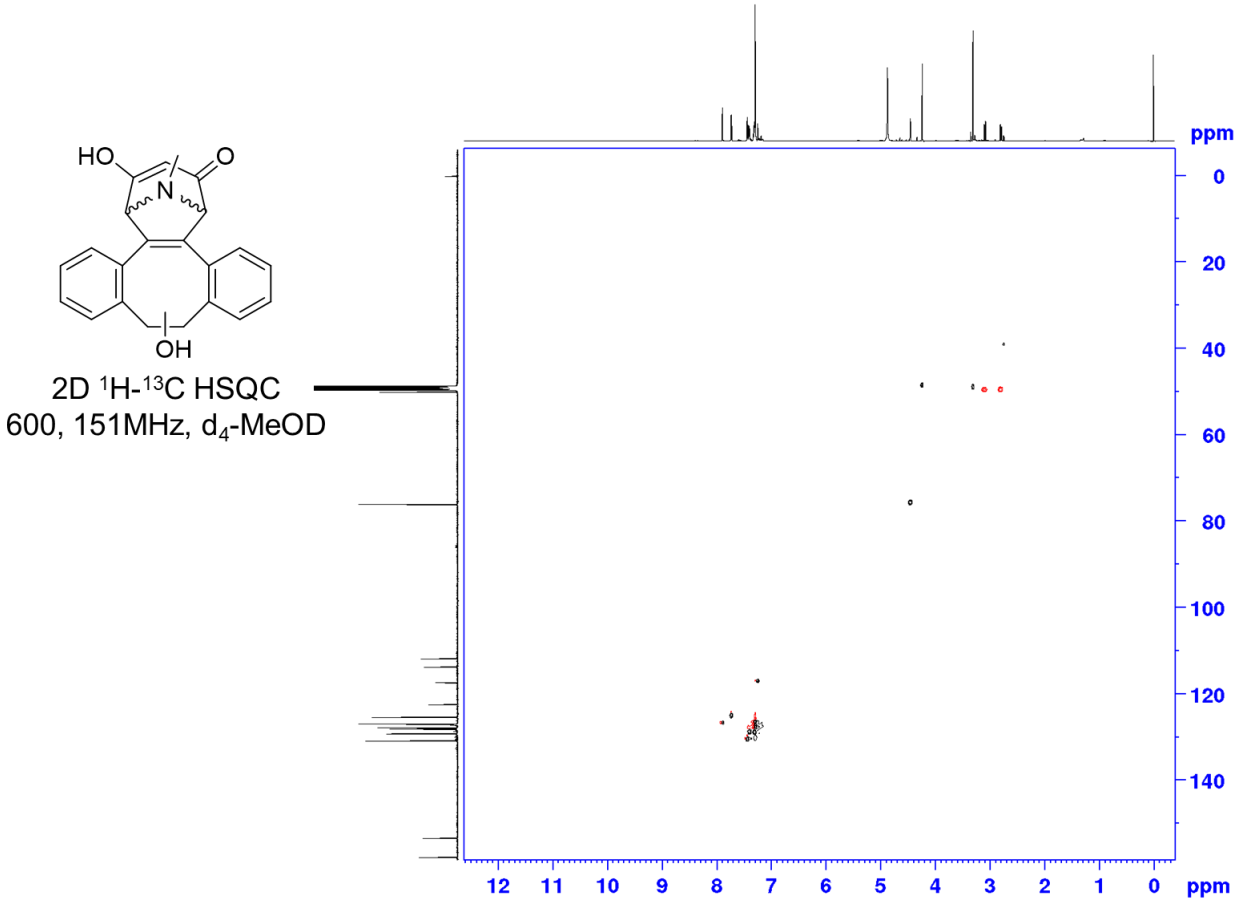

2D ^{1}H-^{13}C HSQC spectrum taken automatically after NMR kinetics experiment.

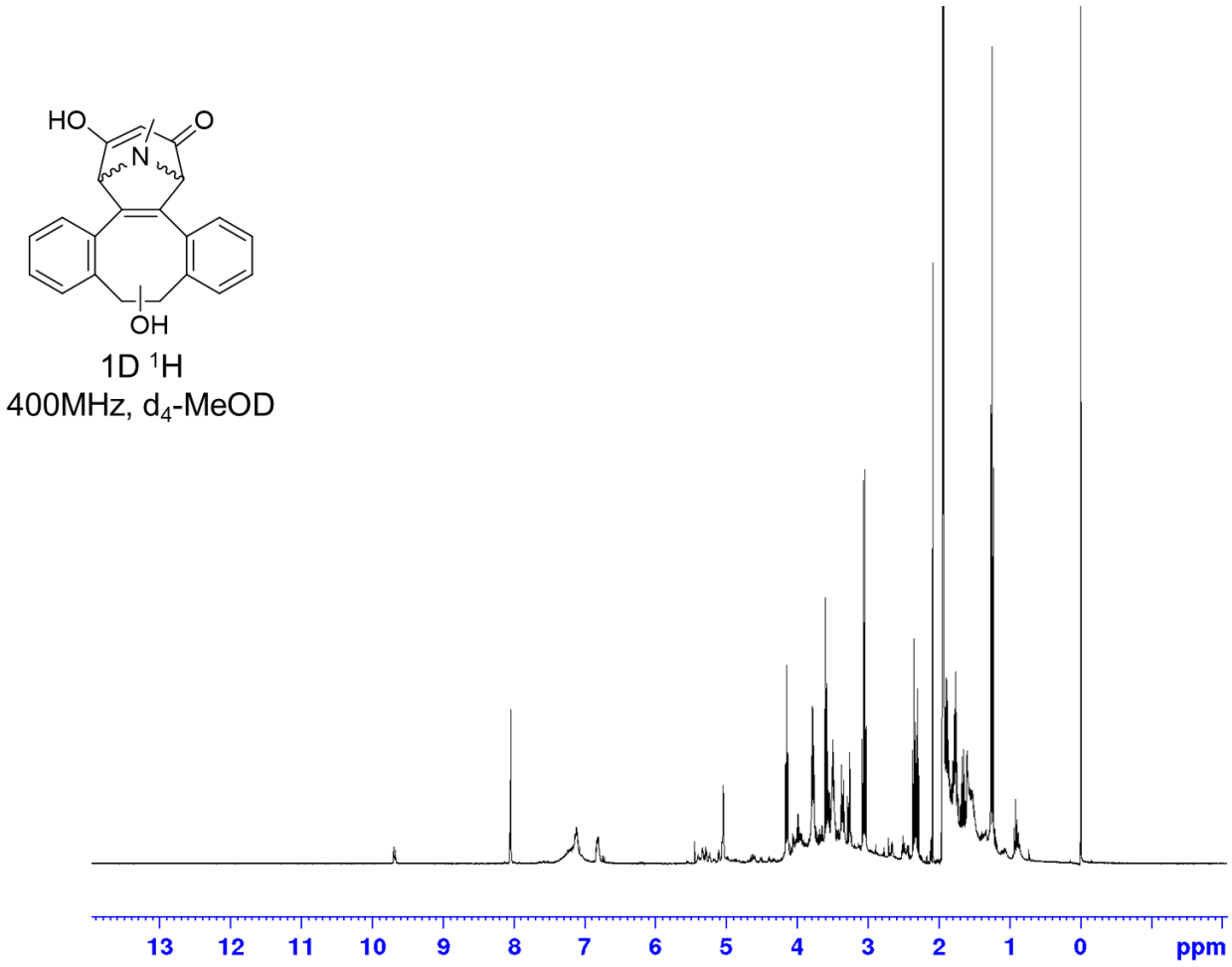

^{1}H spectrum taken after the product from the NMR kinetics experiment was purified.

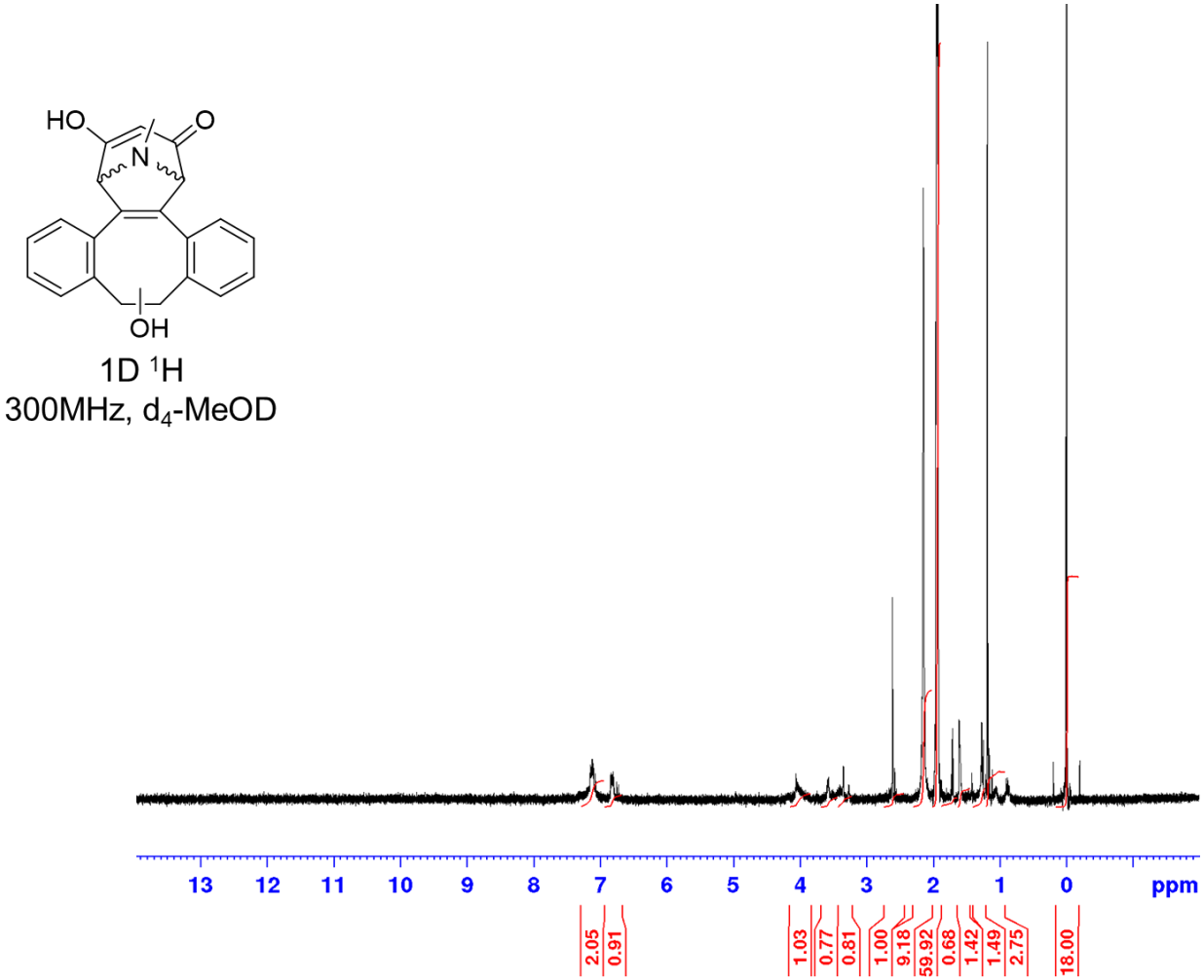

^{1}H spectrum taken after a second attempt at purifying the product with basic alumina.

Spectra from Chapter 3:

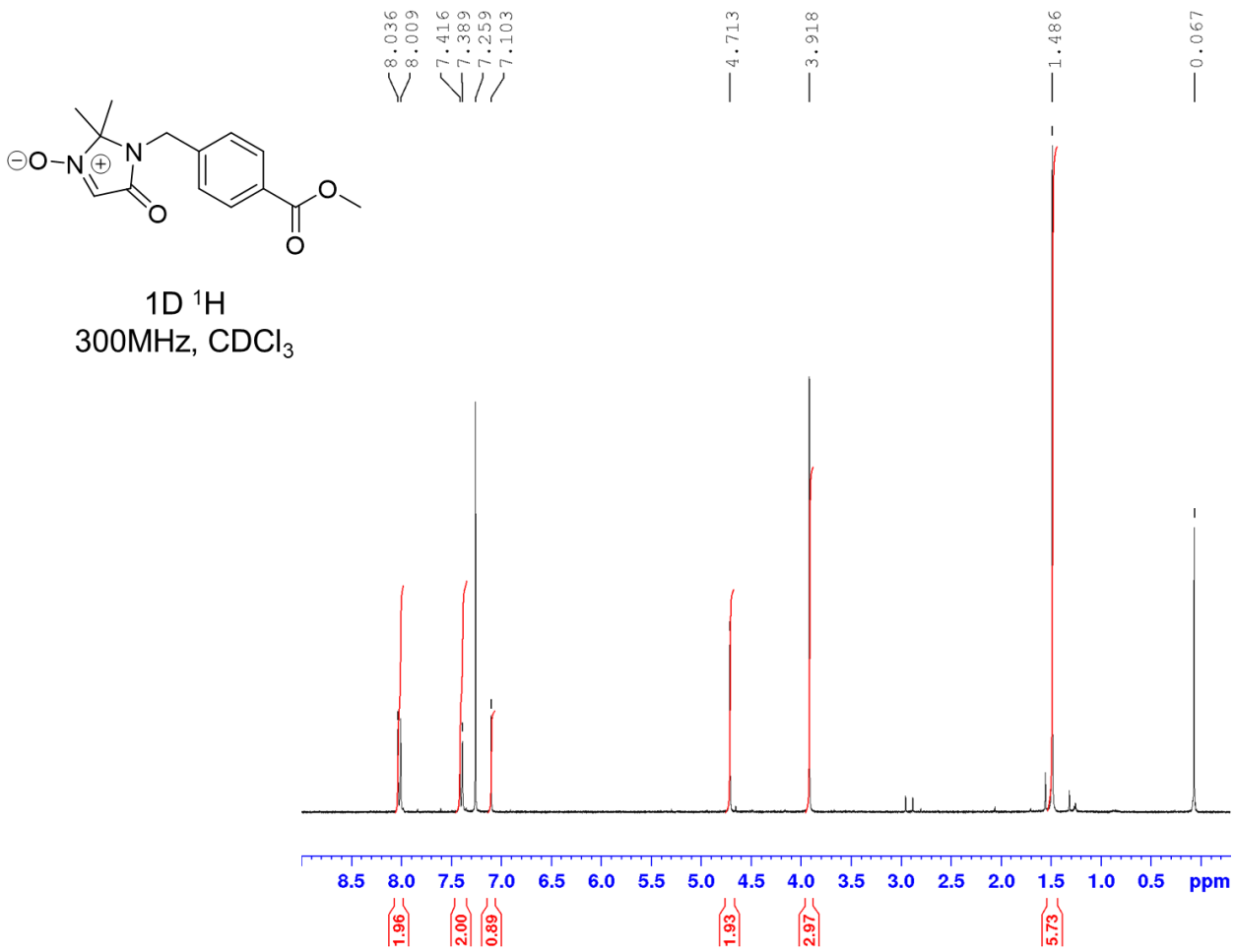

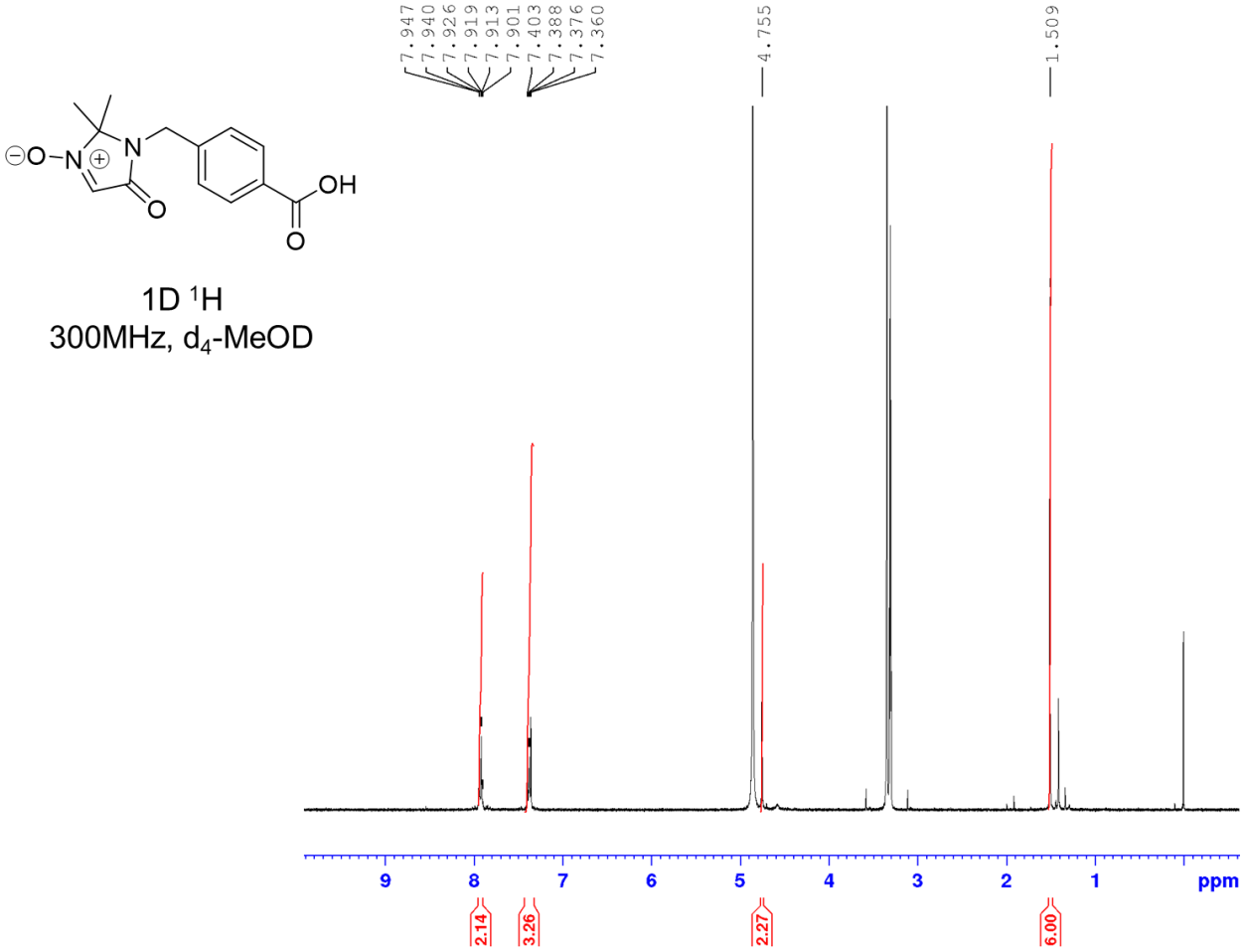

1D ^{1}H
300MHz, d_4-MeOD

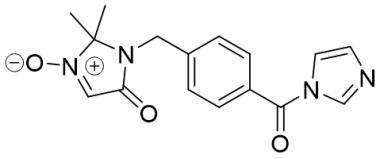

1D ^{1}H
400MHz, d_6-DMSO

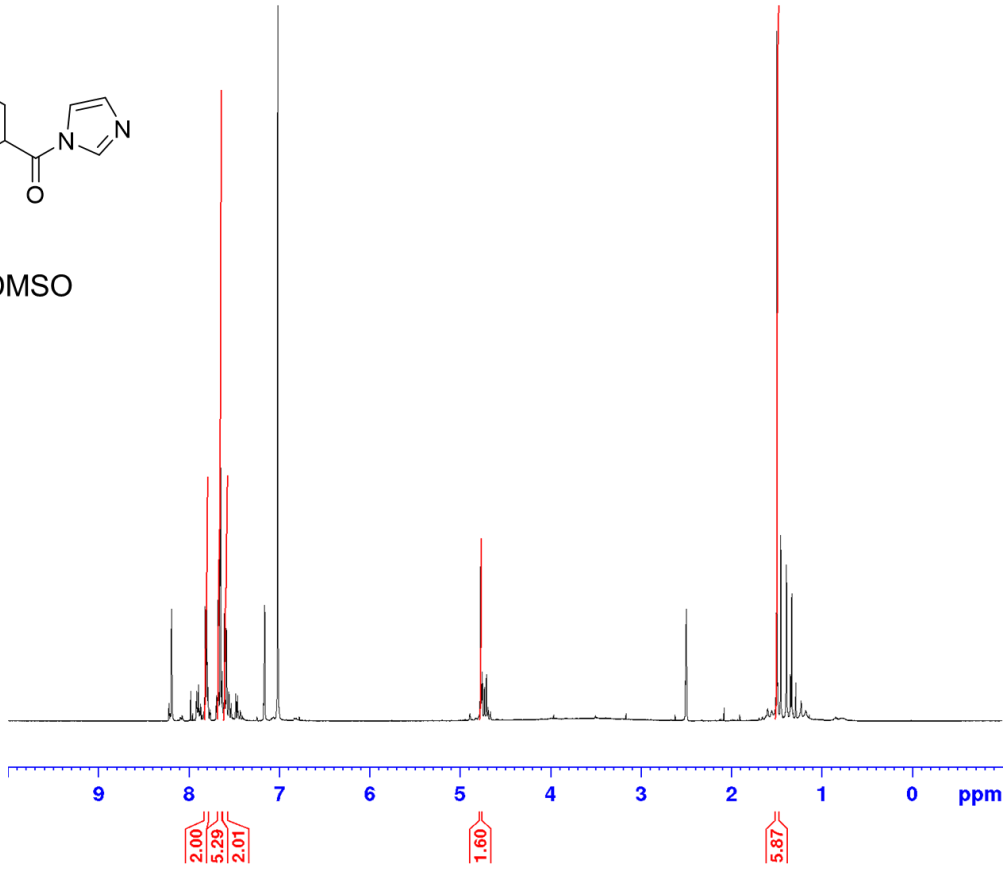

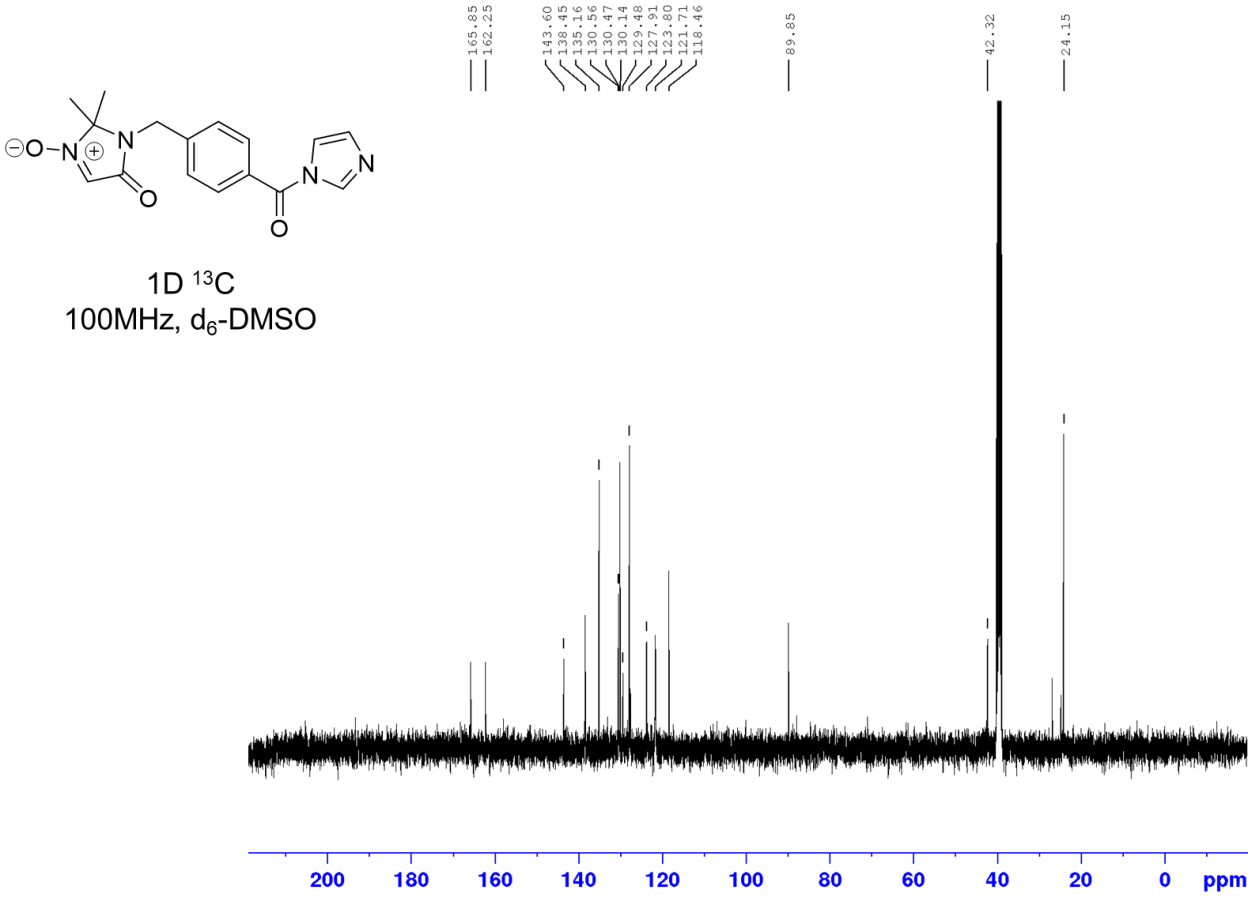

1D ^{13}C
100MHz, d_6-DMSO

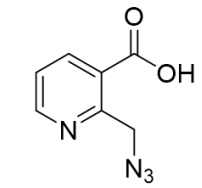

1D ^{1}H
600MHz, $CDCl_3$

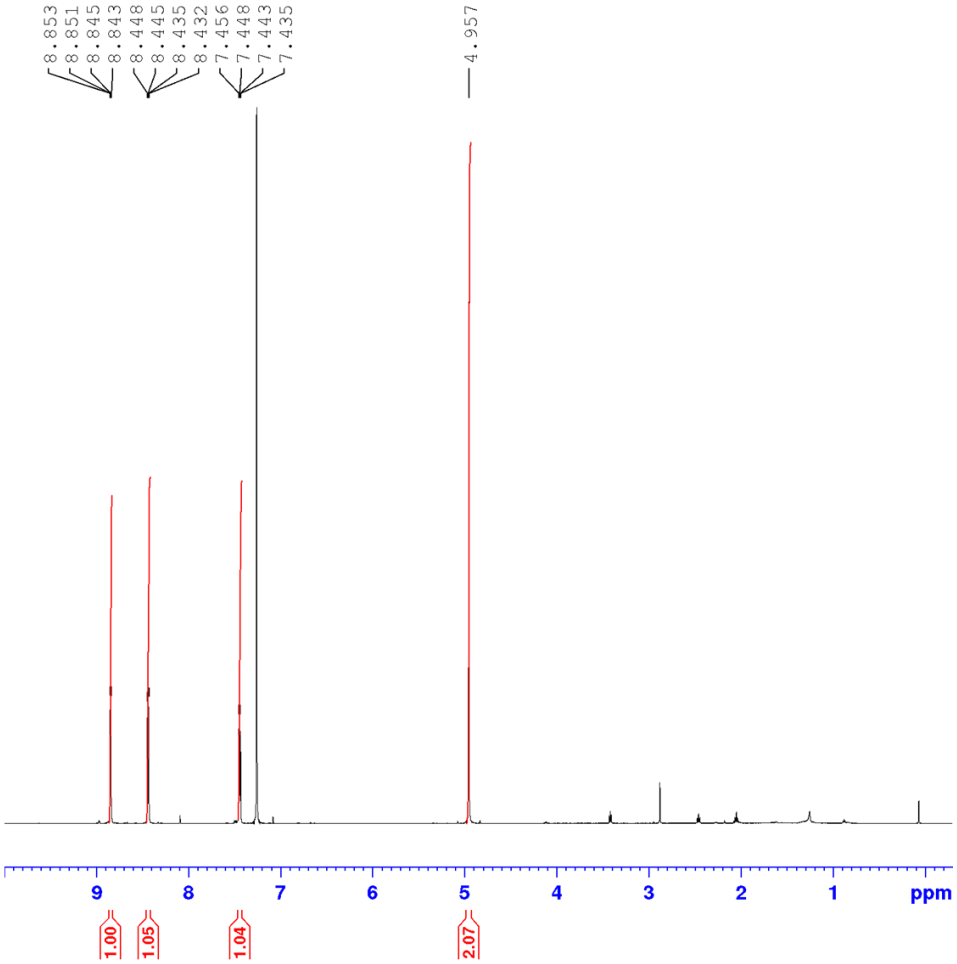

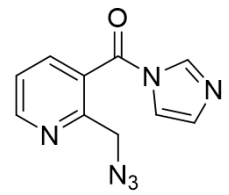

1D ^{1}H
300MHz, $CDCl_3$

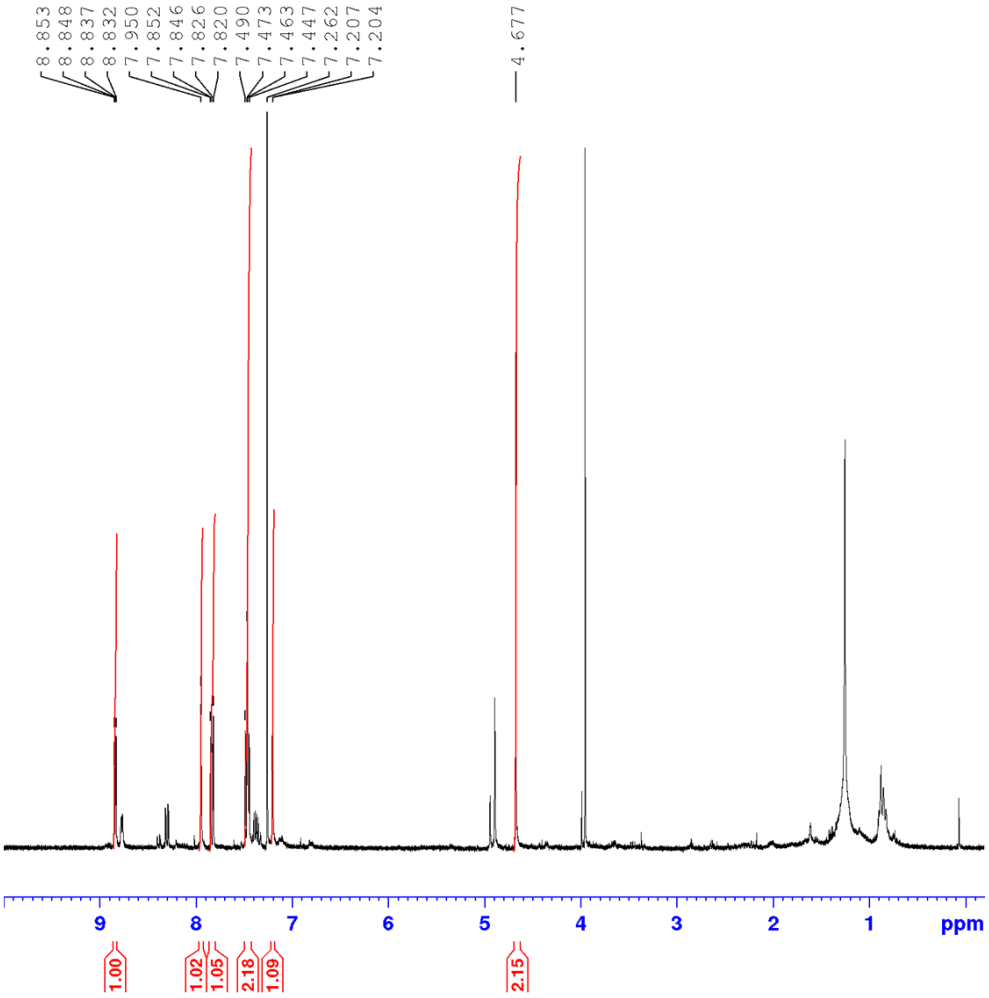

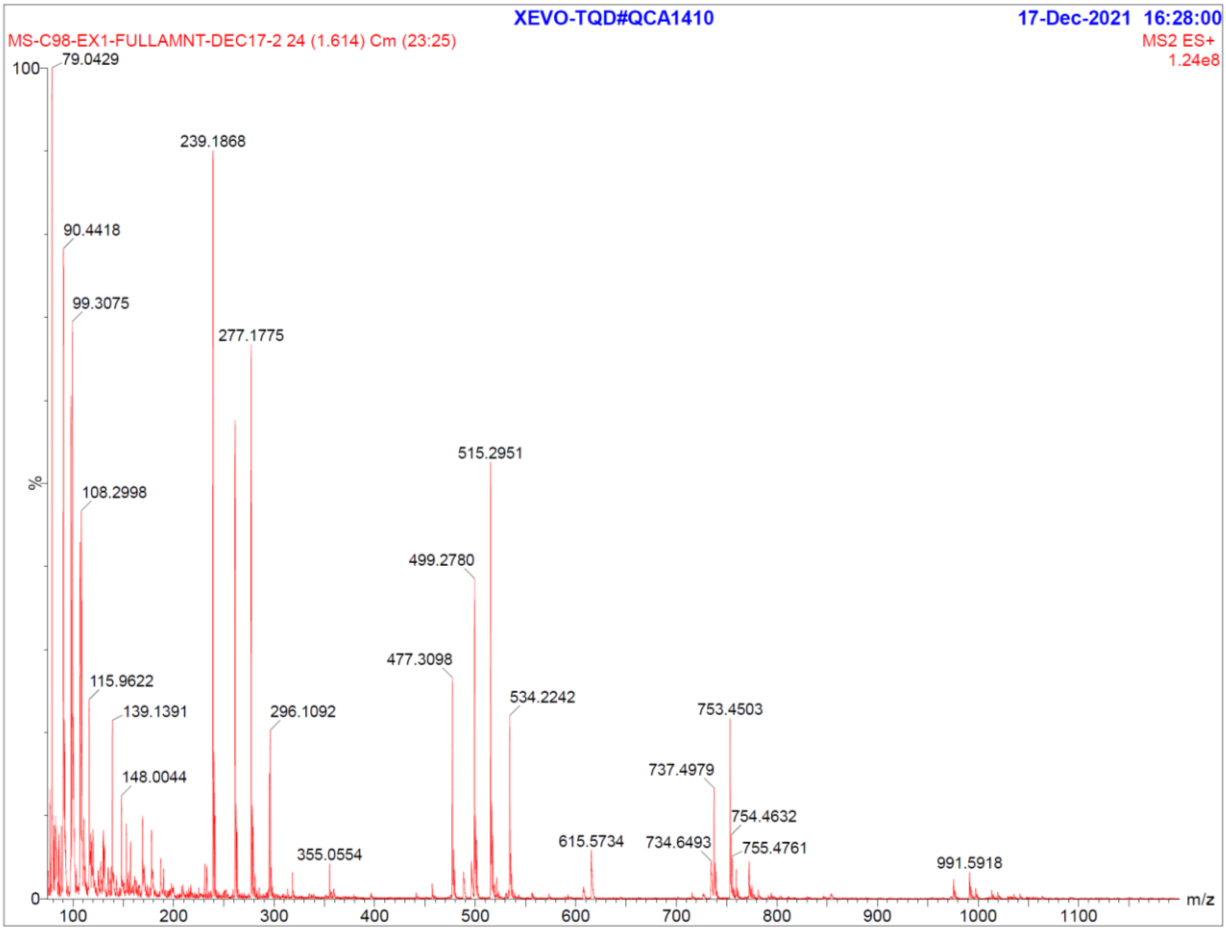

MS analysis of the icSHAPE proxy reaction with DMImO-I, d-ATP, and DIBO using Micromass Q-TOF I mass spectrometer. (ESI+- mode, direct injecton).